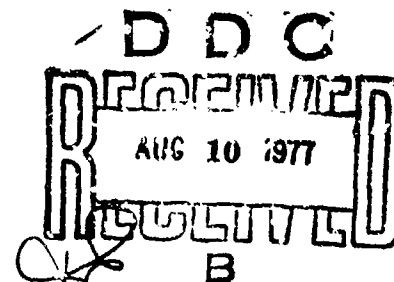ADA042783

A REVIEW OF METHODS FOR ESTIMATION OF AEROACOUSTIC LOADS ON FLIGHT VEHICLE SURFACES

BOLT BERANEK AND NEWMAN INC.
50 MOULTON STREET
CAMBRIDGE, MASSACHUSETTS 02138

FEBRUARY 1977

D D C

AUG 10 1977

B

FINAL REPORT JANUARY 1975 - JULY 1976

Ur 1 - AD-A041 198

NOTICE

When Government drawings, specifications, or other data are used for any purpose other than in connection with a definitely related Government procurement operation, the United States Government thereby incurs no responsibility nor any obligation whatsoever; and the fact that the Government may have formulated, furnished, or in any way supplied the said drawings, specifications, or other data, is not to be regarded by implication or otherwise as in any manner licensing the holder or any other person or corporation, or conveying any rights or permission to manufacture, use, or sell any patented invention that may in any way be related thereto.

This technical report has been reviewed and is approved.

ROBERT W. GORDON
Project Engineer

ROBERT M. BADER, Chief
Structural Integrity Branch

FOR THE COMMANDER

HOWARD L FARMER, Col, USAF
Chief, Structural Mechanics Division

REPORT DOCUMENTATION PAGE

READ INSTRUCTIONS
BEFORE COMPLETING FORM

1. REPORT NUMBER	2. GOVT ACCESSION NO.	3. RECIPIENT'S CATALOG NUMBER
AFFDL-TR-76-91, Vol. 2		

4. TITLE (and Subtitle)

A Review of Methods for Estimation of Aeroacoustic Loads on Flight Vehicle Surfaces.

5. TYPE OF REPORT & PERIOD COVERED

Final Report.
January 1975 — July 1976

6. PERFORMING ORG. REPORT NUMBER

BBN-3260

7. AUTHOR(s)

Eric E. Ungar, John F. Wilby, Donald B. Bliss, B. Pinkel, A. Galaitsis

8. CONTRACT OR GRANT NUMBER(s)

F33615-75-C-3017

9. PERFORMING ORGANIZATION NAME AND ADDRESS

Bolt Beranek and Newman Inc.
50 Moulton Street
Cambridge, Massachusetts 02138

10. PROGRAM ELEMENT, PROJECT, TASK AREA & WORK UNIT NUMBERS

Project No. 1471
W. U. 14710226

11. CONTROLLING OFFICE NAME AND ADDRESS

Air Force Flight Dynamics Laboratory
Air Force Systems Command
Wright-Patterson AFB, OH 45433

12. REPORT DATE

Feb 1977

13. NUMBER OF PAGES

219

14. MONITORING AGENCY NAME & ADDRESS(if different from Controlling Office)

219 p.

15. SECURITY CLASS. (of this report)

Unclassified

15a. DECLASSIFICATION/DOWNGRADING SCHEDULE

16. DISTRIBUTION STATEMENT (of this Report)

Approved for public release; distribution unlimited.

17. DISTRIBUTION STATEMENT (of the abstract entered in Block 20, if different from Report)

18. SUPPLEMENTARY NOTES

19. KEY WORDS (Continue on reverse side if necessary and identify by block number)

Aeroacoustic loads, surface pressures, nearfield noise, jet noise, noise from powered lift systems, propeller noise, engine noise, blasts from armament, boundary layer pressures, cavity noise

ABSTRACT (Continue on reverse side if necessary and identify by block number)

Alternative techniques for predicting the aeroacoustic loads that act on flight vehicle surfaces due to propulsion and powered lift systems, surface flows, and armament are reviewed, evaluated, and compared.

DD FORM 1473 EDITION OF 1 NOV 65 IS OBSOLETE
1 JAN 73

060 /00

FOREWORD

This report was prepared by Bolt Beranek and Newman Inc.,
Cambridge, Massachusetts, for the Structural Integrity Branch,
Structural Mechanics Division, Air Force Flight Dynamics Labora-
tory, Wright-Patterson Air Force Base, Ohio under Contract
F33615-75-C-3017. The work described herein is a part of the
Air Force System Command continuing program to establish methods
of predicting and controlling the aero-acoustic environment of
flight vehicles. The work was directed under Project 1471,
"Aero-Acoustic Problems in Flight Vehicles, Task 147102 Aero-
Acoustics." Messrs. Robert Gordon and Davey L. Smith of
AFFDL/FBE served as Air Force Project Engineers. Their cooper-
ation and assistance are gratefully acknowledged.

The work presented herein was performed by several members
of the staff of Bolt Beranek and Newman Inc., under the techni-
cal direction of Dr. Eric E. Ungar, who also was responsible
for integration and presentation of the results. Dr. John Wilby
and Mr. B. Pinkel contributed the portions dealing with jet
noise, and Dr. A. Galaitsis provided the part addressing fan/
compressor noise. Mr. Richard Hayden prepared the part
pertaining to powered lift devices, Mr. Joseph Smullin contrib-
uted the section dealing with propeller noise, and Mr. Robert White
developed the portion concerned with armament. Dr. Donald Bliss
contributed the sections dealing with surface flows and cavity
noise.

Background information on which this report is based is presented in a companion volume, "A Review of Methods for Estimation of Aeroacoustic Loads on Flight Vehicle Surfaces," AFFDL-TR-76-91, Vol. II.

This report concludes the work on Contract F33615-75-C-3017, which covered a period from January 1975 to October 1976. The manuscript was released by the authors in October 1976.

ACCESSION for		
NTIS	White Section	☑
DDC	Buff Section	☐
UNANNOUNCED		☐
JUSTIFICATION		
BY		
DISTRIBUTION/AVAILABILITY CODES		
Dist.		SPECIAL
A		~

TABLE OF CONTENTS

TABLE OF CONTENTS *(Cont.)*

TABLE OF CONTENTS *(Cont.)*

LIST OF FIGURES

LIST OF FIGURES *(Cont.)*

LIST OF FIGURES (Cont.)

LIST OF FIGURES *(Cont.)*

LIST OF FIGURES *(Cont.)*

LIST OF FIGURES *(Cont.)*

LIST OF FIGURES *(Cont.)*

page

LIST OF FIGURES *(Cont.)*

LIST OF FIGURES *(Cont.)*

LIST OF TABLES

SECTION I

INTRODUCTION

The fluctuating pressures that act on the surfaces of flight vehicles due to noise from propulsion or powered left systems, due to surface flows, and due to armament constitute potentially important loads that need to be considered in the design process.

In order to compile a guide for predicting the significant aeroacoustic loads on flight vehicles that represents the best currently available practice, an extensive review of the litera- ture was undertaken and alternative prediction techniques were evaluated. The results of these reviews and evaluations are pre- sented in the present report, together with some extensions, clarifications, simplifications, and corrections of previous methods.

Although considerable effort has been made to make this re- port self-contained and meaningful to the nonspecialist in aero- acoustics, no attempt has been made to include the fundamentals of acoustics and aerodynamics.

In order to conserve space, computer programs have not been reproduced; since such programs are useful only with extensive documentation, the reader is referred to the original sources. Similarly, the data presentations included here are limited to those that illustrate important trends or that serve as the bases for empirical prediction methods; for more extensive or detailed data collections, the reader is again referred to the original literature.

The present volume does not include discussions of two topics appearing in the estimation guide volume, namely: fan/compressor noise and noise of internal combustion engines. Discussion of

1

fan/compressor noise has been omitted here, because a sufficient treatment appears in the recent literature and because a discussion of the background and physical mechanisms was included in the estimation guide volume, where this discussion also provides some guidance for the user of the prediction methods presented there. Discussion of internal combustion engine noise has been omitted here, because no relevant information has become available since appearance of the publication from which the suggested prediction technique has been taken.

SECTION II

JET NOISE

2.1 Introduction

This section deals with the prediction of noise from the
exhausts of turbojet and turbofan engines, including shock-
free noise and shock noise from nozzles of any practical shape
(circular, slot, annular, coaxial, etc.), but excluding the
noise associated with suppressor nozzles, such as multitube
and multilobe designs. Afterburner and thrust reverser noise
is also included, but such other sources of combustion noise
as core noise are not considered here. Discussion of noise
radiation from jet/airframe interactions is here confined to
the case of thrust reversers.

Most of the published methods for the prediction of exhaust
noise have been concerned with farfield, rather than nearfield,
sound pressure levels. However, for the case of flow from cir-
cular exhaust nozzles, several prediction methods have been
developed during recent years. Since these prediction methods,
of necessity, need to serve as the basis for nearfield predic-
tion methods of other exhaust flow conditions, special emphasis
is given to these methods in the discussion.

Although none of the available prediction methods is ac-
ceptable without reservations, the procedure of Plumblee *et al*
has been selected to serve as the basis for nearfield noise
predictions. Modifications to this method are developed to ac-
count for nozzle shape, afterburner effects, coaxial exhausts,
shock noise and forward motion. However, for thrust reversers,
a new model is constructed, since this noise source mechanism
differs from the others.

3

Reflection and scattering effects associated with the presence of the airframe structure are also discussed, pressure correlation data on the airframe structure are reviewed, and a related prediction model is proposed.

2.2 Subsonic and Shock-Free Supersonic Exhausts

2.2.1 Circular nozzles

The methods for predicting nearfield noise fall into three categories:

1. Analytical methods, in which nearfield noise estimates are derived from basic flow parameters.

2. Curve-fitting methods, in which equations are fitted to test data.

3. Scaling methods, in which a set of test data is taken as the reference base and rules are developed for adjusting the reference values to account for changes in the important parameters.

Analytical Methods

Chen, Benzakein and Knott [1, 2, 3]* have studied the applicability of equations derived by Franz [4]. These equations describe the acoustic pressure field of an axisymmetric jet, as a function of the distance from the jet and the sound power radiated by it per unit volume. Franz's equations are derived for three different assumptions regarding the structure of the jet flow field: (1) laterally oriented quadrupoles, (2) longitudinal quadrupoles, and (3) isotropic turbulence. The equation for isotropic turbulence is the simplest of the three and fits the test data nearly as well as the other two cases. This

---

*Numbers in brackets refer to list of references.

equation, reproduced here for purposes of illustration, is

$$\overline{(p-p_0)^2} = \frac{\rho_0 c_0 W}{4\pi r^2} \left[1 + \frac{2c_0^2}{r^2\omega^2} + 12 \frac{c_0^4}{r^4\omega^4} \right] c^{-5} . \tag{1}$$

The quantity W denotes the radiated sound power per unit volume and is given by

$$W \simeq \beta_1 \frac{\overline{\rho^2 u'^4 V^4}}{\rho_0 c_0^5 \ell} \tag{2}$$

where u' is the fluctuating component of the longitudinal velocity, V is the steady velocity component, and ℓ is the local scale of the turbulence in the jet. Chen et al determine, for each 1/3 octave band, the noise at a point in the nearfield by integrating the contributions from all positions in the jet, making use of data on the distribution of u', V, and ℓ with position in the jet.

Comparisons [1] between values computed by this method and experimental data reveal differences in some areas of as much as 10 dB. Because of the possibility of large errors, and because of its complexity, application of this method for prediction purposes is not recommended.

Maestrello's analytical method [5] is based on first principles, but needs considerable additional development to be applicable to practical nearfield acoustic pressure calculations.

Curve-Fitting Methods

Plumblee *et al.* [6] start with the Lighthill equation and introduce into it: (a) directionality terms suggested by Williams [7], Ribner [8], and Lilley [9] and additional directionality terms needed to improve agreement with test data, and (b) an expression for the effect of distance r, the form of which is suggested by Equation (1) obtained by Franz [4]. The relationship synthesized in this manner is

$$\bar{p}^2(T,M,r,\theta) = \frac{KT^8 M^n (1 + \alpha^2 M^2)^{5/2} (1 + \cos^4\theta)}{\left[\left(1 - \frac{M\cos\theta}{1+C_6 e^{-C_7 r}}\right)^2 + \alpha^2 M^2\right]^{5/2} \left(1 + \frac{C_4 e^{-C_5 \theta}}{1+C_5 e^{-C_7 r/4}}\right)} \left(\frac{C_1}{r^2} + \frac{C_2}{r^4} + \frac{C_3}{r^6}\right)$$

(3)

with the parameters $KT^8 M^n$, α^2, and C_i given by empirically determined functions of M and T, by means of which Plumblee *et al.* attempt to fit this equation to an extensive set of nearfield acoustic pressure data, accounting for the effects of jet velocity, temperature and Mach number on a 3.5 inch diameter jet.

Scaling Methods

Two approaches have been presented: one by Thomson [10], and one by cockburn and Jolly [11] using the test data and methods presented by Hermes and Smith [12]. Sutherland and Browr [13] discuss methods of correcting the nearfield data for ground reflections. Rudder and Plumblee [14] present resumes of the Thomson and the Cockburn and Jolly methods, as well as of the Plumblee empirical equation.

In the empirical methods [10, 11], a set of nearfield noise contours is established as a reference set, and rules are provided for computing adjustments to these values for changes in jet velocity and for determining noise frequency spectra. The reference sets of noise contours for the two scaling methods correspond to the following conditions:

	V_j (ft/sec)	T_j static ($^\circ$R)
Thomson [10]	2000	1252
Cockburn [11]	1920	1130

The reference contours for the Cockburn method consist of the test data obtained by Hermes and Smith on a J57-P21 engine at 100% military thrust.

Accuracy of Empirical Methods

It is of considerable interest to explore the accuracy with which the several empirical methods mentioned above predict experimental results. Published test data references and the range of exhaust jet conditions covered by them are given in Table 1.

7

TABLE 1. SOURCES OF TEST DATA

Reference	Plumblee [6]	Smith et al [15]	Cox et al [16]	Howes et al [17]
Flow Source	Air Supply	YJ-93-GE-3	YJ-79 turbojet	Jet engine
Nozzle	(a)*	Adjustable area converging-diverging*	Adjustable area converging-diverging*	Adjustable area converging-diverging*
Nozzle exit diameter (ft)	0.292	2.85 to 3.23	1.81 to 2.26	2.2 to 2.33
Velocities (ft/sec)	936 to 4326	444 to 3246	1595 to 2290	1850 to 2590
Mach Number	.8 to 1.59	.49 to 1.28	(c)	(c)
Exhaust temperatures static ($°R$)	575 to 3734	1083 to 2950	1241 to 1196	1225 to (b)
Pressure ratios	(c)	(c)	1.73 to 1.82	2.2 to (b)

Note: The high and low values for any one parameter are not necessary for the same operating conditions as the respective high and low values for the other parameters.

(a) Converging for subsonic jets and converging-diverging for supersonic jets.

(b) Temperature and pressure ratio not given for afterburner condition.

(c) Not given.

* For all supersonic flows, converging-diverging nozzles were used with area ratios providing shock-free flow.

8

The Plumblee data cover a much wider range of conditions than are of interest for practical turbojet and turbofan engines at takeoff and cruise thrust. To provide some insight into the range of conditions of practical interest, Table 2 lists take-off conditions for a turbojet and various turbofans based on a level of technology corresponding to the J-93 engine. The jet conditions for other levels of engine technology will differ from those listed in this Table, but may be expected largely to fall within the range of conditions indicated.

Table 3 compares overall sound pressure levels computed by the methods of [10], [11], and [6] with each other and with measured data, for several different measurement locations, for a jet with V_j = 2221 ft/sec, $T_{j \text{ static}}$ = 1360°R. The calculations here involve only small corrections for V_j and T_j, because the selected engine conditions correspond nearly to those of the reference contours. The method proposed by Cockburn involves a correction for jet velocity only; the Thomson method involves corrections for both jet velocity and jet temperature.

Plumblee's measured and computed values are in good agreement with each other. The Cockburn method predicts the highest values. The Thomson method predicts noise values for the most part about 4 dB below the Cockburn method, and the Plumblee method predicts values about 8 dB below the Cockburn method. The Cockburn reference noise contours are based on measurements made on a jet engine. These values contain some machinery noise and would be expected to be higher than values determined from the measurements by Plumblee on a model jet attached to an air supply.

9

TABLE 2. TYPICAL JET PARAMETER VALUES FOR TURBOJET AND TURBOFAN ENGINES AT TAKE-OFF CONDITIONS

(a) Turbojet

Condition	Jet Velocity (ft/sec)	Exhaust Gas Temperature (°R) Total	Static	Mach No.
Military	2466	2066	1661	1.25
Max A/B	3246	3651	2950	1.25

(b) Turbofan at Max Thrust

By Pass Ratio	Fan Pressure Ratio	Fan Jet Velocity (ft/sec)	Fan Jet Static Temp (°R)	Core Jet Velocity (ft/sec)	Core Jet Static Temp (°R)	Core Mach No.
1	2	1190	~519	2060	1630	1.04
2	1.6	960	~519	1920	1620	.97
6	1.3	700	~519	1500	1600	.76

TABLE 3. COMPARISON OF COMPUTED AND MEASURED SOUND PRESSURE FOR*
V_j = 2221 ft/sec and $T_{j \; static}$ = 1360°R

Measurement Coordinates		Overall Sound Pressure Level (dB, re 2×10^{-5} N/m^2)			
		Computed			Measured
$\frac{X}{D}$	$\frac{Y}{D}$	Thomson [10]	Cockburn [11]	Plumblee [6]	Plumblee [6]
0	14	130.8	133.8	125.5	127
5	19	130.9	134.7	126	126
10	23.5	131.0	134.7	–	–
15	28	131.1	134.7	–	–
0	3	–	139.5	–	–
5	7.5	140.9	143.7	137.5	137.5
10	11.7	141.3	144.1	136.0	135.5
15	15	141.4	145.5	135.2	134.0
20	17.7	141.7	144.7	134	133
25	19	141.7	144.4	–	133
5	3	151.1	154.4	150	148
10	5.2	151.9	155.0	144	144
15	5	151.3	155.0	141	140

---

*The engine operating condition corresponds to that of Figure 30 of [6].

11

Table 3 corresponds to non-afterburning operation of a turbojet engine. Table 4 similarly corresponds to the upper end of the jet velocity range of interest, that is, approximately to the Max A/B conditions of Table 2, for which large corrections to the reference values in the Thomson and Cockburn methods are required.

Again, Plumblee's computed and measured values are in good agreement with each other. On the other hand, the Thomson method underestimates the noise, whereas the Cockburn method overestimates it by 5 to 10 dB. These discrepancies are due to inadequate consideration of temperature effects. These are not included at all in the Cockburn method, and are overestimated in the Thomson method.*

It is not surprising that the values computed by the Plumblee equation agree well with most of the noise values measured by Plumblee, because the equation represents an empirical fit to these data. However, Tables 3 and 4 represent only a small part of the range of data of interest, and one needs to consider whether there exist regimes where the Plumblee equation represents the data inadequately. Comparison of values computed by the Plumblee equation to test data reveals discrepancies of less than 5 dB over most of the very extensive test regime covered. The largest discrepancies occur for supersonic

*In the Thomson method the correction for temperature here is -7.8 dB, based on the assumption that the noise varies as ρ_j^2, and that ρ_j^2 varies inversely as T_j^2. The Thomson method may overestimate the effect of temperature. As pointed out by Tanna [18], the temperature that should be used is that near the end of the potential core, at a position where the turbulence is a maximum. The use of this temperature to the second power results in a variation of the noise intensity with T_j^1, where T_j is the temperature at the nozzle exit. This suggests that the correction for temperature should be half of that given by the Thomson procedure. If the values given in Table 4 under the Thomson method correspondingly are increased by 3.9 dB, they would be brought above the Plumblee values by an amount comparable to that in Table 3.

12

TABLE 4. COMPARISON OF COMPUTED AND MEASURED SOUND PRESSURES FOR*
V_j = 3267 ft/sec and $T_{j\ static}$ = 3069°R

Measurement Coordinates		Overall Sound Pressure Level (dB, re 2×10^{-5} N/m²)			
$\dfrac{X}{D}$	$\dfrac{Y}{D}$	Computed			Measured
		Thomson [10]	Cockburn [11]	Plumblee [6]	Plumblee [6]
0	14	128.8	143.9	129	-
5	19	129.1	144.4	132	-
10	23.5	129.2	144.4	135	135
15	28	129.4	144.6	-	-
0	3		146.2		
5	7.5	139.3	153.6	143	145
10	11.7	140.7	155.0	143	145
15	15	141.6	157.4	142.5	142
20	17.5	143.3	154.6	141.5	140
25	19	143.3	156.2	141	-
5	3	150	166.2	155	-
10	5.2	153.9	168.5	151	149
15	5	151.6	168.5	149	144.5

*The engine operating condition corresponds to that of Figure 31 of [6].

13

jets* for values of X/D less than 7, and for the highest octave band investigated, as illustrated in Figures 1,2, and 3.

*Although in each test case the nozzle had a converging-diverging contour, there may have been some shocks in the jet, which may be responsible for these discrepancies. Figure 8 of [6] is a photograph of the Mach 1.5 jet, revealing a characteristic diamond-shaped shock-pattern.

The frequency of the noise generated by shock waves radiat'ng at right angles to the jet is given [19]

$$f = \frac{2c_0}{3D\sqrt{PR - 1.89}} \tag{4}$$

w. 're c_0 denotes the velocity of sound in air (ft/sec), PR is the pressure ratio across the nozzle, and D represents the nozzle diameter (ft).

For a Mach number of 1.25 (i.e., PR ≈ 2.6), the value of fD is ⌐⌐500 Hz-inch. This fa-ls within the octave band 8400-16800 Hz-inch, where Figures 1 and 2 reveal the upswing in measured noise at low values of X/D. For a jet Mach number of 1.5 (i.e., PR ≈ 3.7), the value of fD given by the above equation is 6700 Hz-in h, which falls in the 4200-8400 Hz-inch octave band, where Figure 3 reveals the upswing in measured noise. This upswing is even more marked in the next higher band.
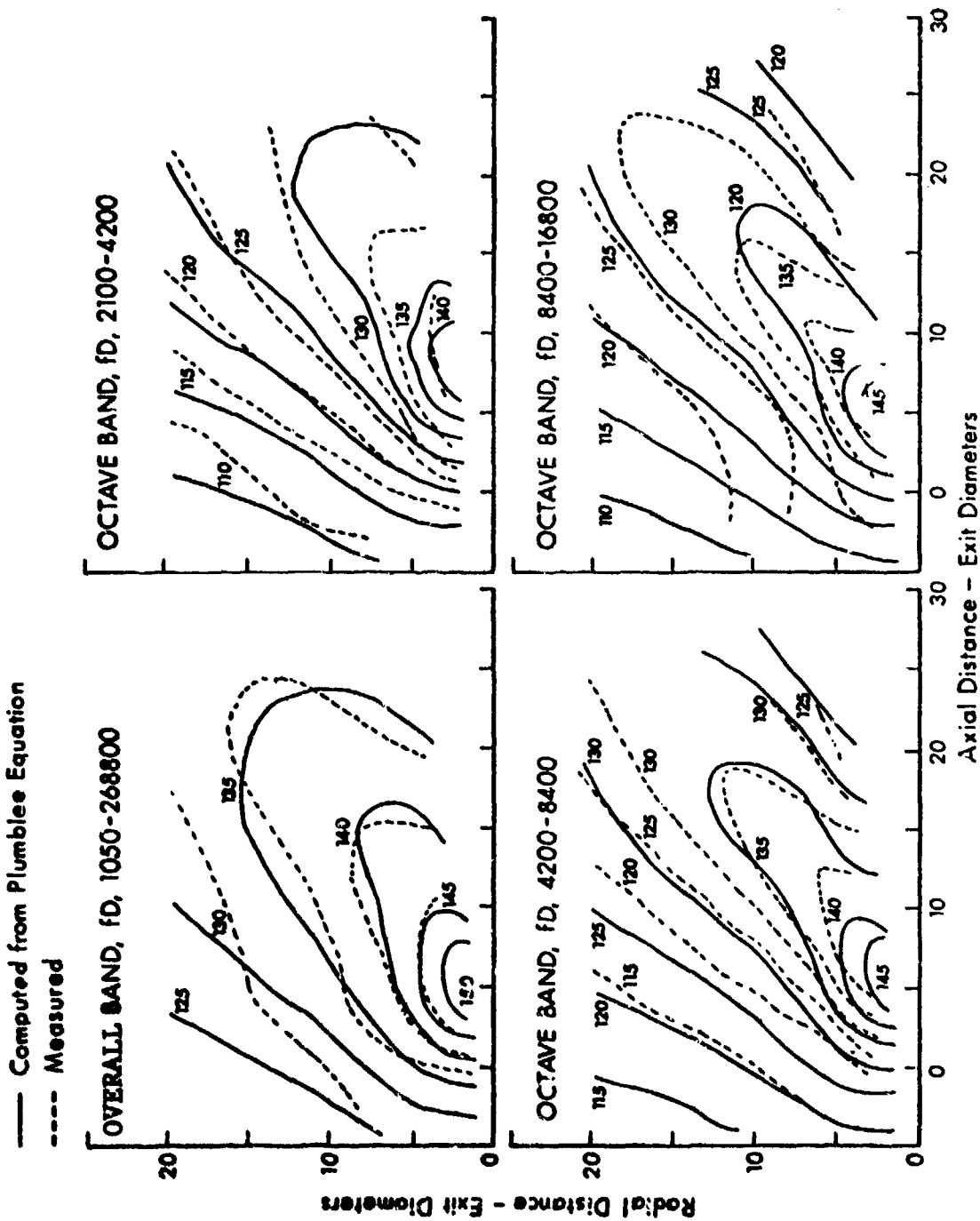
FIG. 1. COMPARISON OF MODEL JET EXPERIMENTAL AND CALCULATED CONTOURS MACH NO. = 1.25, TEMP = 1360°R, VELOCITY = 2221 FPS (FIG. 30, REF. 6).
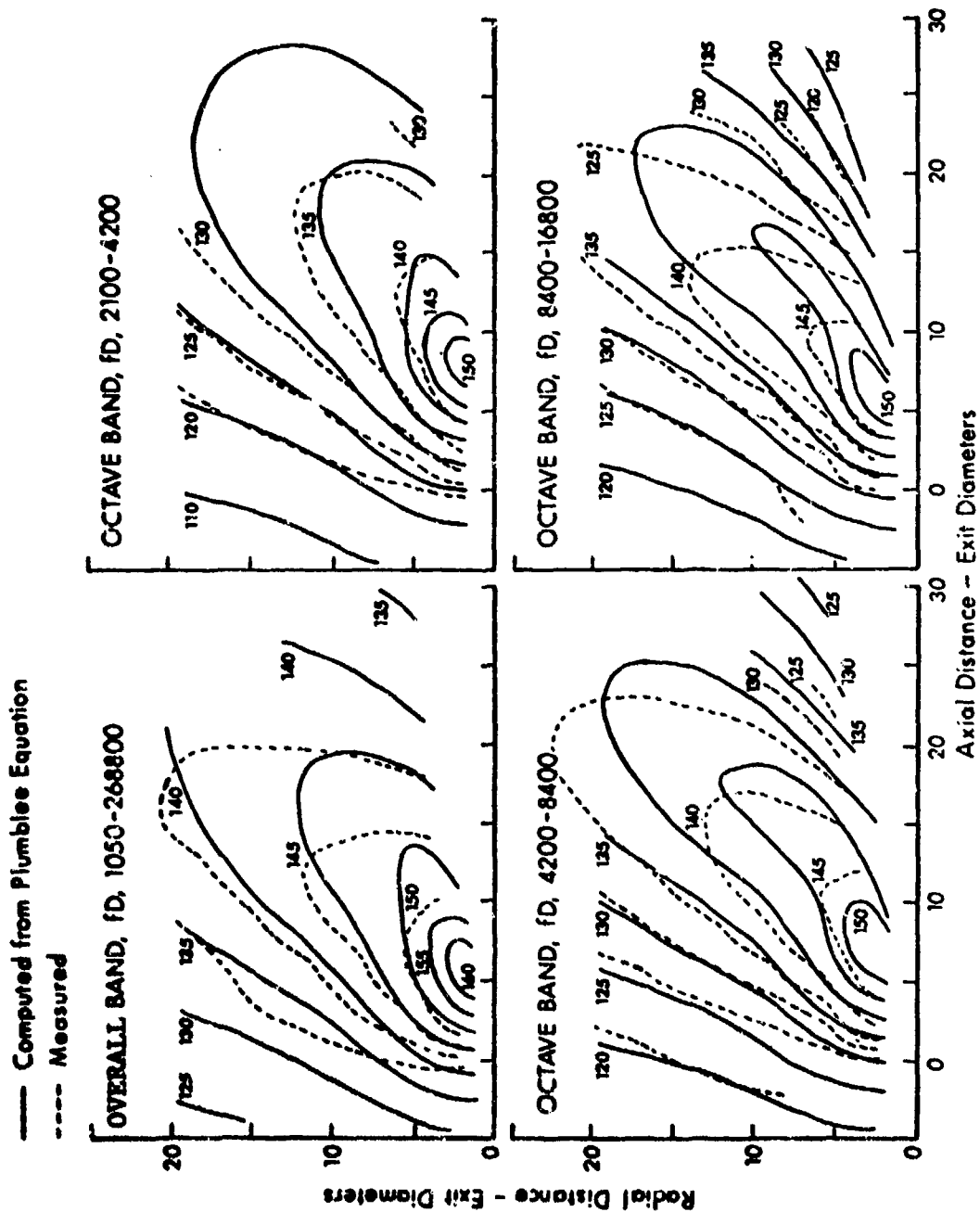
FIG. 2. COMPARISON OF MODEL JET EXPERIMENTAL AND CALCULATED CONTOURS
MACH NO. = 1.25, TEMP = 3069°R, VELOCITY = 3267 FPS
(FIG. 31, REF. 5).

16
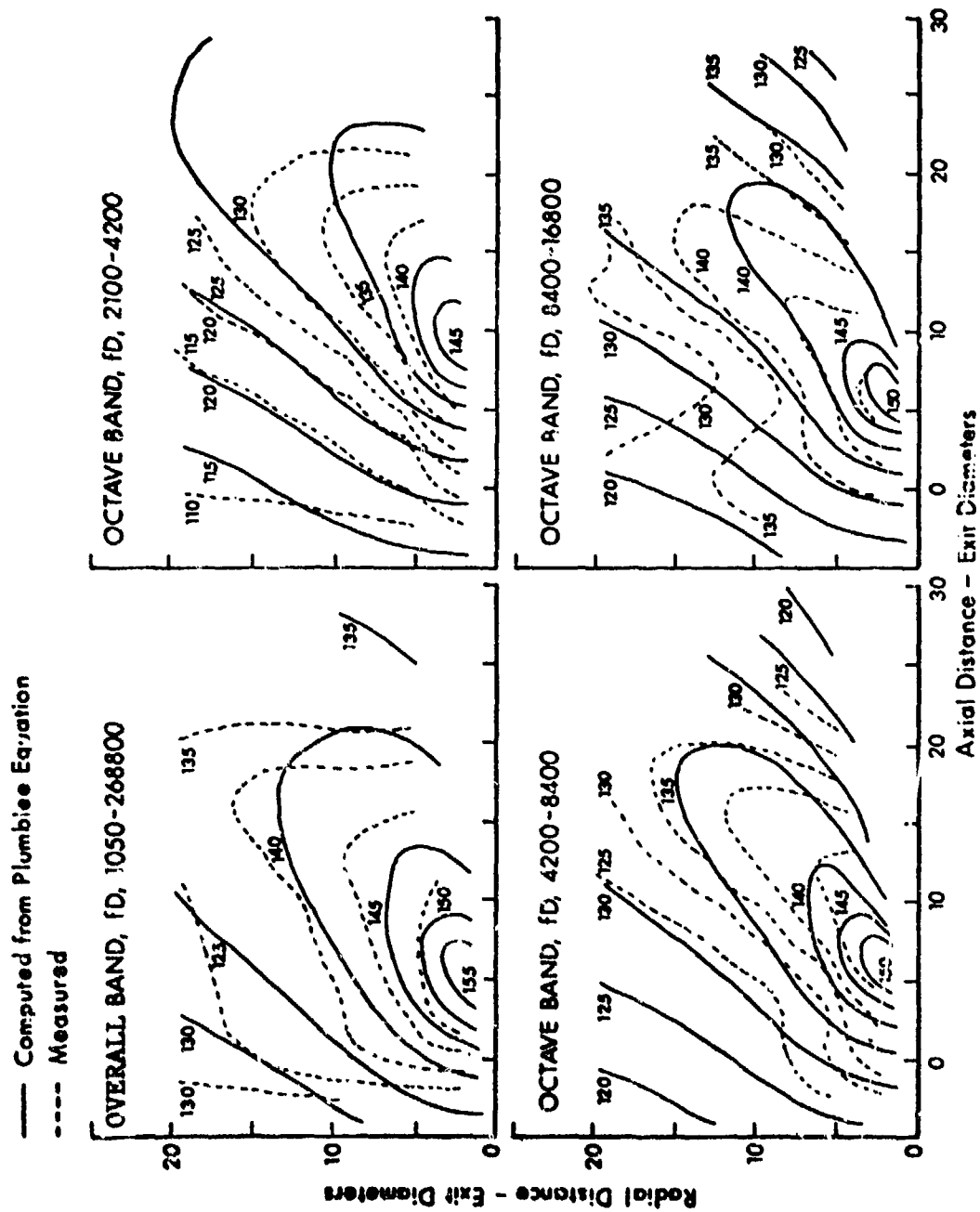
FIG. 3.. COMPARISON OF MODEL JET EXPERIMENTAL AND CALCULATED CONTOURS MACH NO. = 1.50, TEMP = 1360°R, VELOCITY = 2677 FPS (FIG. 34, REF. 6).

17

Figures 4 and 5 show a comparison between the nearfield noise contours measured for a YJ-93 engine and values computed by the Plumblee equation. The conditions to which these figures pertain are as follows:

Fig. No.	Condition	Thrust (lb)	Weight flow (lb/sec)	Total Temp (°R)	Jet Velocity (ft/sec)	Exit Area (ft²)	Exit Mach No.
4	Military	19405	283	2066	2466	6.4	1.28
5	Max A/B	26367	288	3651	3246	8.2	1.26

The agreement between the computed and measured values is very good for most of the range shown.

The YJ-93 engine is equipped with a converging-diverging nozzle. If a shock wave contribution to the noise occurs, one would expect it to be observed in the highest octave band (fD = 8400 to 16800 Hz-inch). A small upswing of the measured noise contours at low values of X/D is indeed noted. Again, the Plumblee equation fails to reflect this upswing.

Possible Modifications of Plumblee Method

As is evident from Equation (3) and the equations for the eleven associated constants, the Plumblee method is somewhat cumbersome to apply. A useful alternative may be based on the use of two sets of reference contours (one for Mach 1.25 and the other for subsonic jets) and on an equation for adjusting the noise levels for changes in jet velocity V and jet static temperature T. For any given case, one would select the set of contours whose Mach number, velocity, and temperature are closest to the parameters of the jet to be considered and the level would be adjusted by

$$\Delta \text{ dB} = 70 \log \frac{V}{V_r} - 10 \log \frac{T}{T_r} \quad , \tag{5}$$

where the subscript r designates the reference parameters.
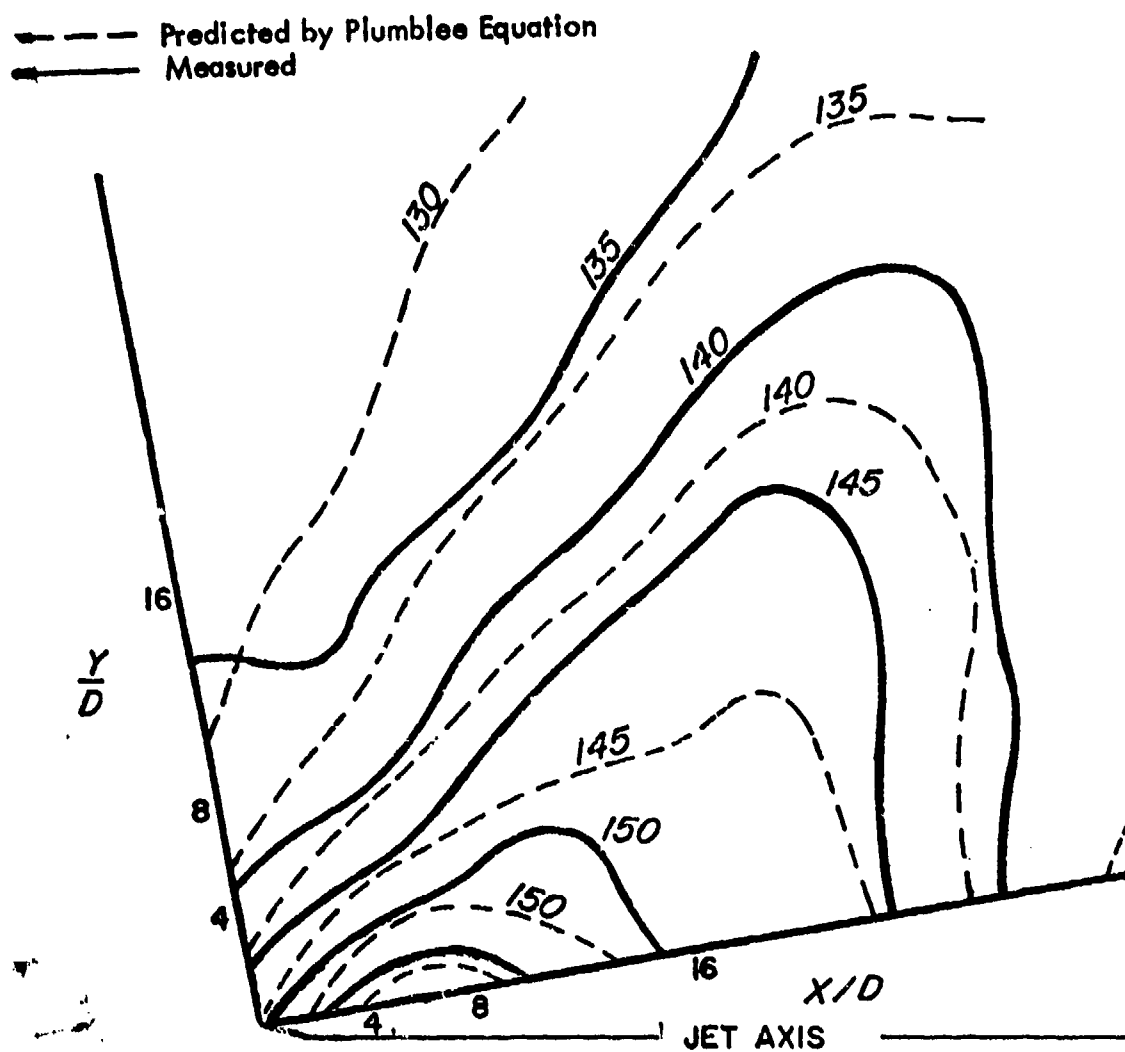
FIG. 4a. COMPARISON OF PREDICTED (INCLUDING REFLECTION) AND
MEASURED SOUND PRESSURE LEVEL (dB) CONTOURS FOR
SINGLE YJ-93 ENGINE OPERATING AT MILITARY POWER.
(a) OVERALL BAND, fD = 1050 to 26880 Hz in.
(FROM FIG. 15, REF. 15).

19
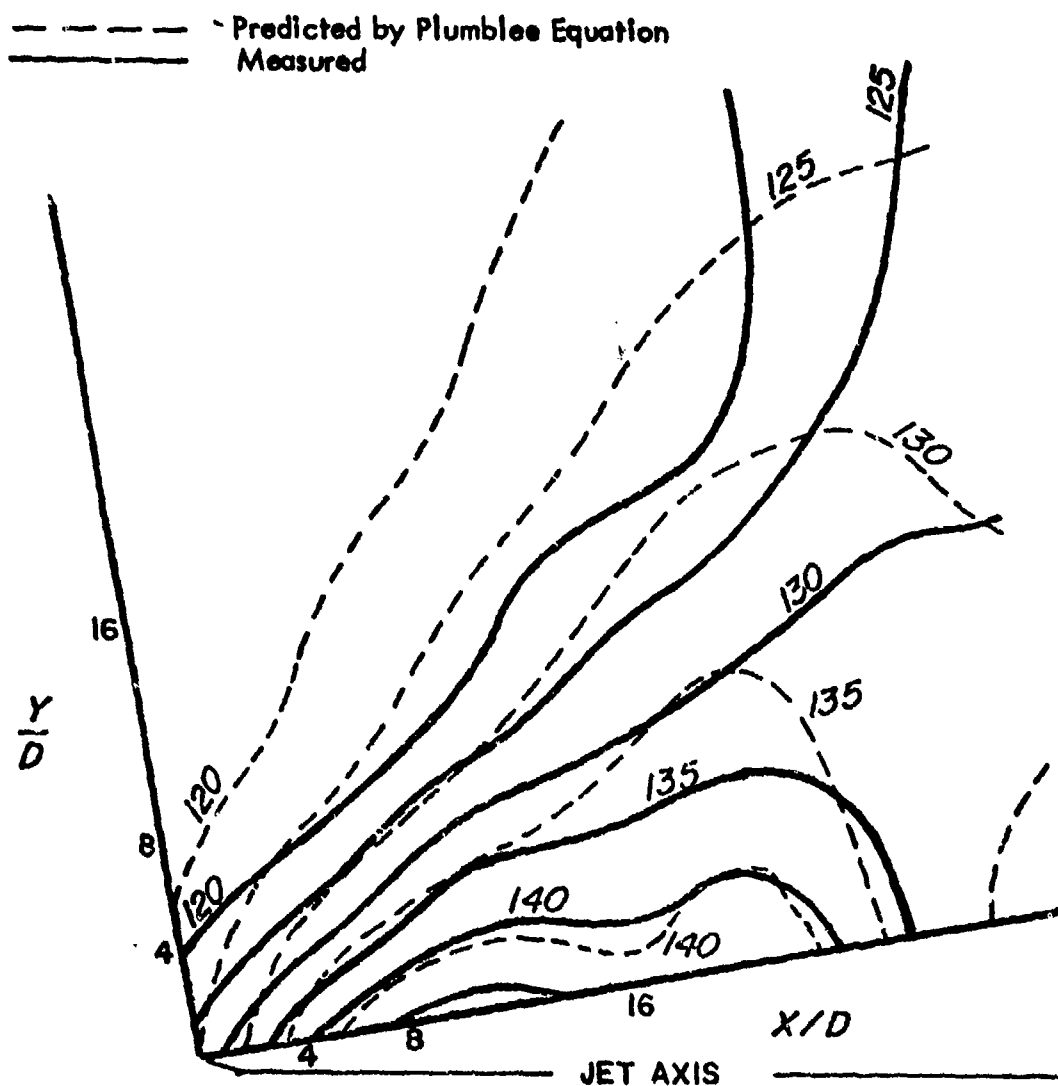
FIG. 4b. COMPARISON OF PREDICTED (INCLUDING REFLECTION) AND
MEASURED SOUND PRESSURE LEVEL (dB) CONTOURS FOR
SINGLE YJ-93 ENGINE OPERATING AT MILITARY POWER.
(b) OCTAVE BAND, fD = 2100 to 4200 Hz in.
(FROM FIG. 15, REF. 15).

20
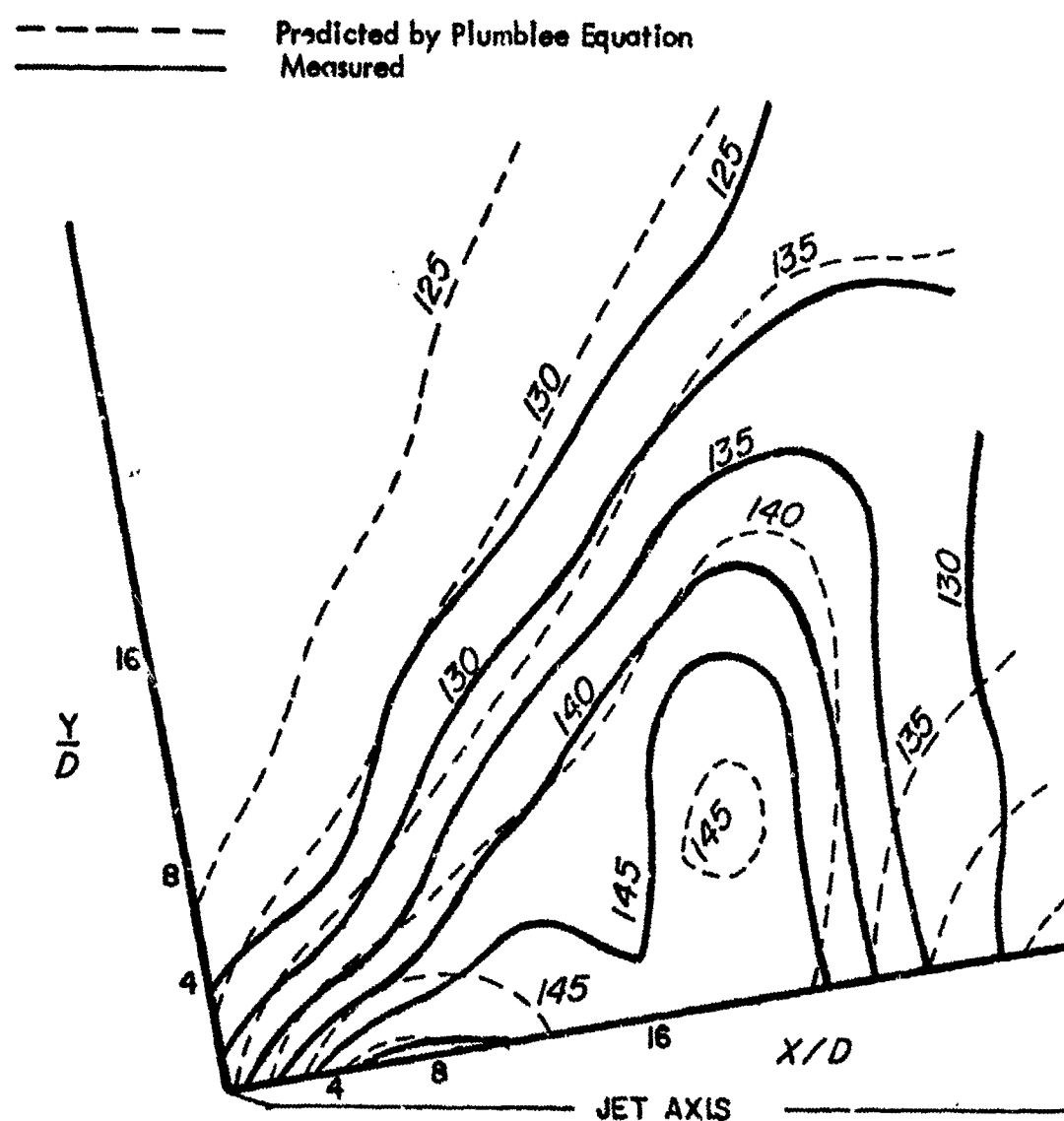
FIG. 4c.   COMPARISON OF PREDICTED (INCLUDING REFLECTION) AND
MEASURED SOUND PRESSURE LEVEL (dB) CONTOURS FOR
SINGLE YJ-93 ENGINE OPERATING AT MILITARY POWER.
(c) OCTAVE BAND, fD = 4200 to 8400 Hz in.
(FROM FIG. 15, REF. 15).

21
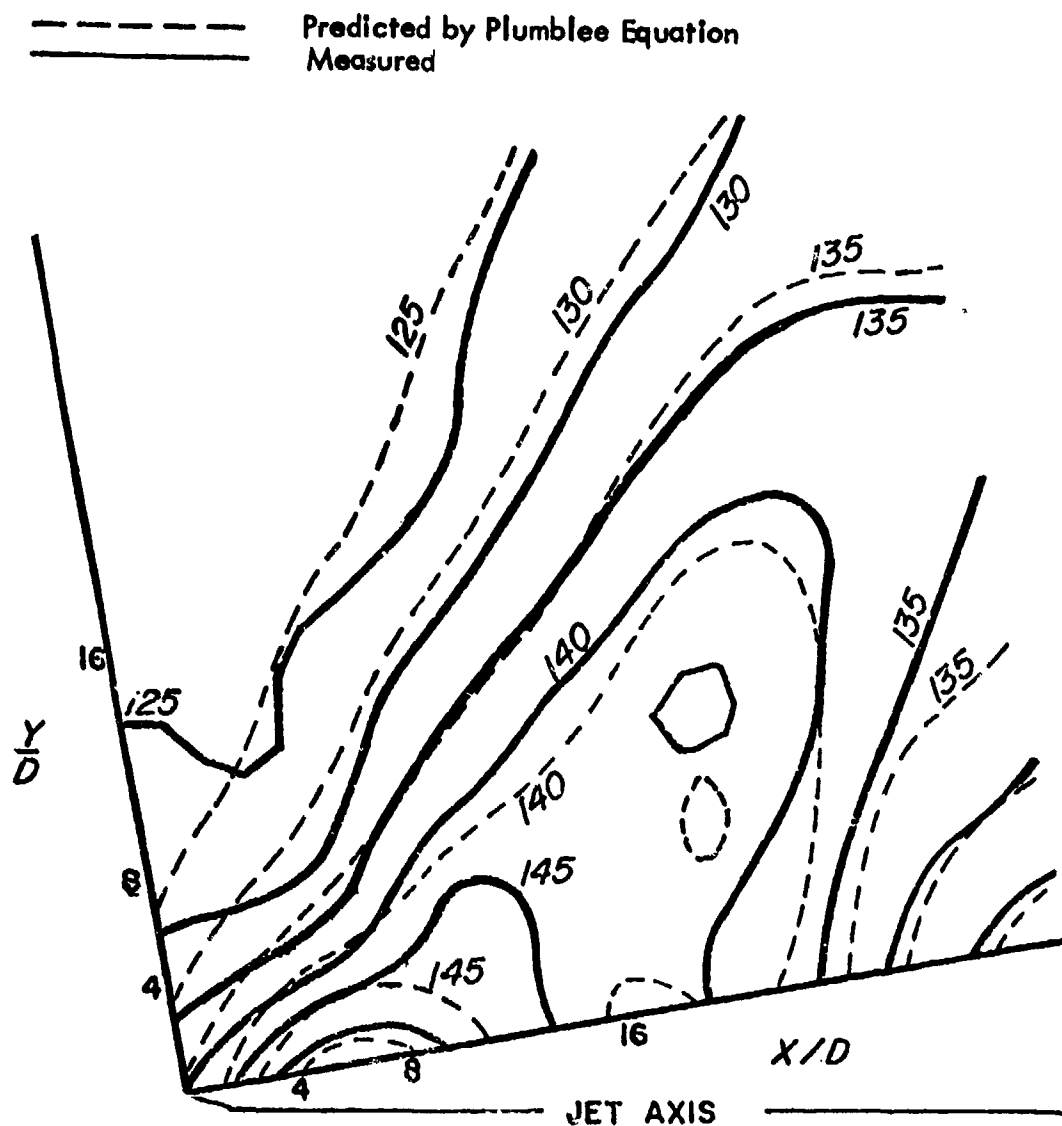
FIG. 4d. COMPARISON OF PREDICTED (INCLUDING REFLECTION)
AND MEASURED SOUND PRESSURE LEVEL (dB) CONTOURS
FOR SINGLE YJ-93 ENGINE OPERATING AT MILITARY POWER.
(d) OCTAVE BAND, fD = 8400 to 16800 Hz in.
(FROM FIG. 15, REF. 15).

--- --- Predicted by Plumblee Equation
——— Measured
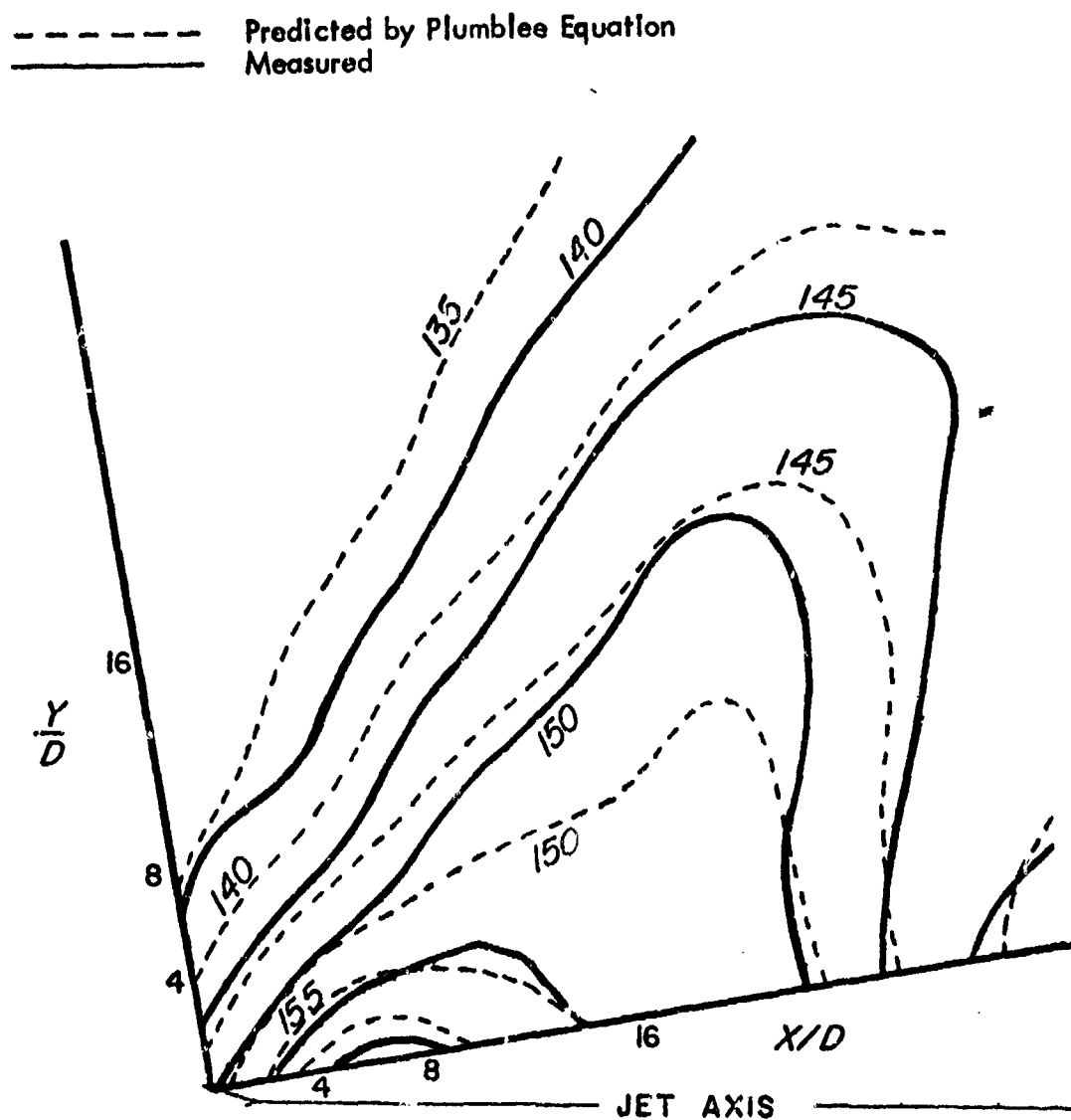
FIG. 5a. COMPARISON OF PREDICTED (INCLUDING REFLECTION) AND
MEASURED SOUND PRESSURE LEVEL CONTOURS FOR SINGLE
YJ-93 ENGINE OPERATING AT MAXIMUM AFTERBURNER.
(a) OVERALL BAND, fD = 1050 to 26880 Hz in.
(FROM FIG. 14, REF. 15).

23
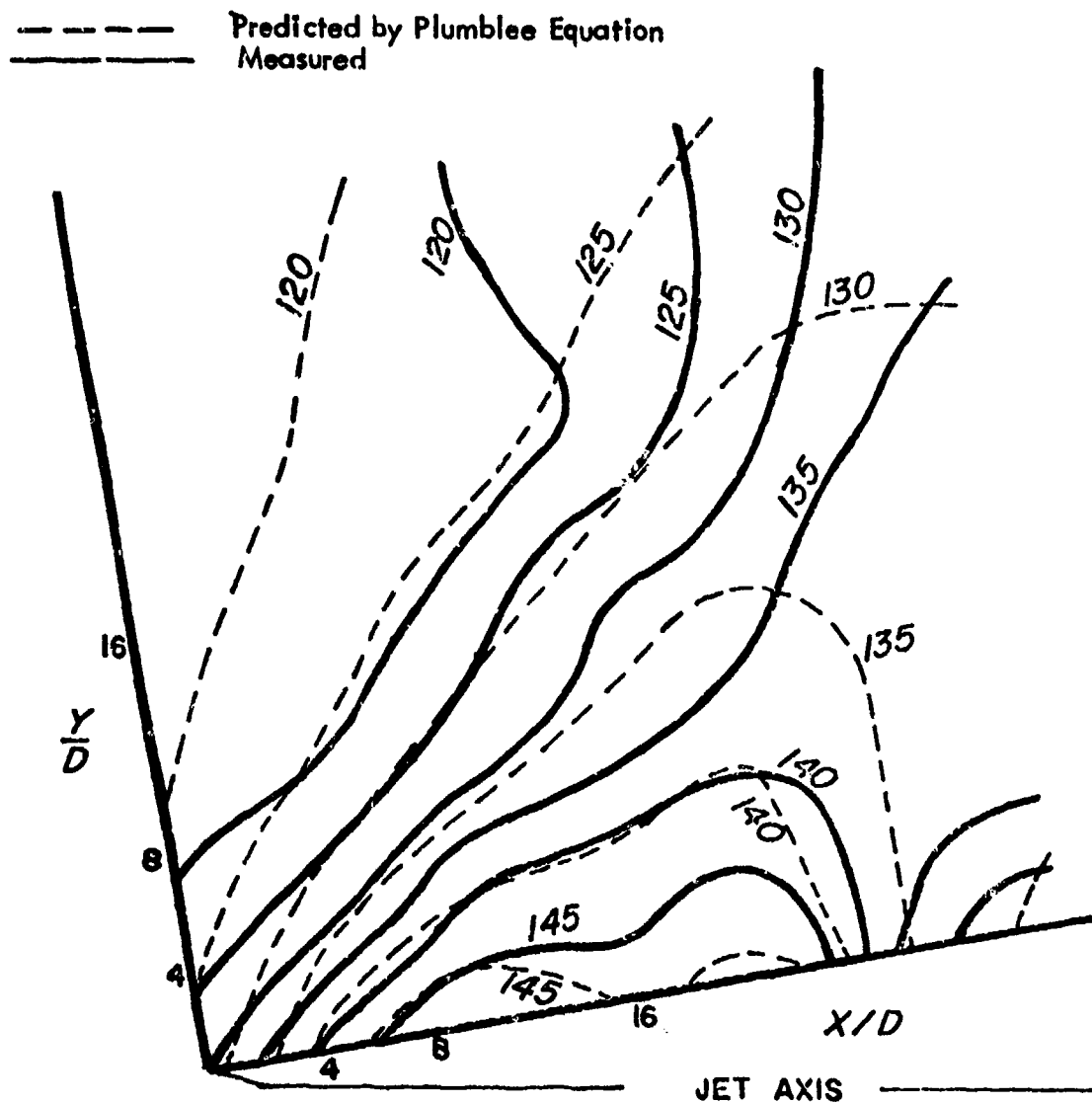
FIG. 5b. COMPARISON OF PREDICTED (INCLUDING REFLECTION) AND
MEASURED SOUND PRESSURE LEVEL CONTOURS FOR SINGLE
YJ-93 ENGINE OPERATING AT MAXIMUM AFTERBURNER.
(b) fD = 2100 to 4200 Hz in.
(FROM FIG. 14, REF. 15).

24
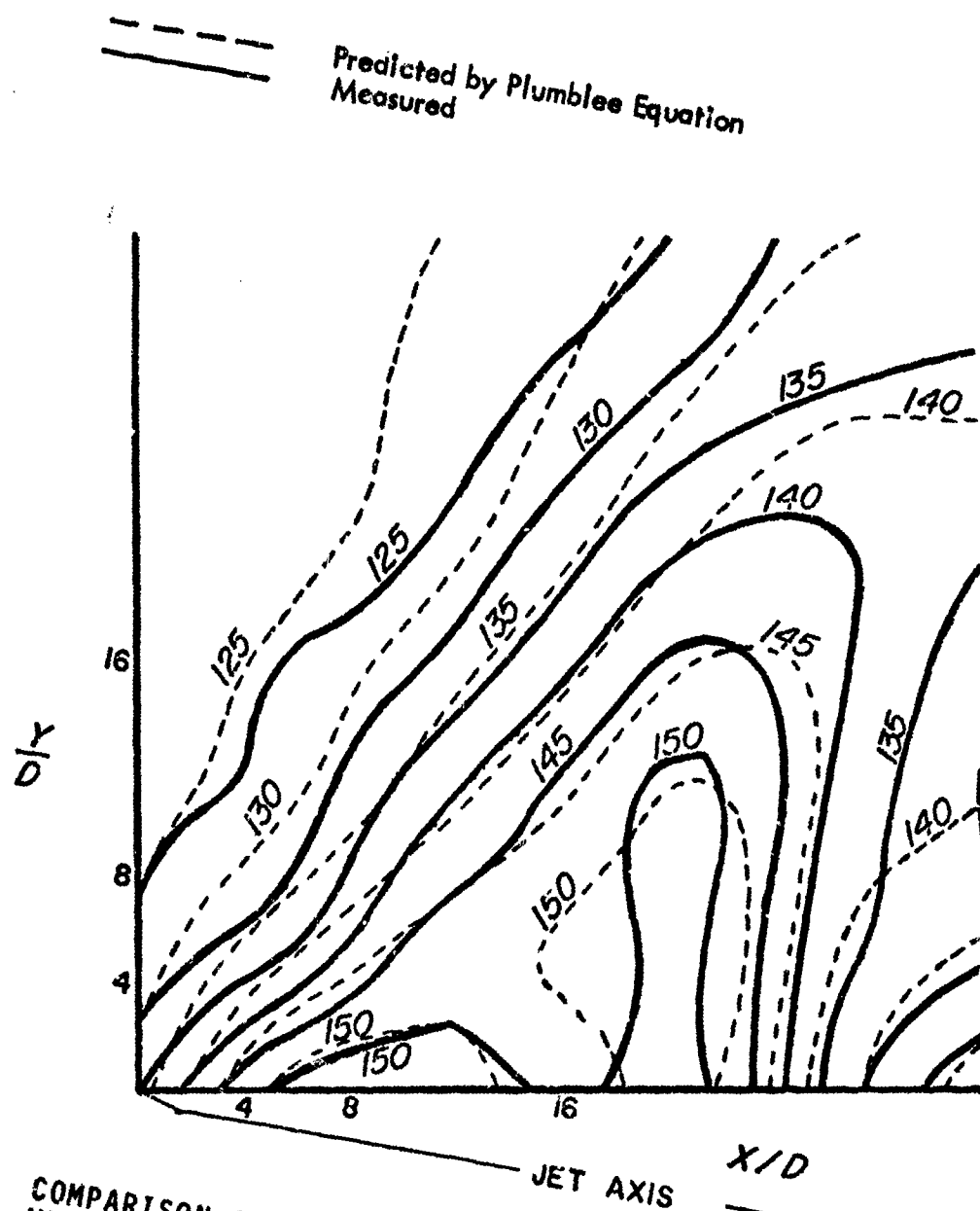
FIG. 5c. COMPARISON OF PREDICTED (INCLUDING REFLECTION) AND MEASURED SOUND PRESSURE LEVEL CONTOURS FOR SINGLE YJ-93 ENGINE OPERATING AT MAXIMUM AFTERBURNER (c) fD = 4200 TO 8400 Hz in. (FROM FIG. 14, REF. 15).

FIG. 5d.   COMPARISON OF PREDICTED (INCLUDING REFLECTION) AND
MEASURED SOUND PRESSURE LEVEL CONTOURS FOR SINGLE
YJ-93 ENGINE OPERATING AT MAXIMUM AFTERBURNER.
(d) fD = 8400 to 16800 Hz in.
(FROM FIG. 14, REF. 15).

26

It is beyond the scope of the present report to establish the reference sets of parameters. (This would require careful consideration of all of the available test data and their respective accuracies.) To provide some insight into the possibilities of the suggested method, one may choose the curves of Figures 4 (for the YJ-93 engine at military thrust) as the reference contours for the regime around M = 1.25. Figure 6 shows the test data from Figure 4, together with those from Figures 5 (Max A/B), adjusted according to Equation (5). (The calculated adjustment is -7 dB.) The agreement here between the curves for military thrust and the reduced max A/B curves is better than the agreement between these curves and the values computed by the Plumblee method (Figures 4 and 5).

Figure 1.7 shows a similar comparison of the test data on the model jet from Figures 1 and 2 with the levels of the curves of Figure 2 reduced by 8 dB (as computed from Equation 5), to adjust these curves to the conditions corresponding to Figure 1. Again, the agreement is seen to be very good, and somewhat better than that between the test data and the values computed by the Plumblee equation (Figures 1 and 2).

Figure 8 compares two sets of test data from [6] with the levels of the curves of one set increase 7 dB in accordance with Equation (5) to account for differences in the parameters. The agreement is seen to be excellent.

A second similar comparison appears in Figure 9. The agreement here again is reasonably good, with the greatest discrepancy

27
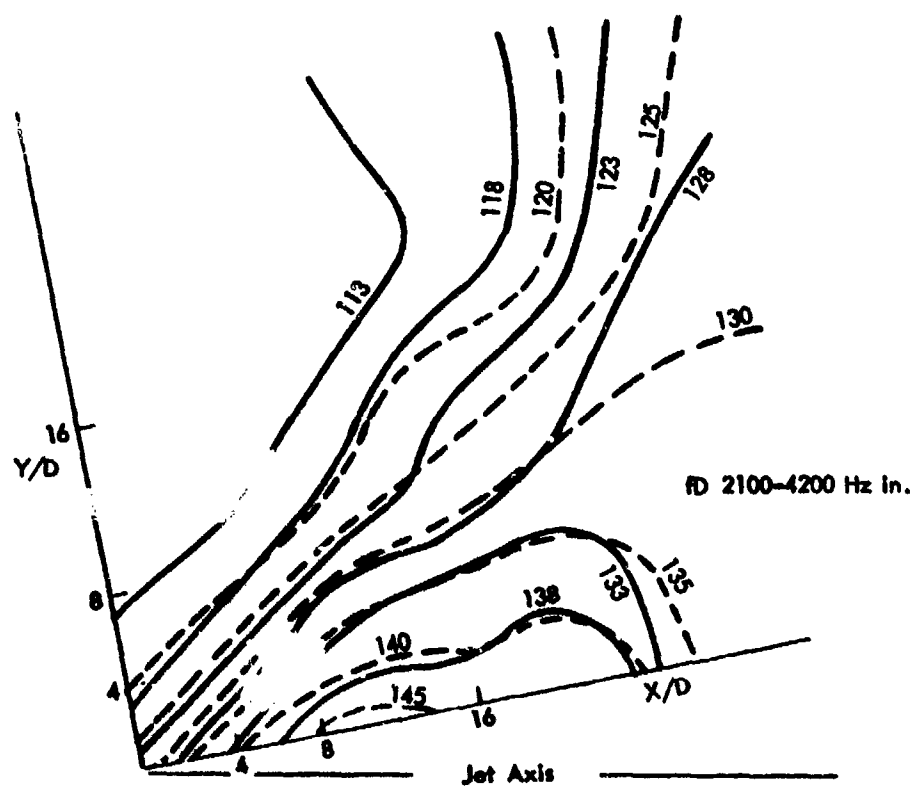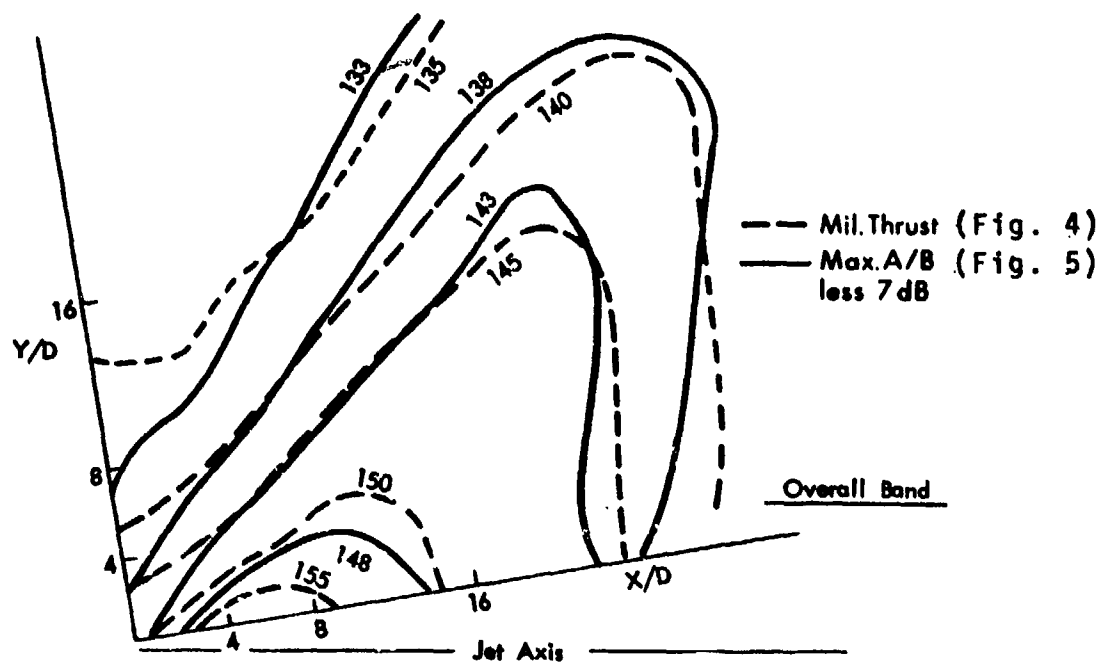
FIG. 6. COMPARISON OF NOISE CONTOURS FOR YJ-93 ENGINE FOR
MILITARY POWER AND MAXIMUM AFTERBURNER.

28

fD 4200-8400 Hz in.

fD 8400-16800 Hz in.
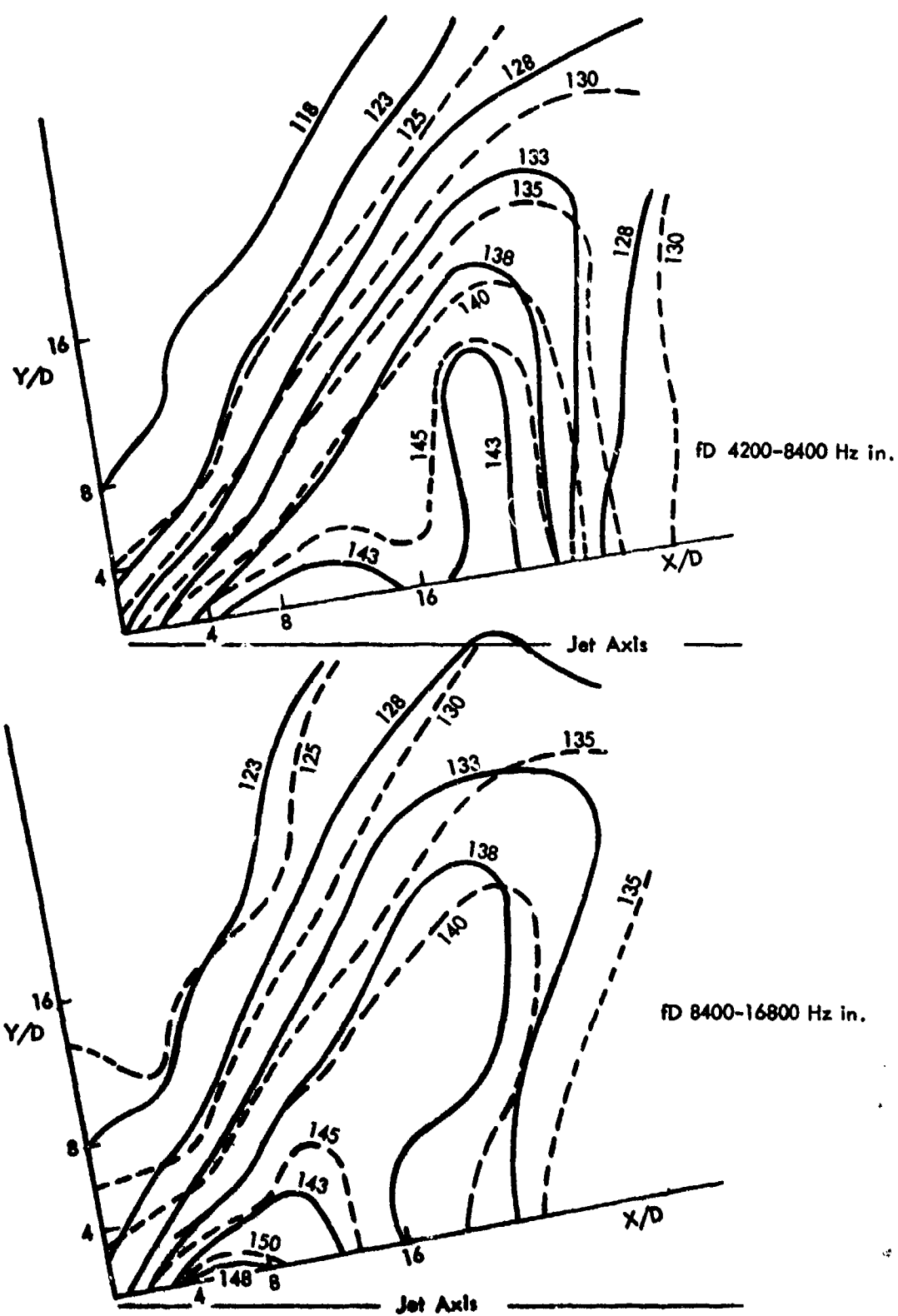
FIG. 6 (Cont.)
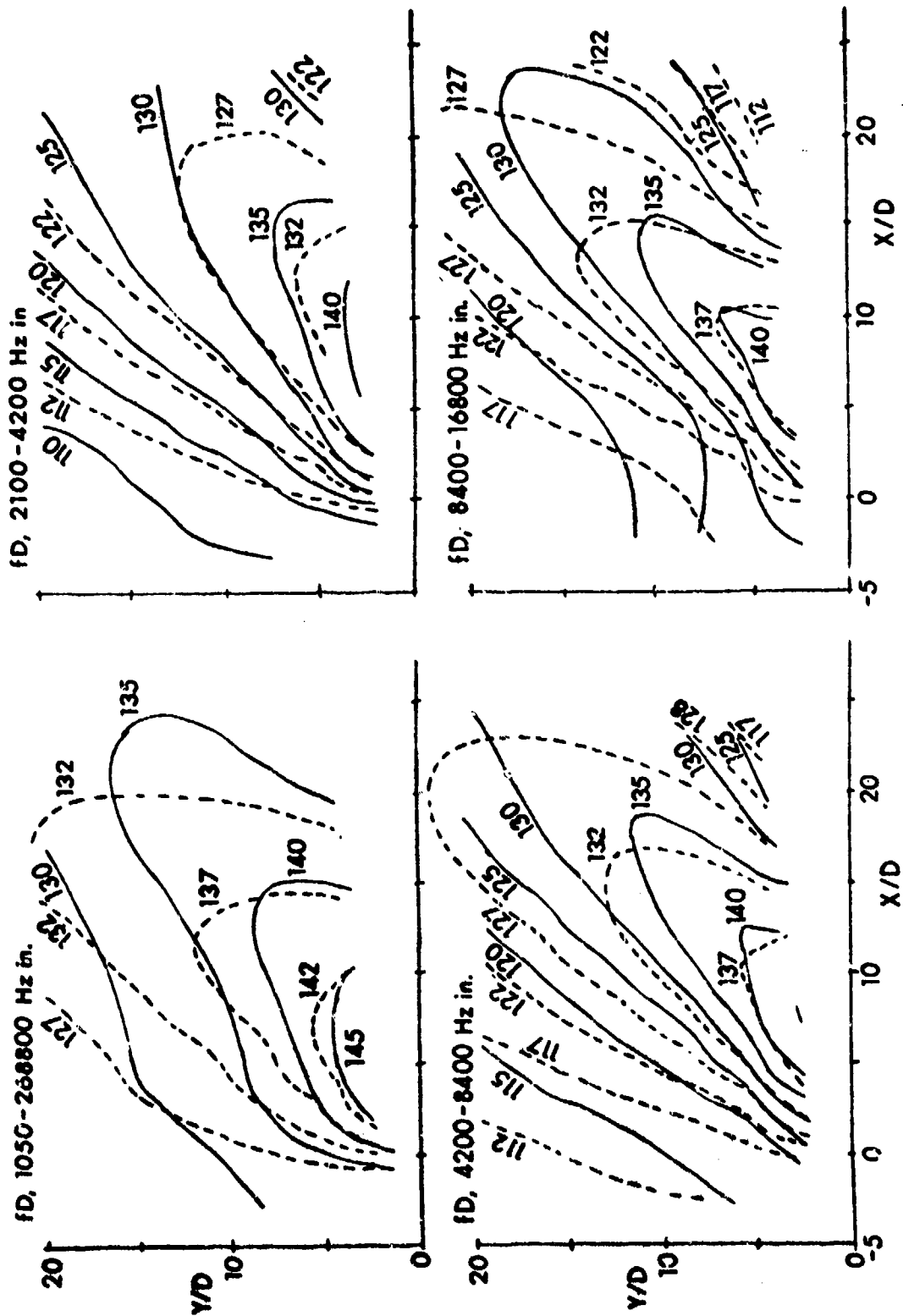
FIG. 7. COMPARISON OF NOISE CONTOURS OF MODEL JET AT MACH NO. 1.25.

30
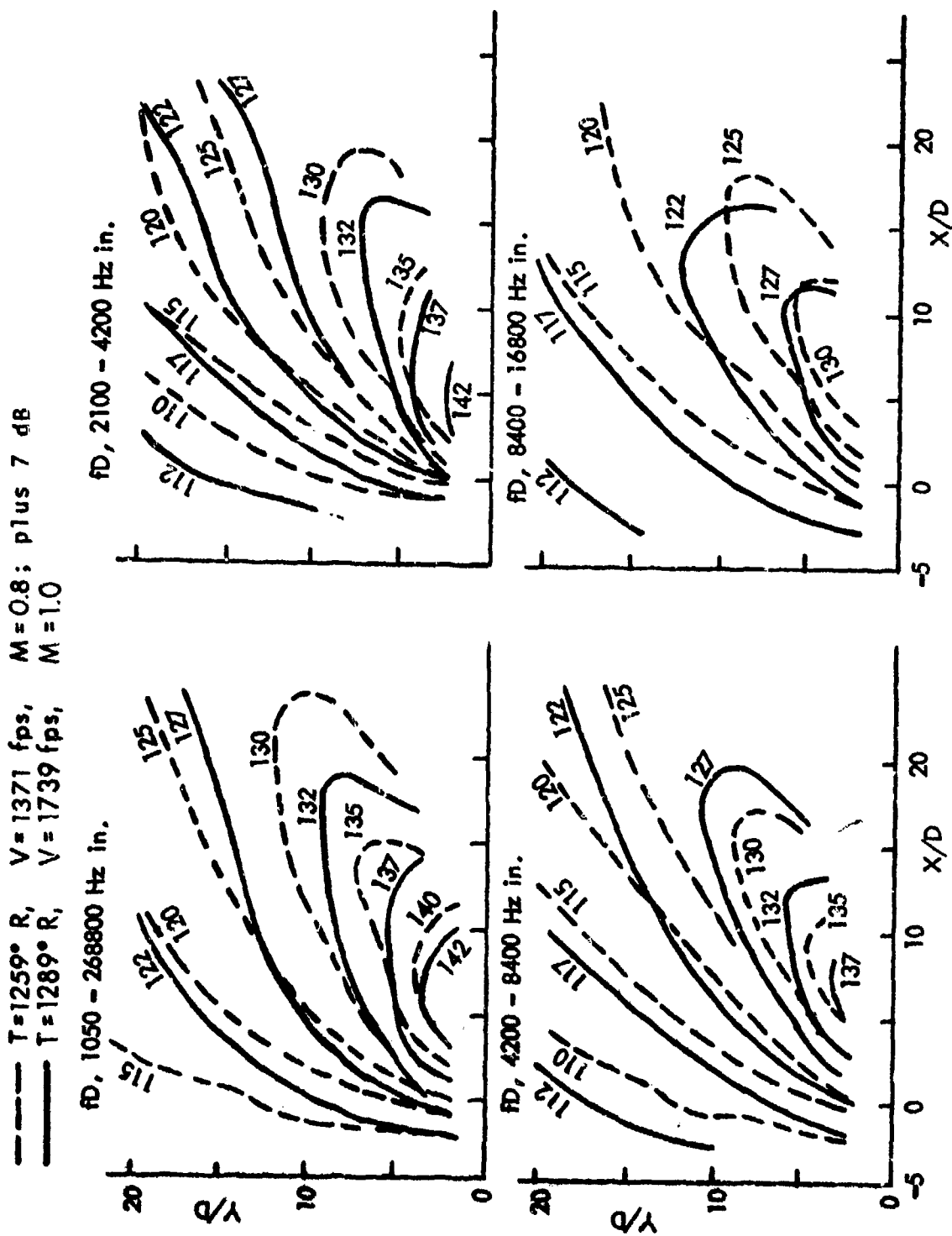
FIG. 8. COMPARISON OF NOISE CONTOURS FOR MODEL JET IN SUBSONIC REGIME, BASED ON FIGS. 24 AND 27 OF [6].

31
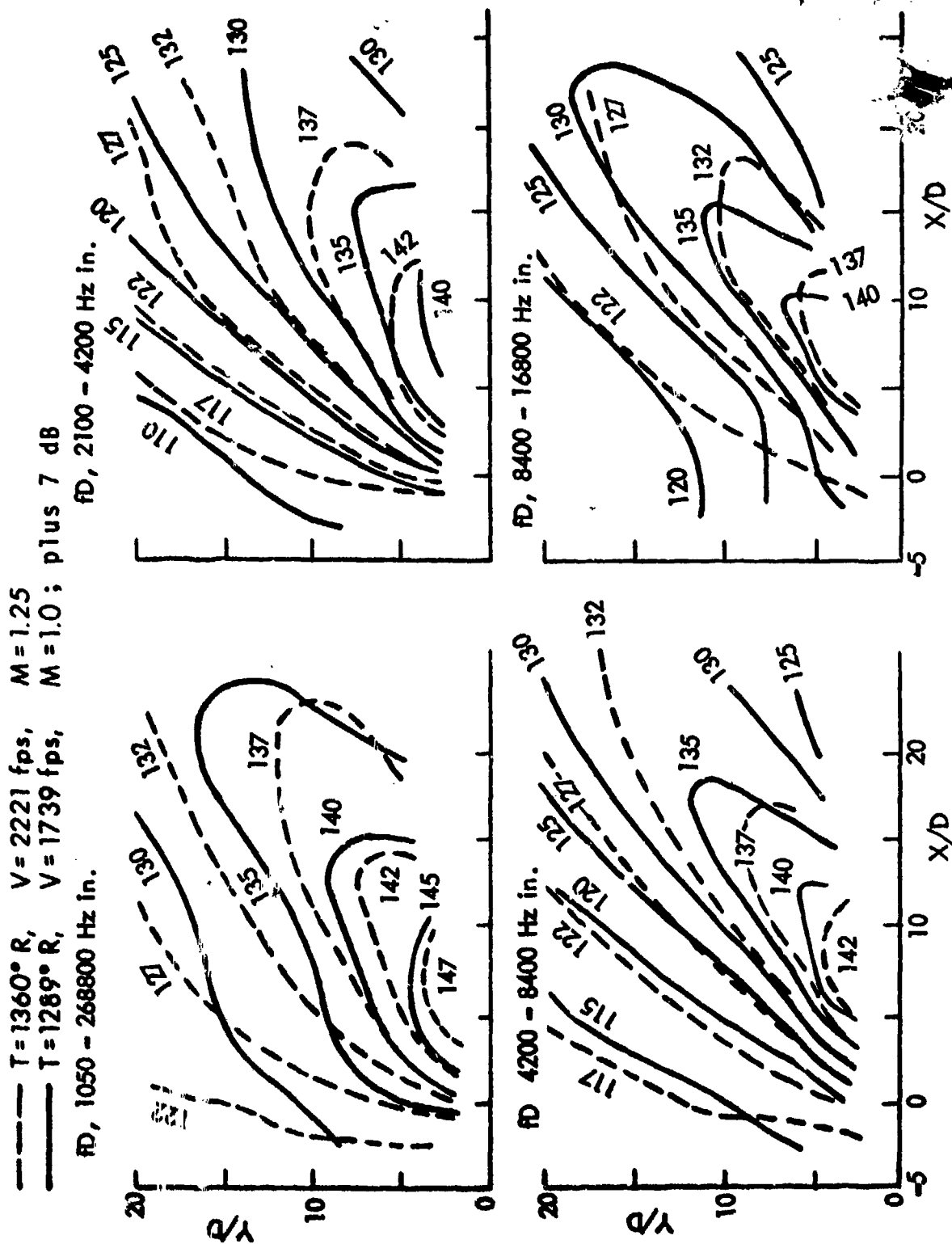
FIG. 9. COMPARISON OF REFERENCE SETS OF CONTOURS, BASED ON FIGS. 27 AND 30 of [6].

occurring in the range previously noted, i.e., for X/D values less than 7 in the fD = 8400 to 16800 Hz-inch octave band, where shock waves in the jet may affect the observed noise. Figure 1.1.9 indicates that two sets of reference contours, rather than a single one, would provide enhanced accuracy.

In the method of Plumblee et al [6], frequency information is restricted to the three octave bands centered on frequencies given by fD/c_0 = 0.221, 0.442, 0.884. Although these bands may include the spectral peak for a given condition and location, more spectrum information may be of interest. Thus, a method is needed for extrapolating the calculated sound levels to higher and lower frequencies.

Perhaps the most appropriate method for this purpose is that of Thomson [10], which specifies four non-dimensional spectra for the nearfield region $0 \leq X/D \leq 30$, $0 \leq Y/D \leq 30$. The spectrum shapes proposed by Thomson are selected here in preference to those of Cockburn and Jolly [11], because the former represent a larger sample of engine sizes and operating conditions. Although Cockburn and Jolly provide more detail, in that they provide spectra for 24 locations, including some upstream of the nozzle exit plane, their spectra are based on only one set of measurements for the J57-P21 turbojet engine [12].

Although the nearfield noise prediction method of Thomson is more accurate than that of Cockburn and Jolly, it is incomplete. The most useful available method involves calculation of the octave band sound pressure levels at three center frequencies, following the method of Plumblee et al, and then using the appropriate spectrum shape from Figure 10 to extrapolate the calculated levels to higher and lower frequencies. (For consistency, the
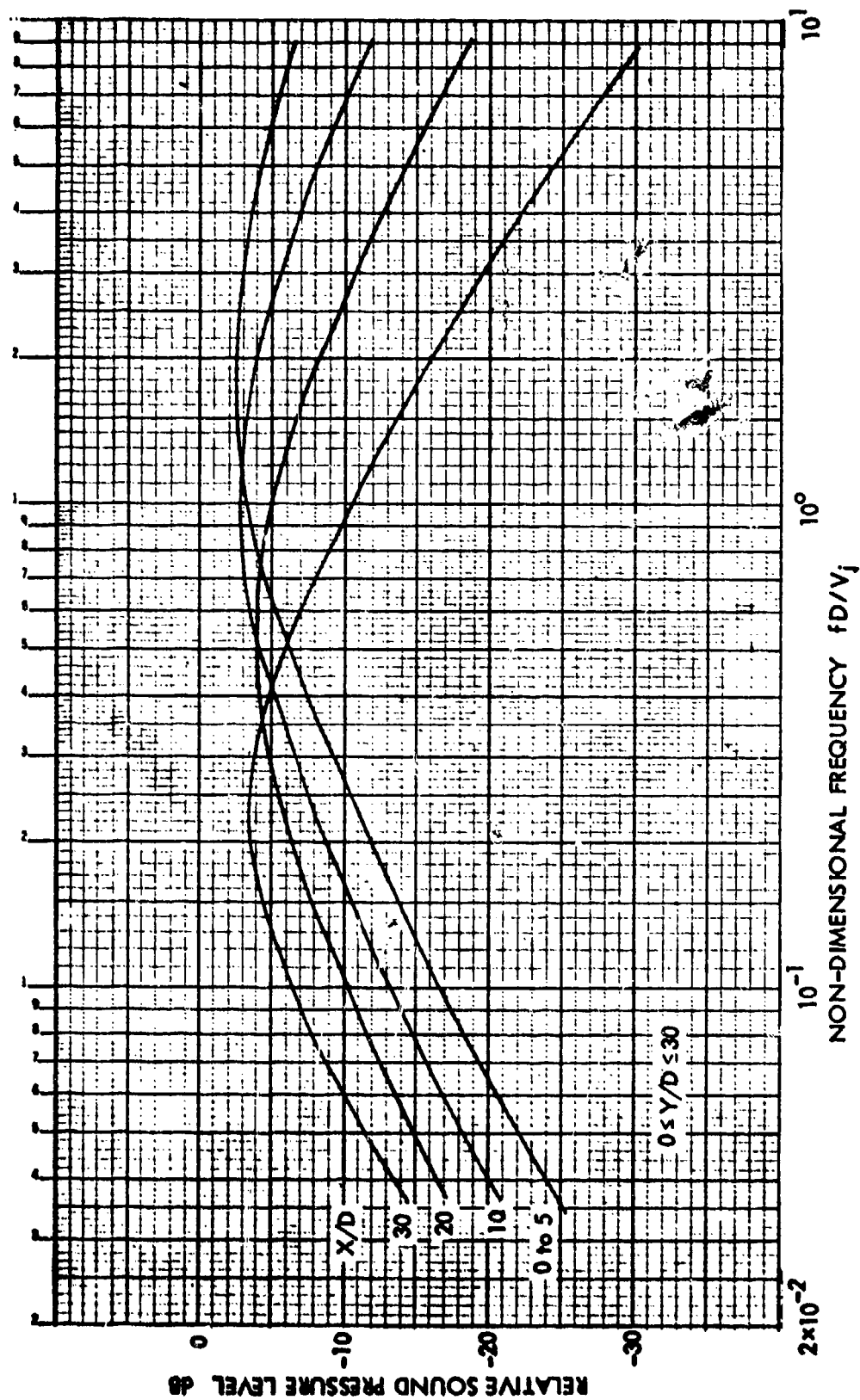
FIG. 10. NON-DIMENSIONAL SPECTRA FOR NEARFIELD JET NOISE (BASED ON [10]).

34

spectrum levels of Thomson have been modified to provide levels in constant percentage bandwidths.)

It would be more satisfactory to extend the method of Plumblee *et al* to other frequencies by extending the table of frequency-dependent parameters; however, this requires considerably more time and effort than available for the present study.

2.2.2 Non-circular nozzles

Of the several types of non-circular exhaust nozzles treated in the literature, only two have any present practical importance, if the various noise suppressor designs are excluded. These are plug and slot nozzles. Conical plugs (Figure 11) are sometimes used with circular nozzles, and slot nozzles are being considered for powered-lift systems, such as the augmentor wing.

The available acoustic data on circular plug and slot nozzles are limited and refer to the acoustic farfield. This data has been reviewed by Stone [20] for application to acoustic farfield prediction methods. Since no better information is available, it is proposed that these farfield methods be applied also for nearfield predictions.

Plug Nozzles

Measurements of the farfield noise from plug nozzles indicate that the levels are slightly lower than those for a circular nozzle of the same cross-sectional area. On the basis of limited experimental evidence, Stone [20] introduce an empirical correction term

$$\Delta_{PN} = 3 \log[0.10 + 2 \ (h/D)] \tag{6}$$

35
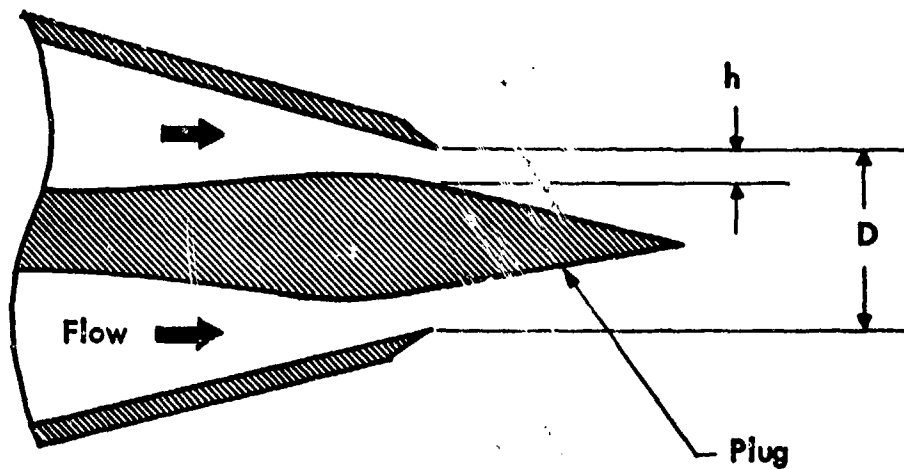
EQUIVALENT DIAMETER, $D_e = 2\sqrt{Dh - h^2}$

HYDRAULIC DIAMETER, $D_h = 2h$

DIAMETER RATIO, $\dfrac{D_h}{D_e} = \sqrt{\dfrac{h/D}{1-(h/D)}}$

FIG. 11.   PLUG NOZZLE GEOMETRY.

36

where h denotes the gap height and D the circular nozzle diameter, as defined in Figure 11. This correction term is to be added to the overall sound pressure level calculated for a circular nozzle of the same cross-sectional area.

The available published data do not indicate any change in the directivity patterns in presence of a plug, but do show some change in the frequency spectrum. Stone [20] accounts for this frequency change by introducing into the Strouhal number a factor $(D_h/D_e)^{0.4}$, where D_h and D_e denote the hydraulic and equivalent diameters, as defined in Figure 11. The Strouhal number for a circular plug nozzle then becomes

$$S = \frac{fD_e(D_h/D_e)^{0.4}}{V_j} \tag{7}$$

In the absence of other information, it is proposed that the above modifications, when applied to the prediction procedure of Section 1.1.1 for circular nozzles, be adopted for nearfield noise predictions.

Slot Nozzles

There exists little reliable information that can be used to establish quantitative prediction procedures, and such data as is available pertains to the farfield, where some of the non-axisymmetric effects may be less pronounced than in the nearfield.

The data analysis of Stone [20] for nozzles with aspect ratios of 4.8 and 69 indicates that in the acoustic farfield the asymmetry effects are small. Thus, Stone neglects these effects and proposes a farfield prediction method that uses the relationships for circular nozzles.

37

However, Stone's proposal must be treated with caution since, as he indicates, all measurements made at ϕ = 90° (i.e., in the plane of the long dimension of the nozzle) may be subject to ground reflection effects. However, his data also lead to other observations which need to be considered:

(a) The overall sound pressure levels at ϕ = 90° may be 1 to 2 dB lower than the corresponding values at ϕ = 0° (in the plane of the short dimension of the nozzle).

(b) The one-third octave band spectrum at ϕ = 90° peaks at a frequency which is about a one-third octave below the peak frequency at ϕ = 0°.

(c) Non-dimensional spectrum levels at high and low frequencies are lower at ϕ = 90° than at ϕ = 0°.

Similar trends may also be observed in other data for rectangular nozzles. In [2] and [22], the peak frequencies at ϕ = 90° are lower than those at ϕ = 0° by between a one-third octave and a whole octave. The frequency spectrum, when non-dimensionalized with respect to the overall level, at low frequency is higher at ϕ = 90° than at ϕ = 0°.

These observations support a qualitative description of the noise field, which associates a decrease in high frequency sound pressure level at ϕ = 90° with shielding of the noise generated in the initial mixing region close to the nozzle, in a manner similar to that found in multitube suppressor nozzles. For such a phenomenon, one would expect to find greater noise reduction at ϕ = 90° in the nearfield than in the farfield. However, this is speculation, and for the present time it is proposed that nearfield noise predictions be obtained following the recommendation of Stone [20], using the approach for axisymmetric circular jets. This approach is expected

38

to give conservative results, i.e., to yield predicted levels that will overestimate the actual levels at frequencies greater than the peak frequency of the spectrum.

2.2.3 Effective location of jet noise sources

In many prediction methods, it is assumed that the noise sources are located near the nozzle exit plane. This assumption is of little consequence in the prediction of farfield sound levels, but is important in the estimation of nearfield noise. Thus, it is useful here to review the available information regarding the effective location of noise sources in a jet.

The experimental techniques that have been used to measure the location of noise sources in a jet efflux include directional microphones, reflectors, jets discharging through a hole in a wall, correlation methods, and analysis of sound pressure level contours. The results indicate that, for any given frequency band, sources are distributed over a fairly large axial distance. Some of this observed spatial distribution may be due to low resolution of the measurement techniques, but there is no physical reason that acoustic energy at a given frequency be generated at a unique location along the jet axis.

On the other hand, it is convenient for predicting nearfield noise levels to assume that sound at a given frequency is generated at a unique axial distance along the jet, the distance being that associated with the maximum in the source intensity distribution curve for the appropriate frequency band. This simplification is used, for example, by Plumblee *et al.* [6]. As another example, the data of MacGregor and Simcox [23] show that the source distribution half-power points (i.e., locations at which the source power is 3 dB below the maximum) occur over axial distances of 4D to 12D, centered approximately at the location of maximum sound generation.

39

In order to apply the experimental results for source location in a noise prediction procedure, one needs an empirical relation between source location, nozzle diameter, Mach number, temperature and/or other parameters. Investigators have non-dim: :nalized source location with respect to nozzle diameter (F:.:e 12), but this does not provide a very satisfactory collapse of the data for different flow conditions. The data collapse is improved if nozzle pressure ratio is introduced as an additional scaling parameter, as in Figure 13, but even then there still exists considerable variation from one test condition to another. Also, the method does not take into account variations of exhaust temperature.

It might be argued from physical reasons that jet core length is a better parameter for non-dimensionalizing the source location X_o, since the core length includes the effects of pressure ratio and temperature and is a more meaningful dimension than jet nozzle diameter. Potter and Crocker [24] have used such non-dimensionalization and have shown that this reduced the data spread considerably, as compared with an X_o/D scaling; however, no comparison is available with scaling in relation to both nozzle diameter and pressure ratio.

One now needs to consider a method for estimating the length ℓ_c of the potential core. Eldred et al. [25] have presented a relationship for calculating the core length of subsonic and supersonic jets. They contend that the data indicate no influence of temperature between 300°F and 2000°F, and therefore include no temperature effect in their empirical relation,

$$\ell_c = 3.45D[1 + 0.38M_j]^2 \tag{8}$$

where M_j is the exit Mach number of the jet.

FIG. 12. JET SOURCE LOCATION, NON-DIMENSIONALIZED WITH RESPECT
TO NOZZLE DIAMETER.

41

FOR LEGEND SEE FIG. 12.

FIG. 13. JET SOURCE LOCATION, NONDIMENSIONALIZED WITH RESPECT TO NOZZLE DIAMETER AND PRESSURE RATIO.

In contrast, Abramovich [26] shows a strong dependence of potential core length on jet exhaust temperature. Figure 14 contains a family of curves relating core length to flow Mach number for several total temperatures. This figure also includes a curve corresponding to Equation (8), from which one may see that the two methods predict similar core lengths for ambient temperature jets, but not for hot jets. The curves of Figure 14 also disagree with the data of MacGregor and Simcox [23] for jets with a temperature ratio $T_j/T_a = 3.1$, which data, as evident from the figure, fall near the values predicted for ambient temperature jets.

Figure 15 shows the source location data of Figure 13 plotted in terms of X_o/ℓ_c, where ℓ_c is the core length calculated from Abramovich's method (Figure 14). It is seen that there is little or no improvement in the data collapse, as compared to Figure 15. If core lengths are calculated on the basis of ambient temperature jets (by the method of Eldred *et al.*), the data collapse is slightly better than that shown in Figure 15. Thus, the question of optimum scaling is unresolved.

The relationship proposed by Plumblee *et al.* [6] does not lend itself readily to plotting in the forms of Figure 13 or 15. However, source distributions can be calculated if specific assumptions are made. The source location is given by

$$\frac{X_o}{D} = C_{1,13} \, M^{C_{1,14}} \left(\frac{T_T}{1000}\right)^{C_{1,15}+C_{1,16}M} \tag{9}$$

where coefficients $C_{1,13}$, $C_{1,14}$, $C_{1,15}$, and $C_{1,16}$ are given in [6] for the three octave bands centered at Strouhal numbers $fD/c_o = 0.221$, 0.442, and 0.884. Under the assumption that
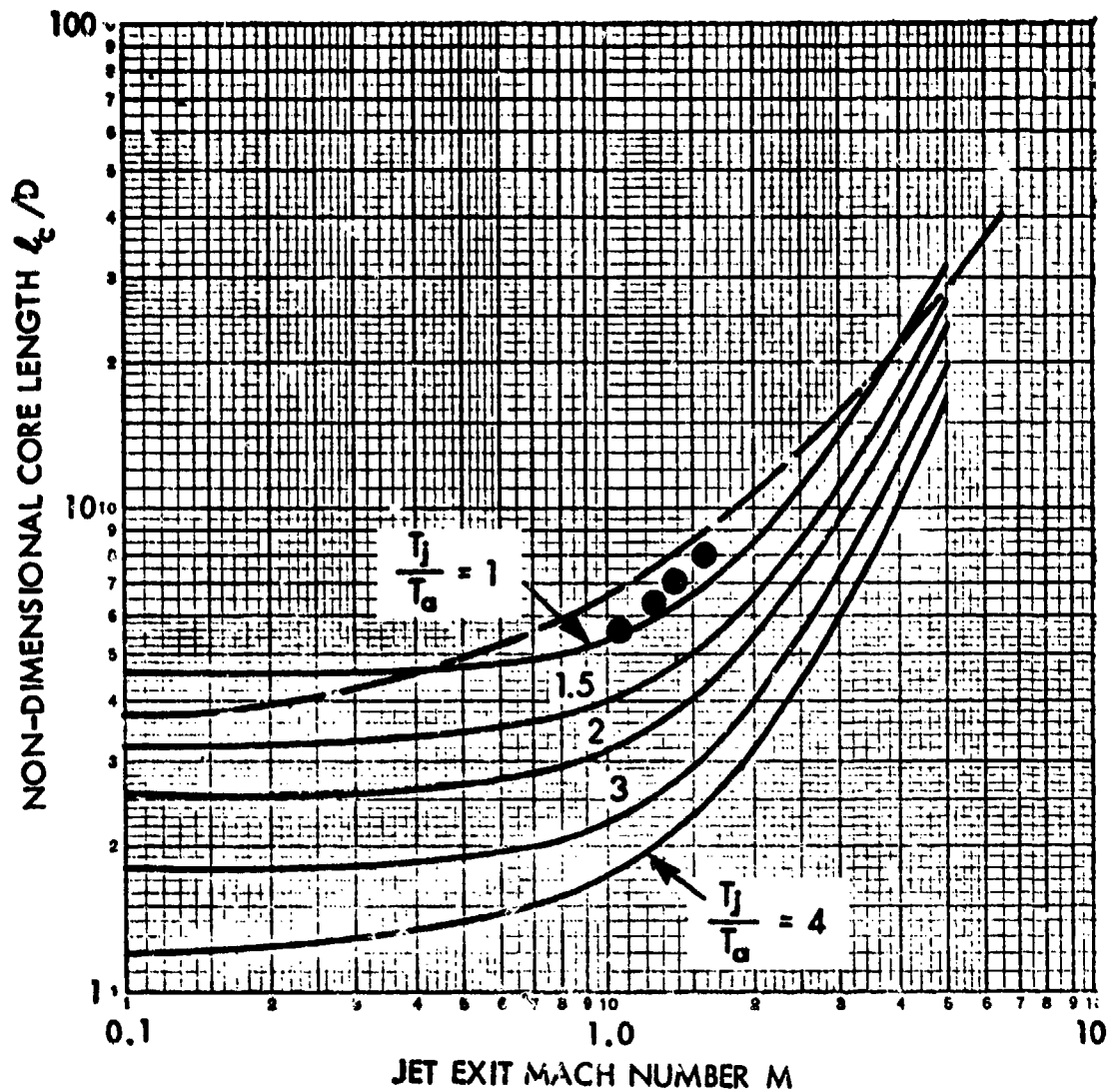
FIG. 14. JET CORE LENGTH AS FUNCTION OF JET TEMPERATURE AND MACH NUMBER.

44
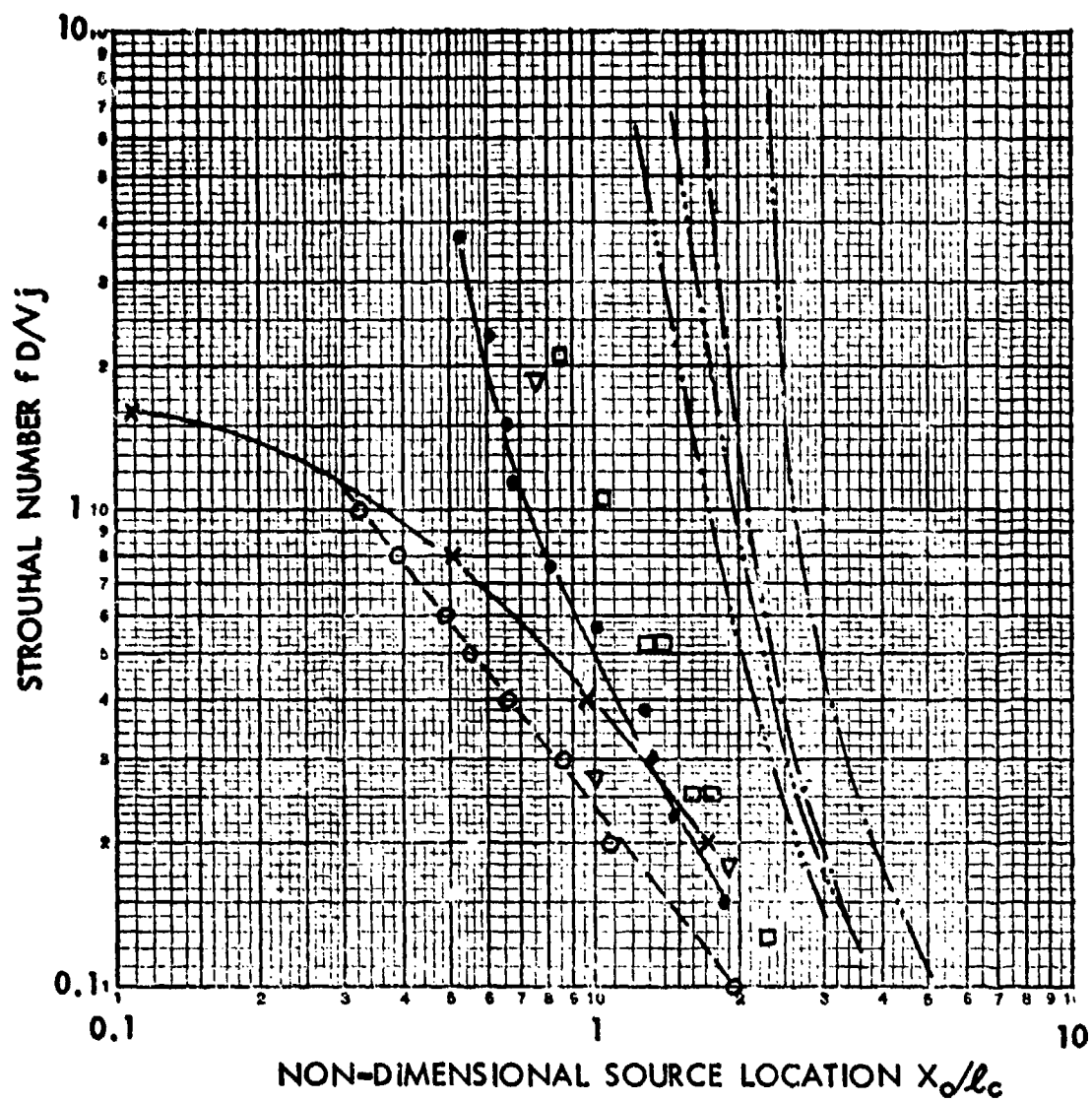
FOR LEGEND SEE FIG. 12.

FIG. 15.   JET NOISE SOURCE LOCATION, NONDIMENSIONALIZED
            WITH RESPECT TO CORE LENGTH.

45

the nozzle pressure ratio is 2.0 and the jet temperature is
either 519° (ambient jet) or 1600°R (typical engine condition),
one obtains the distributions plotted in Figure 16. These
values are consistent with the experimental data of Figure
13.

Apparently there is considerable uncertainty in the interpreta-
tion of available information regarding the location of noise
sources in a jet. The equation derived by Plumblee *et al* pre-
dicts source locations which are within the range of measured
values, but the equation is available for only three frequen-
cies. A method which can be used over a wider range of frequen-
cies is required. Since the scatter associated with each of
three non-dimensionalizing procedures, - that is in terms of

$$\frac{X_o}{D} \cdot \frac{1}{PR} \ , \quad \frac{X_o}{\ell_c(\text{hot flow})} \quad or \quad \frac{X_o}{\ell_c(\text{cold flow})},$$

is approximately the same, no method can be selected on the
basis of superior performance. Thus, the scaling factor $\frac{X_o}{D} \cdot \frac{1}{PR}$

may be selected on the basis of convenience. With this non-
dimensional relationship, a representative curve has been con-
structed that lies approximately in the center of the experimen-
tal range of data and also is consistent with the predictions of
Plumblee *et al*. This proposed model distribution is shown in
Figure 16.

46
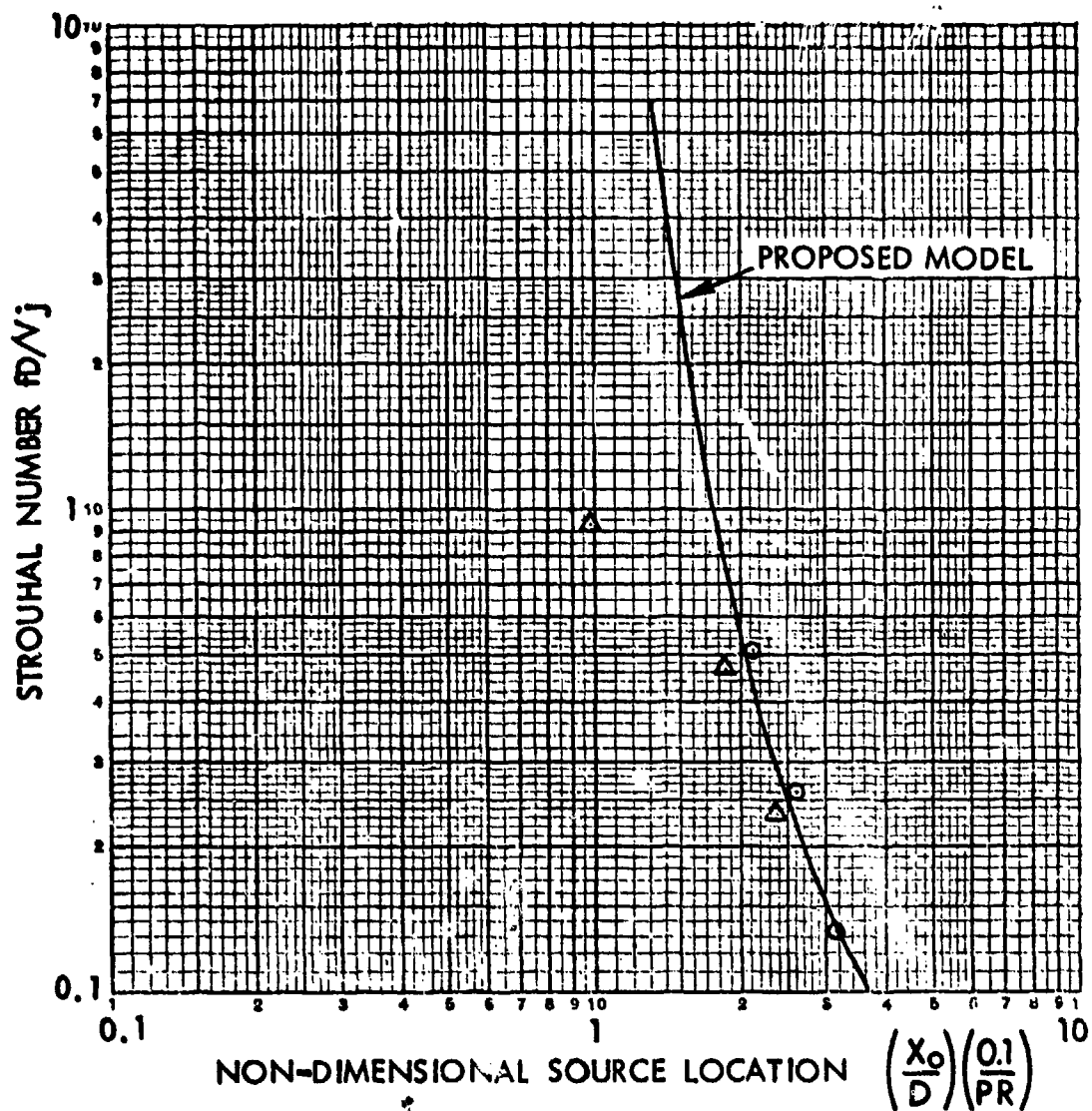
POINTS PREDICTED BY METHOD OF PLUMBLEE ET AL FIG. 6.

o $T_1 = 1600\,^{\circ}R$ △ $T_1 = 520\,^{\circ}R$

FIG. 16. PROPOSED MODEL FOR NOISE SOURCE LOCATION IN JET FLOW.

47

2.3 Afterburner Noise

Combustion noise in a jet engine is generated in the combustion chambers upstream of the turbines and in the afterburner, if such a device is in operation. Combustion chamber noise is important only if the jet exhaust velocities are low. Afterburner noise is generated when fuel is burned in the jet tailpipe, downstream of the turbine, resulting in high-speed jet flow. However, the associated jet Mach number may be no higher than that for the non-afterburning case.

2.3.1 Available data and early prediction methods

Several measurements of afterburner noise have been made, some in the far field [32, 33] and others in the near field [12, 15]. Although no models have been proposed to describe the afterburner noise characteristics, one nearfield study [15] compared the measured sound pressure levels with those predicted by the method of Plumblee *et al.* [6].

An early prediction method for the nearfield noise of a jet engine with afterburner, proposed by Franken *et al.* [34], consists of three steps:

(1) Calculation of overall sound pressure level for military power;

(2) Addition of a correction term for afterburner noise; and

(3) Shifting of the sound pressure level spectrum, based on non-afterburner operation, down in frequency by half an octave.

The method makes no allowance for different levels of afterburner operation, and does not account for directivity.

2.3.2 Proposed nearfield noise prediction method

In order to develop an alternative approach, one may assume the main component of afterburner noise to be due to the increased flow velocity and nozzle diameter, so that one may apply the method of Plumblee. In [13], application of maximum afterburner thrust was reported to produce the following changes in jet characteristics:

	Military Power	Maximum Afterburner	Change
Total Temperature (°R)	2066	3651	+77%
Exit Velocity (ft/sec)	2466	3246	+32%
Exit Area (ft²)	6.4	8.2	+28%
Exit Mach Number	1.28	1.26	-2%

The corresponding comparison between theory and experiment shows agreement here is as good as that for the non-afterburner case. For example, Figure 17 shows the difference between measured and predicted overall sound pressure levels at all microphone locations when ground reflection is taken into account. The mean difference is 1.8 dB for the maximum afterburner stage and 2.6 dB for military power. The corresponding standard deviations are 2.4 dB and 2.1 dB.

Comparisons in terms of octave band sound pressure level contours are shown in Figures 18 and 19, for center frequencies of approximately 80 and 160 Hz, respectively. These are the lower two frequency bands available from the Plumblee *et al* method. Just as for non-afterburner noise, one finds here that the agreement between measured and predicted levels is quite good at the higher frequency, but that the agreement is poor at the lower frequency.

The method of Plumblee *et al.* [6] has the disadvantage that noise due to the combustion process is not included in the
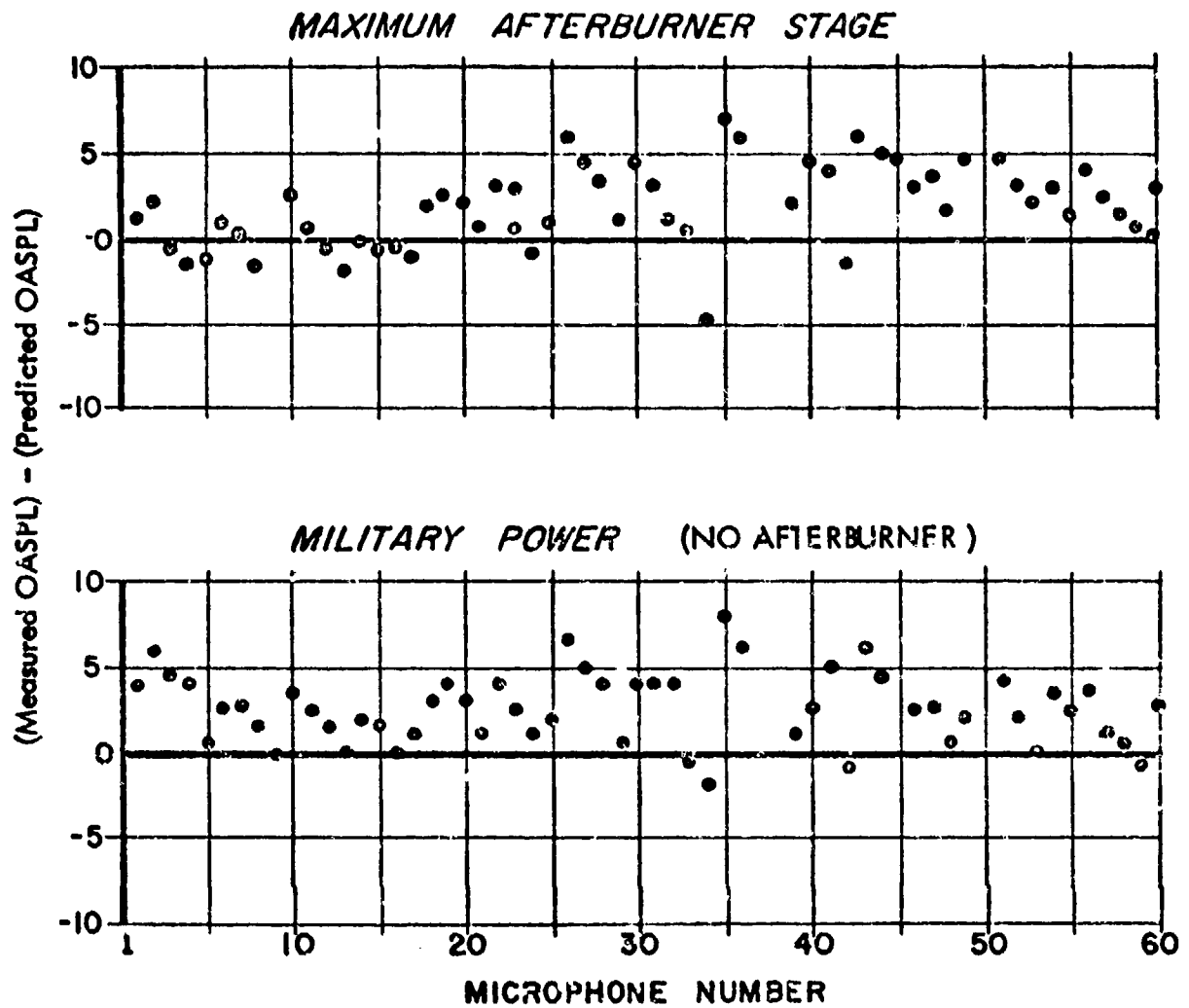
FIG. 17.   COMPARISON OF MEASURED AND PREDICTED OVERALL SOUND
PRESSURE LEVELS FOR AFTERBURNER OPERATION [15].
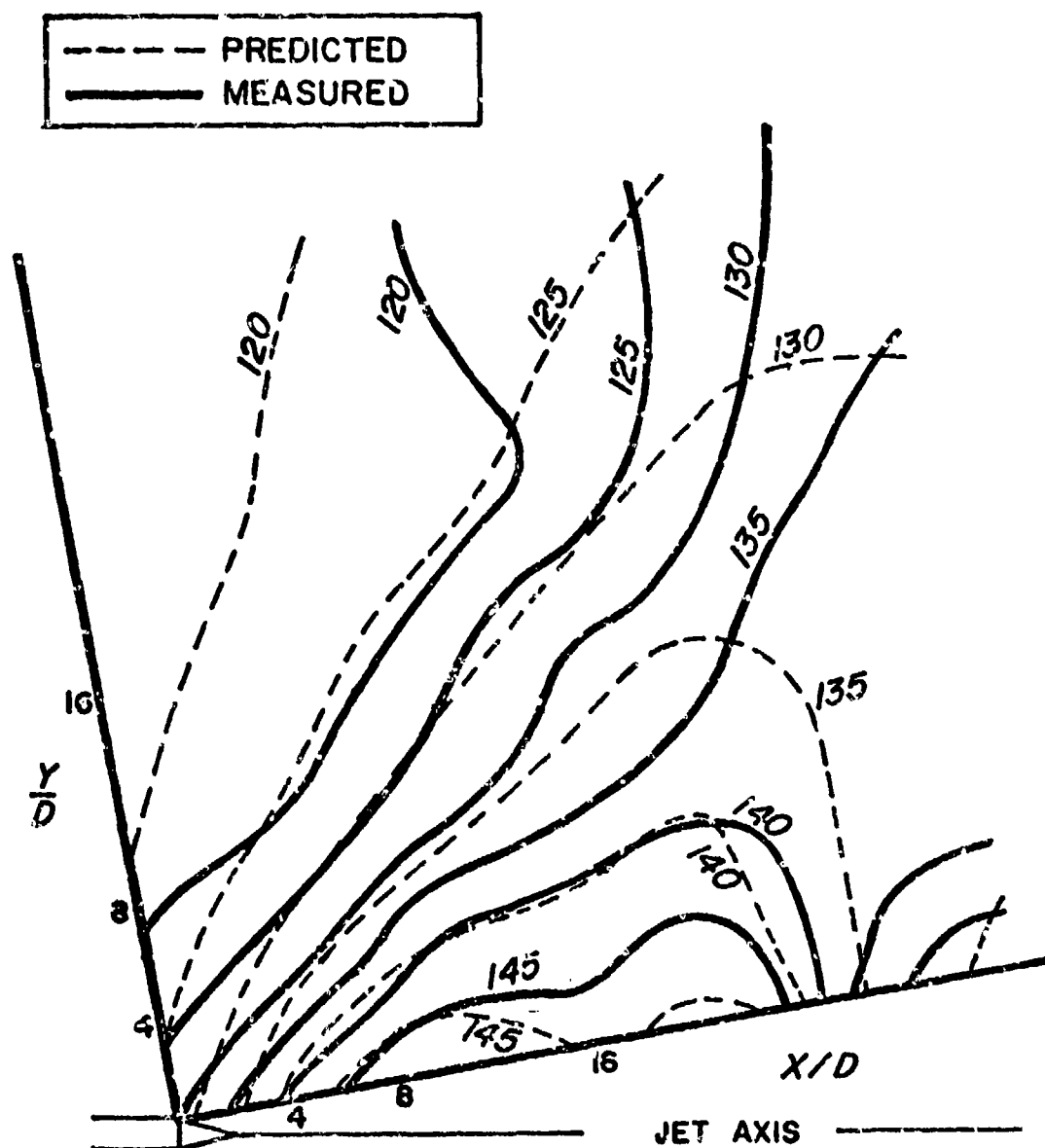
FIG. 18. COMPARISON OF MEASURED AND PREDICTED SOUND PRESSURE
LEVEL CONTOURS FOR OCTAVE BAND CENTERED AT ABOUT
80 Hz. MAXIMUM AFTERBURNER CONDITION [15].

51
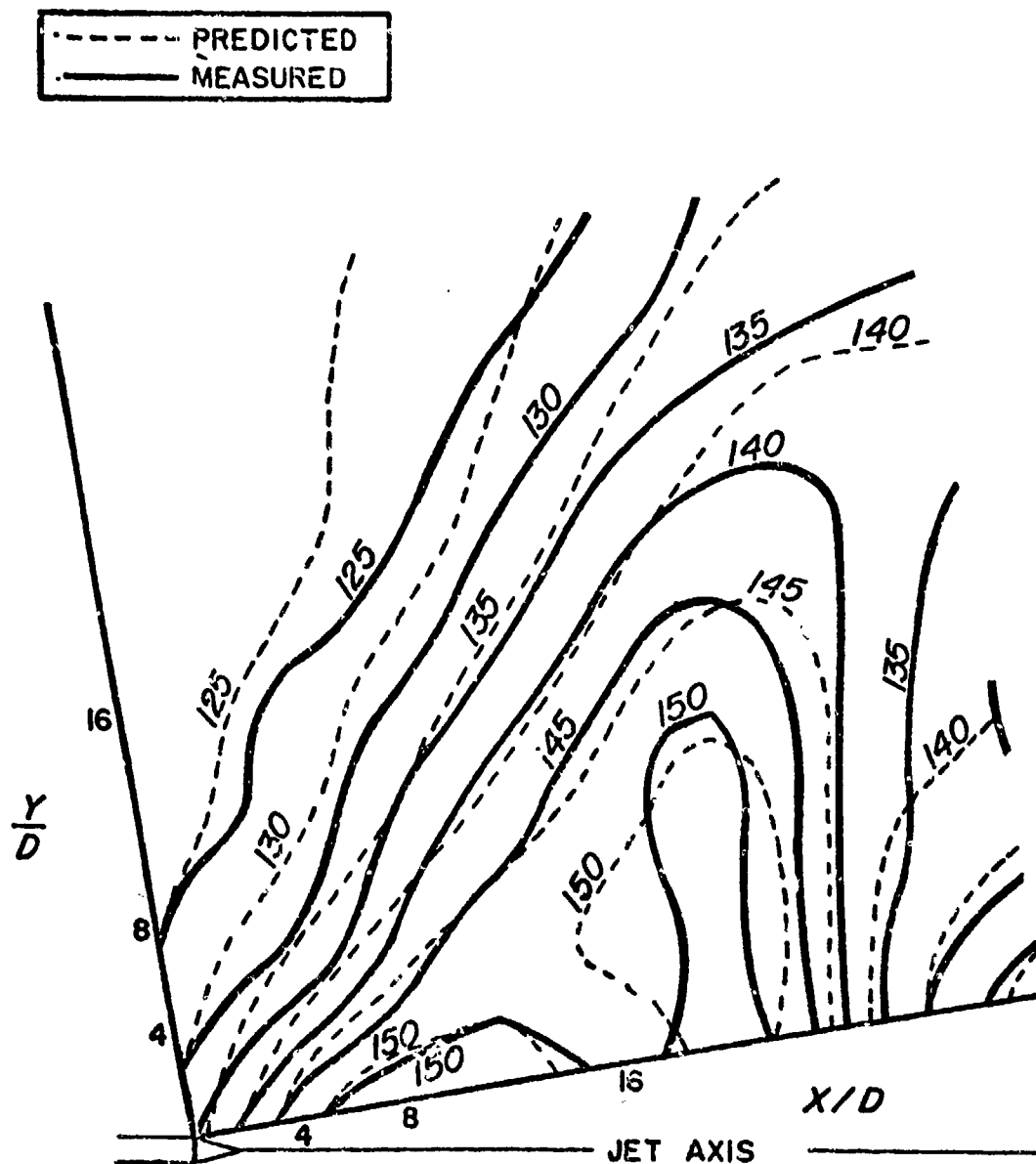
FIG. 19. COMPARISON OF MEASURED AND PREDICTED SOUND PRESSURE
LEVEL CONTOURS FOR OCTAVE BAND CENTERED AT ABOUT
160 Hz. MAXIMUM AFTERBURNER CONDITION [15].

prediction procedure (unless some combustion noise was present, inadvertently, in the basic data used to construct the analytical model). At the present time, there is available no method for predicting the combustion noise, or even for determining whether it is a significant contributor to afterburner noise. Thus, further studies are required, but at present the method of Plumblee may be used as an adequate approximate tool.

2.4 Coaxial Jets

Turbofan engines with bypass flow have coaxial nozzles through which pass flows that usually have different temperatures and velocities. Depending on the particular engine design, the nozzles may be coplanar, the primary nozzle may be retracted (as in the JT8D) or the fan duct or secondary nozzle may be shortened (as in the JT9D). A schematic representation of a coaxial nozzle, showing the various noise source regions, is presented in Figure 20.

2.4.1 Methods for prediction of farfield noise

Several experimental investigations of the farfield noise of coaxial jets have been conducted on model and full-scale engines. The conclusions reached by the investigators differ, and several empirical relationships have been proposed to describe the radiated sound field. The main point of contention is whether the primary jet velocity V_{j1} or the secondary velocity V_{j2} should be used as the principal parameter of the noise field. No attention appears to have been given to the nearfield.

From a physical standpoint, it is logical to consider the noise generation in two parts: (1) the interaction between the primary and secondary flows, and (2) the interaction between the secondary flow and the surrounding air. With this approach the effect of forward motion is assumed to be restricted to the secondary flow region, as discussed in Section 1.5.

Both of the available prediction methods for the acoustical farfield of coaxial jets are empirical and based mainly on model-scale, cold-jet experiments, and both are based on prediction methods for single jets, with suitable modifications added to account for the dual flow.

54
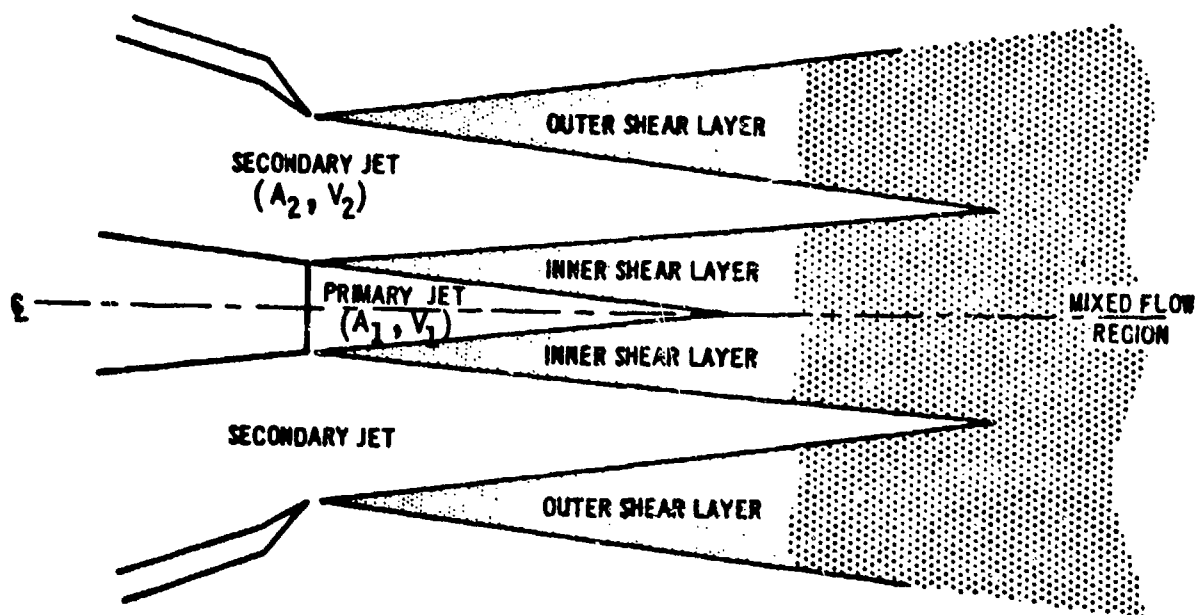
FIG. 20. SCHEMATIC SKETCH OF NOISE SOURCE REGIONS FOR
CO-ANNULAR JETS.

Stone [20] calculated the farfield $OASPL_{90,1}$ at
$\theta = 90°$ for the primary jet alone, and then modifies the result
to account for the secondary flow, according to the following
equation:

$$OASPL_{90} = OASPL_{90,1} + 5 \log [T_{1j}/T_{j2}]$$

$$+ 10 \log \left[\left(1 - \frac{V_{j2}}{V_{j1}} \right)^m + 1.2 \left(1 + \frac{A_2 V_{j2}^2}{A_1 V_{j1}^2} \right)^4 \left(1 + \frac{A_2}{A_1} \right)^{-3} \right]$$

$$(10)$$

The suffixes 1, 2 here refer to the primary and secondary flows,
respectively. The effect of jet temperature is included rather
arbitrarily, since it is not directly associated with the appro-
priate flow area and jet velocity. (An improvement is obviously
required here.) Adjustments can be made to Equation (10) to
give the overall sound pressure level at any required angle θ,
and one-third octave band spectra can be obtained by using typi-
cal shapes for single jets.

Dunn and Peart [35], on the other hand, calculate the
sound pressure levels associated with the primary and secondary
flows separately. (The calculation for the secondary flow can
be applied also to the mixed flow region, when the primary and
secondary flows are mixed.) For the primary jet, they calculate
the one-third octave band spectrum on the basis of the area A_1
and jet velocity V_{j1} of the primary jet. They then account for
the presence of the secondary flow by introducing a relative
velocity correction term $\Delta_{12}(f)$, such that

$$(SPL(f))_1 = SPL(f) + \Delta_{12}(f) \tag{11}$$

56

where $\overline{SPL}(f)$ is the space-averaged one-third octave band sound
pressure level calculated directly from single jet analysis,
$(\overline{SPL}(f))_1$ is the corrected value for the primary flow and
$\Delta_{12}(f)$ is the correction term, where

$$\Delta_{12}(f) = 10 \log \left[\frac{V_{j1} - V_{j2}}{V_{j1}} \right]^m \qquad (12)$$

The index $m = m\,(A_2/A_1,\ f/f_1)$ is given by Figure 21.

For prediction of the noise field from the secondary flow, they
use the prediction method for a single jet directly, but with
the density, area and jet velocity parameters defined as follows:

$$\rho_e = \rho_2 = \text{flow density of secondary flow}$$

$$A_e = A_1 + A_2$$

$$V_j = \left[\frac{A_1 V_{j1}^2 + A_2 V_{j2}^2}{A_1 + A_2} \right]^{1/2} \qquad (13)$$

It should be noted that Equation (13) was taken by Dunn and
Peart from the work of Bielak [36]. His data were measured
on model-scale jets, where the flow from the primary and second-
ary nozzles was at ambient temperature, and he developed the
equation for the effective jet velocity on the basis of con-
tinuity of momentum for ambient temperature flow. Thus, it
appears appropriate to introduce new equations which take into
account hot primary flows, such as occur in a typical turbofan
engine. If one again uses continuity of momentum, one finds
that the effective jet velocity obeys

$$V_j = \frac{\rho_1 A_1 V_{j1}^2 + \rho_2 A_2 V_{j2}^2}{\rho_1 A_1 V_{j1} + \rho_2 A_2 V_{j2}} \qquad (14)$$

A similar approach could be followed for equivalent density, if
required.
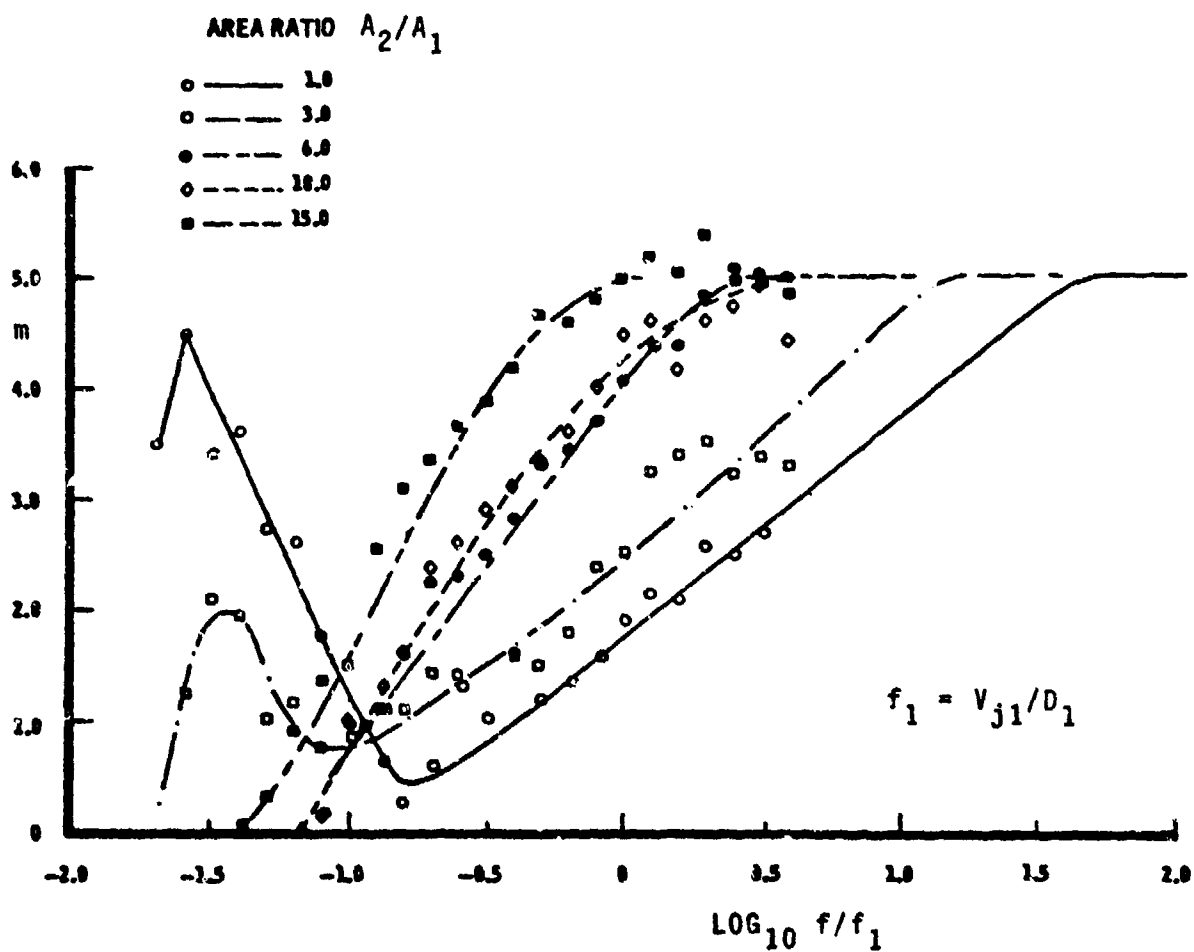
FIG. 21. INDEX m AS FUNCTION OF STROUHAL NUMBER f/f_1 [36].

2.4.2 Suggested method for prediction of nearfield noise

Dunn and Peart [35] have developed their own method for predicting farfield noise of single jets, but have not dealt with nearfield sound. However, since their general approach is more readily adaptable to the prediction procedure developed by Plumblee *et al* (Section 1.1) than is the procedure of Stone, it is proposed that the procedure of Dunn and Peart be used in setting up a preliminary method for predicting nearfield sound levels of a coaxial jet. Of course, comparisons between theory and experiment are required to justify this approach.

The nearfield jet noise procedure of Plumblee *et al.* [6], which was extended to additional frequencies in the present report, requires as input parameters the jet diameter D, exit Mach number M, jet total temperature T, and jet noise source location x_o. These parameters here need to be established for the primary and secondary flows. For the primary flow, the choice of parameters is readily apparent; viz., $D = D_1$, $M = M_1$, $T = T_1$, and the source location x_o may be calculated as for the single jet. Calculation of the correction term $\Delta_{12}(f)$ is also straightforward.

For the secondary flow, the effective diameter D_e can be obtained from the effective area A_e, Equation (13), and the effective jet velocity V_j can be calculated from Equation (14). An approximation to the effective total temperature T_e is given by

$$T_e = \frac{T_1 + \beta T_2}{1 + \beta} , \qquad (15)$$

where β is the engine bypass ratio. (Although Equation (15) is an engineering approximation, rather than an exact relation,

59

its accuracy should be adequate for nearfield noise estimation.*)
The effective jet Mach number M_e can be estimated on the basis
of the above values of effective jet velocity and total temperature.

The total sound pressure level SPL in a given frequency
band then may be determined from

$$SPL = 10 \log \left[10^{(SPL)_1/10} + 10^{(SPL)_2/10} \right] \qquad (16)$$

where $(SPL)_1$ and $(SPL)_2$ are the sound pressure levels calculated
for the primary and secondary flows, respectively, and where the
two noise sources are assumed to be incoherent.

The method of Plumblee et al may be less accurate for the
prediction of coaxial flow noise, because of the low velocities
associated with secondary flow in turbofan engines. Table 2
lists typical fan jet velocities as being in the range of 700
to 1200 ft/sec, whereas the Plumblee method is based on measurements in the range of 1200 to 3000 ft/sec.

---

* The definitions of A_e, V_j and T_e are not mutually consistent
in terms of mass flow. (This is also true of Equation (13)).
However, the proposed definitions provided reasonable approximations for nearfield noise estimation, because much of the
jet noise is generated downstream of the jet core, where the
differences between total and static temperatures are less
than at the nozzle.

2.5 Shock Noise

Most investigations of noise from supersonic jet exhausts
have dealt with shock-free flow. However, additional noise
sources arise from the presence of shock waves in flow which is
not fully expanded. This shock noise can be of broadband or
discrete-frequency nature; broadband noise is caused by inter-
action between turbulence and the shockwave, and discrete fre-
quency noise is generated by a feedback mechanism between the
shock fronts and jet nozzle.

Shocks occur in any supersonic flow from a convergert
nozzle, and in supersonic flow from a convergent-divergent
nozzle operating away from its design point. Shocked flow can
be classified as either overexpanded or underexpanded. In the
overexpanded flow case, the nozzle static pressure p_e is below
ambient $(p_e < p_a)$, whereas in underexpanded flow, $p_e > p_a$. For fully
expanded flow, $p_e = p_a$. Typical flow regimes are illustrated
in Figure 22.

2.5.1 Shock noise vs shock-free noise

Although broadband and discrete-frequency shock noise has
been measured by several investigators, very little effort has
been directed towards establishing prediction procedures, even
for the farfield case. Indeed, most authors, including Chen *et al*
[2] specifically exclude shock noise from their prediction
methods for supersonic jet noise, because of the complexity of
the problem. Stone [20] proposes a method for calculating
farfield, broadband shock noise, but excludes discrete frequency
noise because "such tones can often be eliminated by slight de-
sign moaifications".

From the description of the development of the predition
method of Plumblee *et al* [6] it is not clear whether shock

61

(a) Overexpanded. Nozzle Static Pressure $p_e < P_a$
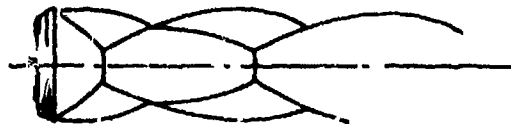
(b) Fully Expanded. $p_e = P_a$

(c) Underexpanded. $p_e > P_a$

Reflected of
Interception Shock

Compression
Shock

Mach Disc or
Riemann Wave

Expansion
Fan

Reflection
Shock

Compression
Shock

Flow
Boundary
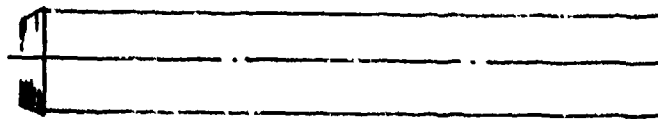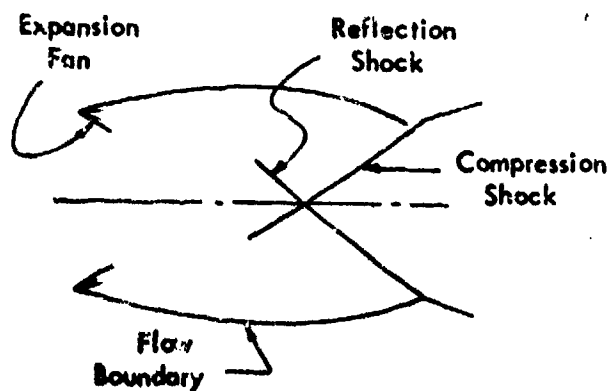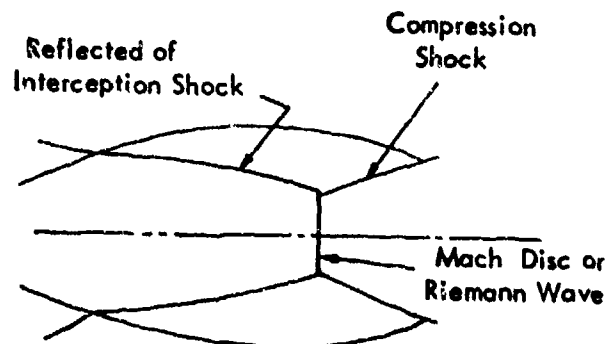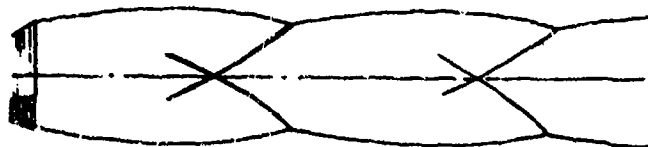
FIG. 22.   TYPICAL SHOCK PATTERNS IN OVER- AND
UNDER-EXPANDED JETS.

noise was included. However, it is possible that some of the discrepancies between predicted and measured levels are due to the presence of shock noise in the experimental data. It is assumed for the present that the Plumblet model does not take shock noise into account, and that a method for predicting this noise needs to be established.

The contribution made by shock noise can be determined by comparing noise data for a convergent-divergent nozzle operating at on-design conditions with data on the same nozzle at off-design conditions, or by comparing data for a convergent-divergent nozzle at on-design conditions with similar data for a convergent nozzle operating at the same nozzle pressure ratio. Such a comparison for far field noise has been made by Simcox [37]; sample data are shown in Figure 23. This figure compares data for a convergent-divergent nozzle designed for $M = 1.4$ operation with measurements for a convergent nozzle. At a flow temperature of 520°R, Figure 23a indicates a decrease in radiated sound in the neighborhood of $M = 1.4$ for the convergent-divergent nozzle, but no corresponding drop for the convergent nozzle. At the higher flow temperature of 2460°R, no decrease in sound level is observed at the on-design condition, and the noise levels for convergent and convergent-divergent nozzles are nearly the same (Figure 23b). Simcox claims that this phenomenon occurs because at a given nozzle pressure ratio the shock-free noise increases much more rapidly with jet temperature than does the shock noise. (In fact, the data suggest that shock noise is independent of temperature.)

63
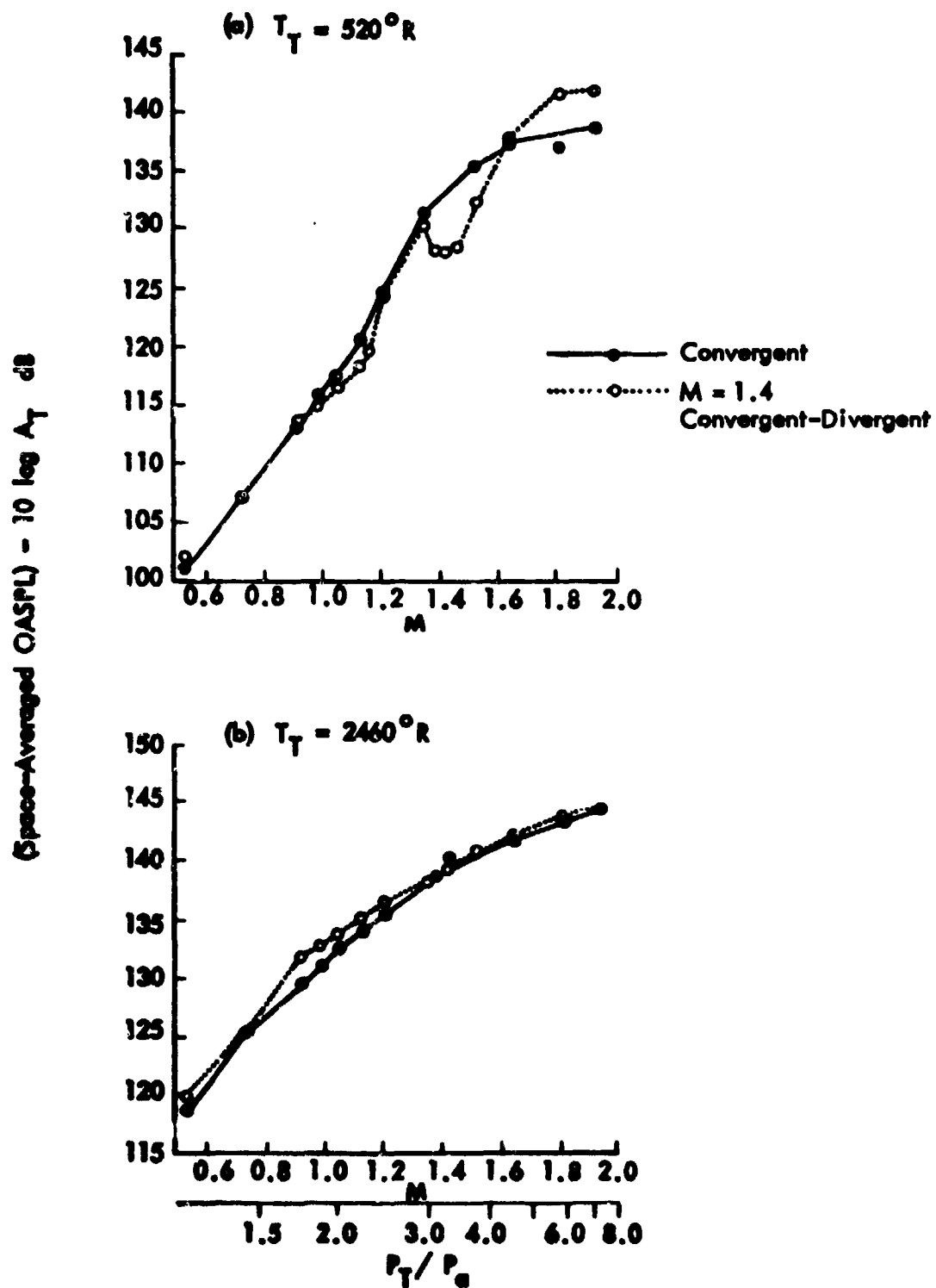
FIG. 23. OVERALL SOUND PRESSURE LEVEL FOR SUPERSONIC
JETS WITH AND WITHOUT SHOCK NOISE [37].

2.5.2 Broadband Shock Noise

An interim prediction method for farfield noise generated
by shock wave effects in supersonic flow has been proposed by
Stone [20]. The method assumes that overall and spectral
sound levels are non-directional and independent of jet temper-
ature. According to this method, the overall sound pressure
level is given by

$$OASPL_s = 147 + 10 \log \left[(A_j/r^2) \ (\rho_o c_o / \rho_{ISA} c_{ISA})^2 \right]$$

$$+ 10 \log \left[12.5 \ (M_j - 1)^3 \ (V_j/c_o)^8 \right]$$

$$- 10 \log \left[0.04 + (M_j - 1)^3 \right]$$

$$- 10 \log \left[1 + 2 \ (M_j - 1)^4 \right]$$

$$- 10 \log \left[1 + (0.05/M_j^3) \ (V_j/c_o)^8 \right]$$

$$- 10 \log \left[1 + (0.0086/M_j^3) \ (V_j/c_o)^8 \right] \tag{17}$$

where $M_j \geq 1$. One-third octave band spectral levels are obtained
from the non-dimensional spectrum shown in Figure 24. The
shock-noise spectrum levels are then added to corresponding lev-
els for shock-free noise.

This approach agrees with the experimental finding of
Simcox [37] that the shock noise is independent of tempera-
ture, but fails to predict the nearfield shock noise levels
measured for a model-scale heated jet by Knott *et al* [38]
A typical example, for a nozzle pressure ratio of 3.067 and jet
total temperature of 2220°R, is snown in Figure 24. If the
irregularities associated with discrete frequency shock noise
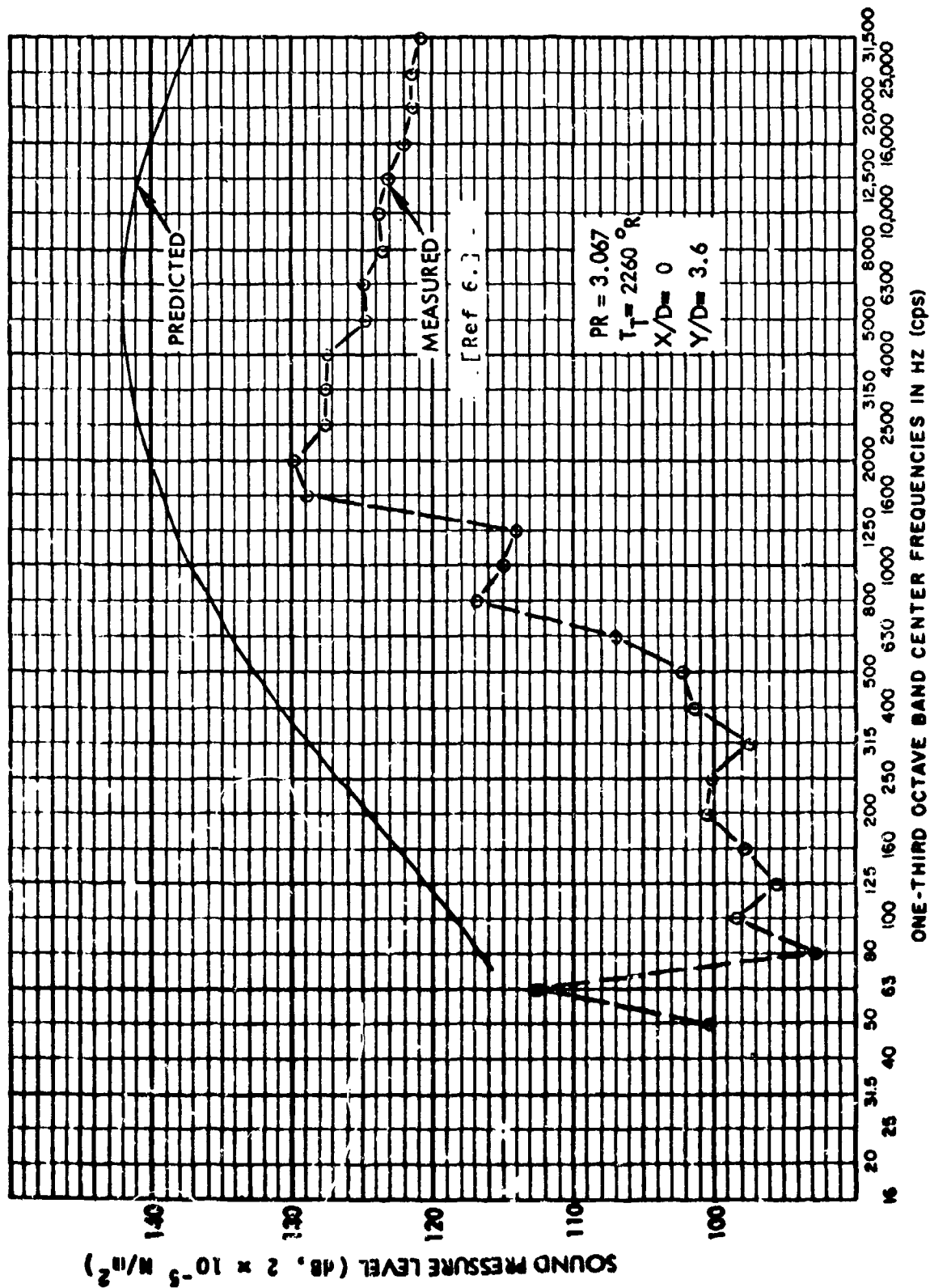
FIG. 24. COMPARISON OF MEASURED AND PREDICTED BROADBAND SHOCK NOISE USING METHOD OF STONE [20].

66

are excluded, the estimated sound levels turn out to be about 16 dB higher than the measured values. The predicted spectrum shapes, on the other hand, agree reasonably well with the observed ones.

Two alternatives present themselves. One is the modification of Equation 17 to bring the predicted and measured levels into agreement. This can be done for the data in Figure 24 by changing the constant in Equation 17 from 147 to 131. However, there still remains the question as to whether the $(1/r^2)$ distance law is adequate for the near field; if it is not, the constant 131 may not be applicable at other locations in the near field.

The second alternative is to use available experimental data to determine incremental changes in spectrum levels due to the presence of shock noise. These incremental changes could then be added to predicted spectra for shock-free noise. That is, if the incremental change due to broadband shock noise is Δ_{SB} dB, the total spectrum level is SPL_s = SPL (shock free) + Δ_{SB} dB.

Experimental results which can be used to determine values of Δ_{SB} are found in [38 and 37]. If one takes for each test condition the increases in sound pressure level due to the presence of shock noise, if one averages these increases over all frequencies above the shock fundamental discrete frequency f_1, and if one plots the resulting values as a function of jet total temperature, one obtains the plot shown in Figure 25. One may then draw a curve to represent the typical relation between the sound level increment and jet total temperature.
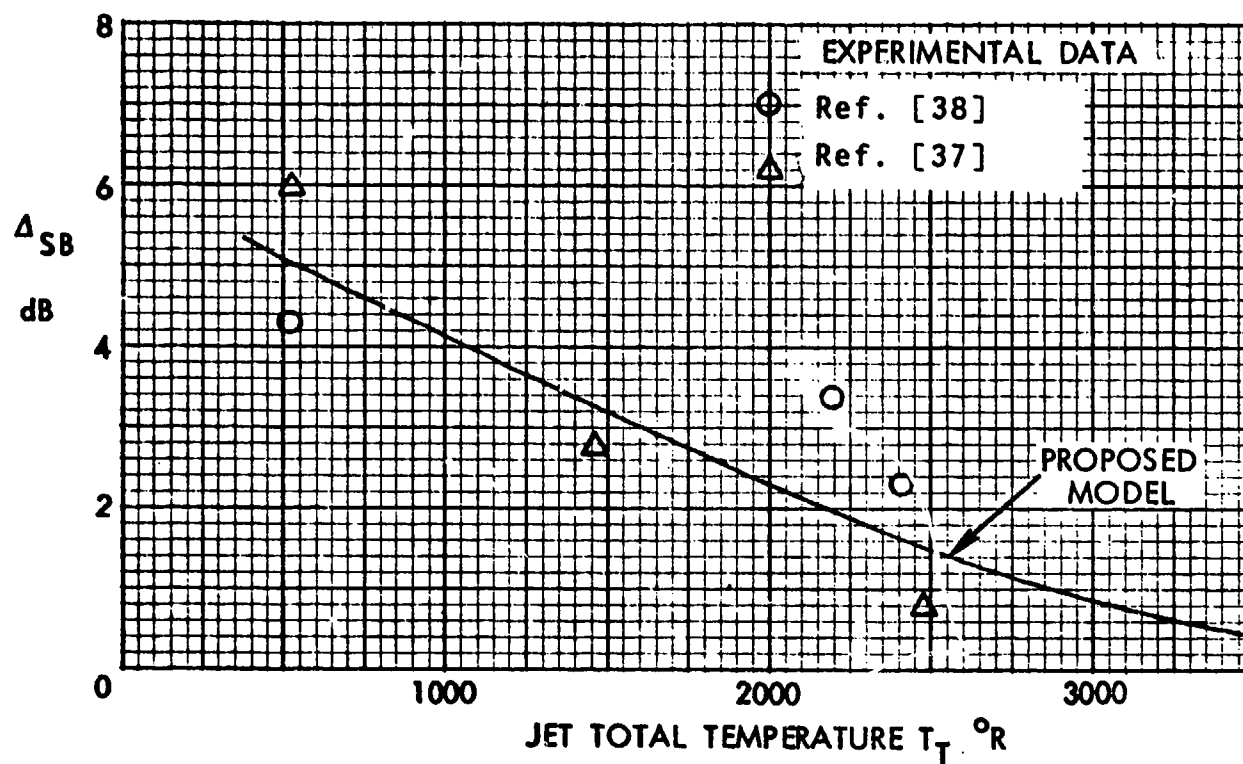
FIG. 25. SOUND LEVEL INCREMENT DUE TO BROADBAND SHOCK NOISE, AS A FUNCTION OF JET TEMPERATURE.

On the basis of the experimental evidence given in [37] and [38], one may introduce the following reasonable approximations:

(1) Shock noise makes a negligible contribution to jet nearfield noise at frequencies below the shock fundamental discrete frequency f_1 (this frequency is discussed in Section 1.4.3).

(2) At frequencies above f_1, the presence of broadband shock noise increases the jet noise spectrum levels by an increment that is independent of frequency, but dependent on jet temperature.

(3) The incremental increase in sound level is independent of jet Mach number when $M \geq 1.4$. Below $M = 1.4$, the increment decreases with Mach number to a value of zero at $M = 1.0$.

(4) An exception to (3) occurs in the neighborhood of the design pressure ratio for a convergent-divergent nozzle. In this case, the increment is zero if the pressure ratio is between 0.9 and 1.1 times the design pressure ratio.

(5) The increment is applied at all measurement locations where $\theta > 45°$. For $\theta < 45°$, the increment is zero.

By means of these simplifying approximations, one may transform the empirical curve in Figures 25 into the family of prediction curves shown in Figure 26.

2.5.3 Discrete-frequency shock noise

Discrete-frequency shock noise has been studied extensively in the laboratory, by use of carefully constructed model-scale nozzles. Under these conditions, high levels of discrete-frequency shock noise were usually observed [37, 39, 40, 41], but, in some cases the tones were low in level or were not observed at all [38, 42]. On full-scale jet engines, discrete-frequency shock noise has been encountered infrequently [42, 43].

69
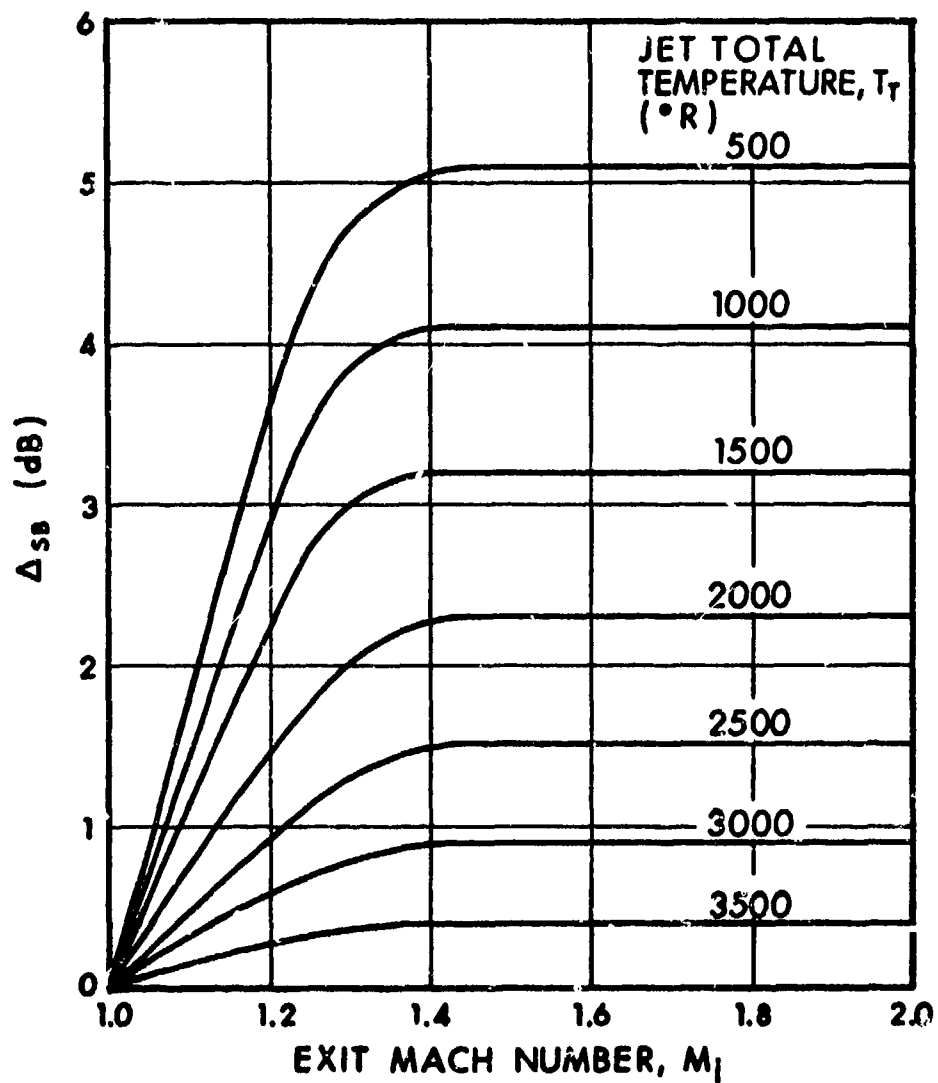
FIG. 26.   PROPOSED INTERIM MODEL FOR PREDICTION
OF BROADBAND SHOCK ، ٦ISE INCREMENT.

70

Two explanations have been suggested for the variability in generation of discrete-frequency shock noise. One explanation relates this effect to the turbulence in the flow upstream of the nozzle; Howlett [42] observed that the level of discrete-frequency shock noise decreased as the turbulence level increased. The second explanation ascribes this effect to irregularities in the construction of the nozzle; Powell [44] demonstrated that a small notch at the nozzle exit of a model-scale jet at ambient temperature would reduce the intensity of the discrete-frequency shock noise or eliminate it completely. Both of these explanations could account for the apparent absence of this form of shock noise in the acoustic fields of many jet engines, even though they may operate at high nozzle pressure ratios. It is also reported [42] that the discrete-frequency noise of the R-R Spey engines on the HS 121 airplane disappeared when a 6-chute suppressor nozzle was fitted to the jet pipe.

There is available no criterion for the onset of discrete-frequency shock noise; this shortcoming is a major obstacle to establishment of a method for predicting nearfield sound levels. Since experimental data necessary to construct such a criterion are not available, an alternative approach is suggested in the following discussion. This approach uses sound field information from model-scale tests which exhibited strong discrete-frequency shock noise and makes the assumption that these sound levels provide an upper bound to the levels likely to be encountered on full scale engines. (Turbulence and nozzle irregularities would normally reduce the full-scale engine discrete-frequency shock noise levels.)

The original work of Powell [19] on ambient temperature jets established an equation for the fundamental frequency of discrete-frequency shock noise. This equation is

$$f_1 = \frac{c_0}{K_1 D_j [R - R_c]^{\frac{1}{2}}} \qquad (18)$$

where
D_j = nozzle diameter
R = nozzle pressure ratio
R_c = critical nozzle pressure ratio = 1.893

and
K_1 = constant.

Powell obtained a value $K_1 = 3.0$, but subsequent experimental studies by other investigators resulted in lower values of K_1. These values are shown in the following table:

Reference	Test Condition	K_1
Howlett [42]	Cold model jet	2.4
Simcox [37]	Cold model jet	2.7
Westley [41] and Woolley	Cold model jet	1.0-1.7
Knott et al [38]	Heated model jet	1.7-2.2
Hay [43]	Full scale engine	1.1

Since the experimental values of K_1 are fairly uniformly distributed in the range between 1.0 and 3.0, a value $K_1 = 2.0$ will be used for the present model. The frequency f_2 of the second harmonic of the shock noise is given by

$$f_2 = 2f_1 \qquad (19)$$

72

In practice, the situation is rather more complicated than is implied by the above two frequency equations. For example, Westley and Woolley [40] have shown that several families of shock tones can be present and the noise field may change from one dominant family to another. However, the simplified approach is adequate for present purposes, if it is acknowledged that the error in predicted frequency may be as large as +50%.

The detailed data on nearfield acoustic pressures for the fundamental of the discrete-frequency shock noise, which have been amassed by Westley and Woolley [40, 41], will be used here to locate the effective source, construct simplified noise contours and determine upper bounds for sound levels. Because the data include very little information for the second harmonic, the proposed model for this component will rely on engineering judgement. Obviously, experimental verification of the proposed model is required.

Westley and Woolley [41] observe that the maximum sound levels for the dominant fundamental frequency occur at a distance from the nozzle which increases with nozzle pressure ratio. E.g., for a nozzle pressure ratio of 2.67, the maximum levels occur in the neighborhood of the third and fourth shock cells, whereas at a pressure ratio of 5.67, the maxima occur at the fifth and sixth cells. For present engines typical nozzle pressure ratios lie below about 3.0 (see Table 2). Hence, the proposed model assumes that the effective location of the sources of discrete-frequency shock noise (fundamental and all harmonics) is approximately 3.5 shock cell lengths downstream of the nozzle exit plane, and lies on the jet centerline.

The characteristic length s of a shock cell can be taken approximately to obey

$$\frac{s}{D} = [R-R_c]^{\frac{1}{2}} \quad , \tag{20}$$

and thus the effective source location x_s may be approximated by

$$\frac{x_s}{D_j} = 3.5 \ [R-R_c]^{\frac{1}{2}} \tag{21}$$

Theoretical directivity patterns constructed by Powell [9] for specific operating conditions show a series of lobes (Figure 27a): for the fundamental, the main lobe is in the upstream direction; for the second harmonic, the main lobe is at right angles to the jet axis. The nearfield measurements of Westley and Woolley [40, 41] show an extremely complicated pattern of sound pressure level contours for the fundamental frequency component, as illustrated in Figure 27b. Because the actual contours are too complicated for use in an engineering prediction model, series of smoothed contours have been constructed to approximate the experimental data, as also shown in the aforementioned figure.

No nearfield data are available for the second harmonic, but circular contours as shown in Figure 27c (with centers on the normal to the jet axis at the effective source location, and tangent to each other at the effective source location) are proposed as a simplified representation of the contours of Powell.

In order to predict upper bounds on the sound pressure level, one may refer to data taken along the normal to the jet axis at the effective source location, which data [40, 41] indicates a sound pressure dependence on the fourth power of

(a)

FUNDAMENTAL   SECOND HARMONIC

(b) FUNDAMENTAL

(c) SECOND HARMONIC
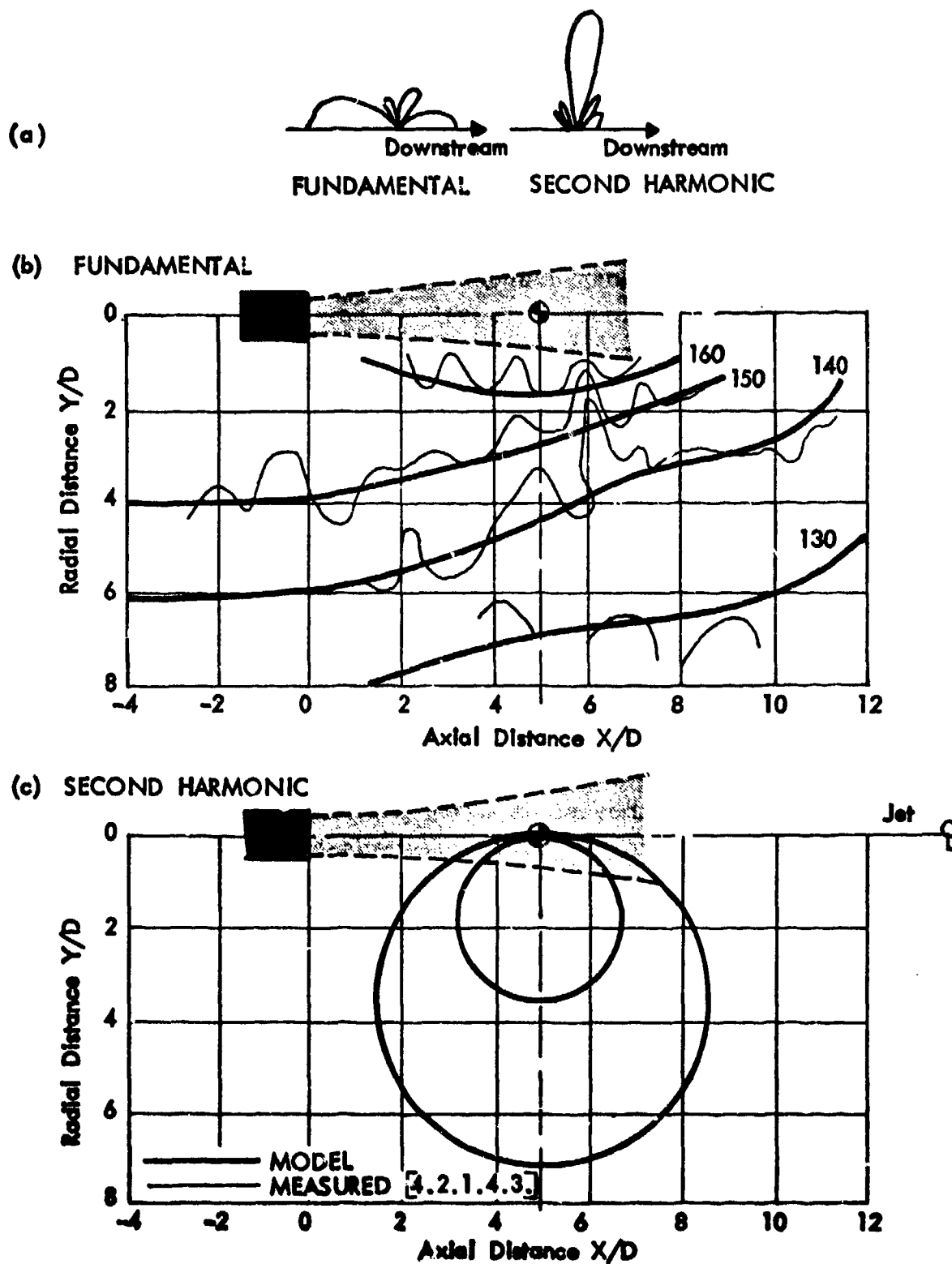
FIG. 27. NEAR-FIELD DIRECTIVITY PATTERNS FOR DISCRETE-FREQUENCY SHOCK NOISE.

75

distance. Although from a physical standpoint it might be more
satisfactory to have a model with an origin located on the jet
boundary, such a model results in a more complex dependence on
distance, and the simpler method is adopted at present for the
sake of simplicity.

If one assumes that the acoustic power generated by the
discrete-frequency shock noise is directly proportional to the
nozzle area A_j, one finds that one may write a reduced sound
pressure level as

$$\phi = SPL_{90} - 10 \log (A_j/A_{ref}) + 40 \log (y/4D) \tag{22}$$

where the reference area $A_{ref} = 0.028$ ft^2, corresponding to the
model tests of Westley and Woolley. Application of this equa-
tion to the data of Westley and Woolley results in the non-
dimensional curves of Figure 28.

A modification to Equation (22) can be made to permit
its application to airplane cruise conditions, under which con-
ditions discrete-frequency shock noise has been found to be a
problem on several airplanes [42, 43]. This modification
involves correcting for the characteristic impedance $\rho_o c_o$
of the ambient air; with it Equation (22) becomes

$$\phi = SPL_{90} - 10 \log \left[\frac{A_j}{A_{ref}} \right] + 40 \log \left[\frac{y}{4D} \right] - 10 \log \left[\frac{\rho_o c_o}{\rho_{SL} c_{SL}} \right] \tag{23}$$

where ρ_{SL}, c_{SL} are sea level values of ambient density and sound-
speed, and where ρ_o and c_o are corresponding values at the cruis-
ing altitude.

Although the preceding discussion has been directed primarily
at convergent nozzles, the method can be applied also to convergent-
divergent nozzles which are operating away from the design pressure
ratio.

76
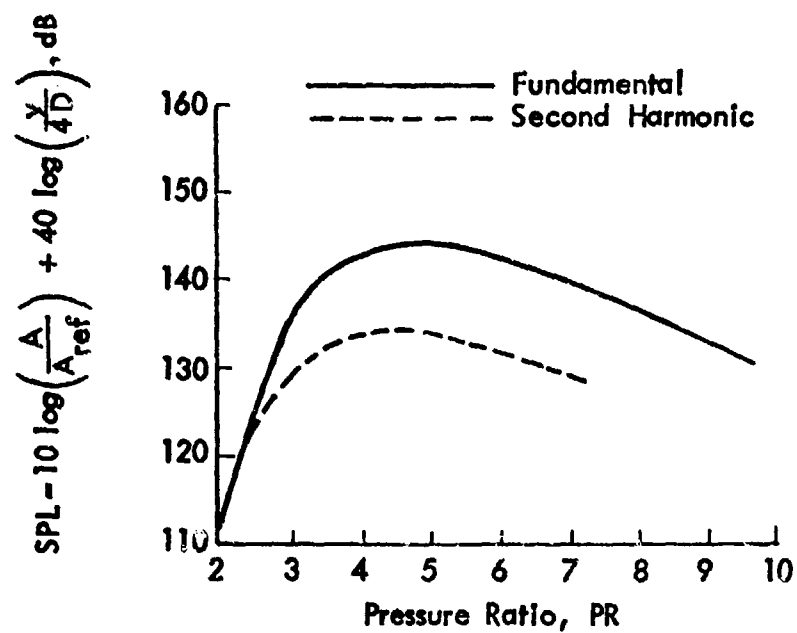
FIG. 28. NON-DIMENSIONAL SOUND PRESSURE LEVELS FOR DISCRETE FREQUENCY SHOCK NOISE (Based on [40]).

77

As for broadband shock noise (Section 2.4.1), it can be
assumed here that no discrete-frequency shock noise occurs for
a convergent-divergent nozzle operating at pressure ratios be-
tween 0.9 and 1.1 times the design pressure ratio. (This is a
gross simplification of the problem, requiring considerable ex-
perimental study.)

It is instructive to compare results calculated by means
of the proposed procedure for prediction of the upper bounds of
the sound pressure levels with the limited amount of published
data. Figure IV-A-3.16 of Knott *et al.* [38] shows that a
model jet with total temperature of 2200°R and nozzle pressure
ratio of 3.066 produced at $x = 0$ $y = 3.63D_j$ a sound pressure
level of 124 dB at the 1680 Hz shock noise fundamental frequency.
The proposed prediction procedure yields a corresponding upper-
bound sound pressure level of 144 dB at a fundamental frequency
of 1440 Hz. The flight test data reported by Hay [43] for
an engine with a nozzle diameter of 22 inches and pressure ratio
of 3.3, operating at an altitude of 35,000 ft, show a maximum
pressure level of 140 dB, measured on the horizontal stabilizer.
The proposed prediction procedure yields a corresponding upper
bound of 148 dB for the second harmonic, if a 6 dB increase is
included to account for pressure doubling due to surface reflec-
tion. In this case the frequency of the second harmonic is in-
fluenced by the airplane speed.

These comparisons appear to justify the use of the upper
bound estimation procedure. However, structures designed to
withstand the estimated acoustic pressures may be excessively
heavy, so that development of a more precise method is desirable.

2.6 Forward Motion Effects

Although there exists much empirical evidence that forward flight reduces the acoustic power generated by a jet flow, the mechanism is not fully understood. Consequently, no widely accepted method is available for predicting the effect of forward motion even on the acoustic farfield, which is the only region that has been investigated. Nevertheless, the available farfield results here will be used as a basis for the construction of an interim nearfield prediction procedure, and the available data (which correspond mainly to turbojet exhausts which are shock-free) will be extrapolated to include shock noise and coaxial jet effects.

2.6.1 Shock-free jet noise

Forward motion affects the jet noise field in terms of its acoustic power generation, a Doppler frequency shift, and the propagation distance and angle. The change in acoustic power generation has been taken into account in several investigations by introduction of the relative velocity $(V_j - V_a)$, where V_j denotes the jet velocity relative to the nozzle and V_a the airplane (or forward) velocity. In early studies, V_j was simply replaced by $(V_j - V_a)$. Subsequent analyses reduced the role played by the relative velocity: Ffowcs Williams [45] suggested that V_j be replaced by $V_j (1-V_a/V_j)^{7/8}$; Kobrynski [46] replaced V_j by $V_j(1-V_a/V_j)^{1/2}$ and, on the basis of recent experimental data [53], Stone [20] proposed that the term $V_j(1-V_a/V_j)^{3/4}$ be used in place of V_j.

Analytical studies by Pinkel [47] showed that the influence of forward flight is more complicated than is suggested by the above relative velocity terms. However, if Pinkel's results are simplified to the form $V_j(1-V_a/V_j)^n$, the exponent n is found

79

to be between 1/2 and 3/4. Cocking and Bryce [48] also obtained exponent values in the same range. Examination of the aforementioned experimental and analytical results indicates that an exponent of 3/4 represents a reasonable average value; this value therefore is proposed for the present prediction model.

Although one might at first glance expect no Doppler frequency shift, because the airframe and engine move together as a rigid body, Franken et al. [49] found no experimental evidence to support this expectation with respect to jet noise. Franken et al. adopted Powell's hypothesis [50] that the airplane moves away from the jet noise sources, with the result that Doppler frequency shifts do occur, and also that there result changes in the distance travelled by a sound wave from a source to the airframe, and in the angle of propagation associated with the given receiver location. The method of Franken et al., which covers these factors has been adopted by Rudder and Plumblee [51] for nearfield noise and is reproduced here, in the absence of any better available method. The notation used here, however, is consistent with that of other parts of this section.

Franken et al. [49] assume that forward motion of the airframe moves the receiver from its actual position r_s relative to the source to an apparent position r_s^* on a line parallel to the direction of motion. (See Figure 29.) Correspondingly, the angle between the jet axis and the source/receiver line is changed from θ_s' to ϕ_s'. Franken et al assumed that all sources are close to the jet exit plane, but this assumption is neither necessary nor desirable; Figure 29 shows a typical noise source located at distance x_o downstream of the exit. (Primed symbols are used here to indicate that the noise sources are assumed to be located on the jet centerline, whereas the jet noise prediction procedure of Plumblee et al. [6] assumes a source distribution along the jet boundary.)

80

FIG. 29. GEOMETRICAL RELATIONSHIP BETWEEN RECEIVER AND
SOURCE FOR FORWARD MOTION EFFECT.

In order to determine the relationship between θ'_s and ϕ'_s, one may note that the sound wave travels a distance r^*_s at velocity c_o in the same time in which the receiver moves through a distance Δx at velocity V_a, so that

$$\frac{r^*_s}{c_o} = \frac{\Delta x}{V_a} \tag{24}$$

From Figure 29,

$$(r^*_s)^2 = y^2 + (x-x_o - \Delta x)^2 \tag{25}$$

Since, by definition, $\cot \theta'_s = \dfrac{x-x_o}{y}$

$$\cot \phi'_s = \frac{x-x_o-\Delta x}{y}$$

and $\quad M_a = V_a/c_o$,

one finds that

$$\cot \phi'_s = \frac{1}{(1-M_a^2)} \left[\cot \theta'_s - M_a \sqrt{1-M_a^2+\cot^2\theta'_s} \right] \tag{26}$$

This relation between θ'_s and ϕ'_s is plotted in Figure 30, from which one may note that for supersonic flight speeds no jet noise propagates upstream of the source, as one would expect.

If one assumes a stationary source and a moving receiver, one finds that there occurs a Doppler shift, such that the observed frequency f^* on the airframe is related to the source frequency f as

$$f^* = (1+M_a \cos \phi'_s) f \tag{27}$$
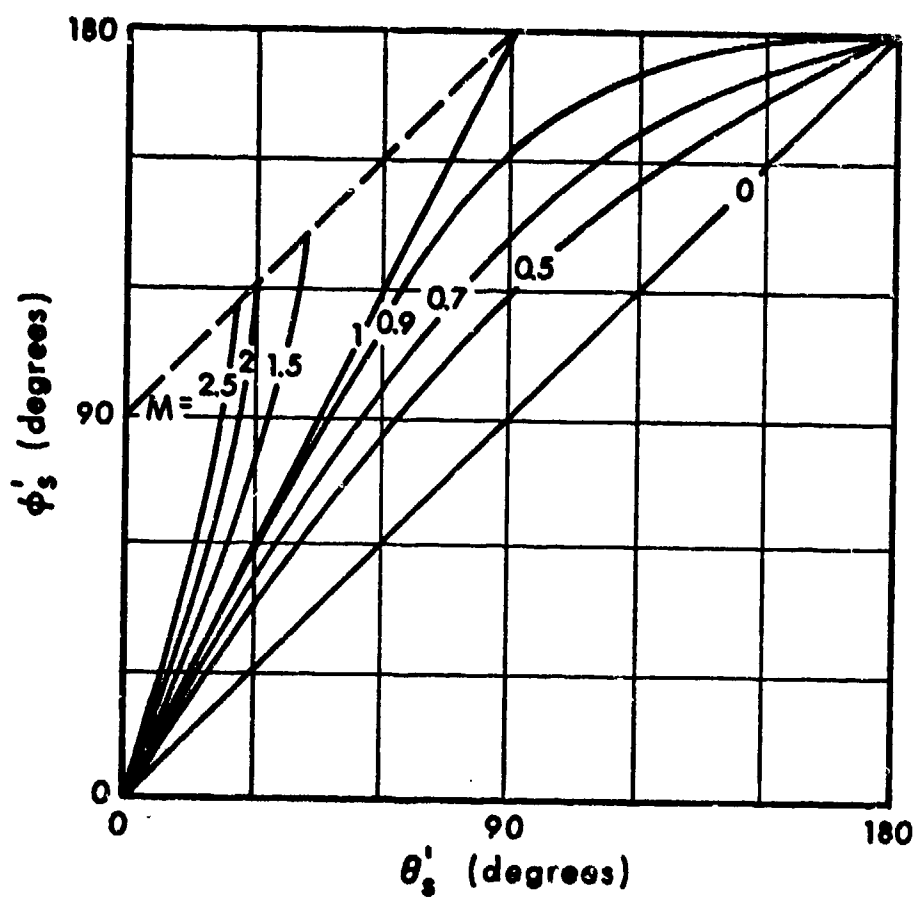
FIG. 30. EFFECTS OF FORWARD MOTION ON ANGLE BETWEEN JET AXIS AND LINE FROM SOURCE TO RECEIVER [49].

This shifted frequency needs to be taken into account when one calculates the Strouhal number associated with a given frequency; for example, if f* is the observed frequency on the airframe, the Strouhal number should be calculated corresponding to the frequency $f = f^*/(1+M_a \cos \phi_s')$.

For illustrative purposes, Franken *et al.* [49] applied their method (which assumes that the sound sources are located near the jet exhaust nozzle) to the nearfield contours of a turbojet engine for a flight Mach number $M_a = 0.8$. Figure 31 shows the corresponding nearfield sound pressure level contours for static operation and forward motion.

It must be noted that the hypothesis that the receiver moves away from the source was originated by Powell [50], passed through the literature by Franken *et al.* [49], and accepted by Rudder and Plumblee [51] without any direct supporting evidence. The hypothesis was based on the observation that the significant increase in sound pressure level that is expected upstream of rigidly connected sources moving near Mach 1 was not observed on rocket structures. No experimental data have been published that show that there exists a Doppler shift, and no data are available that show that there exists no Doppler shift. Under these circumstances, the analysis incorporating a Doppler shift is presented here with strong reservations.

2.6.2 Coaxial jets

The effects of flight velocity on the noise produced by co-axial jets have been studied solely with respect to the acoustic farfield. The corresponding results are reviewed here in terms of acoustic power generated, since the propagation effects here will be essentially the same as those for a single jet (Section 2.5.1).

84
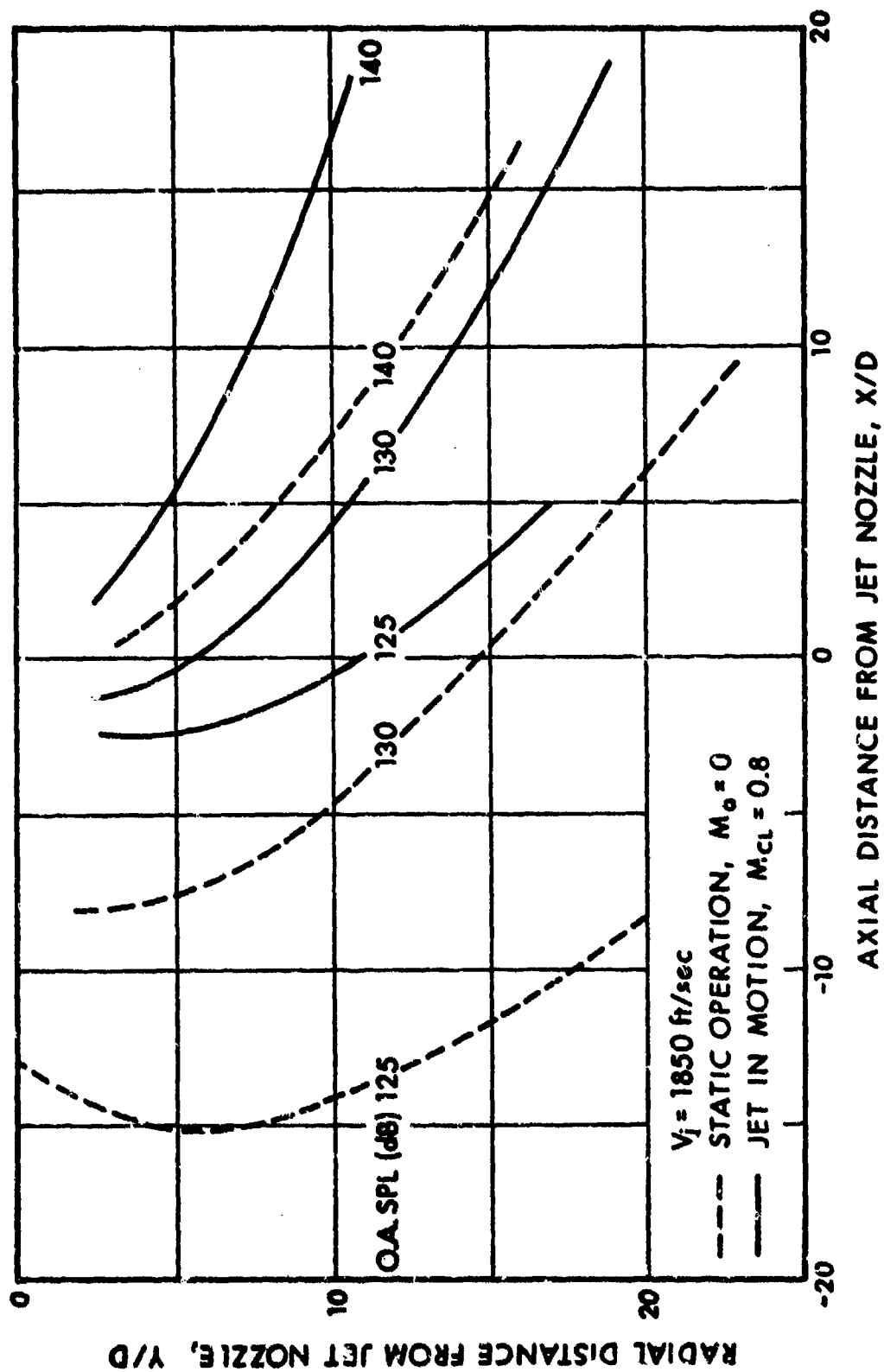
FIG. 31. EFFECT OF FORWARD MOTION ON NEAR-FIELD JET NOISE[49].

85

The results of various published studies show some diver-
gence. Reed [52] and von Glahn et al. [53] consider a dual-
flow jet as a single mixed flow, and relate relative velocity
to the primary jet velocity. In contrast, Cocking and
Bryce [48] and Dunn and Peart [35] consider the primary
and secondary flows separately. Most of the available measure-
ments were obtained from ground tests, using a wind tunnel or
tertiary jet to simulate the forward velocity effect. (Such
tests have the advantage that they exclude the Doppler shift
effect, but they have the disadvantage that the microphone either
is immersed in the moving airstream or outside the flow, in which
case there may be refraction effects.) To minimize the experi-
mental uncertainties, the various reported effects of forward
motion are compared in Table 5 for an angle of 90° to the
jet axis. This table lists the relative velocity terms for the
primary, secondary or combined flows, which terms replace the
appropriate jet velocity term in the prediction of the acoustic
farfield.

The relative velocity exponents indicated in Table 5
show considerable variation, as was the case for single jet flows.
The results of Dunn and Peart show unity exponent, but it is
probable that little data on relative velocity effects was avail-
able at the time of the study; all later studies show exponents
of less than unity. However, the work of Dunn and Peart does
take into account the area ratio A_2/A_1, a factor that should be
included in any general prediction method.

Based on the small amount of available information, it ap-
pears reasonable to assume that forward motion of the airplane
will not influence the noise contribution from the primary flow,
and that the relative velocity effect for the secondary flow
may be taken to be similar to that for single jets. Thus, one

86

TABLE 5. **RELATIVE VELOCITY TERMS FOR ACOUSTIC FAR-FIELD OR COAXIAL JETS.**

REFERENCE	TERM REPLACING JET VELOCITY, TO YIELD CORRECT SOUND PRESSURE VELELS AT 90° FROM JET AXIS
Reed [52]	$V_{j1} \left(1 - \dfrac{V_a}{V_{j1}} \right)^n$; $n = 0.63$ to 0.79
Von Glahn et al. [53]	$V_{j1} \left(1 - \dfrac{V_a}{V_{j1}} \right)^{0.75}$
Cocking and Bryce [48]	Primary: $\left(1 - \dfrac{V_{j2}}{V_{j1}} \right)^{0.5}$
	Secondary: $V_{j2} \left(1 - \dfrac{V_a}{V_{j2}} \right)^{0.63}$
Dunn and Peart [35]	Primary: $V_{j1} \left(1 - \dfrac{V_{j2}}{V_{j1}} \right)$
	Secondary*: $V_j \left(1 - \dfrac{V_a}{V_j} \right)$

*
$$V_j = \left[\frac{A_1 V_{j1} + A_2 V_{j2}}{A_1 + A_2} \right]^{\frac{1}{4}}$$

The expression given here assumes the angle between the gross thrust vector and the direction of motion to be small.

87

may replace the effective flow velocity V_j in the equation for nearfield sound presure levels by the term $V_j(1-V_a/V_j)^{0.75}$, where

$$V_j = \frac{\rho_1 A_1 V_{j1}^2 + \rho_2 A_2 V_{j2}^2}{\rho_1 A_1 V_{j1} + \rho_2 A_2 V_{j2}}$$

Justification of this choice of parameters must wait until corresponding nearfield experimental data are available.

2.6.3 Shock noise

There is little evidence available concerning the effect of forward flight on shock noise. Thus, it appears appropriate for the present to assume that forward motion has no influence on the acoustic power generated by both discrete-frequency and broadband shock noise. However, one may expect a spatial redistribution of acoustic energy, as well as changes in the frequency.

In the case of broadband shock noise, it is reasonable to make the same assumptions regarding Doppler shift and acoustic propagation as those made for shock-free jet noise. These are discussed in Sections 2.5.1 and 2.5.2, and will not be repeated here.

The influence of forward motion on nearfield discrete-frequency shock noise has been investigated by Hay [43] and Howlett [42] under actual flight conditions. However, these investigations refer only to frequency, and do not show the sound pressure level. Both studies are based on the result of Powell [19], which gives the fundamental frequency in still air as

$$f_1 = \frac{c_o}{K_1 D} \cdot \frac{1}{[R-R_c]^{\frac{1}{2}}} \tag{28}$$

with $K_1 = 3$.

Both studies develop semi-empirical r-lations for the shock
noise frequency by adjusting the time taken for the sound wave
to travel in the upstream portion of the feedback loop (i.e.,
in the external flow).

The equation developed by Hay for the fundamental fre-
quency f_1 is

$$f_1 = \frac{c_o}{D} \; \frac{[M_a + K_2 (M_{jo} - M_a)] (1 - M_a) (1 + K_2 M_{jo})}{K_1 (R - R_c)^{\frac{1}{2}} [1 + K_2 (M_{jo} - M_a)] K_2 M_{jo}} \qquad (29)$$

where R = jet pressure ratio

R_c = critical jet pressure ratio = 1.89

M_{jo} = Jet Mach number relative to ambient
speed of sound

M_a = Airplane Mach number

D = jet diameter

c_o = ambient speed of sound

K_2 = 0.625

K_1 = 1.1

There is some divergence here between the K_1 = 3 of Powell and
K_1 = 1.1 of Hay, but the results of several investigations at
zero forward speed also show considerable variation in the
value of K_1, as was discussed in Section 1.4. Thus, for a
general prediction procedure, it appears appropriate to use
Equation (29) with K_1 = 2.0, so that the prediction methods
for static and moving aircraft would be consistent. The corre-
lation between Equation (29) and related experimental data
on BAC1-11 and VC1p airplanes [54] is shown in Figure 32.
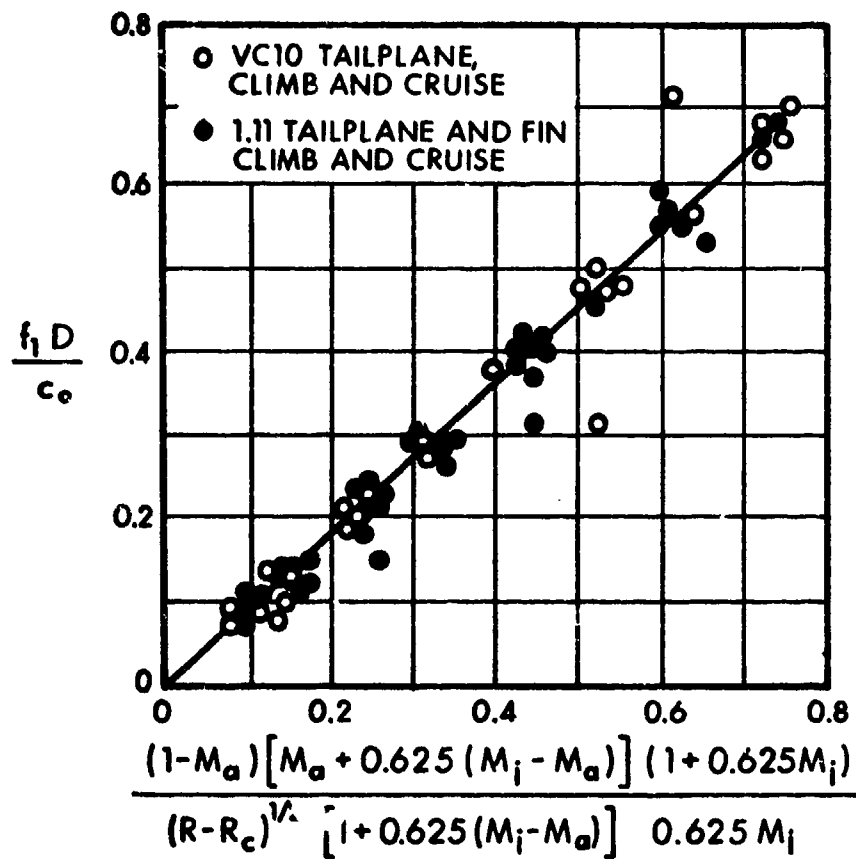
FIG. 32. SHOCK NOISE FUNDAMENTAL FREQUENCY AS A
FUNCTION OF JET AND AIRPLANE MACH
NUMBER [54].

The frequency f_2 of the second harmonic is given by

$$f_2 = 2f_1, \qquad\qquad (30)$$

as is the case for zero forward motion.

The spatial distribution of the sound pressures associated with discrete-frequency shock noise will be affected by forward motion, as for broadband shock noise. However, no Doppler shift may be expected, because the mechanism of the discrete-frequency noise is fixed in relation to the jet nozzle.

2.7 Thrust Reversers

Thrust reverser noise has been investigated only recently and such little information as is available refers to far-field sound. M jt of the available data is concerned with target-type thrust reversers. Stone [20] has summarized the data into prediction procedures for far-field noise, and his summary forms the basis of the present discussion.

2.7.1 Target-type reversers

Target-type thrust reversers (Figure 33) have been investigated by several authors [55, 56, 57] and their results have been analyzed by Stone [20] for the purpose of developing generalized relationships for overall sound pressure levels and one-third octave band spectra. This analysis indicates that the radiated sound is dominated by noise due to interaction between the jet and the airplane structure; there is no evidence that the exhaust jet noise itself plays a significant role.

Stone proposes the following empirical relation for the far-field overall sound pressure level at an angle of 90° to the inlet axis:

$$OASPL_{90} = K_{tr} + 10 \log (A_j/r^2) + 10 \log \left[\rho_j \rho_0 c_0^4 / \rho_{ISA}^2 \, c_{ISA}^4 \right]$$

$$- 10(\cos^2 \psi) \log[D_h/D_e] + 55 \log (V_j/c_0)$$

$$- 10 \log [1 + 0.01(V_j/c_0)^{2.5}] \tag{31}$$

where ψ is the angle between the source to observer line and the y axis

and $K_{tr} = \begin{cases} 149 \text{ for semi-cylindrical reversers} \\ 154 \text{ for V-gutter reversers} \end{cases}$

92

SEMICYLINDER
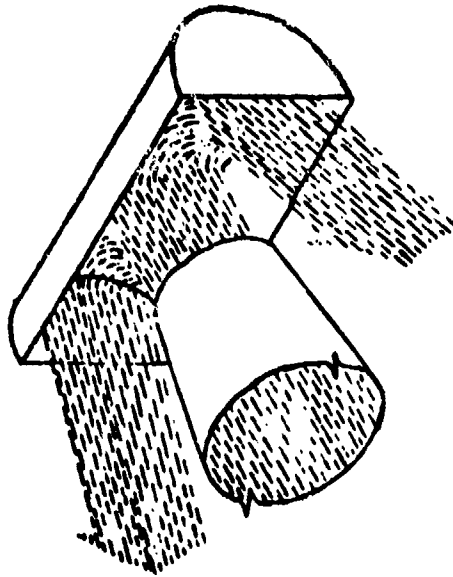
V-GUTTER
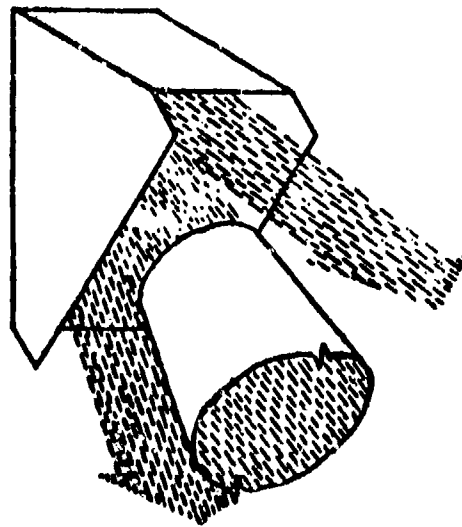
CIRCULAR NOZZLE
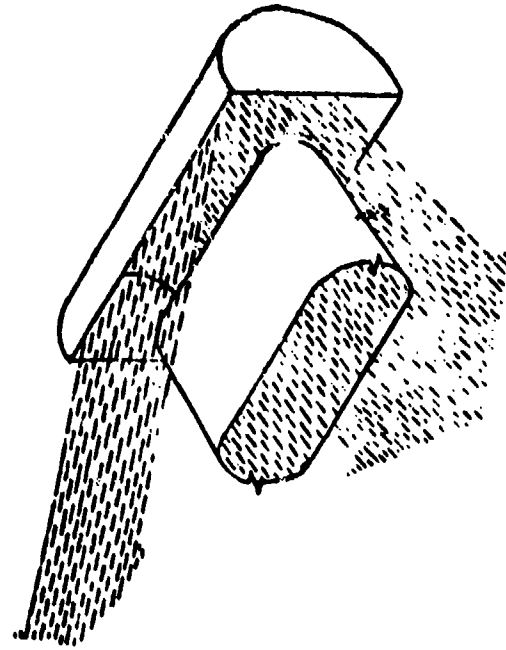
SLOT NOZZLE
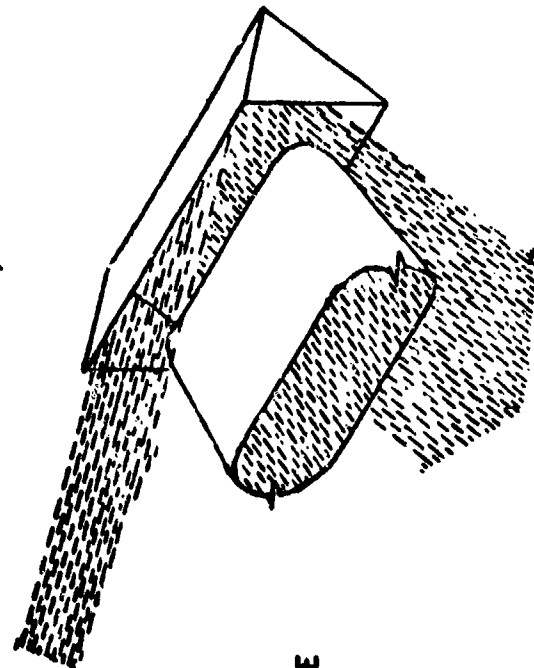
FIG. 33. DIAGRAMMATIC REPRESENTATION OF TARGET-TYPE THRUST REVERSERS.

93

Stone configured the velocity terms arbitrarily to give a V^3 relationship at high velocities, to match his formulation for jet noise at high supersonic speeds. However for $V_j/c_o \leq 1$, the intensity varies approximately as $V_j^{5.5}$, which is similar to the V_j^6 relationship for dipole noise. Dipole-like noise sources would be expected to occur from sources associated with flow impact on relatively small-scale structures.

As an interim procedure, one may take the directivity in the θ-plane to be given by

$$OASPL_\theta = OASPL_{90} + 20 \log \left[\frac{\cos(\theta/3)}{\cos 30^\circ} \right] \tag{32}$$

This differs from the directivity corresponding to a single dipole, but this influence is not surprising, because in a thrust reverser one encounters dipole sources arrayed along several axes.

It is likely that in the nearfield the sound does not spread according to the farfield inverse-square law. For jet noise, Plumbblee et al [6] and Chen [1] used the formulation of Fink [57] for the nearfield of quadrupole noise sources. Franz's work also includes a formulation for the nearfield of a dipole source; this result will be adopted here for thrust reversers. In order to represent this distance-dependence, one may add to the right-hand side of equation (31) the term

$$\Delta OASPL = 10 \log \left[1 + (c_o/r\omega_o)^2 \right] \tag{33}$$

where ω_o is a characteristic radian frequency, discussed below.

For jet noise, Chen [1] introduced a characteristic frequency that changes with axial position in the jet. In contrast, Plumblee *et al* [6] obtained an empirical relationship that is indep.ndent of frequency.

It is proposed that for target-type thrust reversers the characteristic frequency be taken as the peak frequency in the noise spectrum, which frequency is given by

$$\omega_o = \frac{2\pi\ V_j}{D_e\ (D_h/D_e)^{0.4}\ (T_j/T_a)^{0.4}\ (1 + \cos\theta'')} \tag{34}$$

where D_e = equivalent circular nozzle diameter = $(4A/\pi)^{1/2}$

D_h = hydraulic diameter = $(4A/\text{perimeter})$

θ'' = effective angle = $\theta(V_j/c_o)^{0.1}$

T_j = jet total temperature

It is assumed here that the noise sources associated with thrust reverser operation move with the airframe. Consequently, no Doppler shift corrections have been applied.

A directivity correction term to account for the effect of forward motion of the aircraft should be applied to the overall sound pressure level. This term is

$$\Delta\text{OASPL} = 10\ \log\ \left(1 + M_a\cos\theta\right). \tag{35}$$

However, since thrust reverser operation occurs only at low airplane Mach numbers, the correction usually is likely to be negligible.

The frequency distribution of target thrust reverser noise has been represented by Stone [20] in terms of a single reduced one-third octave band spectrum. The collapse cf the data is shown

95

by Figure 34, together with the curve proposed by Stone for far-field noise prediction. This proposed curve has its maximum at a Strouhal number of unity, and this value was used in deriving equation (39). The Strouhal number S is defined by

$$S = \frac{f \, D_e (D_h/D_e)^{0.4} \, (T_j/T_a)^{0.4} \, (1 + \cos \theta'')}{V_j} \qquad (36)$$

where it has been assumed that no Doppler shift occurs for receivers located on the airplane.

2.7.2 Cascade-type reversers

Information on the noise fields of cascade-type thrust reversers (Figure 35) is extremely sparse, so that any prediction method must be regarded as very approximate. The small amount of data available [38] suggests that cascade-type reversers are somewhat quieter than those of the target-type; consequently, jet noise may make a significant contribution to the farfield (and presumably the nearfield) noise. The method proposed by Stone accounts for the jet noise contribution in addition to that arising from interaction of the jet with the reverser structure. In a manner similar to that used for target-type reversers, Stone derives an empirical equation for the farfield noise at an angle of 90° to the inlet axis of a cascade-type reverser:

$$OASPL_{90,cr} = K_{cr} + 10 \log (A_j/r^2) + 10 \log \left(\rho_j \rho_0 c_0^4 / \rho_{ISA}^2 c_{ISA}^4 \right)$$

$$+ 50 \log (V_j/c_0) - 10 \log [1 + 0.01(V_j/c_0)^2] \qquad (37)$$
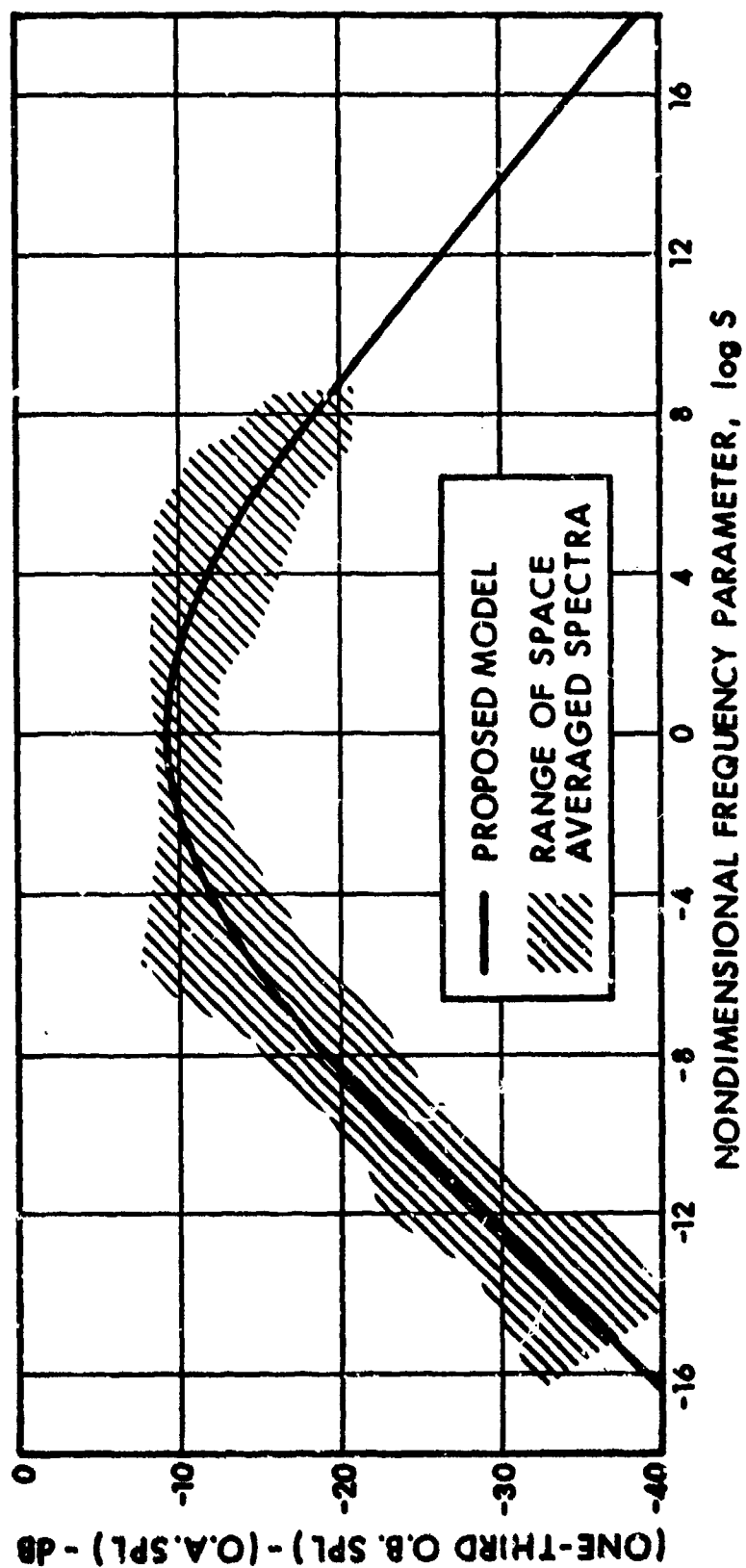
FIG. 34. NUN-DIMENSIONAL ONE-THIRD OCTAVE BAND SPECTRUM
FOR TARGET-TYPE THRUST REVERSERS [60]

97
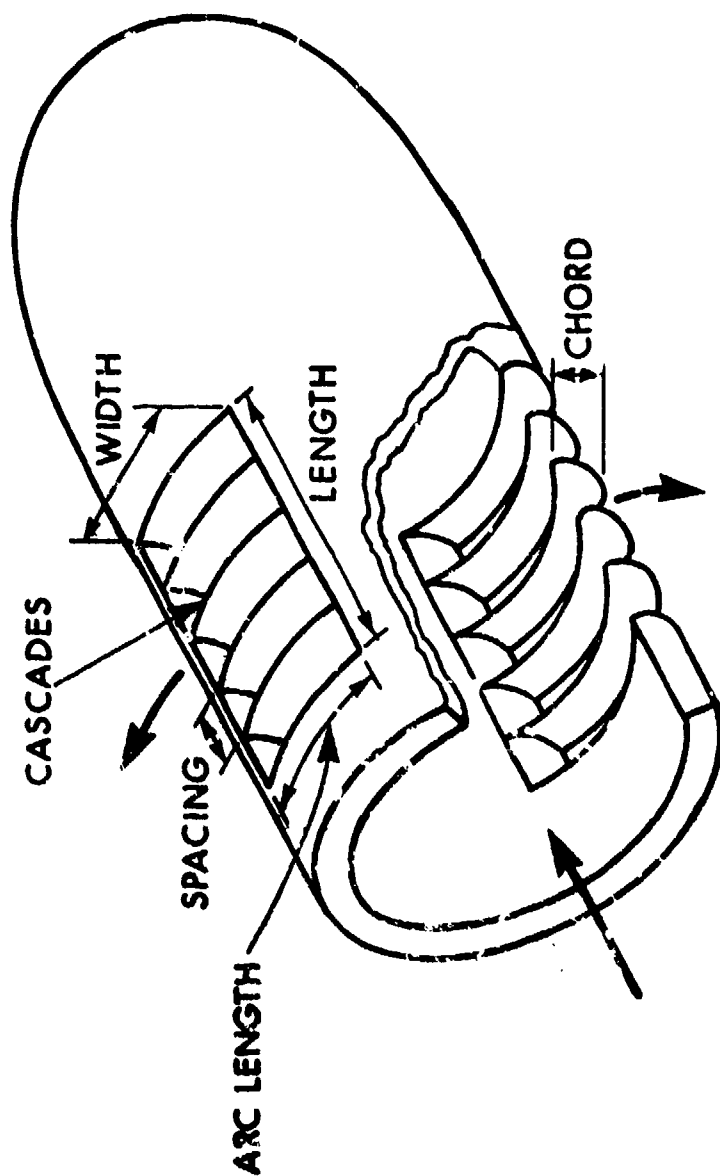
$D_e = \sqrt{(\text{Number of Ports}) \times (\text{Arc Length}) \times (\text{Cascade Length}) \times (4/\pi)}$

$D_h = 4(\text{Arc Length}) \times (\text{Cascade Spacing}) / \left[2(\text{Arc Length}) + 2(\text{Cascade Spacing})\right]$

FIG. 35. TAIL-PIPE CASCADE THRUST REVERSER

Here the empirical constant K_{cr} is given by

$$K_{cr} = 136 + K_{cr,1} + K_{cr,2} + 7.2 \ (A_e/A_t) \tag{38}$$

with

$$K_{cr,1} = \begin{cases} 0 & \text{if there is an internal flow deflector to guide} \\ & \text{the flow into the cascades} \\ 5 & \text{if there is no deflector} \end{cases}$$

$$K_{cr,2} = \begin{cases} 0 & \text{if airfoil-shaped vanes are used} \\ 6 & \text{if constant-thickness vanes are used} \end{cases}$$

A_e/A_t = ratio of cascade exit area to tailpipe area
(generally greater than unity)

Equation (36) can be adapted to nearfield conditions by the
same reasoning as for target-type reversers: an additional term,
given by equation (33) is added to the right-hand side of
equation (37) and the characteristic frequency $\hat{\omega}_o$ is here
given by

$$\omega_o = \frac{2.8\pi \ V_j}{D_e \ (D_h/D_e)^{0.4} \ (T_j/T_a)^{0.4} \ (1 + \cos \theta'')} \tag{39}$$

where D_e and D_h are defined in Figure 35, and θ'' has been
defined earlier. As before, experimental justification of this
nearfield modification is required.

Following the proposed procedure of Stone [20], the over-
all sound pressure level at 90°, as estimated by equations (37)
and (39) is combined with the predicted jet noise contribution
to give the total overall sound pressure level:

$$\text{OASPL} = 10 \ \log \left[10^{(OASPL_{90,cr})/10} + 10^{(OASPL_{90,j})/10} \right] \tag{40}$$

Measurements of cascade-type thrust reverser noise show directivity patterns which are complicated in shape, although the variations are relatively small in magnitude. Stone proposes a simplified relationship for the directivity of the farfield noise:

$$OASPL_\theta = OASPL_{90} + 20 \log (1 + \tfrac{1}{2} \sin 2\theta) \qquad (41)$$

It is proposed that this also be used for the nearfield.

The effect of forward motion is more difficult to include for cascade-type type than for target-type reversers. For the jet-structure interaction noise, the same approach can be followed as in the case of target reversers, with the correction term being given by equation (35). For the jet exhaust noise, the situation is different from that of a typical jet engine, because with reversers the exhaust axis is not parallel to the direction of the airplane motion, so that the relative velocity factors discussed in Section 1.5 do not apply here. Extensive analysis will be required to establish a detailed procedure. For the present, it is proposed that the correction term given by equation (35) be used for the jet noise also. Thus, the correction can be applied directly to equation (41).

The one-third octave band spectrum levels measured for cascade-type thrust reverser have been reduced by Stone [35] as shown in Figure 36. This figure also shows a curve proposed by Stone for a farfield prediction procedure. It is suggested that the same curve be used for nearfield noise prediction, with the overall sound pressure level given by equation (41), the Strouhal number given by equation (36), and assuming that there is no Doppler shift.
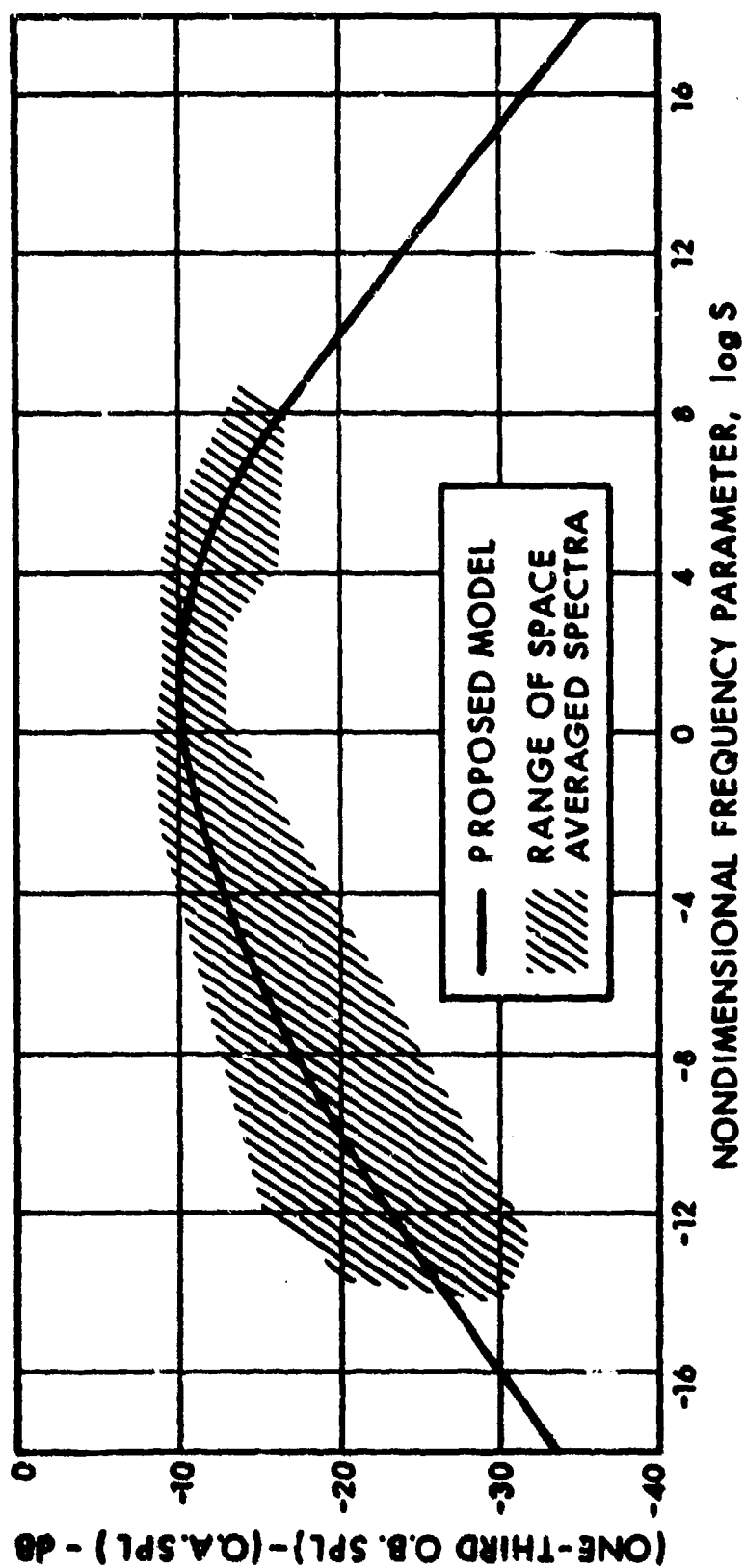
FIG. 36. NON-DIMENSIONAL ONE-THIRD OCTAVE BAND SPECTRUM FOR CASCADE-TYPE THRUST REVERSERS [20]

2.8 Reflection of Acoustic Pressures At The Fuselage

The preceding prediction methods pertain to acoustic pressures that occur under free-field conditions, where there are no reflecting surfaces. In a practical environment, however, there occur reflections due to the presence of the ground plane and of the airframe structure. Only the effect of the latter is discussed here.

It is well known that for the simplest case of normal incidence of an acoustic wave on a large plane surface, reflection at the surface produces a 6 dB increase in the sound pressure level at the surface. However, for grazing incidence, there occurs no increase, and for oblique incidence on a curved surface, the increase lies between 0 and 6 dB. Increases greater than 6 dB can occur at the intersection of two planes, such as the junction of the horizontal stabilizer and the rear fuselage structure.

In considering the influence of only the cylindrical fuselage, one can analyze the two limiting cases: (1) that where an engine is mounted near the fuselage, and (2) that where the engine is at a considerable distance from the fuselage. These two cases were analyzed by Cockburn and Jolly [11] and the results were applied by Rudder and Plumblee [14] to jet engine noise.

2.8.1 Engines Close To The Fuselage

For an engine mounted within 15 nozzle diameters of the fuselage, as illustrated in Figure 37 for a rear-mounted engine, an analysis based on scattering is not appropriate. Rudder and Plumblee calculate the pressure p at a point on the

FUSELAGE

ENGINE

α

FUSELAGE

P_o

$3/2 \, P_o$

$45°$

$2 \, p_o$

$45°$

$3/2 \, P_o$

P_o
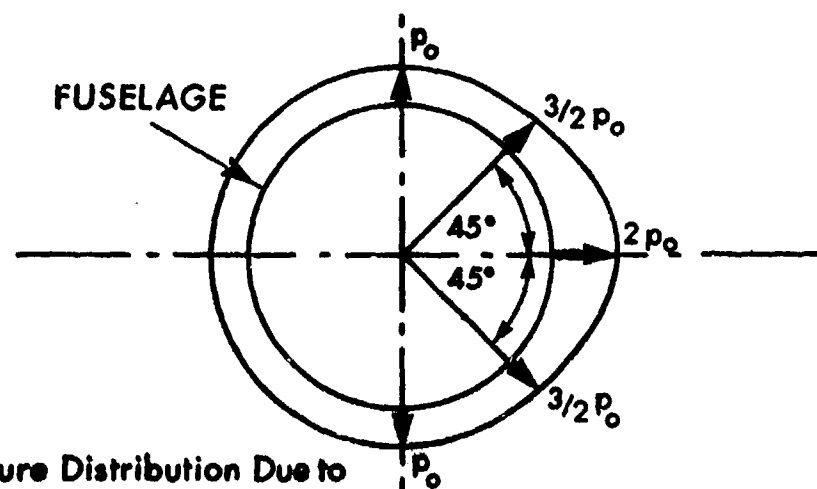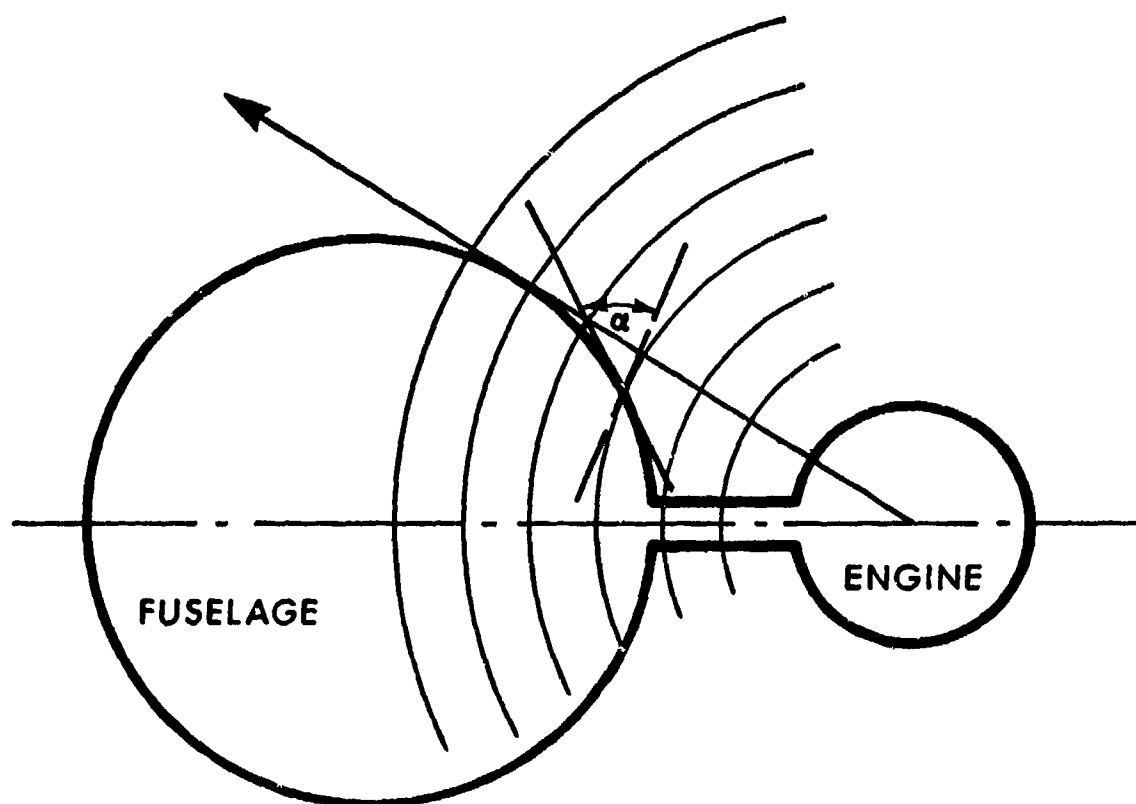
**Pressure Distribution Due to
Single Engine of Geometry
Shown Above to Scale
(p_o = Free Field Sound Pressure)**

FIG. 37. GEOMETRY AND PRESSURE DISTRIBUTION FOR
ENGINES MOUNTED CLOSE TO THE FUSELAGE

103

fuselage surface from

$$p \approx p_o \frac{3 + \cos 2\alpha}{2} \tag{42}$$

where α is the angle between the wavefront and the tangent to the fuselage surface $(-\pi/2 < \alpha < \pi/2)$ and p_o is the free-field pressure. A typical pressure loading on the fuselage is shown at the bottom of Figure 37.

Equation (42), when rewritten in terms of the sound pressure level $(SPL)_o$, becomes

$$(SPL)_s = (SPL)_o + 20 \log \left[\frac{3 + \cos 2\alpha}{2} \right] \tag{43}$$

2.8.2 Engines Far From The Fuselage

For an engine mounted more than 15 jet nozzle diameters from the fuselage, one may use the acoustical scattering analysis of Potter [59]. A typical geometric configuration for this case is shown in Figure 38, where a source location is identified in the jet flow. The analysis involves determination of the sound field for a single source S at a point Q on the fuselage surface, for single frequency ω, and later accounting for all sources and frequencies.

The analysis assumes that the acoustic wave arriving at the fuselage is a plane wave of strength p_o and with the wave direction such that the normal to the wave front makes an angle β with the normal to the axis of the fuselage (see Figure 39). The point on the surface of the fuselage is specified by coordinate (a, x, ψ), where a is the radius of the fuselage, x the dimension along the axis and ψ the angle around the fuselage measured from the plane containing the source and the fuselage center-line. (ψ is zero when the point is on the far side of
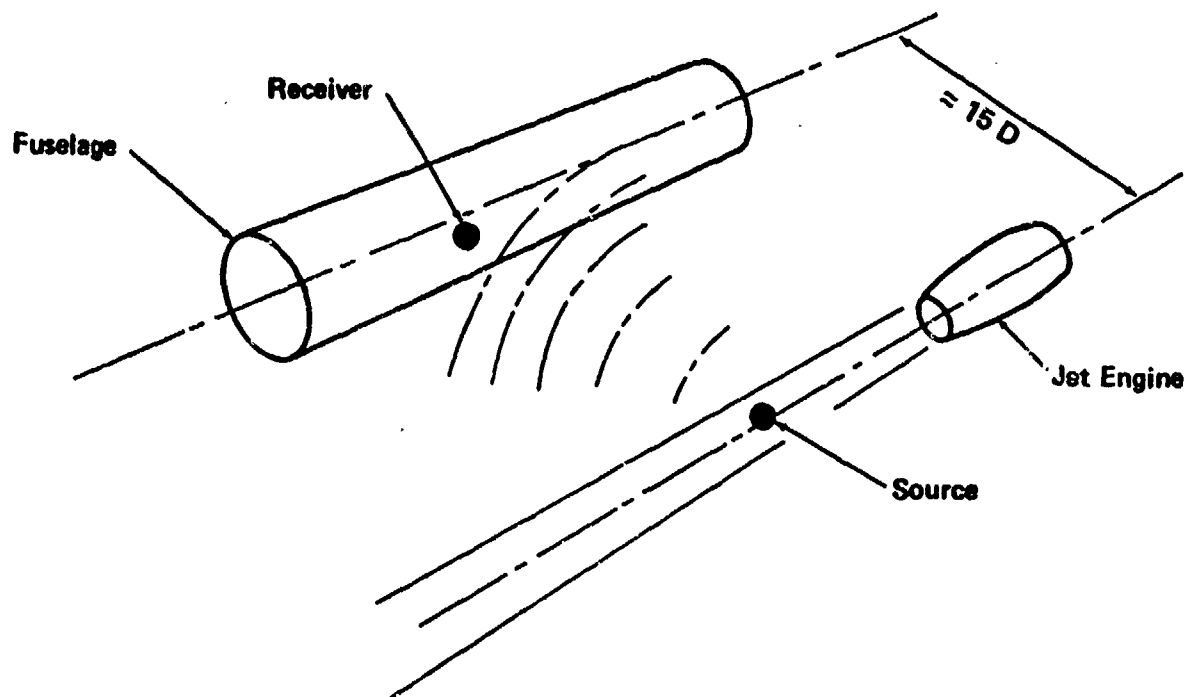
FIG. 38.   GEOMETRY OF FUSELAGE AND ENGINE MOUNTED FAR FROM
THE FUSELAGE.

FIG. 39. COORDINATE SYSTEM FOR ANALYSIS OF REFLECTION
OF PLANE WAVE FROM CYLINDRICAL FUSELAGE.

the fuselage, completely hidden from the source.)

The surface pressure has been shown [59] to be given
by the real part of

$$p = \frac{4p_0}{ka \cos\beta} \sum_{m=0}^{\infty} \frac{\cos m\psi}{C_m'} \exp[i(-\gamma_m' + \pi m/2)] \exp[ikx \sin\beta_e] \exp[-2\pi ift]$$

(44)

where

$$C_0' = 2\left[J_1^2(ka \cos\beta) + N_1^2(ka \cos\beta) \right]^{1/2}$$

$$C_m' = \frac{1}{2}\left[\left\{ J_{m+1}(ka \cos\beta) - J_{m-1}(ka \cos\beta) \right\}^2 \right.$$

$$\left. + \left\{ N_{m-1}(ka \cos\beta) - N_{m+1}(ka \cos\beta) \right\}^2 \right]^{1/2}$$

$$\gamma_0' = \tan^{-1}\left[\frac{-J_1(ka \cos\beta)}{N_1(ka \cos\beta)} \right]$$

$$\gamma_m' = \tan^{-1}\left[\frac{J_{m+1}(ka \cos\beta) - J_{m-1}(ka \cos\beta)}{N_{m-1}(ka \cos\beta) - N_{m+1}(ka \cos\beta)} \right]$$

(45)

and where J and N are Bessel functions of the first and second
kind, respectively.

It should be noted that this result is applicable only to
wing-mounted engines, where the sound field for a given source
can be approximated as a plane wave at the point where it strikes
the fuselage; the effects of spherical radiation have not been
included. Furthermore, the surface of the fuselage was assumed
to be perfectly rigid, which is not the case in practice. The

complete solution would be extremely complicated and the present
method is considered to be sufficiently accurate for practical
situations.

Rudder and Plumblee present equation (44) in a more con-
venient form for computation; they express the pressure at a
point on the fuselage surface due to an obliquely incident plane
wave at frequency f as

$$p = Ap_0 \cos(2\pi ft + \Phi) \tag{46}$$

where

$$A^2 = \xi^2 + \eta^2$$

$$\Phi = \tan^{-1}(\eta/\xi)$$

$$\xi = D_0 (EG-FH)$$

$$\eta = D_0 (FG+EH)$$

$$D_0 = \frac{4}{\pi ka \cos\beta}$$

$$E = \sum_{m=0}^{\infty} \frac{\cos m\psi}{C_m'} \sin\left(-\gamma_m' + \frac{\pi m}{2}\right)$$

$$F = \sum_{m=0}^{\infty} \frac{\cos m\psi}{C_m'} \cos\left(-\gamma_m' + \frac{\pi m}{2}\right)$$

$$G = \cos (kx \sin\beta)$$

$$H = \sin (kx \sin\beta)$$

and p_0 is the strength of the free-field sound pressure.

2.9 Pressure Correlations

Although pressure correlation coefficients in the near-field of model and fullscale jets have been measured by several investigators [16, 30, 60-65], very little effort has been directed to providing a corresponding generalized analytical model, and no attempt appears to have been made at studying the effects of parameters, such as nozzle pressure ratio and jet temperature. The published information on nearfield pressure correlations is reviewed here, so that a provision: analytical model can be proposed for use in a prediction procedure.

2.9.1 Subregions

Clarkson [65, 66] postulated that, from the point of view of pressure correlations, the region around a jet can be divided into two subregions:

In *Subregion 1* (near the jet boundary) the pressure fluctuations are strongly influenced by the convection of the aerodynamic turbulent field. This subregion extends up to about 2 nozzle diameters out from the jet boundary, and downstream to a plane about 12 to 15 diameters from the nozzle exit plane.

In *Subregion 2* (nearfield) the spatial distribution of the noise sources is on a scale comparable to the dimensions considered in correlation measurements. This subregion extends to about 10 diameters out from the jet boundary, 20 diameters downstream and 10 diameters upstream of the nozzle exit plane. The position of the outer surface of this subregion is not clearly defined and is probably frequency-dependent.

109

Clarkson does not identify the criteria which he used to define these two subregions.

Eldred *et al* [25] observed a conflict between different sets of published experimental data: some indicated that the close-in correlations were dominated by the aerodynamic field, while other results showed domination by acoustic radiation. Eldred *et al* argued that the radiated sound field varies on the average as V_j^8, whereas the aerodynamic pressure field increases as V_j^4, so that the field of influence of the aerodynamic pressures would decrease as V_j increases.

2.9.2 Freefield Data

Figure 40 summarizes the locations at which various investigators have carried out correlation measurements. (In most cases the correlation coefficients were measured along axes parallel to the jet centerline.) At locations identified by a angular symbol only broadband correlation measurements were made; at those indicated by a circular symbol, narrowband (one-third or one-half octave band) measurements were made. Open symbols indicate that the convection velocity was supersonic for ll frequencies measured; filled-in symbols indicate that all ch velocities were subsonic; half filled-in symbols correspond to the case where the convection velocities were subsonic at some frequencies and supersonic at others.

Figure 40 also indicates the extent of the two subregions postulated by Clarkson [65]. It is seen that it is difficult to reconcile the subregions with the data on the basis of convection velocity.
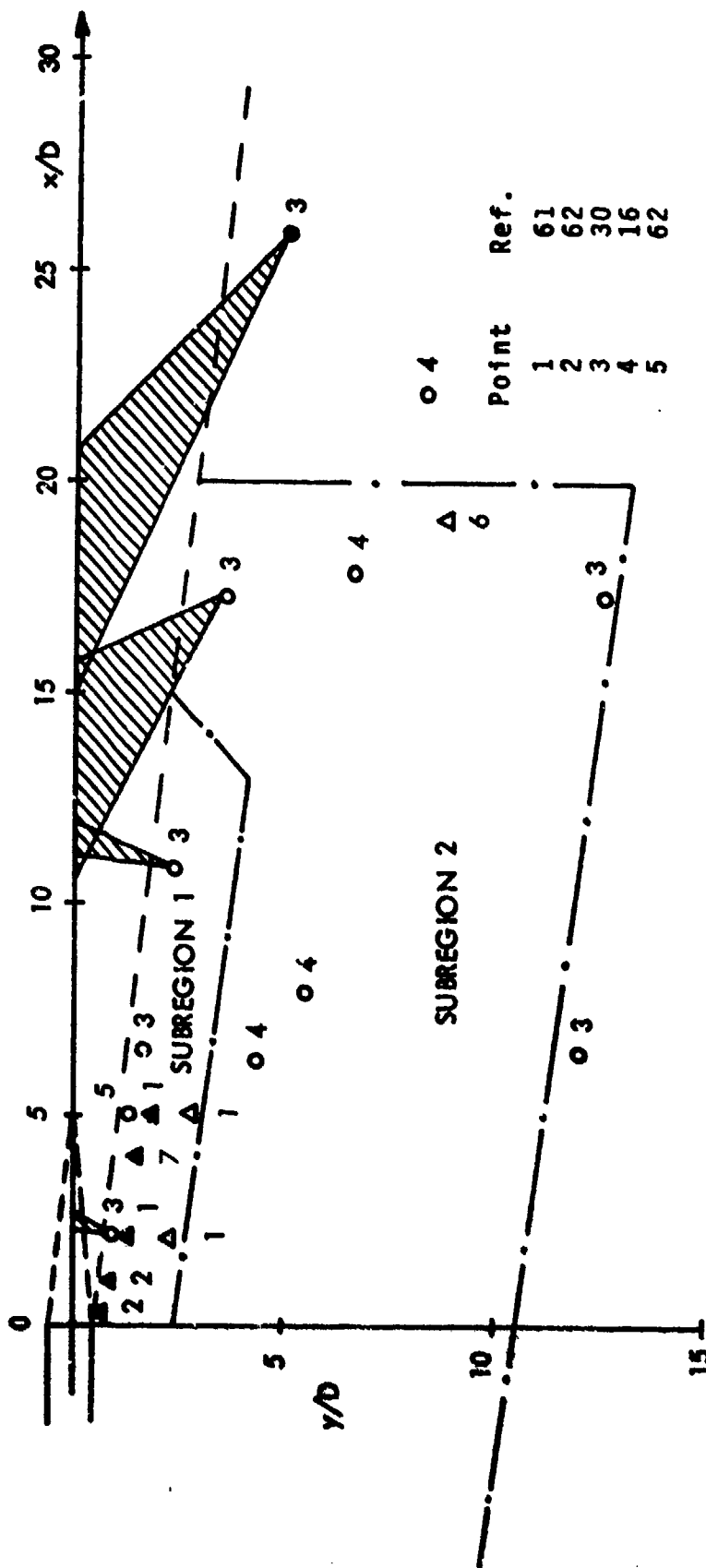
FIG. 40. SUMMARY OF PRESSURE CORRELATION MEASUREMENT LOCATIONS

SEE TEXT FOR EXPLANATION OF SYMBOL CODES.

Broadband Correlations

Two investigations have resulted in analytical models
for the broadband pressure correlation coefficient. Unfor-
tunately, in both cases the model referred to only one loca-
tion in the acoustic field, at which location the investiga-
tors also made response measurements on a model panel.
Maestrello *et al* [64] found that the local pressure field
was dominated by aerodynamic effects and proposed an analyti-
cal model for the pressure correlation coefficient of the
form

$$\rho(\xi_1,\xi_3,\tau) = e^{-\alpha_1 |\tau|} e^{-\alpha_2 |\xi_1|} e^{-\alpha_3 |\xi_3|} \cos \omega_0(\tau-\xi_1/U_c)$$

$$(47)$$

where U_c denotes the convection velocity of the pressure field,
τ the time delay and ξ_1 and ξ_3 the separation distances in the
axial and lateral directions, respectively.* The coefficients
in the exponents of this equation were found to have the values

$$\alpha_1 = 300 \text{ sec}^{-1}$$

$$\alpha_2 = 0.49 \text{ ft}^{-1}$$

$$\alpha_3 = 1.42 \text{ ft}^{-1}$$

and the convection velocity was found to be 0.65 times the jet
velocity V_j. The characteristic frequency ω_0 corresponds to
the peak in the pressure spectrum; Maestrello *et al* propose for

---

* It is implicit in this type of representation that the pressure
field is homogeneous. This assumption is not correct and the
representation is thus only an approximate form.

the frequency ω_0 at any axial distance x the relation

$$\omega_0 = \frac{2\pi V_j}{D} \frac{1.4}{[1 + 0.2x/D]^3} \tag{48}$$

where D denotes the jet nozzle diameter.

Mollo-Christensen [61] did not express his measurement results for the aerodynamic region in analytical form, but his data indicate an average convection velocity of 0.68 V_j, which is close to the above indicated value obtained by Maestrello *et al*.

Olson and Linderg [63] made measurements in the acoustic region and proposed a model of the form

$$\rho \, (\xi_1, \xi_3, \tau) = e^{-\alpha_1 |\tau - \xi_1/c_0|} e^{-\alpha_2 |\xi_1|} e^{-\alpha_3 |\xi_3|} \cos \, \omega_0(\tau - \xi_1/c_0) \tag{49}$$

where c_0 represents the ambient speed of sound. The characteristic frequency in this equation is $\omega_0 = 8000$ radians/sec (1273 Hz) and the coefficients in the exponents have the values

$$\alpha_1 = 4500 \, \text{sec}^{-1}$$

$$\alpha_2 = 0.60 \, \text{ft}^{-1}$$

$$\alpha_3 = 0.44 \, \text{ft}^{-1}$$

Narrowband Correlations

In principle, the correlation coefficients given by equations (47) and (49) can be transformed into the frequency domain by application of the Fourier transform. However, an

alternative approach that is widely used in practice consists of filtering the pressure signals prior to correlation. The correlation coefficients obtained in this manner are functions of frequency and also depend to some extent on bandwidth.

Important frequency-dependent correlation measurements were performed by Howes *et al* [30], Cox *et al* [16] and Clarkson [62, 65], all on fullscale jet engines. The frequency bandwidths used ranged from a one-third octave to slightly over a one-half octave.

Narrowband correlation coefficients have the general form of a decaying cosine. The experimental results refer mainly to the spatial correlation coefficient (for $\tau=0$), which can be represented by a function of the type $\cos(\omega\xi/U_c)$, where ω is the center frequency of the band. In the present context, the two important parameters of the correlation coefficient are: (1) the first zero crossing, which provides a measure of the length scale of the correlation coefficient, and (2) the spatial rate of decay.

For correlations along an axis parallel to the jet center-line, the first zero crossing of the correlation coefficient is given by

$$\xi_{1,0} = U_c/4f , \tag{50}$$

where U_c is the convection velocity of the pressure field along the axis of correlation. For the aerodynamic region, U_c is equal to the flow velocity, and for the acoustic region U_c is given by

$$U_c = c_o/\cos\theta \tag{51}$$

where θ is the angle between the direction of propagation of
the incident acoustic wave and the axis of correlation. Be-
cause of the implicit assumption of an incident plane wave,
this is essentially a farfield approximation.

In the region dominated by the aerodynamic pressure field,
Clarkson [65] assumes that U_c is proportional to f^n, so that
the first zero crossing is proportional to f^{n-1}. He obtained
values of n between 0.37 and 0.50 for fullscale engines and
between 0.61 and 0.71 for model scale jets. For the acoustic
field, Clarkson takes n=0. However, this latter value is not
strictly correct, since θ in equation (51) is frequency-
dependent.

In order to demonstrate the contribution of θ, the results
of interpreting the data from [30] in terms of equation
(51) are indicated by hatched regions in Figure 40, which
regions indicate the corresponding range of angles of propaga-
tion. In all cases the higher-frequency components come from
areas in the flow that are closer to the nozzle exit plane.
(This is typical of the noise source distribution within a jet
exhaust, but the locations of the noise sources estimated on
the basis of correlation data are not in close agreement with
more directly measured source locations, probably because of
the simplifications incorporated in the correlation model.)
The results of an analysis by Clarkson [65], consisting of
application of equations (50) and (51) to the measured
first zero crossings, are shown in Figure 41. Figure 42
shows the results of another analysis, where the angle θ is
determined by source locations obtained from the proposed model
curve of Figure 16. The theoretical value of 0.25 for
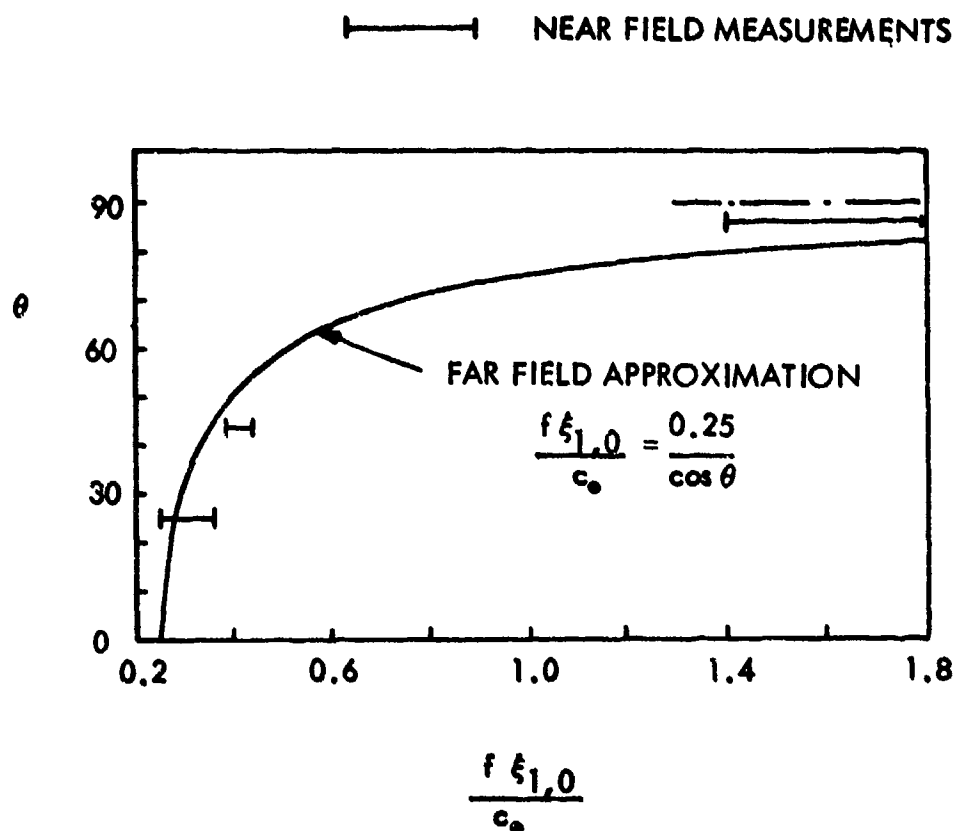
FIG. 41. EFFECT OF ANGLE θ ON FIRST ZERO CROSSING OF
ACOUSTIC PRESSURE CORRELATION COEFFICIENT [65].

116
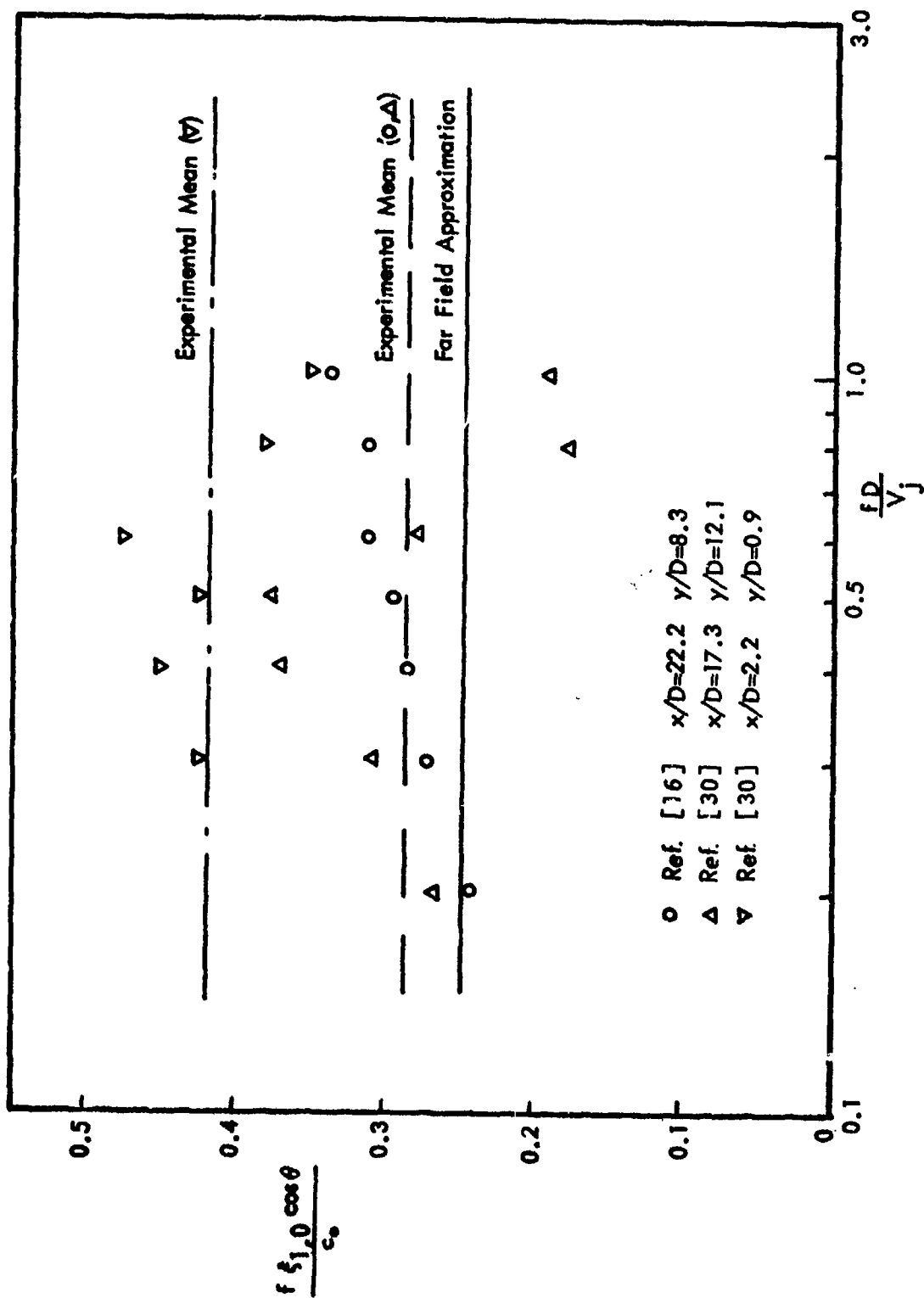
FIG. 42. COMPARISON OF NON-DIMENSIONAL VALUES FOR PRESSURE CORRELATION FIRST ZERO-CROSSING LENGTH.

117

$f\xi_{1,0}(\cos\theta)/c_o$ shown in this figure follows from equation (50). It is seen that the experimental values here tend to be higher than the predicted ones, particularly for small values of x/D and y/D).

In relation to the correlation decay in the longitudinal direction, if one assumes that the correlation coefficient can be written as

$$\rho\,(\xi_1,0,0) = \exp\left(\frac{-m_1\omega\xi_1\cos\theta}{c_o}\right)\,\cos\left[\frac{\omega\xi_1\cos\theta}{c_o}\right] \qquad (52)$$

then the experimental results show that m_1 lies between 0.06 and 0.73, with an average value of 0.23. The value of m_1 depends to some extent on the filter bandwidth, but the variation is small and can be neglected for practical purposes. The highest value of m_1 was obtained close to the nozzle exit; however, the data show no consistent trend with either distance from the nozzle exit or angle from the jet axis. Thus, it is proposed that the average value of 0.23 be used in the preliminary model.

Correlation data for the lateral or circumferential directions are very sparse. Some measurements were made by Howes *et al* [30] in a direction normal to the plane passing through the jet centerline. The resulting correlation coefficients showed characteristics similar to those for the longitudinal direction. However, it is more difficult here to relate the first zero crossing of the correlation to acoustic wave propagation parameters.

If plane wave acoustics (farfield) are applied to the data obtained by Howes *et al* [30] for $x/D = 17.3$ and $y/D = 3.49$, one finds the first zero crossing $\xi_{3,0}$ to be given approximately by

$$\frac{f \, \xi_{3,0} \, \sin \chi}{c_o} = 0.06 \quad , \tag{53}$$

corresponding to the correlation measured along an axis perpendicular to a plane through the jet axis; χ denotes the angle between this plane and a typical ray from the effective acoustic source to the mean measurement location.

When one compares equation (53) with

$$\frac{f \, \xi_{1,0} \, \cos \theta}{c_o} = 0.25 \ , \tag{54}$$

which is obtained from equations (50) and (51), one notes that the correlation length in the lateral direction is shorter than that predicted on the basis of farfield plane wave propagation. Part of this discrepancy is probably due to the fact that the noise at a given frequency does not come from a single coherent source, but from a spatial distribution of uncorrelated sources. (The circumferential distribution of the sources will have a greater influence on the lateral correlation than will the axial distribution on the longitudinal correlation.)

The lateral correlation decay index m_3, which is used in association with the function $\omega\xi(\sin \chi)/c_o$, in analogy to equation (52) is found to have a value of 1.21 on the basis of the very limited data of Howes *et al* [30].

2.9.3 Surface Pressure Data

The preceding discussion referred to correlation measurements under freefield conditions. Several investigators have also measured pressure correlation coefficients on flat or curved surfaces, with diverse results.

For the case of a single surface, such as a panel, data of Howes *et al* [30] and Cox *et al* [16] show that the correlation coefficients are similar in form to those obtained in the freefield, and that the distance to the first zero crossing and the decay rate also are similar. Figure 43 contains typical data from [16], comparing pressure correlations measured in the freefield, on a rigid panel, and on a flexible structure of skin-stringer configuration, with a skin thickness of 0.04". The data show no significant change due to the presence of either panel.

The situation is more complicated where there are two surfaces, such as near the intersection of the vertical and horizontal stabilizers. Clarkson [65] presents data measured on a configuration of this type, for both model and fullscale systems. Here the reflected pressure field resulting from the second surface influences the shape of the spatial correlation and the distance to the first zero crossing point (see Figure 44). In certain frequency ranges, the distance to the first zero crossing is constant or increases with frequency, in contrast to the freefield case, where distance to the first zero crossing decreases as frequency increases. Clarkson constructs a simple model for noise sources in the jet to describe the reflection effect, but the results show only qualitative agreement with the measurements. The presently proposed prediction model
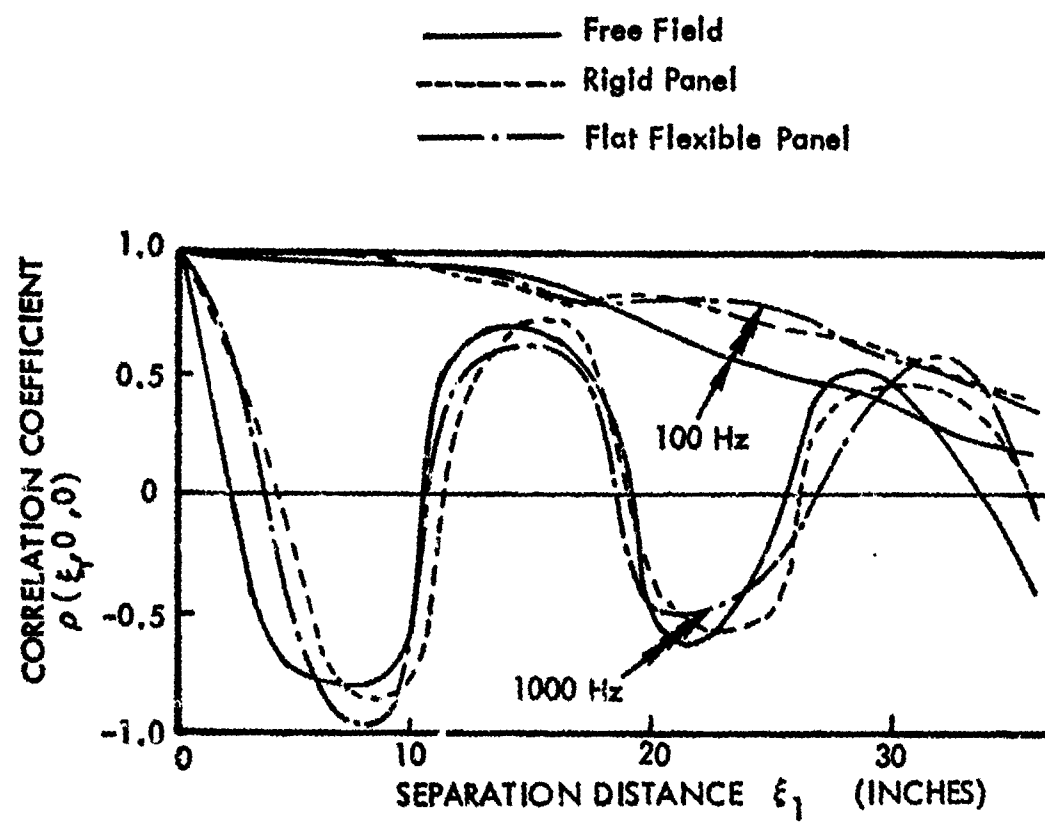
FIG. 43. COMPARISON OF SPATIAL PRESSURE CORRELATION
COEFFICIENTS IN FREE FIELD AND ON PANEL. [16].

121
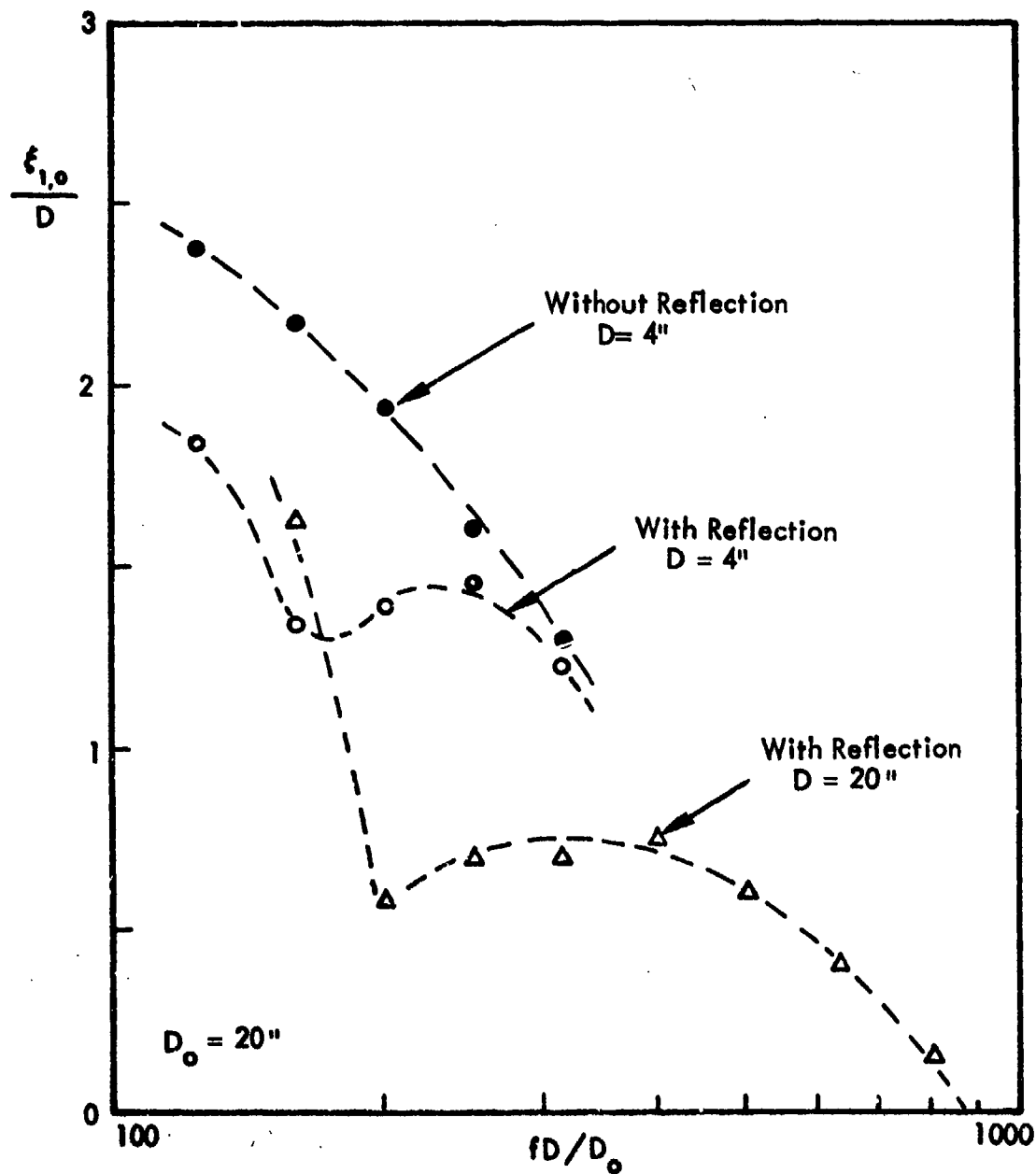
FIG. 44. EFFECT OF REFLECTION FROM PERPENDICULAR PLANE ON ZERO CROSSING POINT OF CORRELATION COEFFICIENT IN LONGITUDINAL DIRECTION [65].

does not account for the effects of reflecting surfaces. The correlation coefficient is assumed to have a form which is separable in the coordinates ξ_1 and ξ_3, and is taken to obey

$$\rho\ (\xi_1,\xi_3,0) = \exp \left[\frac{-0.23\omega\xi_1 \cos\ \theta}{c_o}\right] \exp \left[\frac{-1.21\omega\xi_3 \sin\ \chi}{c_o}\right]$$

$$\cdot \cos \left[\frac{\omega\xi_1 \cos\ \theta}{c_o}\right] \cos \left[\frac{4.17\ \omega\xi_3 \sin\ \chi}{c_o}\right]$$

(55)

A factor of 4.17 has been introduced in the terms involving χ, in order to provide agreement with the small amount of experimental data; it is an artifact which has no physical interpretation at the present. Obviously there is a need for further understanding and for improvement of the pressure correlation model.

2.10 List of Symbols for Sec. II*

Symbol	Definition	Units†	
A	nozzle area	ft²	(m²)
D	nozzle diameter	ft	(m)
D_e	equivalent diameter	ft	(m)
D_h	hydraulic diameter	ft	(m)
J_n	Bessel function of first kind	---	
M	Mach number	---	
M_a	Mach number of aircraft	---	
M_j	exit Mach number of jet		
N_n	Bessel function of second kind	---	
OASPL	overall sound pressure level	dB	
PR	nozzle pressure ratio	---	
R	nozzle pressure ratio	---	
R_c	critical nozzle pressure ratio	---	
S	Strouhal number	---	
SPL	sound pressure level	dB	
T	absolute temperature	°R	(°K)
T_T	total temperature of jet	°R	(°K)
T_a	temperature of ambient air	°R	(°K)
T_j	jet temperature	°R	(°K)
T_r	reference temperature	°R	(°K)
U_c	convection velocity	ft/sec	(m/s)
V	flow velocity	ft/sec	(m/s)
V_a	speed of aircraft	ft/sec	(m/s)

---

*Specially defined symbols, such as those for empirically determined constants, which are used only once in the text, are not included here. Such symbols are defined in the text where they occur.

†The units given here are typical ones. SI units are given in parentheses where appropriate. Note that some empirical prediction methods require the use of specific units.

Symbol	Definition	Units	
V_j	jet velocity	ft/sec	(m/s)
V_r	reference velocity	ft/sec	(m/s)
W	sound power per unit volume	$(lb/ft^2 sec)$	$(N/m^2 s)$
X	axial distance	ft	(m)
X_o	source location along axis	ft	(m)
Y	lateral distance	ft	(m)
c_{ISA}	sound speed in international standard atmosphere	ft/sec	(m/s)
c_{SL}	sound speed in air at sea level	ft/sec	(m/s)
c_o	speed of sound in ambient air	ft/sec	(m/s)
f	frequency	Hz	
h	thickness of annulus	ft	(m)
ℓ	local scale of jet turbulence	ft	(m)
ℓ_c	length of potential core	ft	(m)
p	sound pressure	lb/ft^2	(N/m^2)
p_o	free-field sound pressure	lb/ft^2	(N/m^2)
r	source-to-observer distance	ft	(m)
s	characteristic length of shock cell	ft	(m)
u'	fluctuating velocity	ft/sec	(m/s)
x, y	coordinates	ft	(m)
α	impingement angle (Fig. 37)	deg	
β	engine bypass ratio	---	
θ	angle fron jet axis	deg	
ξ_1	separation distance	ft	(m)

Symbol	Definition	Units	
ρ	density of jet flow	slug/ft^3	(kg/m^3)
ρ_{ISA}	density of international standard atmosphere	slug/ft^3	(kg/m^3)
ρ_{SL}	air density at sea level	slug/ft^3	(kg/m^3)
ρ_e	equivalent flow density	slug/ft^3	(kg/m^3)
ρ_0	density of ambient atmosphere	slug/ft^3	(kg/m^3)
$\rho(\xi_1, \xi_3, \tau)$	pressure correlation coefficient	---	
τ	time delay	sec	(s)
ϕ	angle in nozzle exit plane	deg	
ω	radian frequency	sec^{-1}	(s^{-1})
ω_0	radian frequency at spectrum peak	sec^{-1}	(s^{-1})
Φ	reduced soundpressure level	dB	

SECTION III

POWERED LIFT DEVICES

3.1 Introduction

Powered lift devices, which have been the subject of
active study in only the past few years, serve to increase
lift coefficients and thus to reduce landing and takeoff
distances.

Powered lift or "propulsive lift" systems are characterized
by considerable integration of the propulsion and flap
systems. Therefore, the noise of powered lift systems tends to
depend on more parameters than propulsion noise by itself.
Because of this complexity and the relatively newness of powered
lift concepts, the available noise prediction methods are
largely based on empirical data based on model studies;
fortunately, the scaling laws are known well enough to permit
extrapolation of model data to full scale.

3.1.1 Overview of powered lift systems

Propulsive lift systems fall into two basic categories,
called "externally blown" and "internally blown" configurations.
In externally blown systems, the lift-producing flow produced
by the propulsion system is entirely outside of the flap
structures; in internally blown configurations this flow begins
inside a portion of the flaps.

Externally blown configurations are of two types: (1)
under-the-wing externally blown flaps, where the jet exhaust
impinges directly on the flaps and is turned downward by them,
and (2) upper surface blown flaps, where the jet exhaust stream
is directed along the upper surface of the wing and the
attached flow is turned downward by (the upper surfaces of) a

series of flaps. The internally blown configurations also
have developed into two classes: (1) internally blown flaps,
which are basically jet flaps, where high-pressure engine
air is ducted to a slot nozzle blowing over a downward directed
flap, and (2)augmenter wings, which essentially use a jet
flap with a second flap (or shroud) above it, so as to form a
channel that guides the slot nozzle flow and entrains
additional flow from the upper wing surface. Numerous
variations and hybrids of these propulsive lift system
classes have also been proposed and investigated to various
extents.

3.1.2 General noise mechanisms

All powered lift systems involve the impingement of
high-speed flow on flaps and other parts of the airframe
structure. This impingement produces noise as the result of
the several separate acoustic mechanisms summarized below.

1. Body Sources. Lift and drag fluctuations that act
   in phase over a substantial portion of the surface
   of a flap radiate sound like an acoustic dipole
   at low frequencies (for which the acoustic wave-
   length is greater than the flap chord).

2. Edge Sources. Pressure fluctuations of small
   spatial extent, interacting with the leading or
   trailing edges of a flap, radiate sound like span-
   wise distributions of partially baffled dipole
   sources. Edge sources are important primarily at
   frequencies at which the acoustic wavelength is
   smaller than the flap chord.

128

3. **Surface Sources.** Small-scale pressure fluctuations, such as present in a turbulent shear layer on a flap surface or in a region where flow interacts with surface discontinuities or protuberances, radiate sound directly.

The aforementioned acoustic sources result from fluid-dynamic disturbances, which may be separated into the following three categories for the cases of interest here:

1. **In flow Turbulence,** such as that arising from the shear layer at a jet edge or from internal engine turbulence, may produce lift and drag fluctuations over the entire flap surface and also tends to contain small-scale fluctuations in pressure and velocity, which interact with the leading edge.

2. **Boundary Layer and Attached Wall Jet Flow** leads to edge noise generation as it passes over the trailing edge and also produces surface sources.

3. The **Turbulent Wake** of an airfoil can produce whole-body lift and drag fluctuations associated with large-scale eddies, as well as aerodynamic interactions of smaller-scale eddies with the trailing edge. In multiple-flap systems or airfoil cascades, the wake from one flap also produces inflow turbulence for the next one downstream.

3.1.3 Acoustic source characterization

The predominant sources of noise produced by flow/surface interaction have the character of acoustic dipoles. The acoustic intensity I in the far field of such an interaction source obeys

$$I(\omega) = \int_{S_a} \frac{\omega^2 \, \phi_F(\omega) \, \cos^2\theta}{\rho c^3 \, r^2} \, dS \quad , \tag{56}$$

where ω denotes the radian frequency, $\phi_F(\omega)$ the local aero-
dynamic force spectrum, θ the angle between the dipole axis
and the source-to-observer line, r the source-to-observer
distance, ρ the density, and c the speed of sound in air.
For distributed sources, ϕ_F, θ, and r differ for each
component on a surface S_a, and the net effect must be obtained
by integration over this surface.

For evaluation of Equation (56), the force spectrum dis-
tribution must be known. Since this information is not available
in practice, direct evaluation of Equation (56) cannot be accom-
plished. However, the form of this equation has served as
the basis for scaling laws that have been useful for extra-
polating model data to full-scale conditions. Table 6
summarizes the scaling relationships for the various dipole-
like source mechanisms that have been investigated experimen-
tally.

The directivity of an isolated flap element source
depends on the mechanism, as shown schematically in Figure 45.

Figure 46 illustrates the near-field directivity of a
trailing edge source. Note that the sound is maximum along
the surface. In a plane that is normal to the surface, the
experimentally observed directivity differs from that of an
ideal dipole because of scattering and finite-source-size
effects.

TABLE 6. PARAMETRIC DEPENDENCES OF FLOW/SURFACE - INTERACTION NOISE MECHANISMS [67].

Body Source: $\quad\quad\quad\quad I \propto \omega^2 F^2 \cos^2 \theta$

  Trailing or $\quad\quad\quad\quad \propto U^6 A_{co} \cos^2 \theta$

  Leading Edge Dipole: $I \propto n\omega^2 F^2 \sin^2 \theta \cos^2(\psi/2)$

$\quad\quad\quad\quad\quad\quad\quad\quad\quad \propto U^6 \ell_y W \sin^2 \theta \cos^2(\psi/2)$

I = acoustic intensity

ω = radian frequency

F^2 = mean-square fluctuating force

U = mean velocity of flow

A_{co} = correlation area

n = effective number of sources on surface

ℓ_y = spanwise eddy scale

W = wetted span

See Figure 45 for definition of angles θ and ψ.
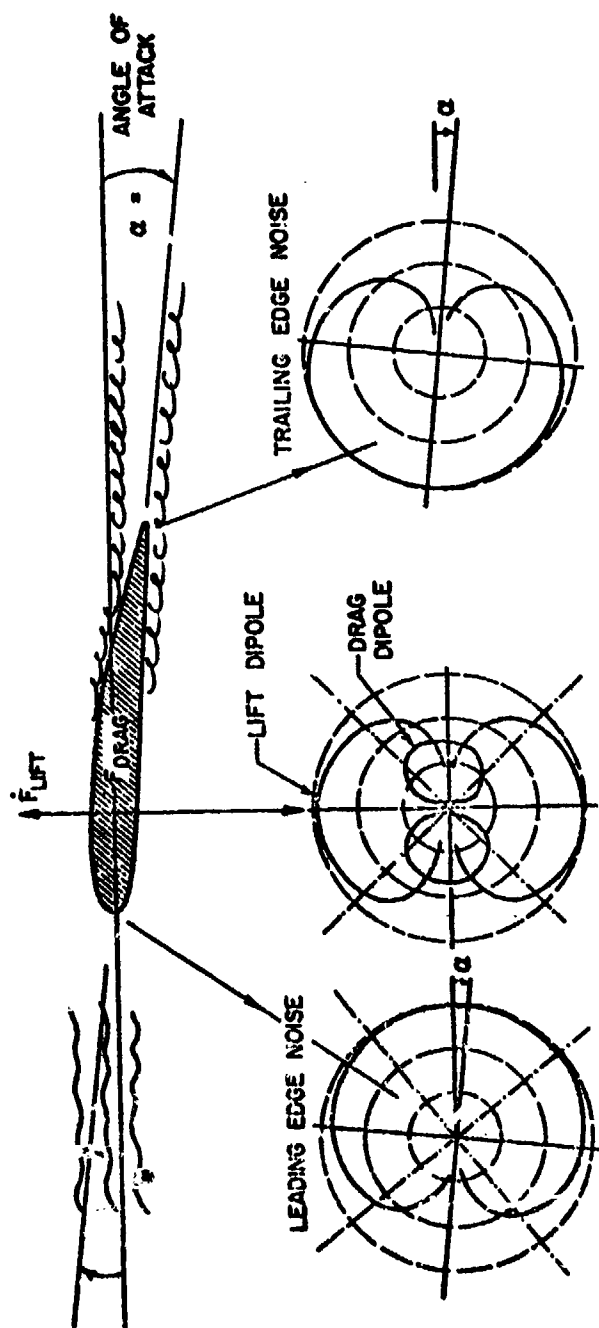
FIG. 45. DIRECTIVITY OF FLOW SURFACE INTERACTION NOISE MECHANISMS.
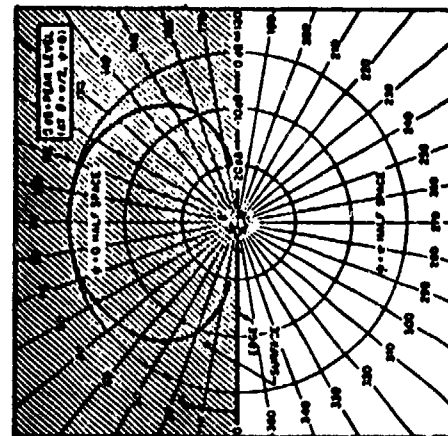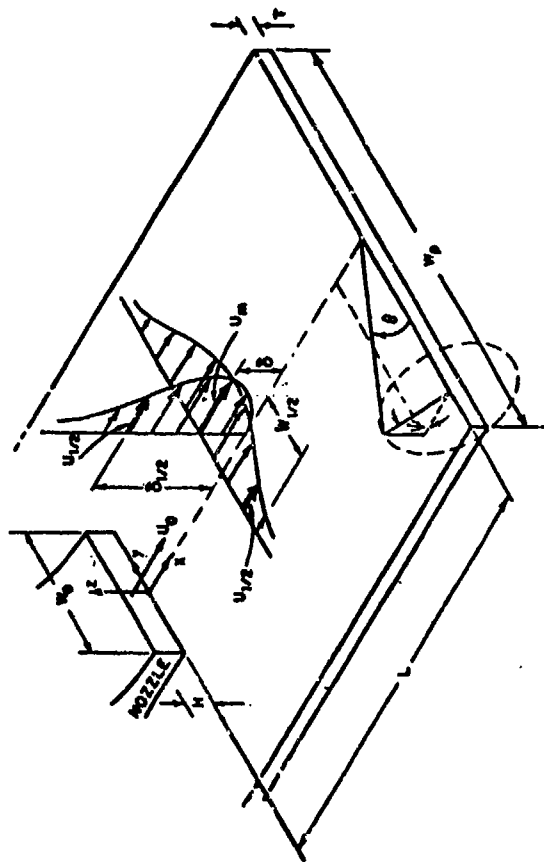
(a) In plane normal to surface and to span

(b) In plane normal to surface and parallel to span

(c) In plane of the surface

FIG. 46. DIRECTIVITY OF EDGE SOURCES [88].

133

3.2 Nearfield Noise from Spatially Distributed Sources

In powered lift devices, the noise sources typically are spread over a significant portion of the wing span. Thus, only observation points at considerable distances can be expected to be in the geometric farfield, where the source can be approximated by a single point.

It is instructive to compare the results one obtains by assuming farfield (point source) conditions with similar results for the nearfield of a line source made up of a linear array of incoherently radiating point sources. Such a comparison is made in Figure 47, from which one may observe that the point source (farfield) and line source (nearfield) results are appreciably different only if the distance r from the center of the line source to the observation point is smaller than the length w of the line source.

The foregoing observation suggest that one may calculate the sound pressure levels in the geometric nearfield of distributed sources simply by subdividing each source into elements that are short compared to the observation point distance (i.e., w < r), calculating the contribution of each such element as if it were a point source, and then combining the results to account for all elements.

3.3 Externally Blown Configurations

Both the under-the-wing externally blown flap (EBF) and the over-the-wing upper surface blown (USB) configuration produce low-frequency noise due to flow interaction with turning flaps, and both may be expected to expose the fuselage to some jet flow. As shown schematically in Figure 48, the EBF

134
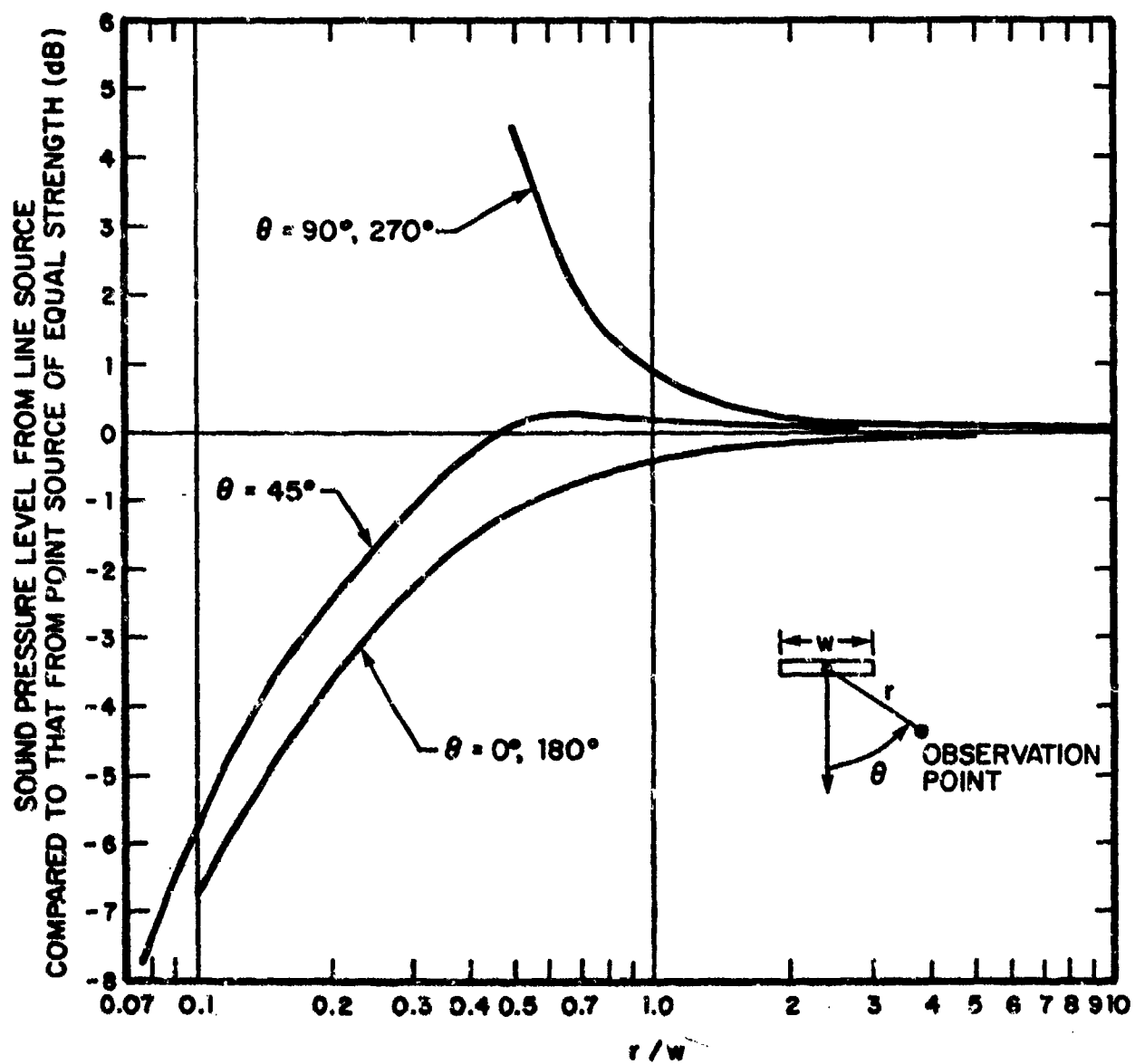
FIG. 47. GEOMETRIC NEAR FIELD EFFECTS FROM AN INCOHERENT DISTRIBUTED LINE SOURCE [91].

135
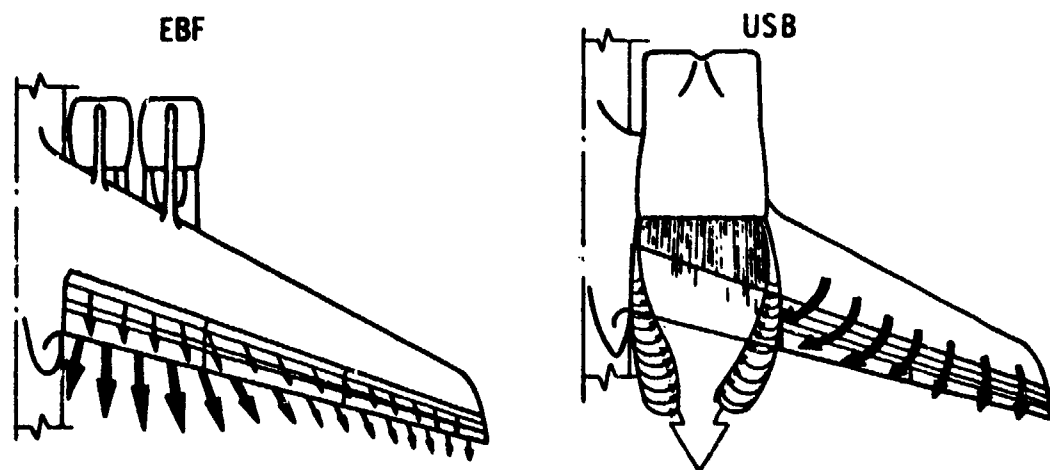
FIG. 48.   SCHEMATIC FLOW PATTERNS ON EXTERNALLY
BLOWN FLAP AND UPPER SURFACE BLOWN
CONFIGURATIONS [92].

136

results in a lateral spreading of the jet flow, increasing
the likelihood of its impingement on the fuselage at low
forward speeds; in the USB configuration the induced flow
is directed inward, leading to the possibility of having
highly turbulent shear layers impinge on the fuselage. Thus,
flow excitation must be considered in addition to acoustic
excitation.

3.3.1 Externally blown flaps (EBF)

General

EBF configurations typically involve high bypass ratio
engines, arranged under the wing, blowing on two or three
enlarged flaps. In such configurations one encounters noise
due to the engine and its free exhaust jet, in addition to
the noise due to sources associated with interaction of flow
with the flaps. The present discussion focuses on the
latter noise sources; however, flap noise is caused by pressure
fluctuations in the flow that reaches the flaps, and this
inflow is due to the jet. Indeed, a variety of mixer or
"decayer" nozzles – e.g., see [68] – have been considered
for reducing inflow turbulence and flap noise.

Flap noise

Figure 49 illustrates some typical noise spectra measured
on a large-scale EBF model. The shape of the spectrum measured
at the wing tip corresponds to what one may expect to observe
on the fuselage.
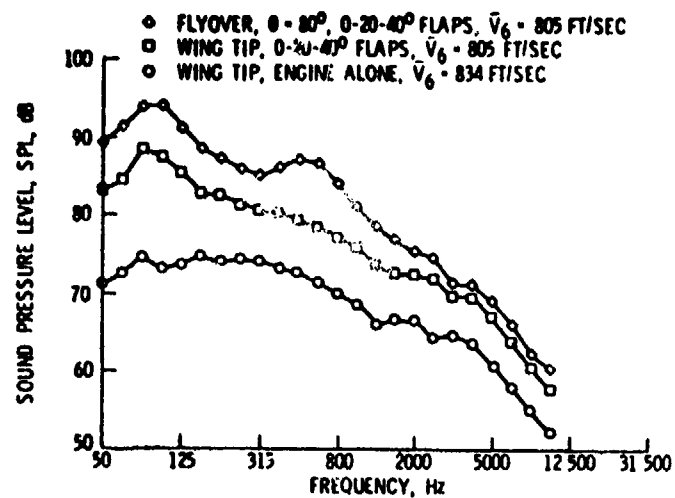
FIG. 49. SOUND SPECTRA MEASURED AT 500 FT. WINGTIP
SIDELINE AND MAXIMUM FOR 500 FT. FLYOVER.
THREE-FLAP EBF MODEL WITH SINGLE TF-34
ENGINE (6000 LB. MAXIMUM THRUST) [68].
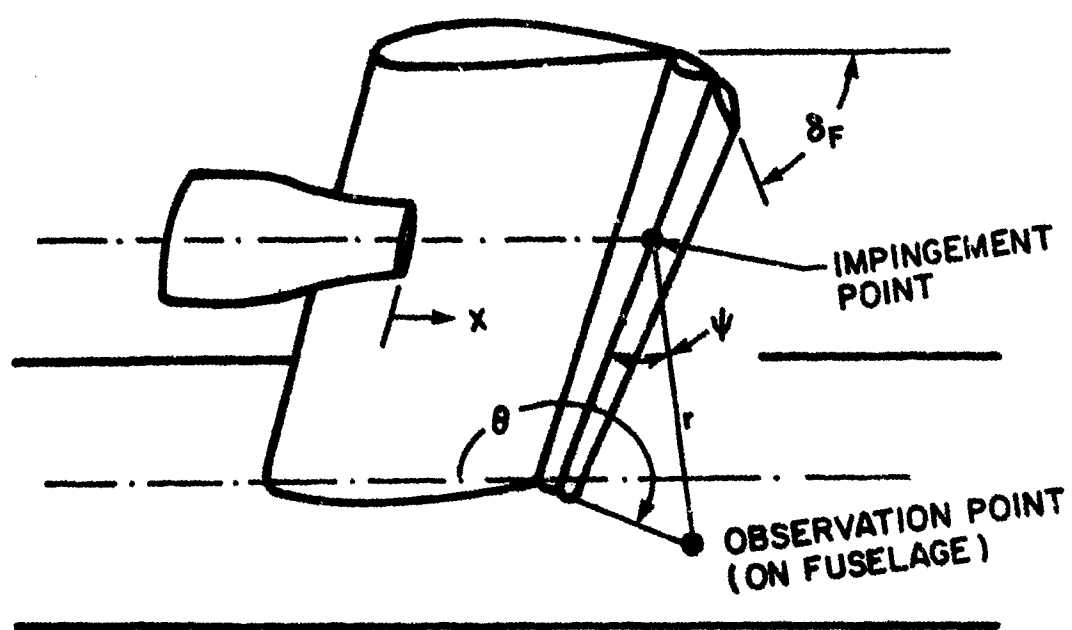
FIG. 50. DEFINITION OF COORDINATES FOR EXTERNALLY
BLOWN NEAR-FIELD RADIATED NOISE CALCULATION.

A prediction method has been synthesized from two methods previously reported by Hayden *et al.* [69, 70] and Clark *et al.* [71]. This suggested method is summarized below.

The overall sound pressure level resulting from an individual jet nozzle/flap interaction is given by

$$OASPL = 29 + 0.14\ \delta_F + 10\ \log\ (\rho_e^2\ U_e^6\ D_0^2)$$

$$+ 10\ \log\left[\frac{1+\sin\psi}{2}\ \cos^2\left(\frac{\theta+\delta_F}{2}\right)\right] - 20\ \log\ r \tag{51}$$

where   OASPL = overall sound pressure level, (dB, re
2×10^{-5} N/m^2)

ρ_e = mean density of jet (slugs/ft^3)

U_e = effective velocity of jet (ft/sec), discussed below.

D_0 = effective nozzle diameter (ft); discussed below

r = distance from flow impingement point to observer (ft)

δ_F = flap angle (degrees); see Figure 50

θ, ψ = observation point coordinate angles (degrees); see Figure 50.

The effective velocity U_e of the jet at the impingement point depends on the nozzle type and on the axial distance x from the jet exit plane to the impingement point. The variation of jet velocity with axial distance is illustrated in Figure 51 for several types of nozzles. Note that the exhaust gas velocity from conical nozzles decreases only slightly for the first few diameter's distance, whereas the velocity from decayer nozzles decreases markedly within two diameters.

140
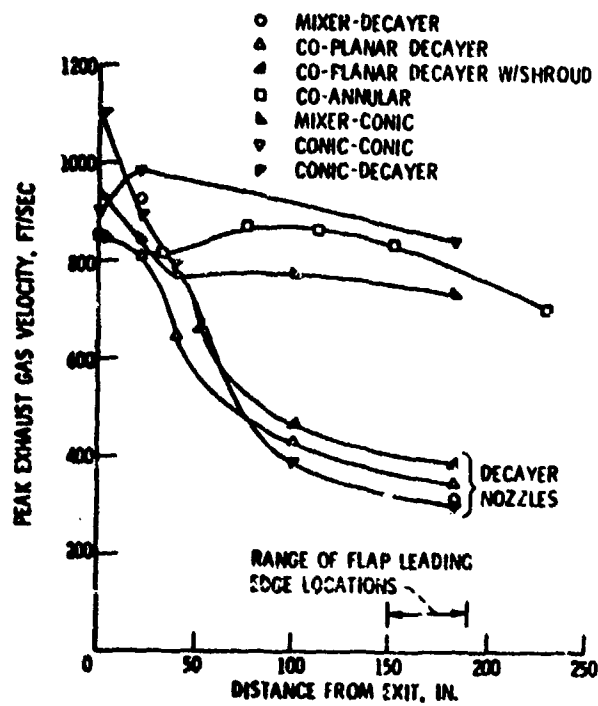
FIG. 51. VELOCITY DECAY CHARACTERISTICS OF TYPICAL EBF NOZZLES [68].

141

The first flap of typical two engine EBF configurations
is between 1.0 and 3.0 nozzle diameters from the exit plane,
whereas the first flap of four-engine configurations is
between 2.0 and 4.5 diameters from the exit plane. Thus,
all but decayer nozzles can be approximated by distance-inde-
pendent jet velocity expressions for the EBF application of
interest here.

For nozzles other than external mixers (decayers), one
may calculate the effective jet velocity U_e from the following
expressions (which apply for $x/D_0 \leq 5$):

For simple round nozzles,

$$U_e = U_0 = \text{mean exit velocity} \tag{58a}$$

For ω annular nozzles (without internal mixing),

$$U_e = \left[\frac{A_c V_c^6 + A_f V_f^6}{A_c + A_f} \right]^{1/6} \tag{58b}$$

For nozzles with internally mixed flows,

$$U_e = \frac{BPR \cdot V_f + V_c}{BPR + 1} \tag{58c}$$

where

A_c = area of core exit nozzle
A_f = area of bypass nozzle annulus
V_c = core exit velocity
V_f = fan (annulus) exit velocity
BPR = bypass ratio

142

For decayer nozzles, one may estimate the effective jet velocity at a given x/D_0 by using the appropriate ratio of decayer velocity to the conical jet velocity derived from Figure 51.

The effective nozzle diameter D_0 is equal to the actual nozzle exit diameter where there exists a single jet. For coannular jets,

$$D_0 = \sqrt{\frac{4}{\pi} (A_c + A_f)} \tag{59}$$

The one-third octave band sound pressure levels associated with the foregoing overall levels (for nozzles other than decayers) are given by

$$SPL_{1/3OB} = OASPL - 7.5 + 10 \log \left[S_p \, S^4 (S^{4/3} + S_p)^{-2} \right] \tag{60}$$

where

S_p = strouhal number at spectrum peak
$\approx$ 0.3 for typical EBF configurations

S = fD_0/U_e = Strouhal number at center frequency
f (Hz) of band

The relation of Equation (60) has been found to correspond within at most ± 3 dB to data for all azimuth angles. For decayer nozzles, the 1/3-octave band spectrum is nearly flat (within ± 2 dB; see Figure 52) for such nozzles,

$$SPL_{1/30B} = OASPL - 11 + C , \quad (\text{for } 0.1 \leq S < 4.0) , \quad (61)$$

where
$$C = \begin{cases} 0 & \text{for } x/D_0 \text{ between 3 and 5} \\ 60 \log [U_{e, \text{ decayer}} / U_{e, \text{ conical}}], \text{ for } x/D_0 < 3 \end{cases} \quad (61a)$$

and $U_{e, \text{decayer}}$ is the gas velocity of a decayer, and $U_{e, \text{conical}}$ is the gas velocity of a conical nozzle at the x/D_0 value of interest, as found from Figure 51.

Unsteady Aerodynamic Pressures

The sources of fluctuating pressures on blown flaps are summarized in Figure 53. Figure 54 presents the results of a survey of flap pressures carried out on a large-scale EBF model, which indicates the greater spatial variability that may be expected in general.

Figure 55 indicates the distribution of overall fluctuating pressure levels measured on an EBF configuration in a plane through jet center line. Considerable variability is again evident. The pressure data may be normalized with respect to the dynamic pressure of the jet, and spectra may be related to the corresponding Strouhal number. Figures 56 and 57 show some typical reduced spectra. The latter figure and related extensive measurements show that the reduced spectrum shape is essentially the same under a wide variety of conditions.
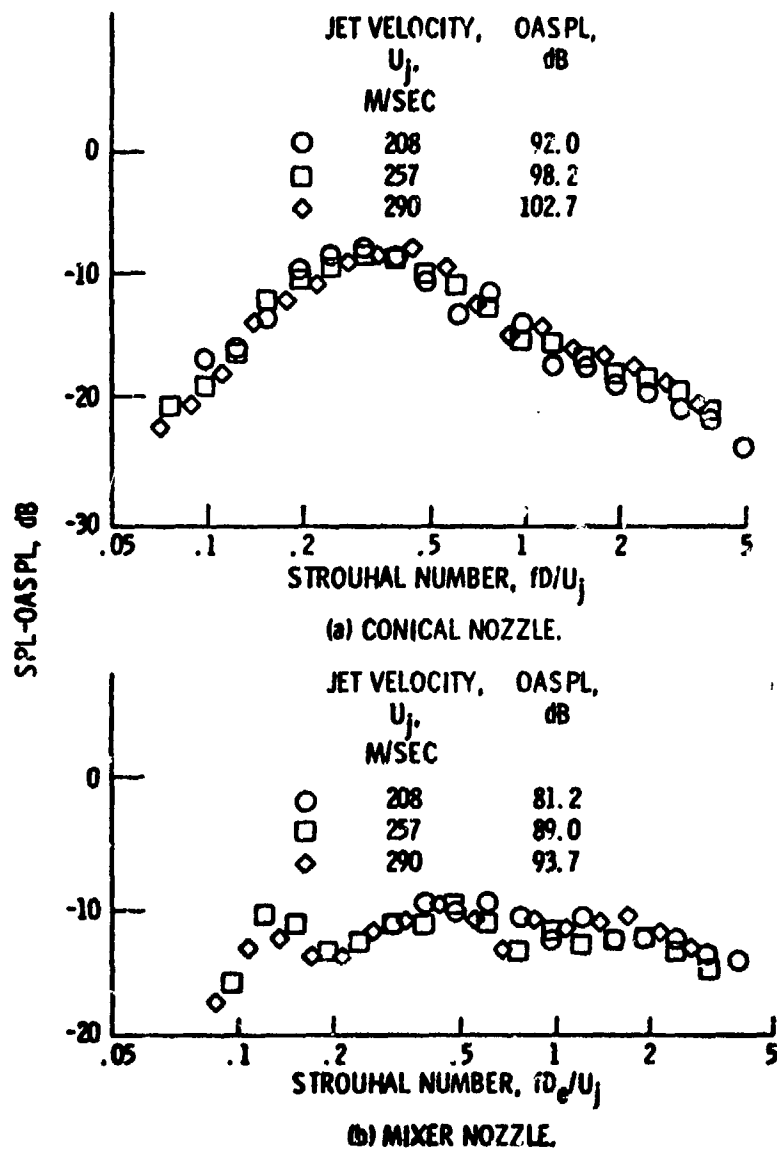
FIG. 52. NORMALIZED SPECTRA AS A FUNCTION OF STROUHAL NUMBER FOR FLAP DEFLECTION OF 10°-20°. DIRECTIVITY ANGLE, 100°; U_c, 53 m/sec [72].

EXTERNALLY BLOWN FLAP
BYPASS TURBULENT MIXING REGION

BOUNDARY LAYERS
SLOT TURBULENCE

COMBUSTION TURBULENCE

SEPARATED EDGE FLOW

UPPER SURFACE BLOWN FLAP

CORE AIR TURBULENT MIXING REGION

BOUNDARY LAYER

JET MIXING

ENGINE TURBULENCE

TRAILING EDGE
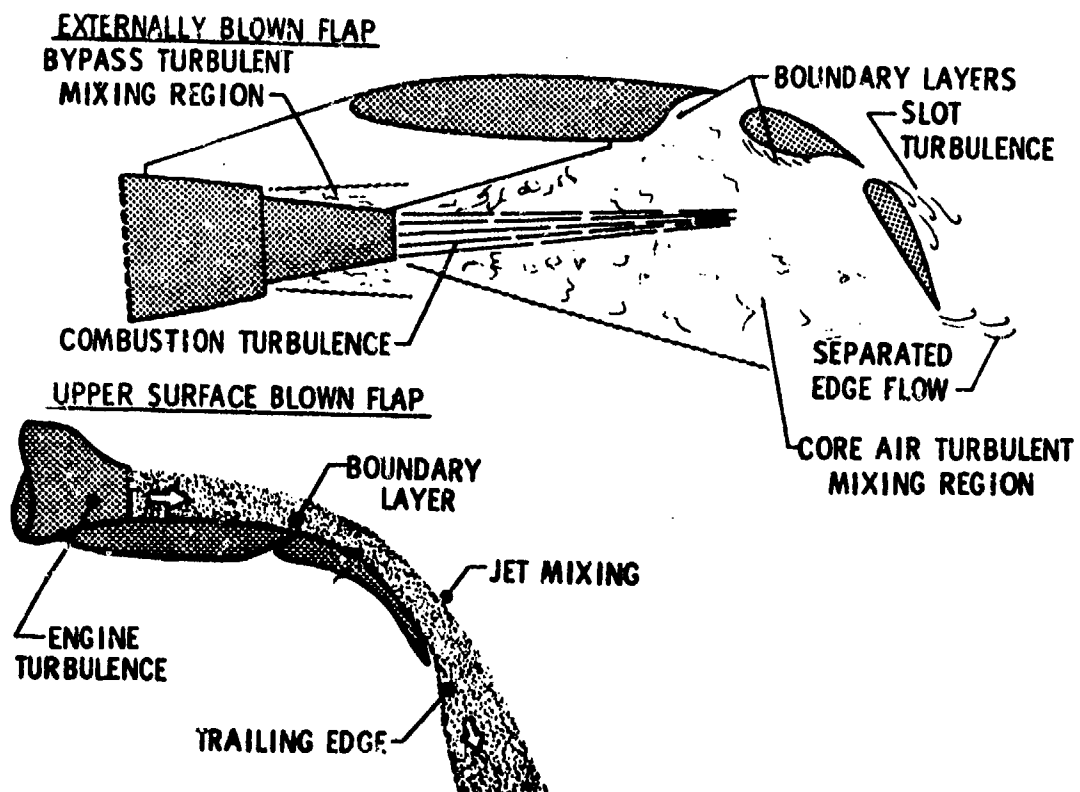
FIG. 53. SOURCES OF FLUCTUATING PRESSURE
ON EXTERNALLY BLOWN FLAPS [92].

APPROACH FLAP SETTING

RMS PRESSURE
>80% OF MAXIMUM PRESSURE
>50% OF MAXIMUM PRESSURE
≥20% OF MAXIMUM PRESSURE

NO DATA

TAKE-OFF FLAP SETTING

RMS PRESSURE
>80% OF MAXIMUM PRESSURE
>50% OF MAXIMUM PRESSURE
≥20% OF MAXIMUM PRESSURE

NO DATA
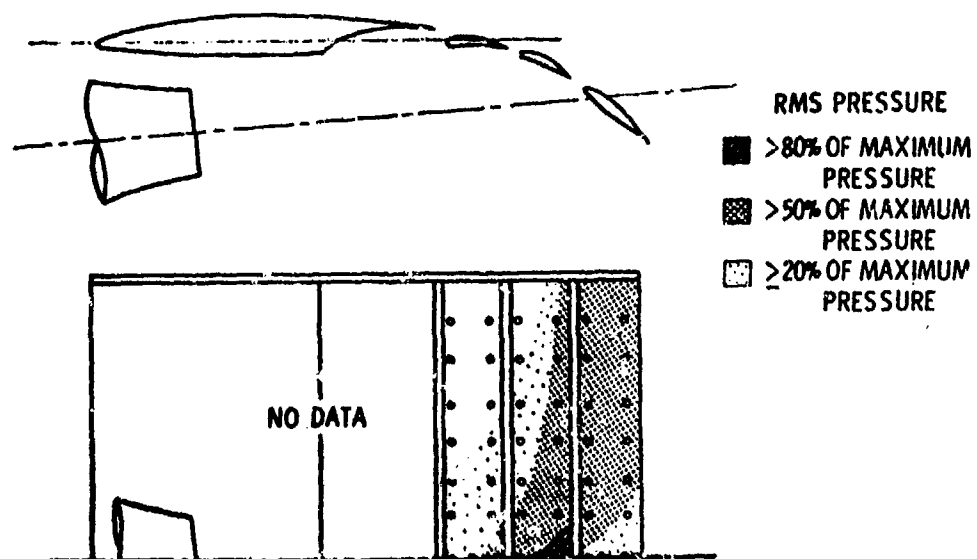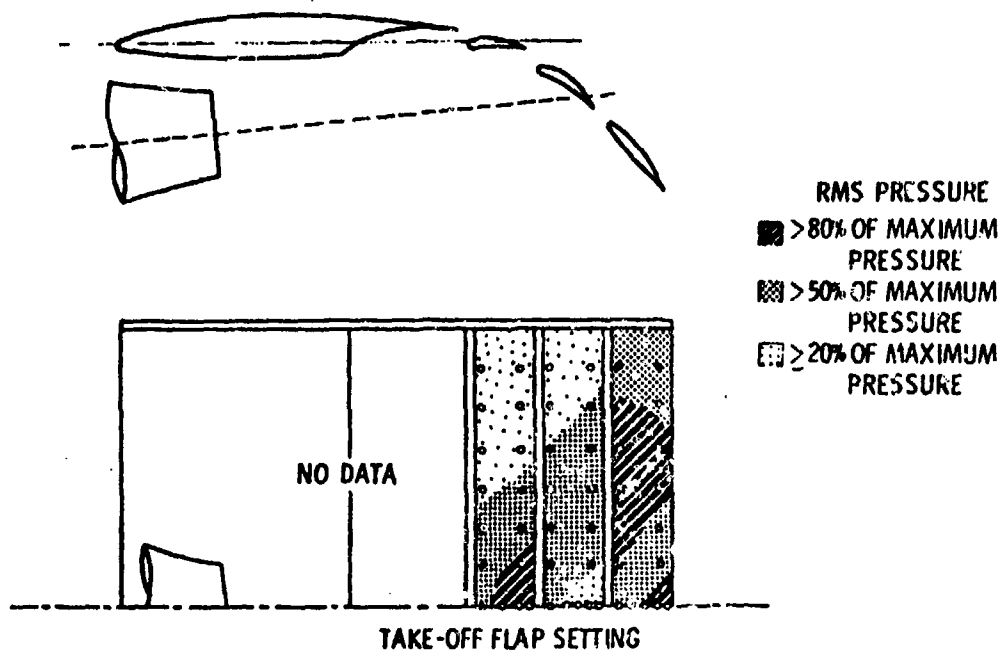
FIG. 54. DISTRIBUTION OF DYNAMIC SURFACE PRESSURES ON SMALL-SCALE EBF MODEL [73].

147

TAKE-OFF (0-20-40°)

LANDING (15-35-55°)

Transducer	OAFPL, dB (ref. 20 µPa), at Mach number of –									
	Take-off flaps (0°-20°-40°)					Landing flaps (15°-35°-55°)				
	0.33	0.45	0.51	0.57	0.59	0.33	0.44	0.49	0.55	0.59
1	149	155	156	158	159	150	156	158	160	162
2	151	157	159	160	161	148	154	156	159	160
3	152	158	160	162	163	148	153	155	157	159
4	149	154	156	159	160	146	152	153	156	157
5	145	150	152	155	156	147	152	154	156	156
6	143	148	150	152	153	148	154	155	156	157
7	144	149	151	--	154	148	153	155	157	157

FIG. 55   OVERALL LEVELS OF FLUCTUATING
SURFACE PRESSURES ON TF-34
EBF MODEL (75).
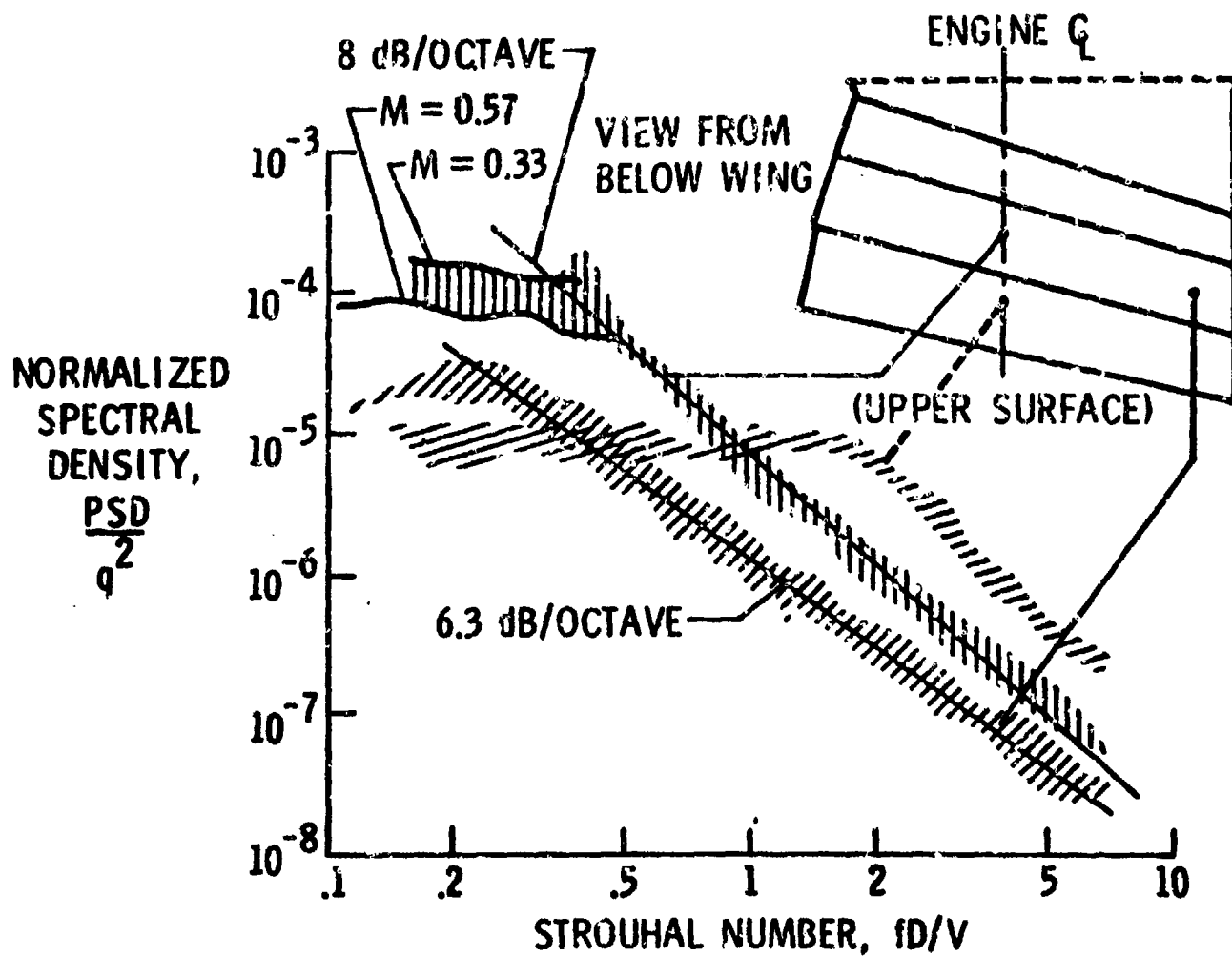
FIG. 56 VARIATION IN NORMALIZED POWER SPECTRAL
DENSITY WITH STROUHAL NO. FOR THREE
LOCATIONS ON HIGH BYPASS ENGINE AND EBF
MODEL (74).

149
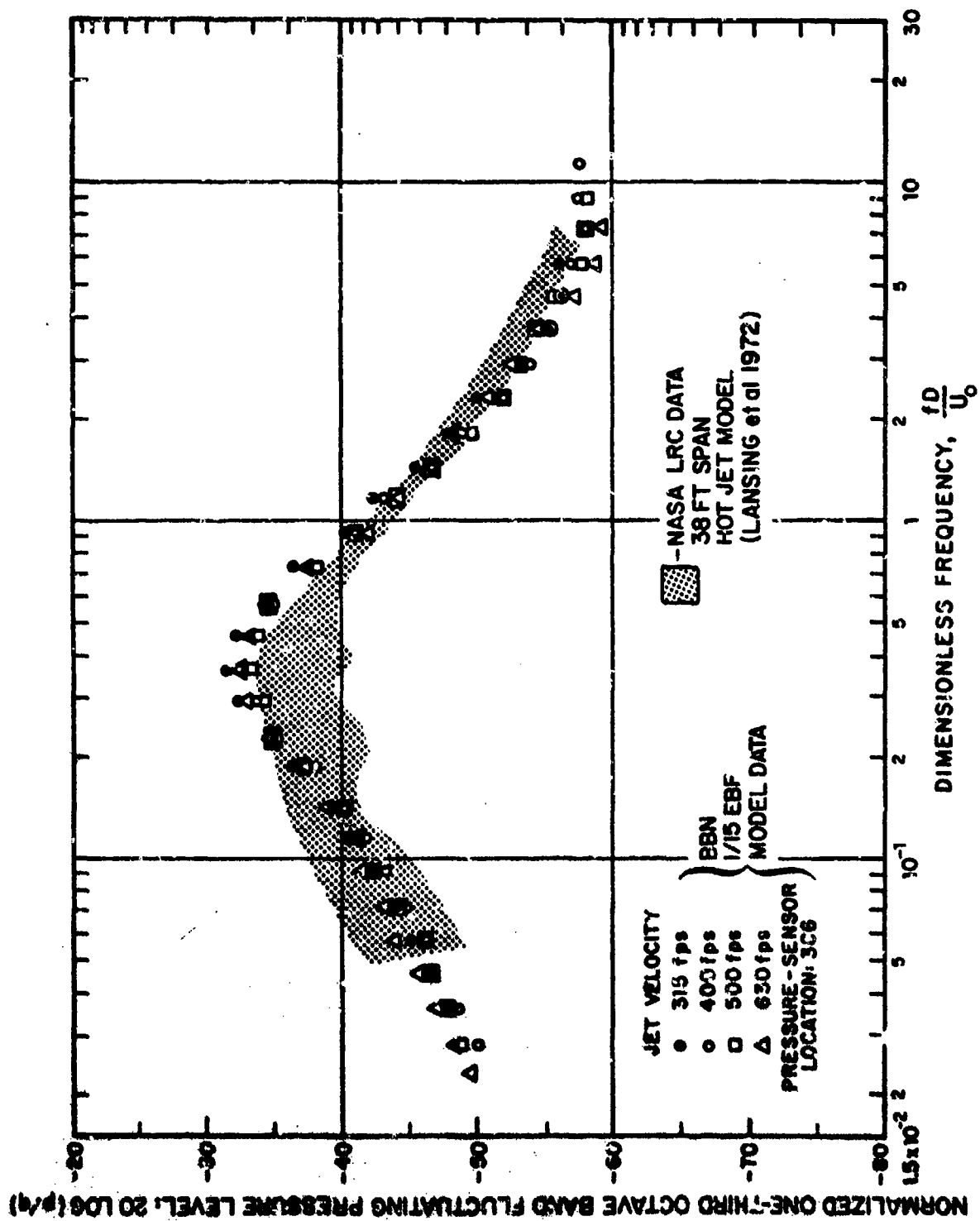
FIG. 57. NORMALIZED THIRD OCTAVE BAND PRESSURE SPECTRA AT LEADING EDGE OF THIRD FLAP; APPROACH FLAP SETTING [69].

Correlation length information is sparse; only spanwise correlations have been reported [76]. A corresponding reduced parameter curve suitable for estimation purposes appears in Figure 58.

3.3.2 Upper surface blown flaps (USB)

General

In USB systems, flow turning is produced by the Coanda effect. Complex flow fields, as illustrated in Figure 59, are associated with such systems. The flow fields are characterized by wall-jet flows along the jet exit direction and a pair of vortices on the edges of the wall jet. Fluctuations of these vortices produce a low-frequency peak in the radiated noise, as well as in the fluctuating pressure spectra.

Flap Noise

In addition to the aforementioned low-frequency peak, the spectrum of flap noise contains a peak at higher frequencies associated with the attached flow. As the nozzle exit velocity increases, the high-frequency peak becomes predominant, as illustrated in Figure 60. [67, 70, 77, 78].

The presence of two peaks complicates the prediction of USB noise; the low-frequency dipole force varies as the fourth power of nozzle exit velocity (due to the finite size of the surface), whereas the dipole forces responsible for the high-frequency part of the spectrum vary as the sixth power of this velocity [70].
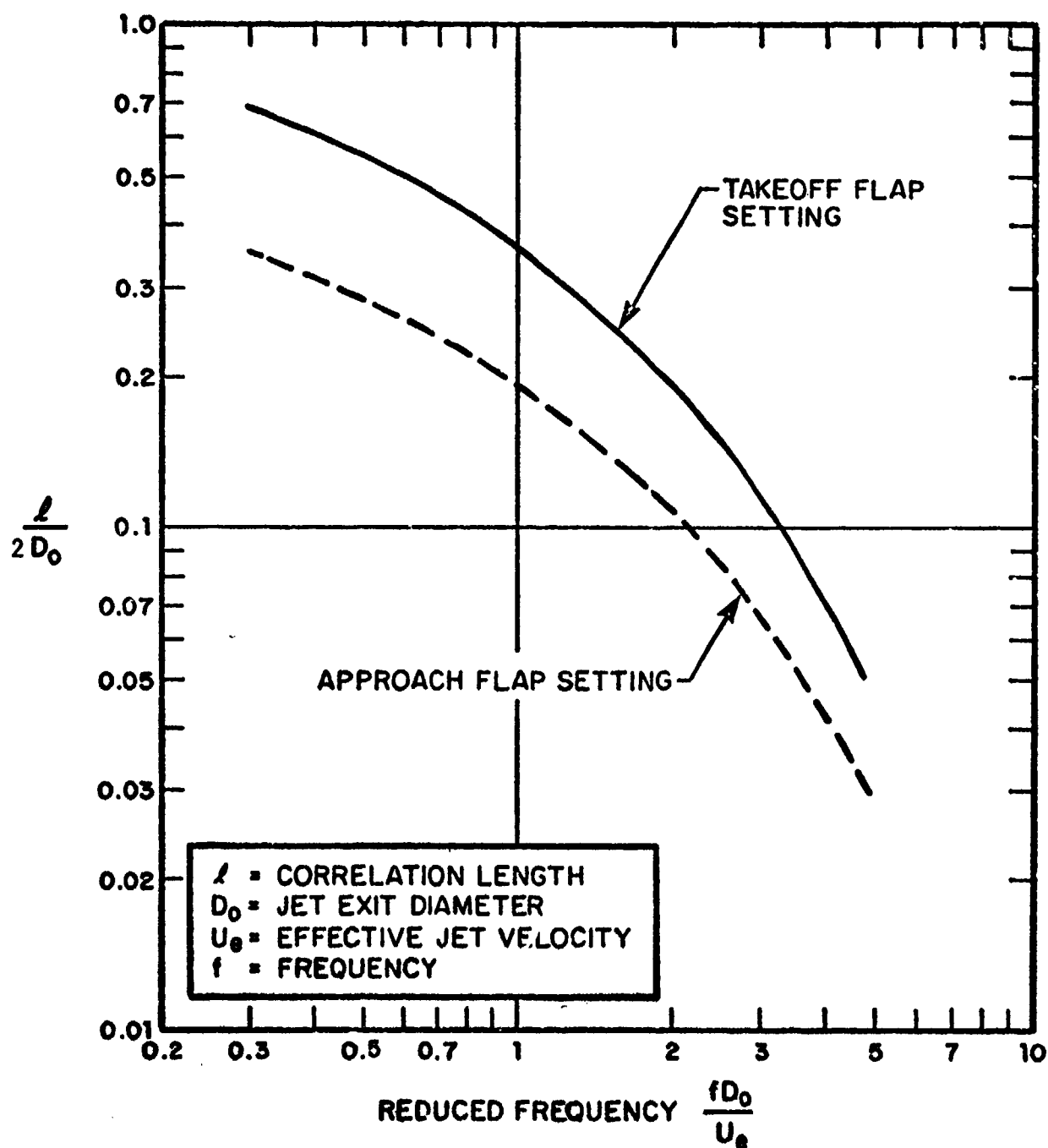
FIG. 58. SPANWISE CORRELATION LENGTHS ON 3RD FLAP
OF A TRIPLE-SLOTTED EBF AT X/D ≈ 3.0 [76].

NACELLE WITH STRAIGHT NOZZLE

NACELLE WITH DEFLECTED NOZZLE
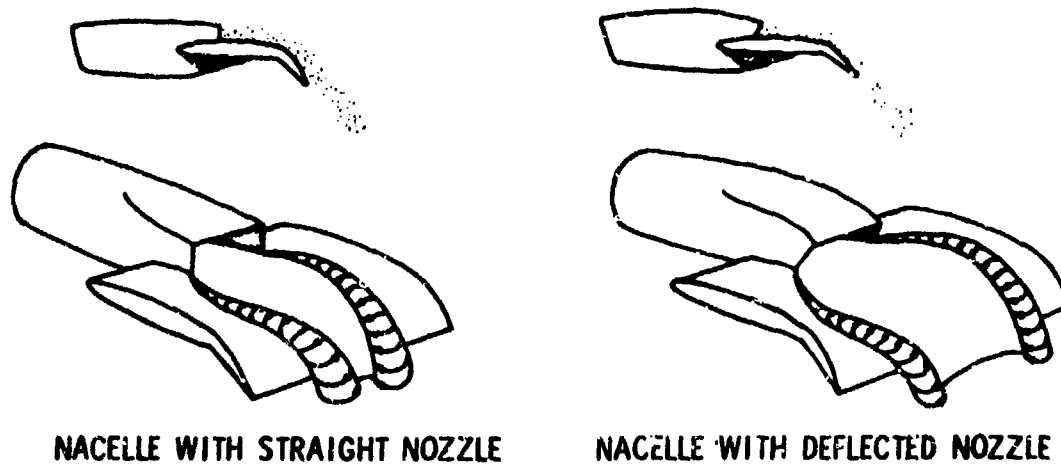
FIG. 59. FLOW FIELDS ON UPPER SURFACE BLOWN
CONFIGURATIONS [92].
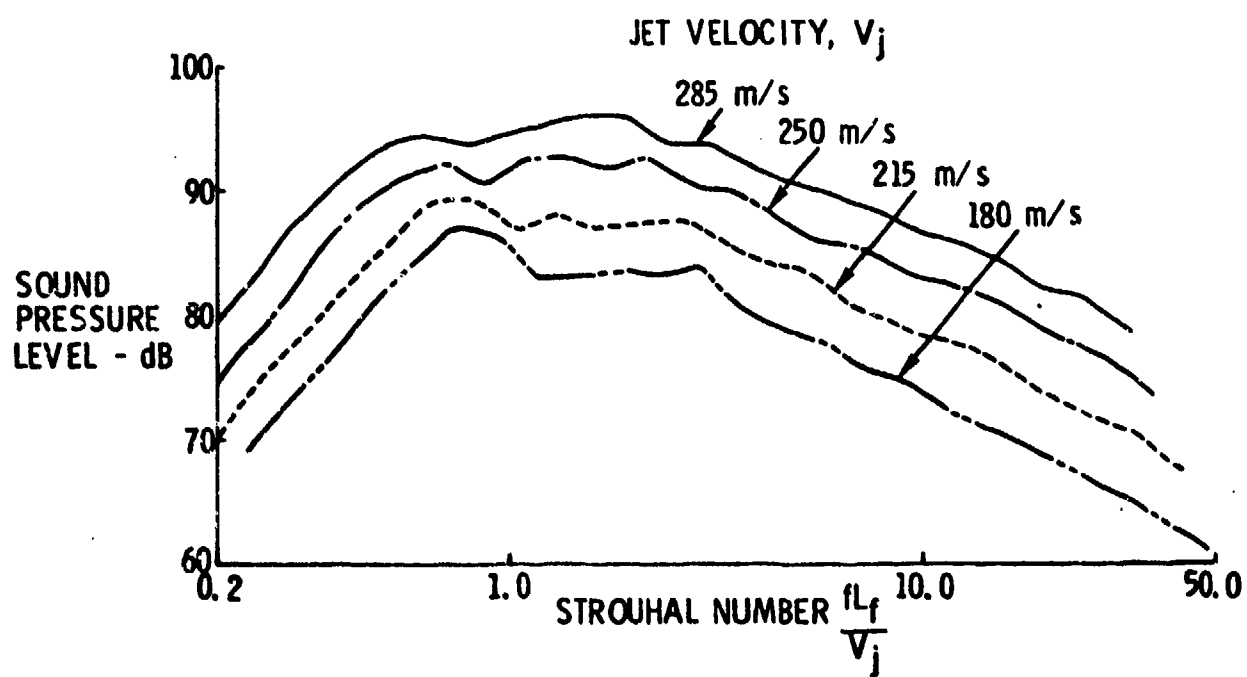
FIG. 60.   EFFECT OF JET VELOCITY ON NOISE
          OF USB CONFIGURATION [78].

(AR4 NOZZLE, NOZZLE IMPINGEMENT ANGLE 20°,
NOZZLE LOCATION 20% CHORD, 30° FLAP ANGLE)

Nearfield Noise Data

Figure 61 illustrates the considerable variations in magnitude and spectrum shape that have been observed even over small areas on fuselage sidewalls. The dependences of the corresponding overall fluctuating pressure levels on jet velocity are shown in Figure 62; the fact that these dependences exhibit different slopes - corresponding to different powers of velocity - indicates that different mechanisms predominate.

Figures 63 and 64 show some detailed data obtained from measurements on a USB model. Figure 63 indicates the measurement (microphone) locations on a simulated fuselage wall; Figure 64 shows the spectra observed at these locations at a particular jet exit speed. One may note that the high-frequency portions of all these spectra are comparable, but not the low-frequency portions. A thorough study of this and related data [80] revealed that different portions of the various spectra varied differently with jet velocity, as shown in Figures 65 and 66.

Accurate estimation of the nearfield noise requires one to understand and predict all of the contributing noise sources. Such understanding can be developed for specific configurations only on the basis of extensive measurements; a general prediction technique applicable to all configurations appears to be beyond the present state of the art.

In absence of such a general technique, use of Figure 67 is recommended for spectrum prediction purposes, with the overall sound pressure level estimated by application of Equation (57), modified by replacing 0.14 δ_F by 0.01δ_F. Figure 67

FLUCTUATING
PRESSURE LEVEL,
dB (ref. 20 μPa)
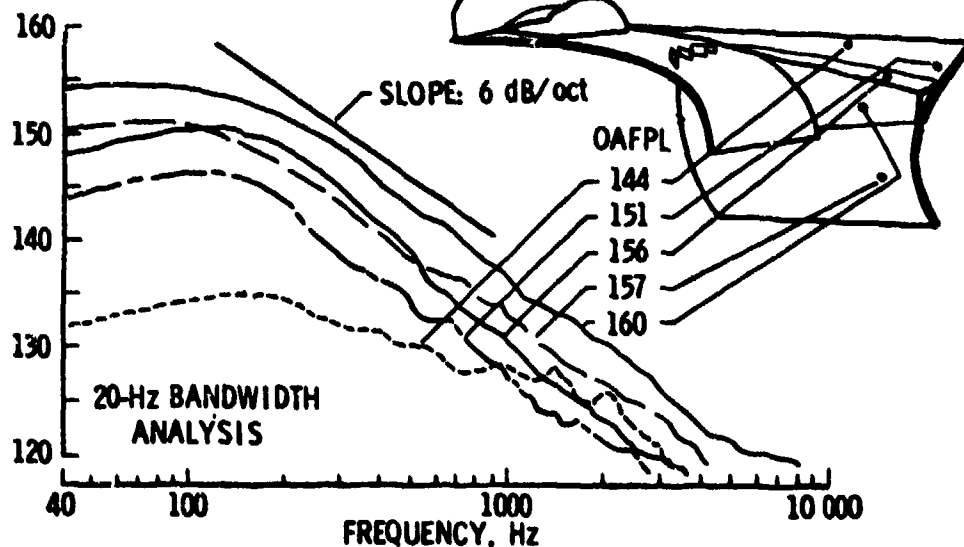
FIG. 61. FLUCTUATING PRESSURES ON
FUSELAGE SIDEWALL OF YC-14
SCALE MODEL [79].
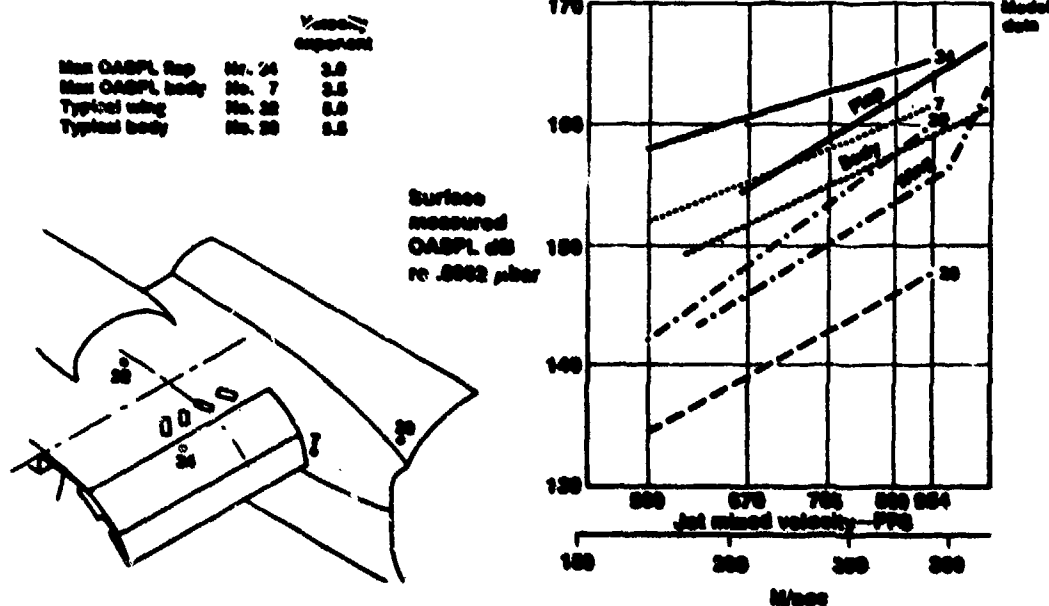
FIG. 62 DEPENDENCE OF OVERALL FLUCTUATING
SURFACE PRESSURE LEVELS ON USB JET
VELOCITY.   (YC-14 TESTS, FULL SCALE
AND 1/8 SCALE MODEL)   (79).

156
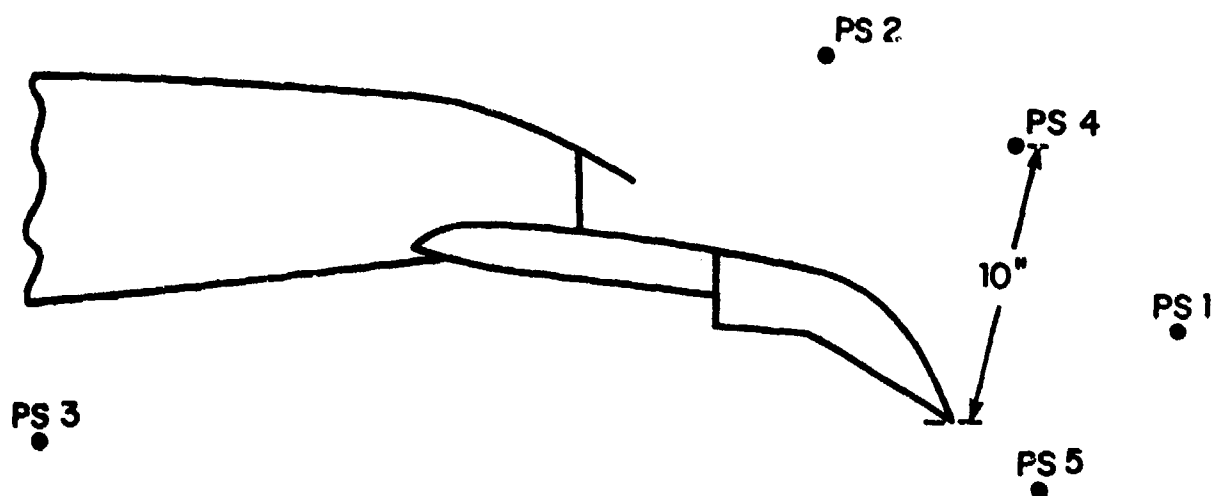
FIG. 63. LOCATION OF FUSELAGE MICROPHONES WITH RESPECT
TO SECTION OF MODEL USB FLAP. FUSELAGE IS 20"
FROM JET CENTERLINE [80].
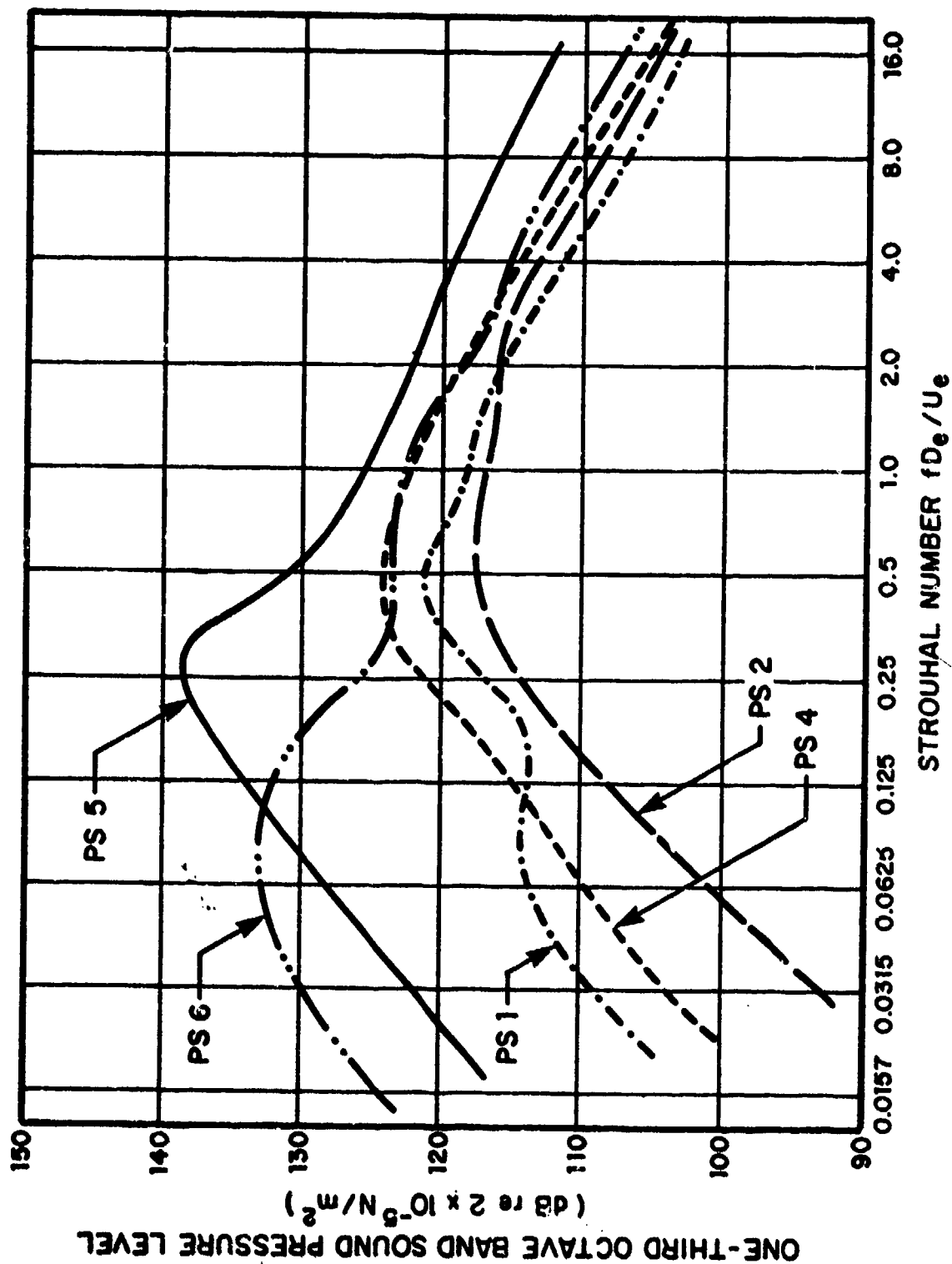
FIG. 64. NEARFIELD NOISE LEVELS ON USB MODEL FUSELAGE SIDEWALL AT 680 fps. JET VELOCITY [80J].
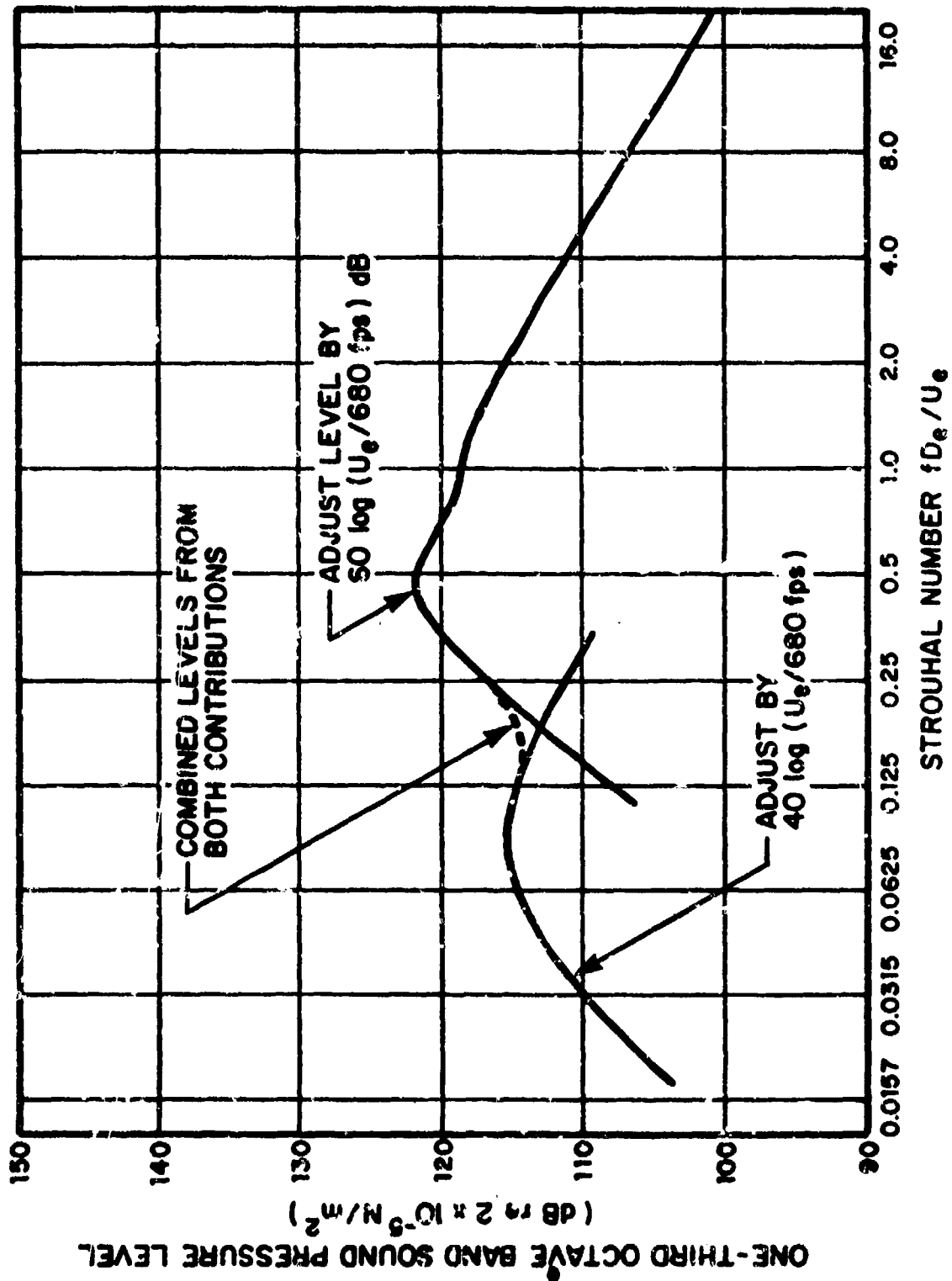
FIG. 65. NEARFIELD NOISE SCALING FOR SENSOR LOCATION PS#1 [80].

159
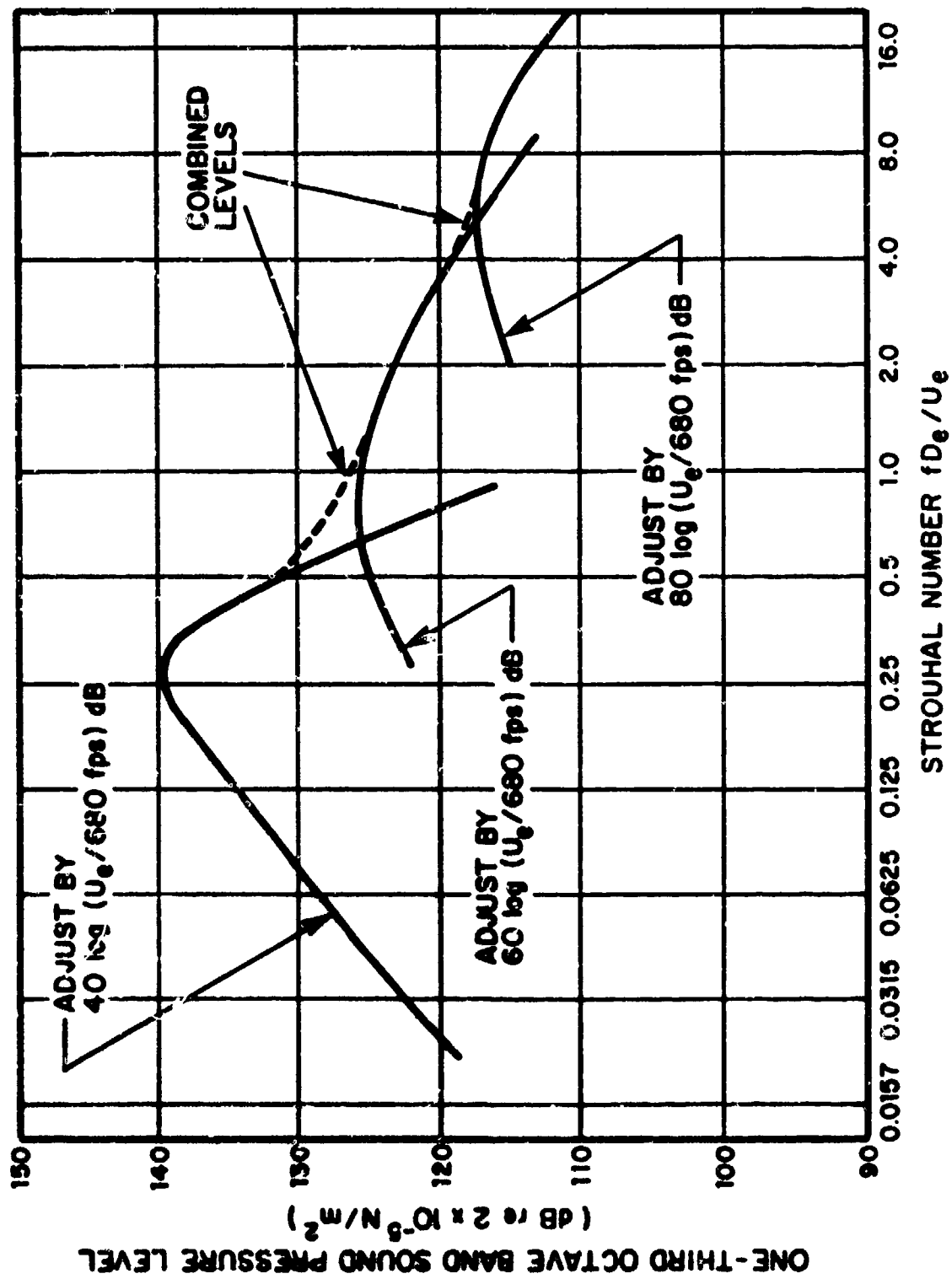
FIG. 66. NEARFIELD NOISE SCALING FOR SENSOR LOCATION PS#5 [80].

160
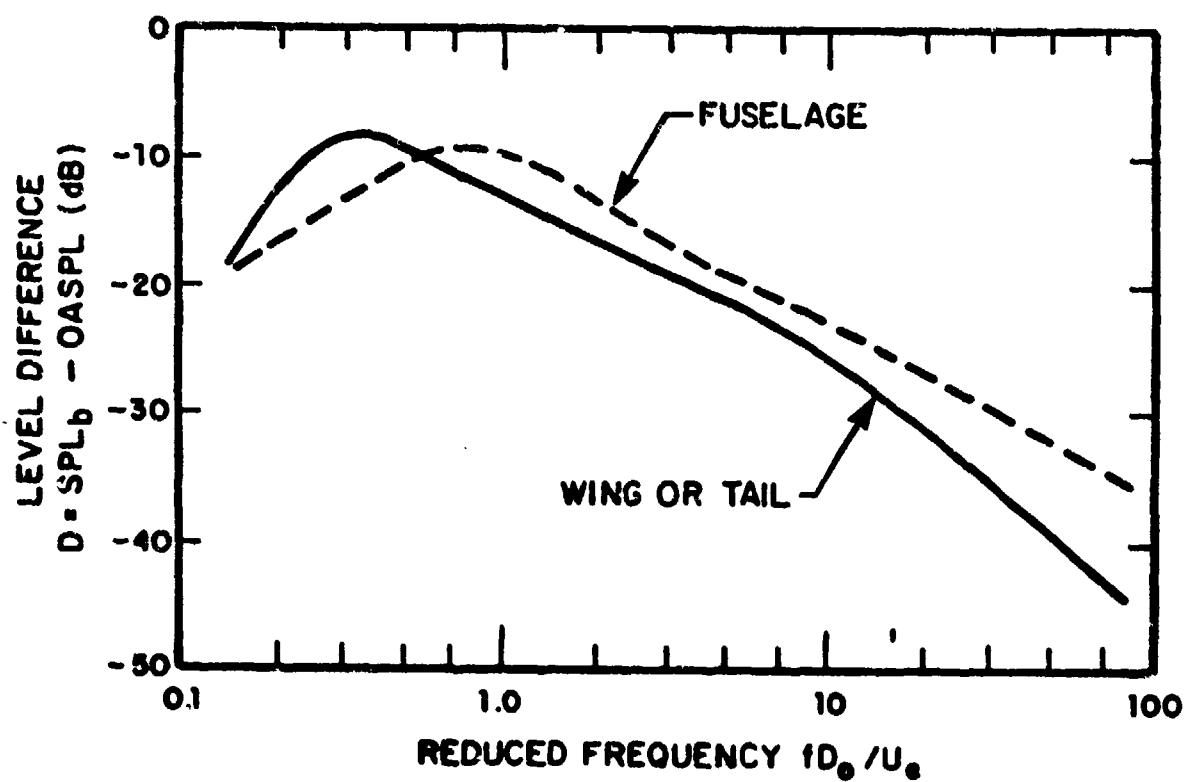
FIG. 67. NORMALIZED NOISE SPECTRA ON SURFACES OF USB CONFIGURATIONS [after 71].

applies for a nominal nozzle aspect ratio of 4 for a nominal
jet impingement angle of 20°; the effects of these parameters
are discussed below.

Effects of Nozzle Shape and Impingement Angle

The shape of the nozzle and the "kickdown" angle at which
the jet impinges on the upper surface of the wing have been
shown to influence the USB noise spectrum peak [78, 79]. Fig-
ure 68 shows noise spectra (in terms of Strouhal number,
referred to L_f, the axial distance from the nozzle exit plane
to the flap trailing edge) for nozzles with several aspect
ratios and the same impingement angle; Figure 69 shows similar
spectra for the same aspect ratio and several impingement
angles.

For nozzle aspect ratios other than 4.0 and impingement
angles other than 20°, one may use the differences between
corresponding spectra shown in Figures 68 and 69 to obtain
corresponding approximate corrections to the general
estimated spectrum of Figure 67.

If a deflector is used, its effect on the spectrum may
similarly be determined by use of Figure 70.

Unsteady Aerodynamic Pressures

Flap pressures on USB configurations have been found to
vary considerably with location on the flap, nozzle shape,
and exit velocity. Figure 71 summarizes some data taken
on the USAF YC-14 USB transport aircraft. The observed low-
frequency peak that occurs at pressure ratios above 1.36 is as
yet not understood.
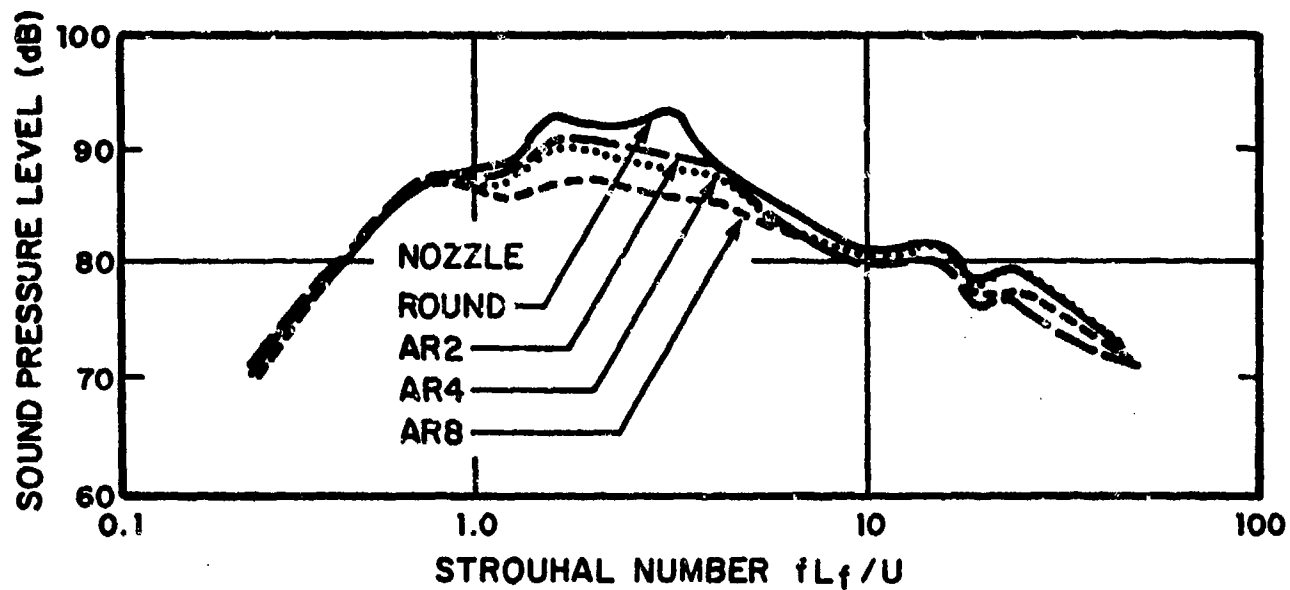
FIG. 68. EFFECT OF NOZZLE SHAPE ON USB NEARFIELD NOISE [after 78].
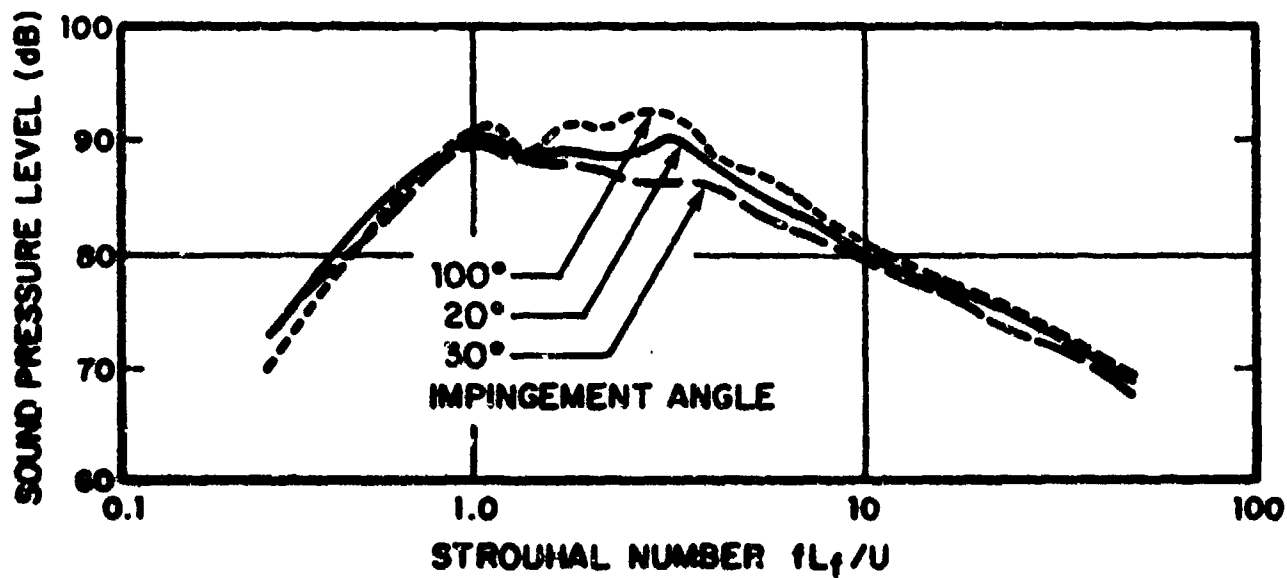
FIG. 69. EFFECT OF NOZZLE IMPINGEMENT ANGLE ON USB NEARFIELD NOISE [after 78].

ONE-THIRD OCTAVE BAND SOUND PRESSURE LEVEL (dB)

10 dB

With Deflector

Without Deflector

0.125   0.25   0.5   1.0   2.0   4.0   8.0   16.0

STROUHAL NUMBER fD_e/U_e
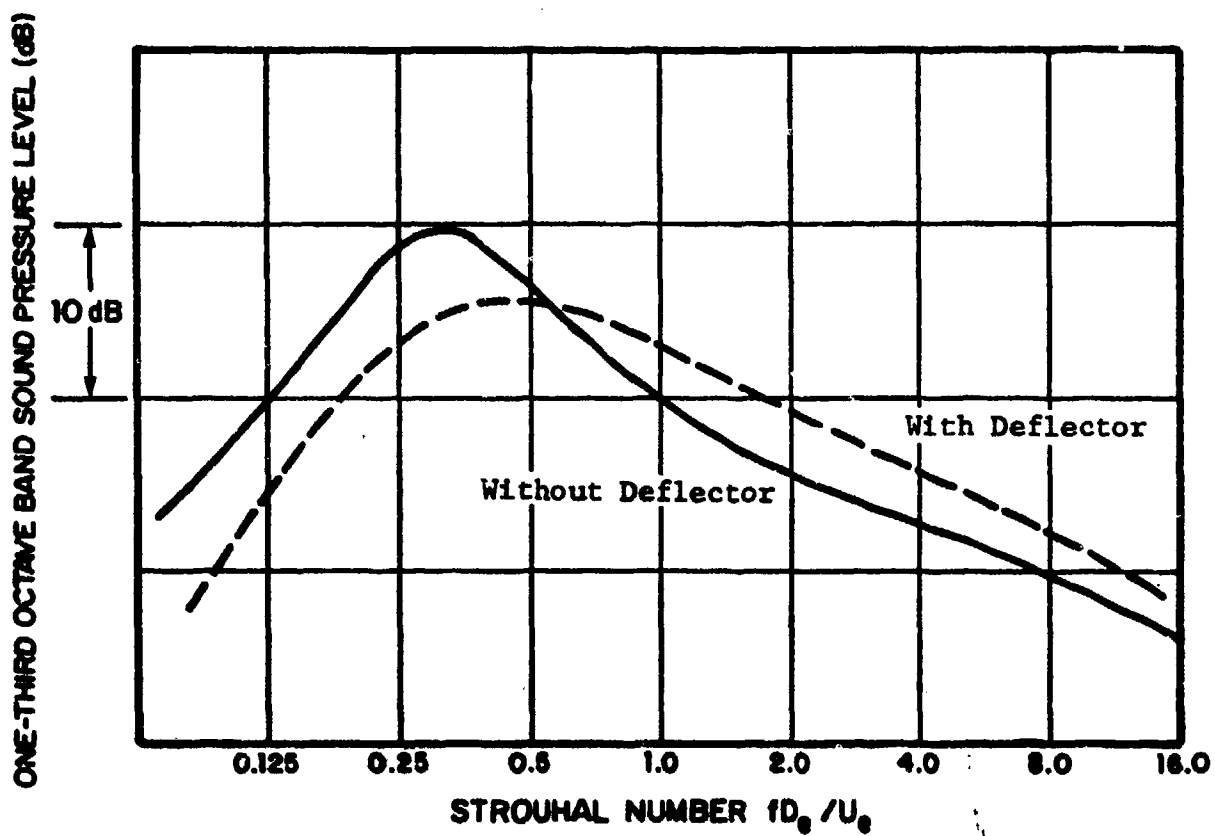
FIG. 70.   EFFECT OF DEFLECTOR ON USB SPECTRUM IN FLYOVER
PLANE [80].

184
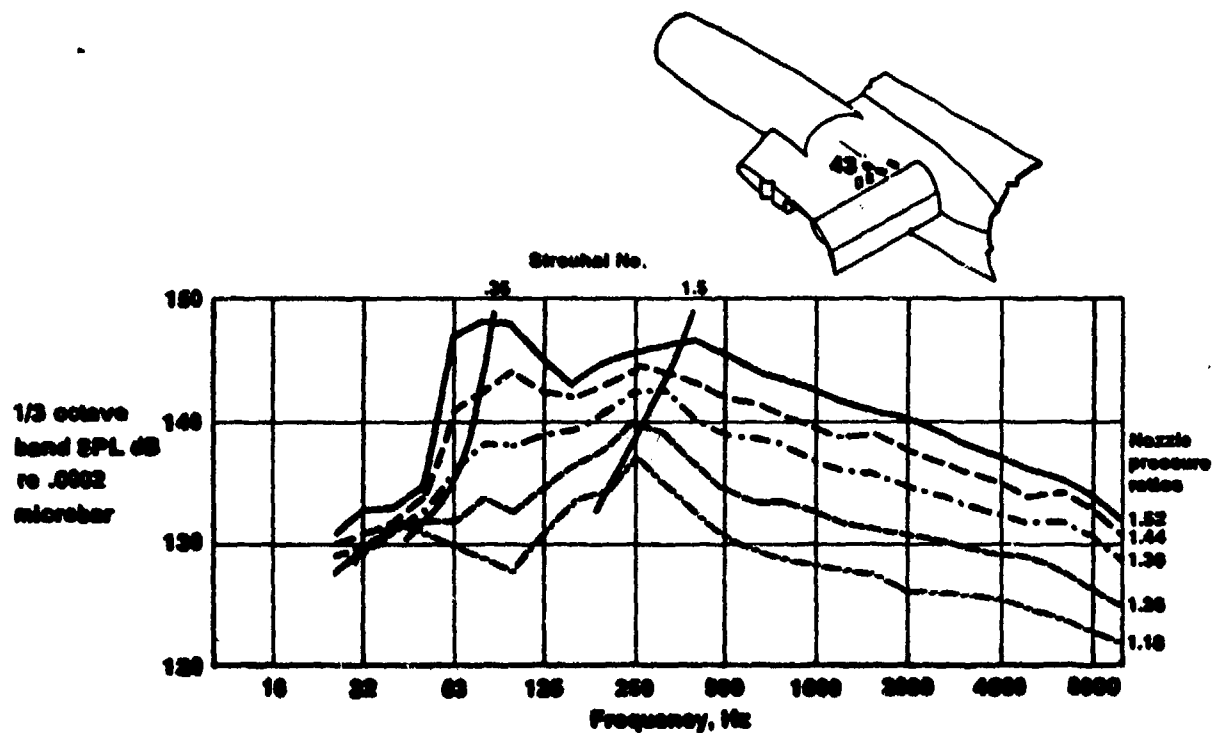
FIG. 71. TYPICAL WING SURFACE PRESSURE DATA
OBTAINED ON YC-14 AIRCRAFT (31.5°/54°
FLAP SETTING) FOR SEVERAL NOZZLE
PRESSURE RATIOS [81].

Reduced data from a full-scale USB static tests are shown in Figure 72. This reduced data, when normalized in terms of Strouhal number, may be used for general first-approximation estimates. Figure 73 indicates correlation length information.

3.4 Internally Blown Configurations

Both the augmenter wing and the jet flap involve the ducting of high-pressure air to a slot nozzle or to a series of small nozzles spanning essentially the entire wing trailing edge. Because of the associated large spatial distribution of noise sources, the geometric nearfield of internally blown configurations is quite extensive.

3.4.1 Augmenter wing (AW)

Noise

For an augmenter wing, a typical cross-section of which is shown schematically in Figure 74, noise generation can be treated in two frequency regions [82]:

1. At high frequencies, jet noise components are generated within the augmenter, and their noise levels typically are 15 dB below those due to fluctuating aerodynamic pressures on the flap and shroud. (However, this jet noise may dominate farfield noise levels if the augmenter is not treated acoustically.)

2. At low frequencies, jet noise is generated outside the augmenter. This noise and that from interaction of flow with the trailing edges of the flap and shroud both make significant contributions.

Some augmenter wings have been observed also to produce intense "screech" tones due to an aeroacoustic feedback action involving the nozzle flow impinging on the leading edge of the flap [83]. Because of the relative rarity of this phenomenon and a lack of understanding of it, it is not treated further in this report.

The sound field from an augmenter has a complex spectrum and directivity, as will be illustrated here for a particular design that has been studied extensively. This design, which is shown in section in Figure 75, was provided with a screech suppressor consisting of flutes (about 0.1 in. wide and 2.0 in. long, spaced 1.75 in. apart) cut into the nozzle edge near the flap. Some observed farfield noise spectra and the far-field directivity are shown in Figures 76 to 78. From these figures one may deduce, for example, that in the 143° direction (where there occurs a general directivity peak), noise due to the slit jet predominates, whereas in the 82° direction, low-frequency noise from the flaps and augmenter exhaust predominates.

The best available prediction method [86] gives a somewhat different dependence of noise on velocity than that observed for the previously discussed configuration [85]. This prediction method results in levels that are too high (by no more than 10 dB), and thus conservatively overestimates the aeroacoustic environment for design purposes.

167
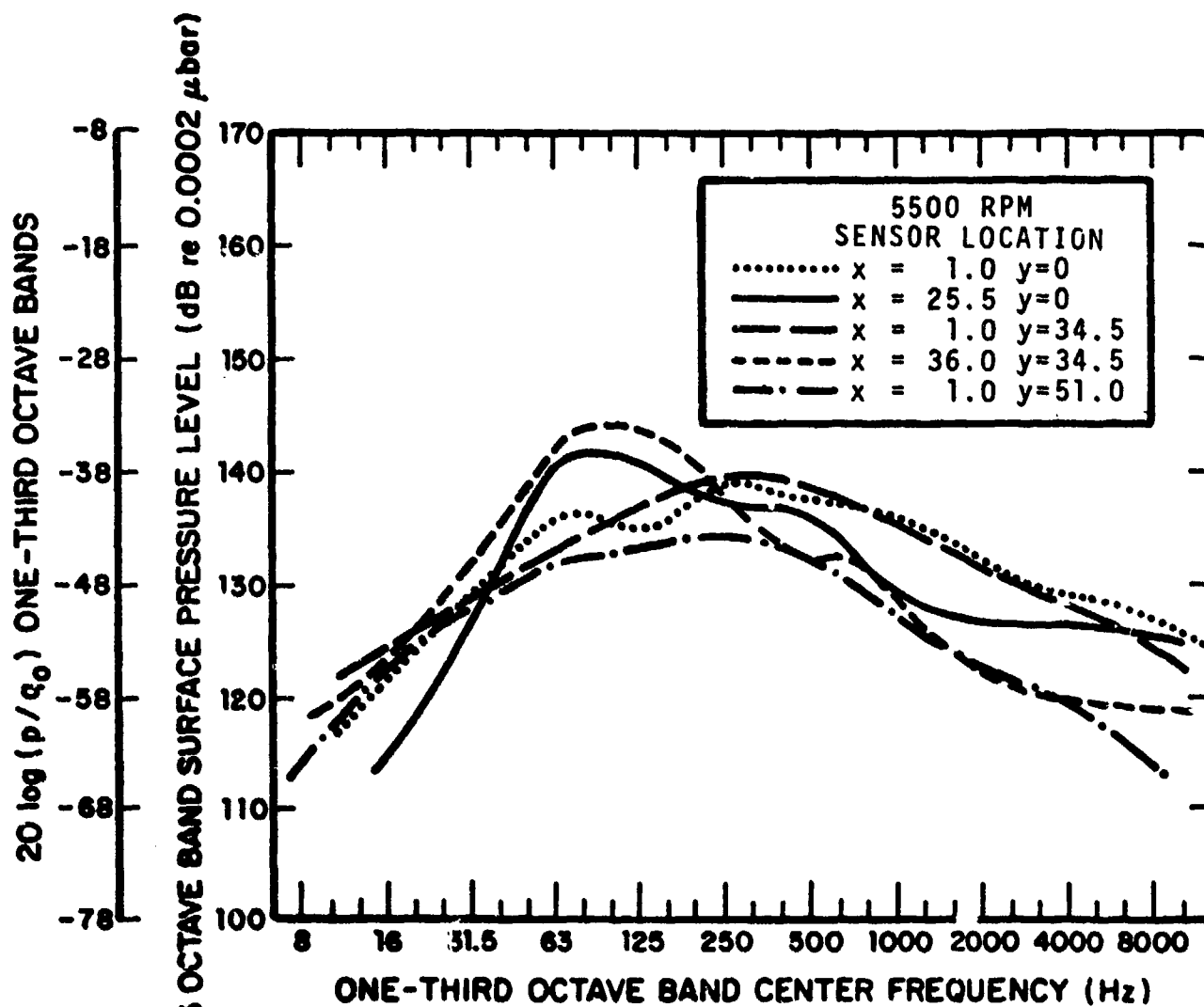
FIG. 72. SURFACE PRESSURES MEASURED IN STATIC
TEST OF FULL-SCALE USB MODEL. [93].
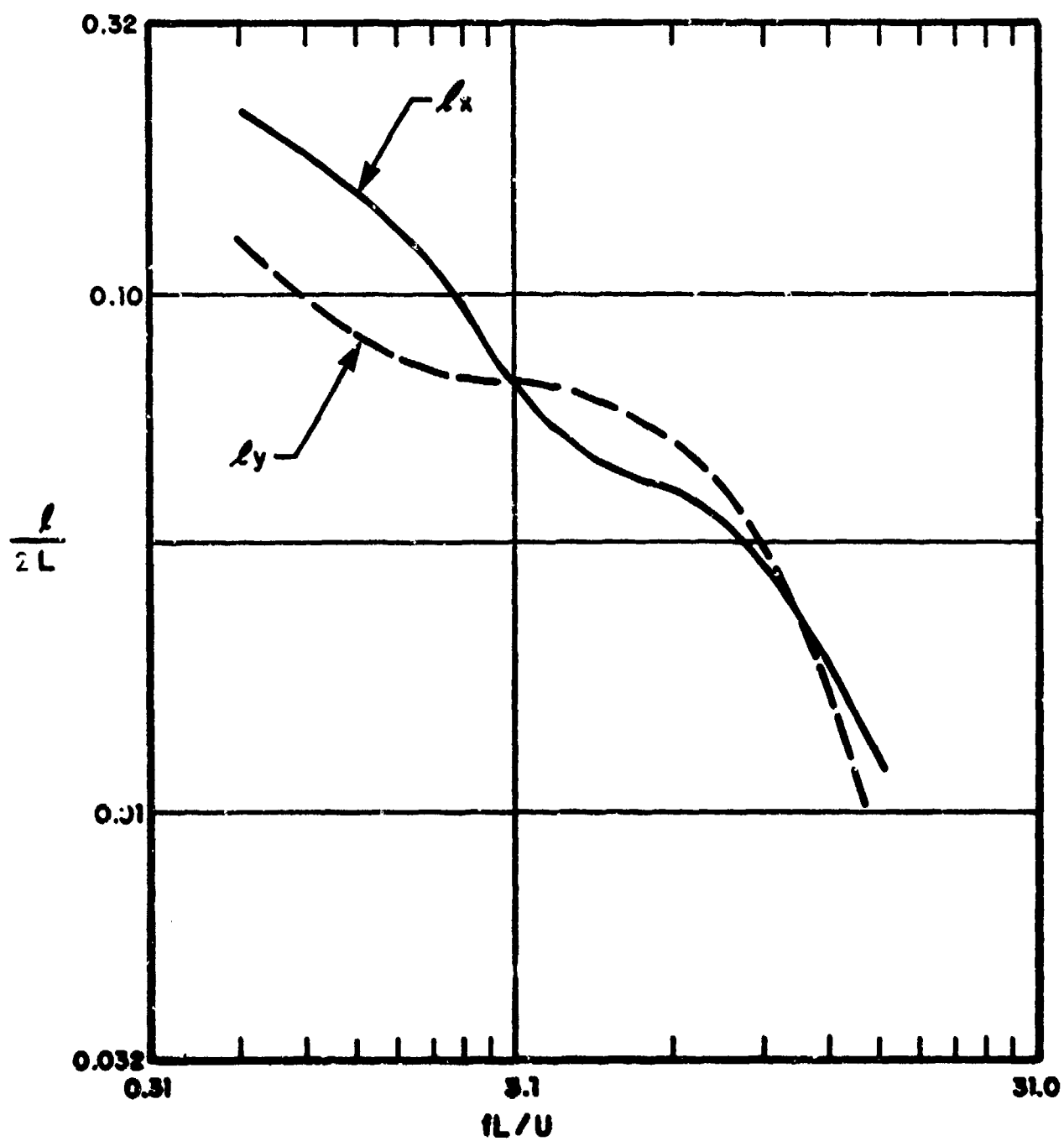
FIG. 73. USB LENGTH SCALES ON FLAP [93].

169
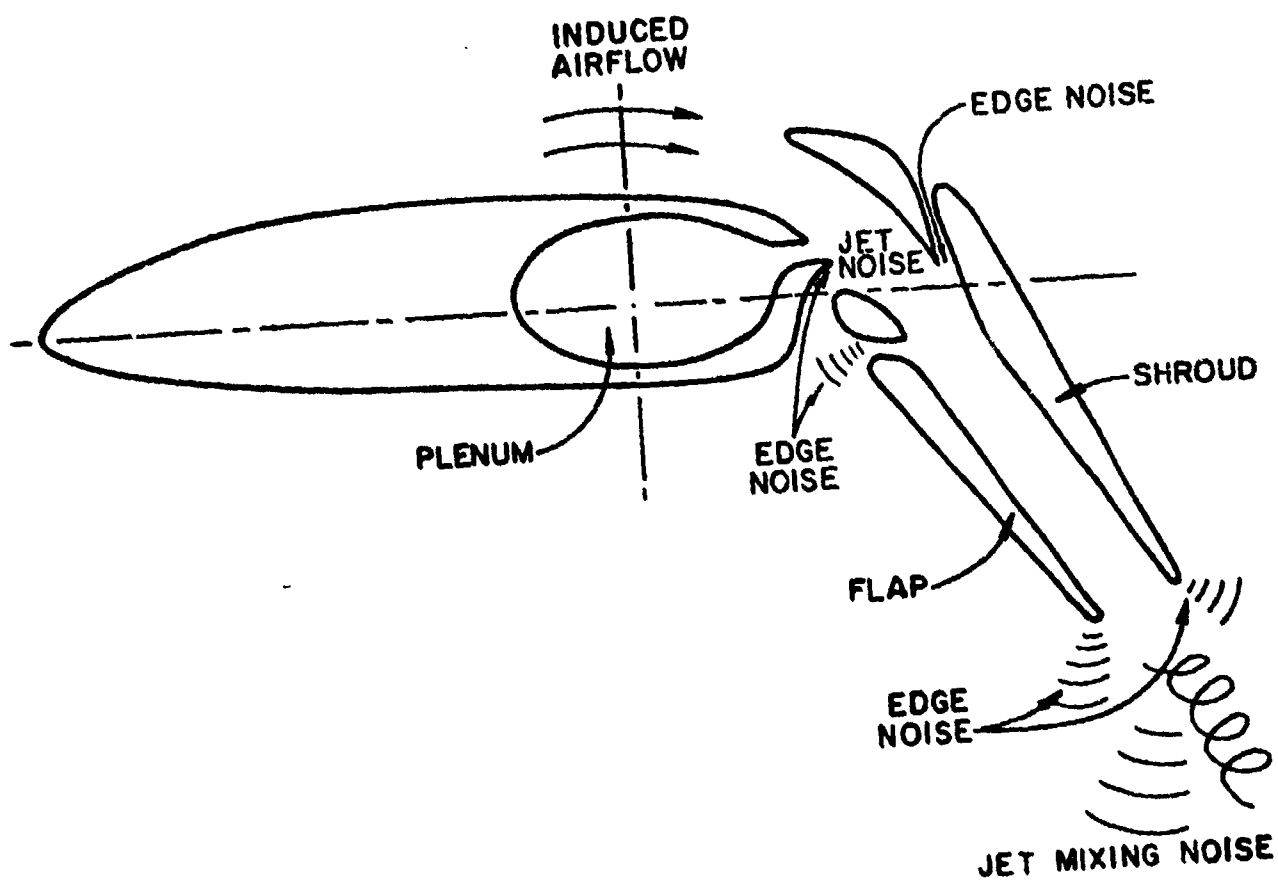
FIG. 74. SCHEMATIC SECTION OF AUGMENTER WING AND
ITS NOISE SOURCES [84].

FIG. 75. SHROUD CROSS-SECTION OF ADVANCED DESIGN AUGMENTOR WING [85]. Circled numbers identify surface pressure transducers.
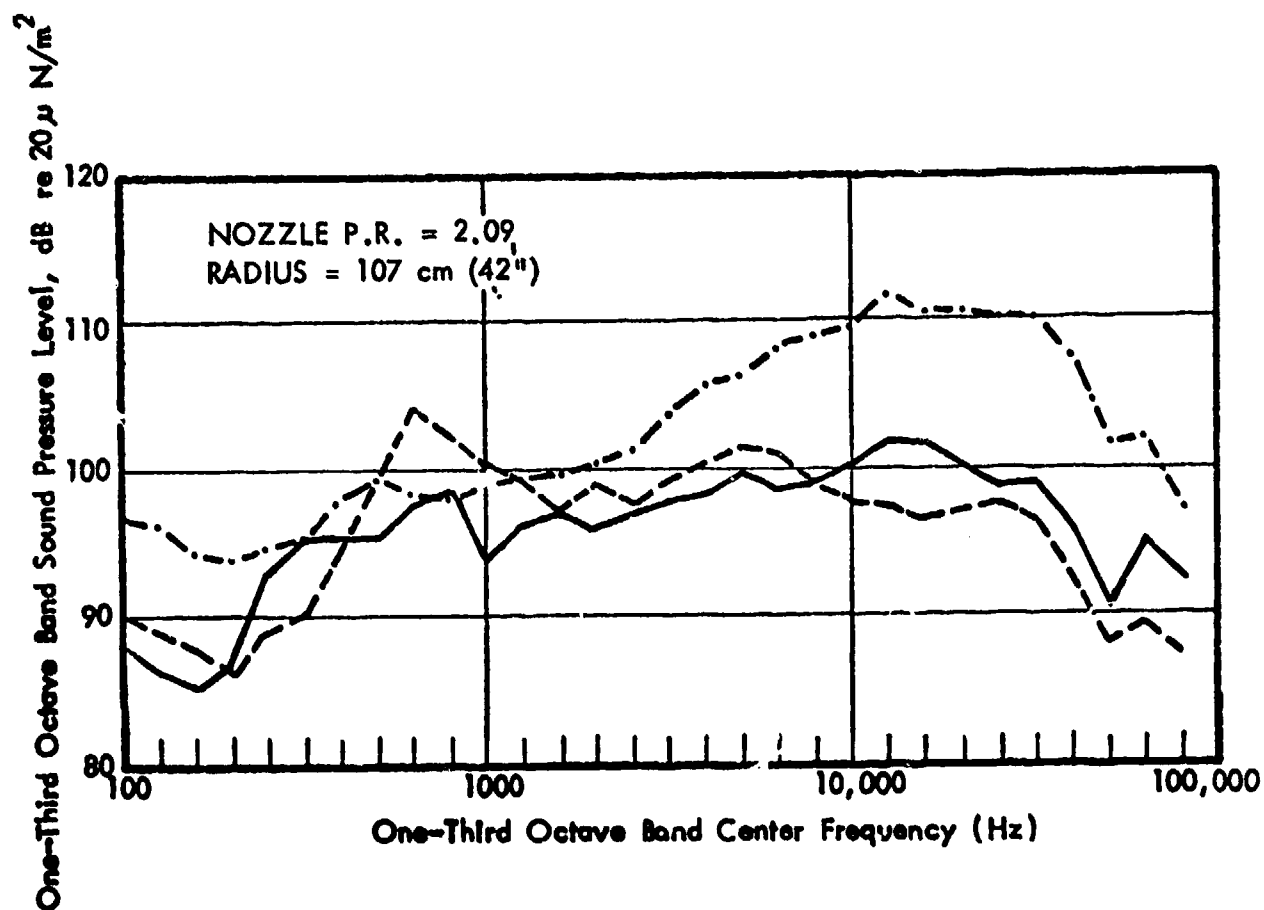
FIG. 76. ACOUSTIC FAR FIELD SPECTRA FOR AUGMENTER WING
OF FIGURE 75 AT 0 FORWARD SPEED [85].

172
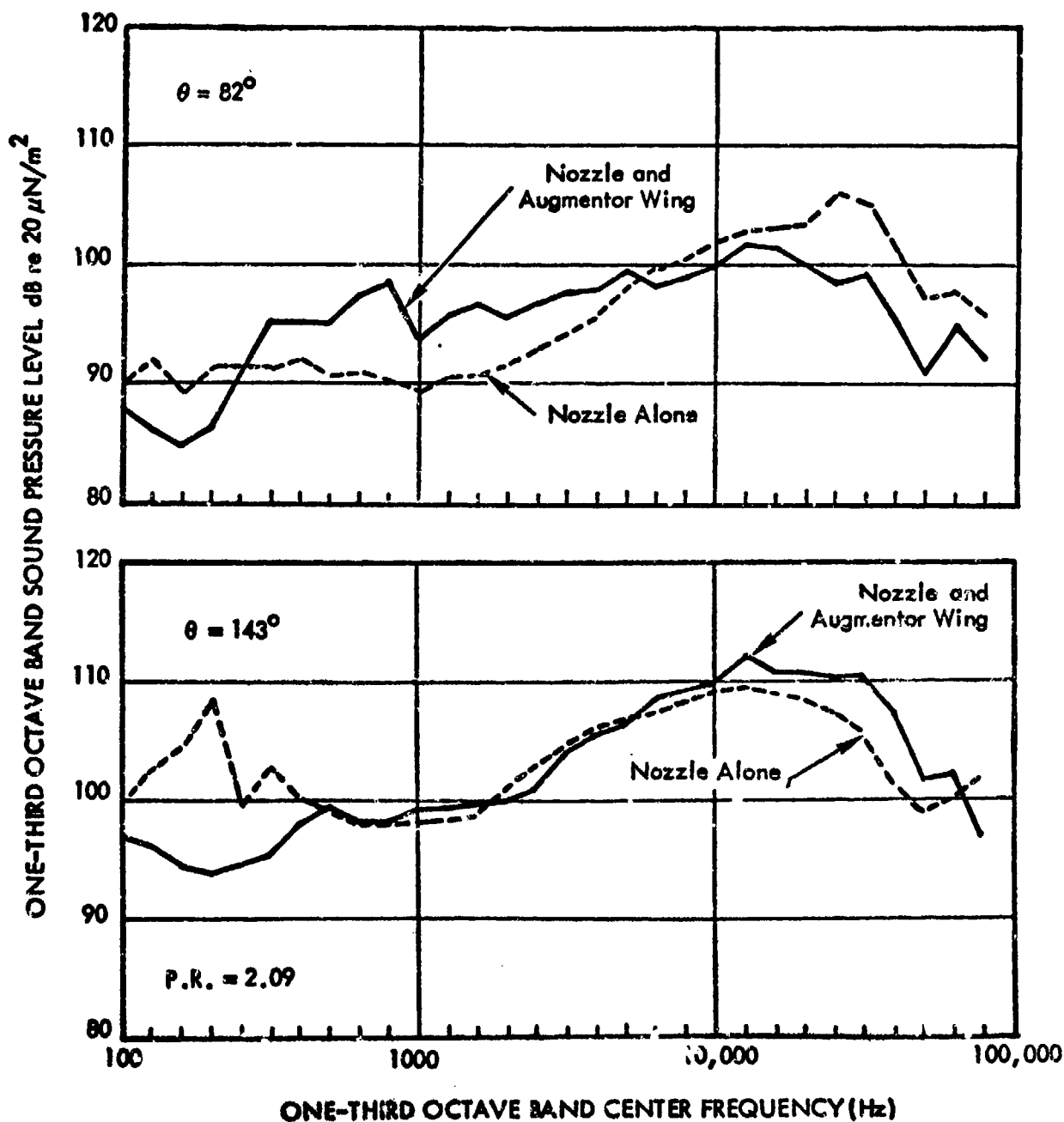
FIG. 77. FAR FIELD ACOUSTIC SPECTRA FOR MODEL NOZZLE WITH AND WITHOUT AUGMENTOR WING [85].

173

FIG. 78. POLAR PLOT OF ACOUSTIC FAR FIELD OF
AUGMENTER WING OF FIGURE 75 [85].

174
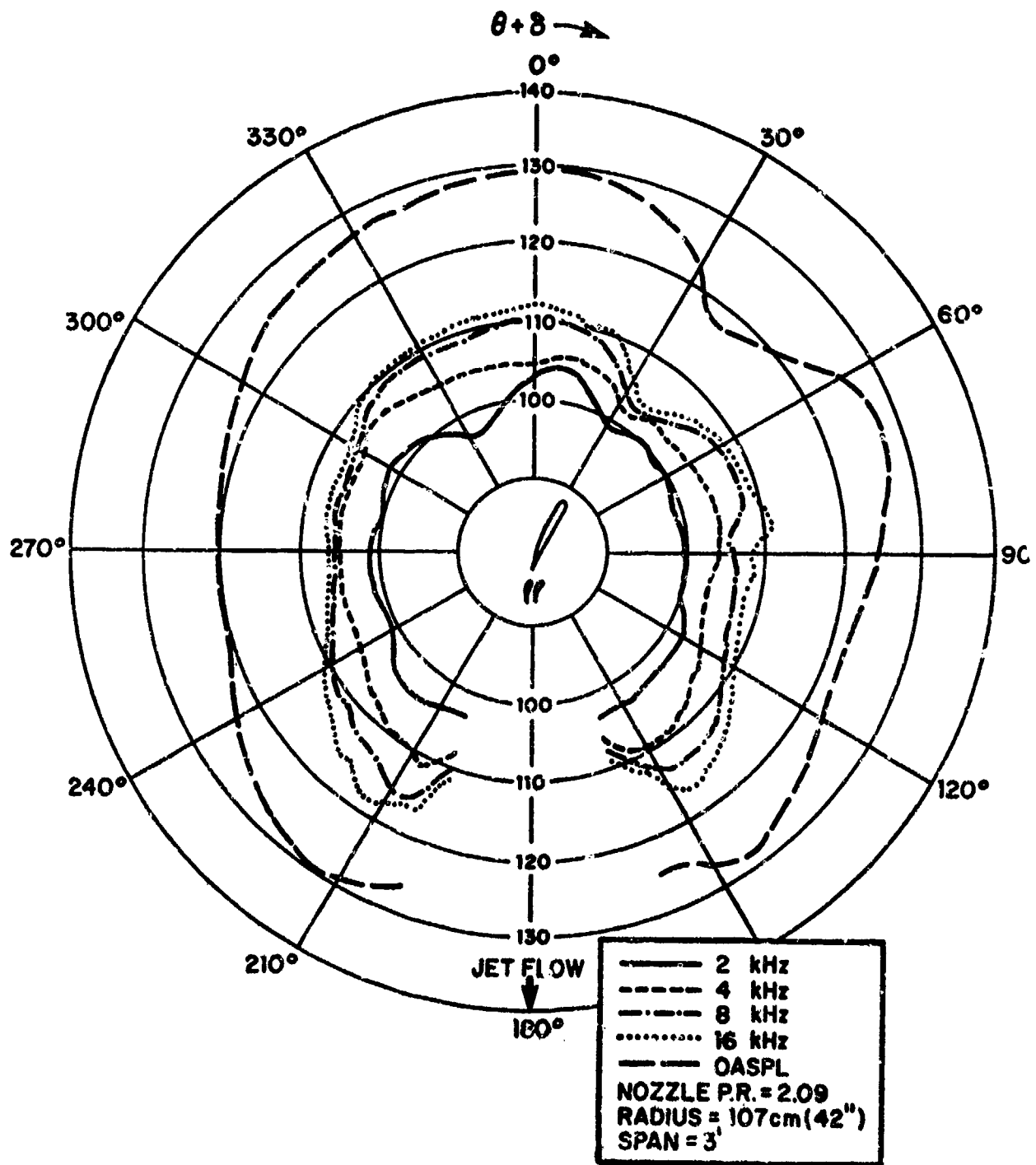
Surface Pressures

The only data on unsteady aerodynamic pressures on the flap and shroud that are available to date are those of [85]. Some of this data is reproduced here in Figures 79 to 81. In absence of better information, this data, normalized with respect to the dynamic pressure of the jet, may be used for predictive estimates.

Data on correlation lengths is extremely limited; what there exists exhibits such unusual behavior that the data's validity is questionable [85].   Thus, only very gross estimates can be made.

3.4.2 Jet flap (JF)

The jet flap, of which a schematic sketch appears in Figure 82, has been studied much less extensively from the noise standpoint than have the three other powered lift concepts. The most definitive available study, which was published in 1959 [87], provided evidence that two sources of noise are important: (1) jet noise from the slot nozzle, radiating into the hemisphere above the wing only, and (2) sources associated with the flap (now known to be "trailing edge noise").

One may therefore synthesize an estimation approach by accounting separately for jet noise and for flap noise, treating the latter in terms of a two-dimensional wall-jet [88].

No data is available on surface pressures. For first order estimates, similar augmenter wing data [85] and related wall jet data [89] should be useful.
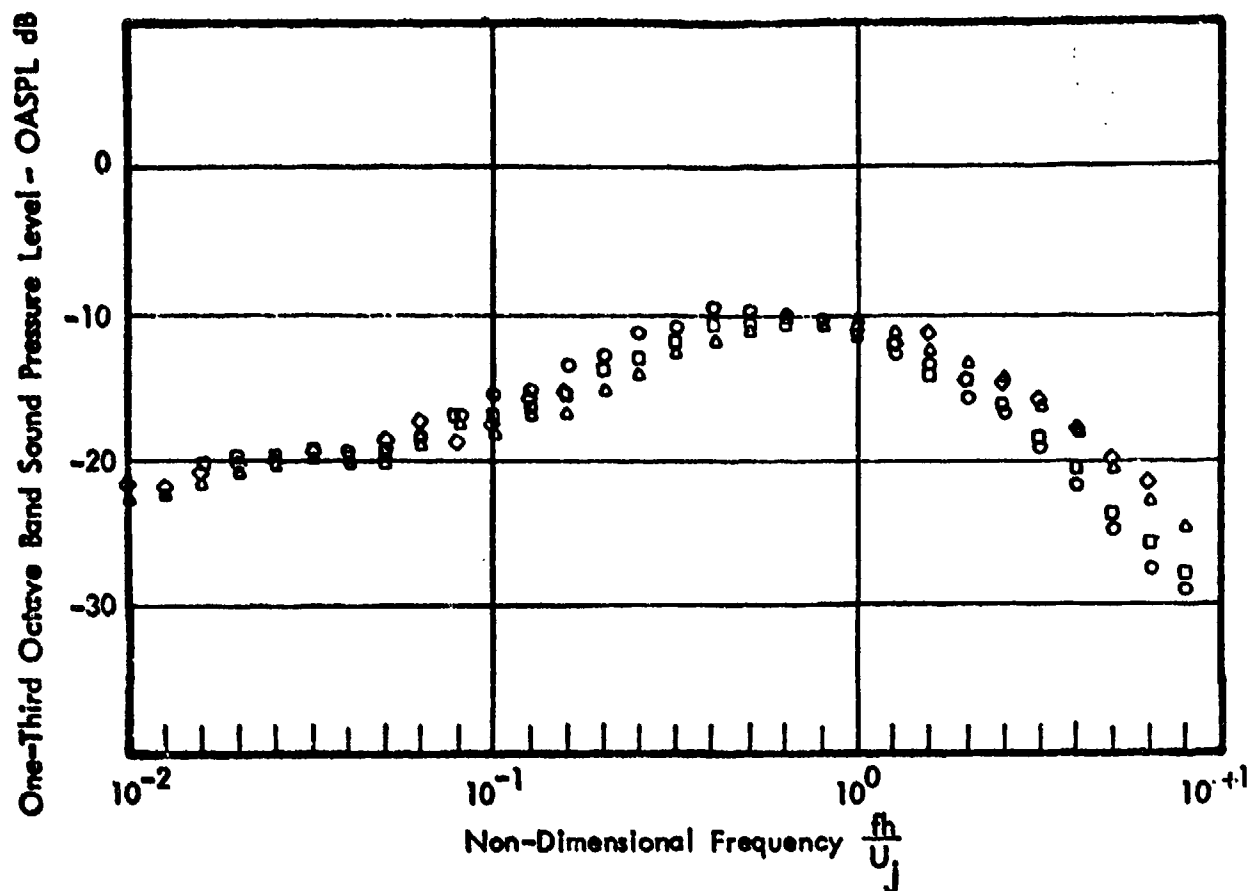
FIG. 79.   NON-DIMENSIONAL SURFACE PRESSURE SPECTRA AT
LOCATION 11 ON FLAP. FOR FOUR NOZZLE PRESSURE
RATIOS BETWEEN 1.27 AND 2.09.   SEE FIGURE 75
[85].
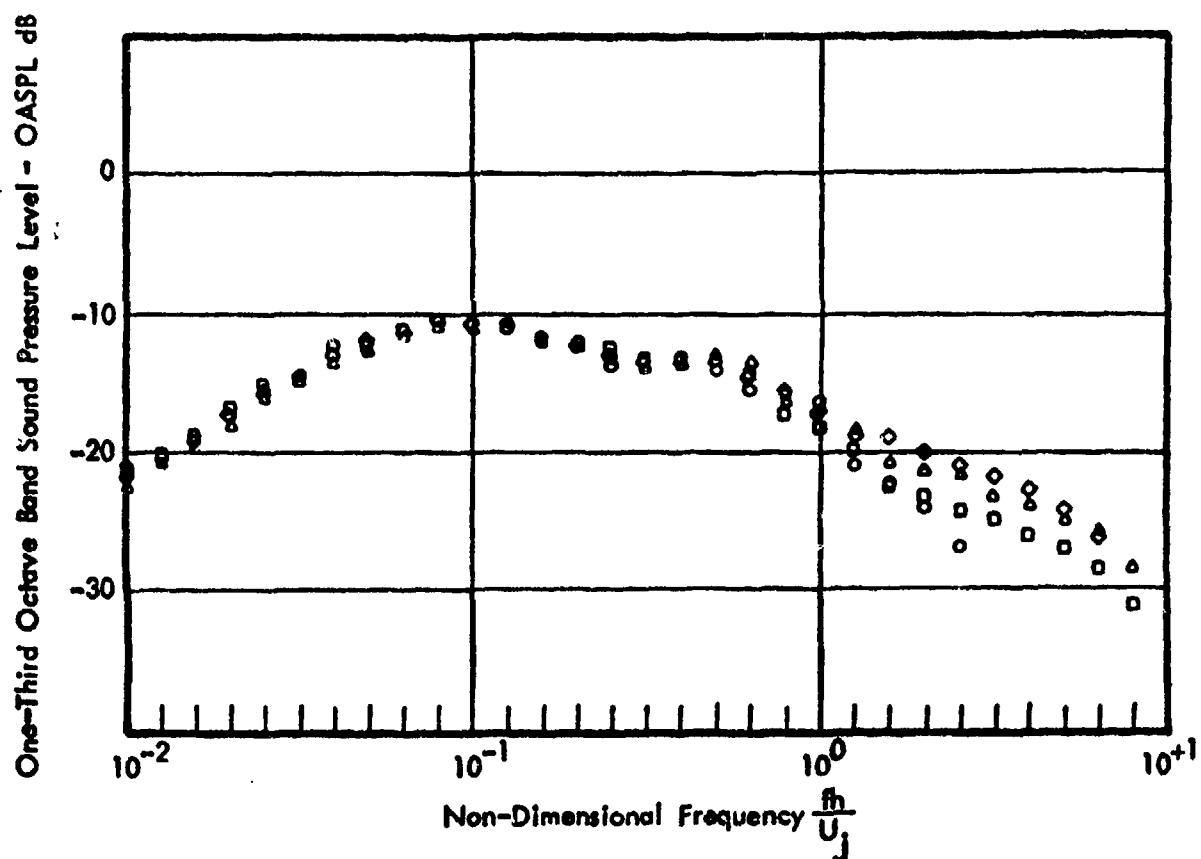
FIG. 80. NON-DIMENSIONAL SURFACE PRESSURE SPECTRA
AT LOCATION 40 ON SHROUD FOR FOUR NOZZLE
PRESSURE RATIOS BETWEEN 1.27 AND 2.09 [85].
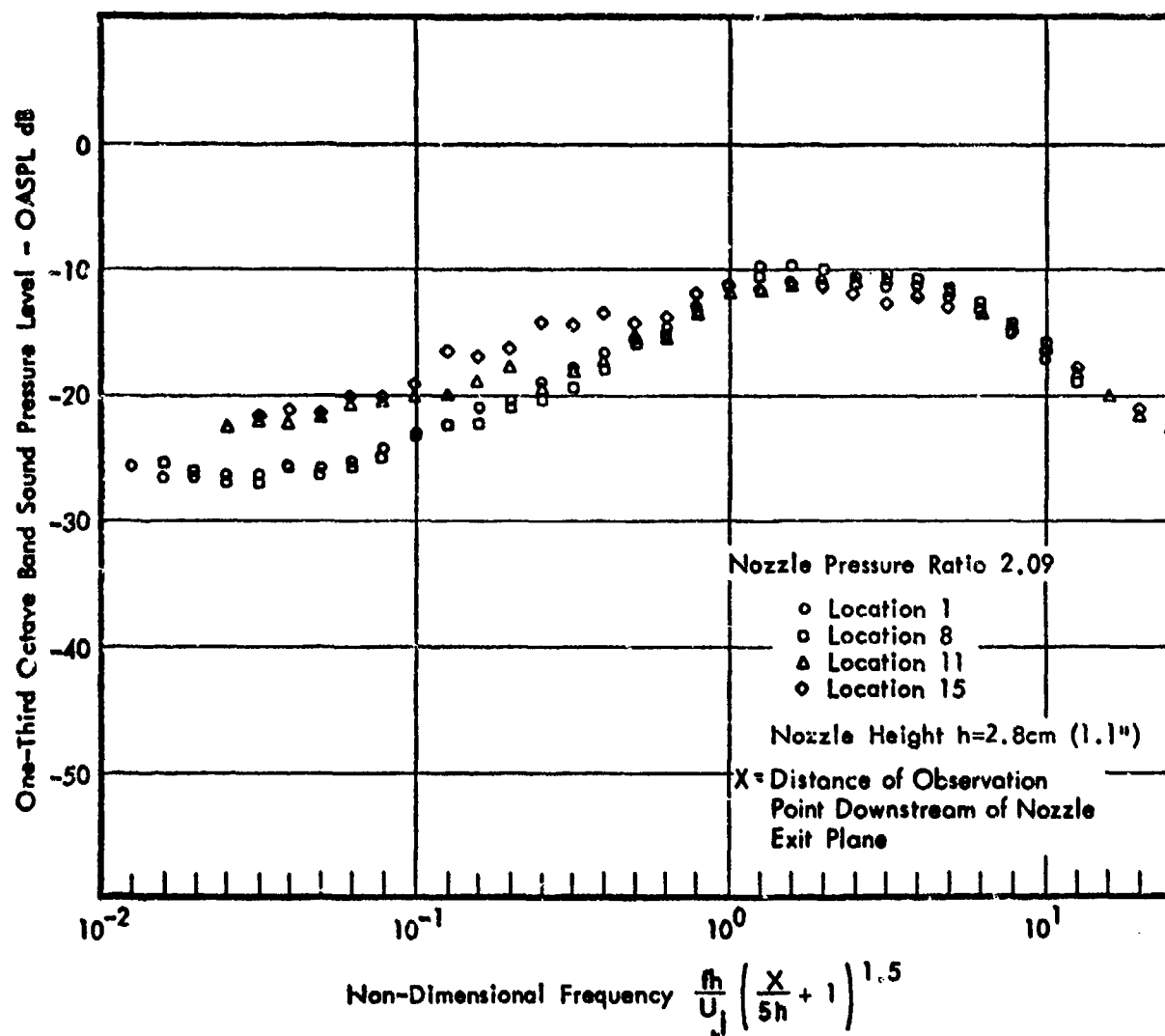
FIG. 81. NON-DIMENSIONAL PRESSURE SPECTRA AT DIFFERENT
CHORDWISE LOCATIONS ON SURFACE OF FLAP
SEE FIGURE 75 [85].
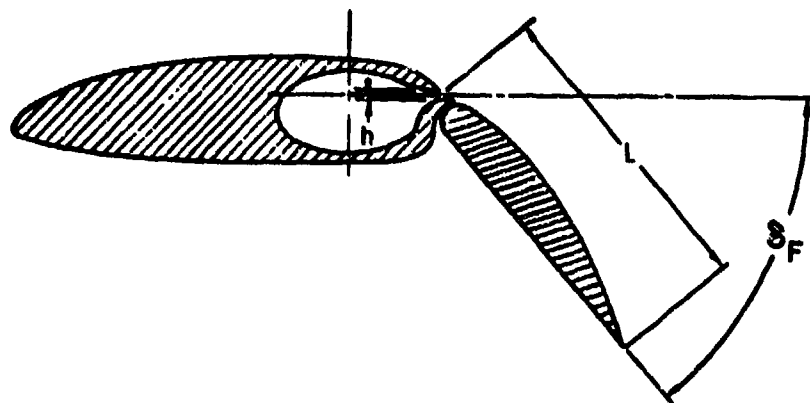
FIG. 82. SCHEMATIC SECTION OF JET FLAP.

3.5 Forward Speed Effects

Because of the complex, multi-component nature of the
noise of propulsive lift devices, the evaluation of the
effects of freestream velocity (aircraft motion) on propulsive
lift noise are extremely difficult to predict analytically.
However, generalized empirical relations have been derived
[86] on the basis of studies performed by several investigators.

These empirical relations give the change Δ dB in the
sound pressure level due to forward motion at speed V_a as

$$\Delta \text{ dB} = \begin{cases} 10 \log \left| 1 - \dfrac{V_a}{V_j} \right|^K & \text{for EBF, USB, AW} \\[4mm] 10 \log \left[1 - \dfrac{V_a \cos\delta}{V_j} \right]^K & \text{for JF} \end{cases} \tag{62}$$

where V_j denotes the jet exhaust velocity and δ the flap
angle (see Figure 82). The exponent K is a function of the
powered lift configuration and observation position, as
given in Table 7.

TABLE 7. RELATIVE AIRSPEED EXPONENTS K AT 90° AZIMUTH [86].

Configuration	Flyover Plane	30° Sideline Plane	0° Sideline Plane
EBF, Take-off Flaps			
Triple-Slotted Flap	4.0	1.8	-0.8
Double-Slotted Flap	5.05	3.0	0.25
Single-Slotted Flap	6.1	4.2	1.3
USB	1.8	0.8	0
AW (Hardware with Slot Nozzle)			
Take-off Flaps	1.8	1.0	0
Landing Flaps	-1.8	-1.0	0
IBF	5.0	5.0	5.0

3.6 List of Symbols for Section III*

Symbol	Definition	Units[†]
A_c	area of core exit nozzle	ft^2 (m^2)
A_{co}	correlation area	ft^2 (m^2)
A_f	area of bypass nozzle annulus	ft^2 (m^2)
BPR	bypass ratio	
D_o	effective nozzle diameter	ft (m)
F^2	mean-square fluctuating force	lb^2 (N^2)
$I(\omega)$	acoustic intensity	lb/ft sec (N/ms)
OASPL	overall sound pressure level	dB
S	Strouhal number	
SPL	sound pressure level	dB
S_a	surface area	ft^2 (m^2)
U_e	effective velocity of jet	ft/sec (m/s)
V_a	speed of aircraft	ft/sec (m/s)
V_c	core exit velocity	ft/sec (m/s)
V_f	fan annulus exit velocity	ft/sec (m/s)
W	wetted span	ft (m)

*Specially defined symbols, such as those for empirically deter-
mined constants, which are used only once in the text, are not
included here. Such symbols are defined in the text where they
occur.

[†]The units given here are typical. SI units are given in paren-
theses where appropriate. Note that some empirical prediction
methods require the use of specific units.

Symbol	Definition	Units
c	speed of sound in ambient air	ft/sec (m/s)
ℓ	correlation length	ft (m)
ℓy	spanwise eddy scale	ft (m)
n	number of sources	
r	source-to-observer distance	ft (m)
w	width of line source	ft (m)
x	axial distance	ft (m)
δ_F	flap angle	deg
θ	angle (see Eq. 56, Figs. 45,47)	deg
ρ	density of ambient air	slug/ft^3 (kg/m^3)
ρ_c	mean density of jet	slug/ft^3 (kg/m^3)
$\phi_F(\omega)$	aerodynamic force spectrum	lb^2/ft^2 (N^2/m^2)
ψ	angle (see Figs. 45,50)	deg
ω	radian frequency	sec^{-1} (s^{-1})

SECTION IV

PROPELLER NOISE

4.1 Introduction

In propeller-driven aircraft, the propellers frequently
constitute the dominant sources of farfield and nearfield
noise. Propeller noise typically is considered in terms of
two categories: (1) rotational noise includes all tonal
(single-frequency) components at integer multiples of the blade
passage frequency, and (2) broadband or vortex noise includes
all of the non-tonal noises.

4.2. Noise Generation Mechanisms

4.2.1 Rotational Noise

Rotational noise, which usually dominates the overall sound
pressure level and is most pronounced at low frequencies, is
due to: (1) rotation of the steady forces acting on the pro-
peller blade, as the blade generates thrust and torque and as
the blade displaces air by virtue of its thickness, and (2) the
unsteady thrust and torque (or "harmonic loading") acting on
the blades as the result of spatial variation of the inflow to
the propeller disk. The steady force sources of rotational
noise have received the most attention to date. The noise due
to harmonic loading has been studied less intensively, and gen-
erally not enough is known about the inflow nonuniformities that
cause this type of noise.

4.2.2 Broadband Noise

Broadband noise is principally caused by (1) dipole radia-
tion due to the turbulent boundary layer flowing off the blade
trailing edge and (2) turbulence in the inflow to the blade

leading edge. The latter is negligible in standard tractor propeller installations.

4.3 Extent of the Nearfield

The *geometric nearfield* of a propeller is the region in which the propeller disk can not be approximated as a point source. The *acoustic nearfield* is the region in which the "inverse-square" spherical spreading law does not hold for the variation of the pressure with distance from a source. As a consequence of the large size of aircraft propellers and of the low frequencies at which they generate noise, the nearfield of aircraft propellers generally is quite large.

4.3.1 Rotational Noise

Figure 83 illustrates the difference between sound pressure levels calculated on the basis of a farfield approximation and those obtained by considering the acoustic and geometric nearfields, for a particular propeller. One may observe that here the nearfield is significant at distances that are less than 1.75 diameters from the center of the propeller disk. For typical propeller aircraft configurations, the fuselage, nacelle, and part of the wing are likely to be exposed to the nearfield.

4.3.2 Broadband Noise

None of the available literature appears to treat the subject of the nearfield region for broadband noise. Because the broadband noise is significant principally at middle and high frequencies, the importance of its nearfield is confined to locations that are considerably closer to the propeller disk than those where rotational nearfield becomes significant.
Because of the non-coherent nature of broadband noise, there
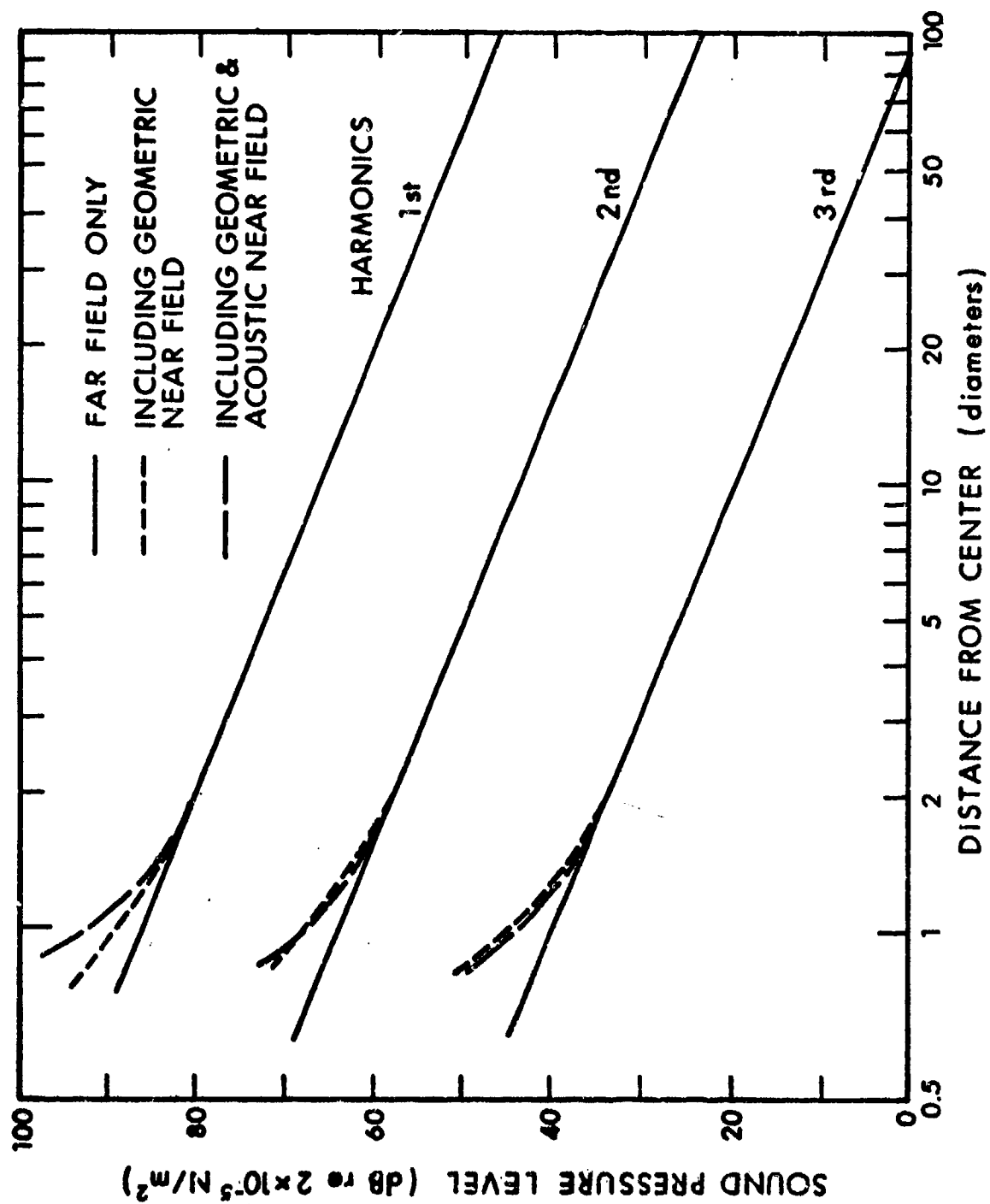
FIG. 83. NEAR-FIELD EFFECTS AT 10 DEGREES BEHIND PROPELLER PLANE [99].

186

are no distance-related or angle-related interference patterns
to distinguish a nearfield. However, one expects a geometric
nearfield effect, because of the location of the sound sources
within the propeller disk.

4.4   Rotational Noise Analysis

Since forces that cause rotational noise are distributed
over the surface of the propeller blades, calculation of the
sound generated by the propeller requires integration of the
effects of these forces over the entire propeller disk, both
in the radial and the circumferential directions. At observa-
tion points located at large distances from the propeller, the
distances to all points in the propeller disk may be considered
as equal. Then the farfield circumferential integral may be
simplified to yield the Bessel function directivity derived by
Gutin [100], eliminating the requirement to recompute this
integral in each case. A further approximation to the farfield,
which has been used by Gutin and by Garrick and Watkins [101],
among others, makes use of the "effective ring" concept, in
which all propeller forces are assumed to lie in a ring at a
single radius - usually taken as 0.8 times the propeller radius.
This approximation eliminates the radial integration.

In the nearfield, the assumptions governing the approxima-
tion leading to elimination of the circumferential integral cer-
tainly do not hold; path lengths and angles to a listening point
from different points on the propeller disk may vary by large
percentages. However, the effective radius approximation is
workable for the nearfield. Thus, the calculation of the near-
field noise of a propeller in each case requires at least evalu-
ation of the circumferential integral over the disk.

4.5 Prediction Methods

4.5.1 Rotational Noise

The nearfield noise prediction technique of Kerwin and Franken [34] was developed by combining the Gutin noise model [100] with the static propeller noise measurements of Hubbard [102]. This recommended prediction method, which is applicable at distances of one propeller diameter or less from the edge of the propeller disk, is accurate only for positions outside the axial projection of the propeller disk.

The most recently developed prediction method [105] is not recommended, because its results differ drastically from those of earlier ones; in effect, this method is based on the assumption that the noise due to torque is negligible.

At distances greater than one propeller diameter from the disk, the farfield prediction method from Reference [103] is recommended.

4.5.2 Broadband Noise

The most useful prediction method here is that of Reference [104] this method is a theoretical/empirical hybrid and differs from earlier ones in that it predicts finite levels at points in the plane of the propeller, where the earlier methods predict a null, at variance with test data. This difference is obviously of great significance for predicting noise on the fuselage sides adjacent to the propellers. This prediction method is valid for the farfield, and tends to result in some underestimation at the pressures very near the propeller in the propeller plane, and in overestimation of pressures near the propeller axis at distances that are within about 0.7 of the

propeller radius from the edge of the propeller disk.

4.5.3 Reflective Surfaces

The effect of flat and cylindrical reflective surfaces on
the nearfield pressures has been studied by Hubbard [102] and
used in the nearfield prediction technique of [103]

4.5.4 Spectral Coherence and Correlation

Past work on propeller noise prediction has generally over-
looked the subject of spectral coherence and correlation
patterns. The generation mechanisms for propeller rotational
noise, however, allow for making some simple observations,
which are summarized below.

The rotational noise from the thrust, torque, and thickness
effects has a phase pattern which is fixed relative to the pro-
peller blades and rotates with them. The phase speeds in the
radial and axial directions are sonic, but a doppler correction
must be applied to the wave length and to the phase speed as
measured along the aircraft longitudinal axis.

The acoustic field of harmonic loading noise differs from
that from thrust, torque, and thickness, because its pattern
consists of standing waves that are determined by the inflow
distribution. Otherwise, all of the wavelengths and phase
speeds are the same as for the rotating sound field.

SECTION V

SURFACE FLOWS

5.1 Pressure Fluctuations In Turbulent Boundary Layers

5.1.1 Introduction

Boundary layers develop as a consequence of the effect of viscosity. These boundary layers become turbulent where the Reynolds number, based on the distance from the point of streamline attachment, becomes sufficiently large. This critical Reynolds number depends on the local pressure gradient; for zero pressure gradient it typically is of the order of 5×10^6, but it can be smaller or greater by a factor of about 100 for non-zero gradients.

The structure of a turbulent boundary layer is affected not only by the basic fluid properties (e.g., viscosity, density) and the Reynolds number and Mach number, but also by the surface roughness, the pressure gradient, and the velocity field outside of the boundary layer. For prediction of the surface pressure fluctuations associated with a given boundary layer, one needs to know certain of its local properties, particularly the appropriate thickness. Unfortunately, these properties are difficult to predict, because they depend on the upstream history of the boundary layer.

Current prediction methods are based largely on experimental data obtained on a limited number of configurations, and for a limited range of parameters. Thus, the available empirical data often may not correspond well to the case for which a prediction is desired.

5.1.2 Boundary Layer Thickness Parameters

Two different thickness parameters are used to nondimensionalize boundary layer data: the boundary layer thickness δ and the boundary layer displacement thickness δ^*.

The boundary layer thickness is defined as the distance, measured from the surface, at which the flow velocity reaches 99% of its local free-stream value.

The boundary layer displacement thickness is defined by

$$\delta^* = \int_0^\infty \left[1 - \frac{\rho(y)u(y)}{\rho U} \right] dy \tag{63}$$

and represents the distance for which $\rho U \delta^*$ equals the mass flow deficit produced by the presence of the boundary layer (as compared to the mass flow based on the free stream velocity). Here U denotes the free-stream velocity, ρ the fluid density in the free stream, and $u(y)$ and $\rho(y)$ denote the corresponding properties in the boundary layer, at distance y from the solid bounding surfaces. Clearly, δ^* depends on the velocity and density profiles in the boundary layer. For an incompressible turbulent boundary layer on a flat plate, $\delta \approx 8\delta^*$.

5.1.3 RMS Pressure Fluctuations

Data indicating the overall level of pressure fluctuations beneath developed turbulent boundary layers is available for several configurations (tunnel models, flight tests; flat plates, cones, aerodynamic surfaces) and for a broad range of Mach numbers. As indicated in Figure 84, the data falls within a fairly narrow band, if it is nondimensionalized with respect to the local free-stream dynamic pressure q. Several investigators
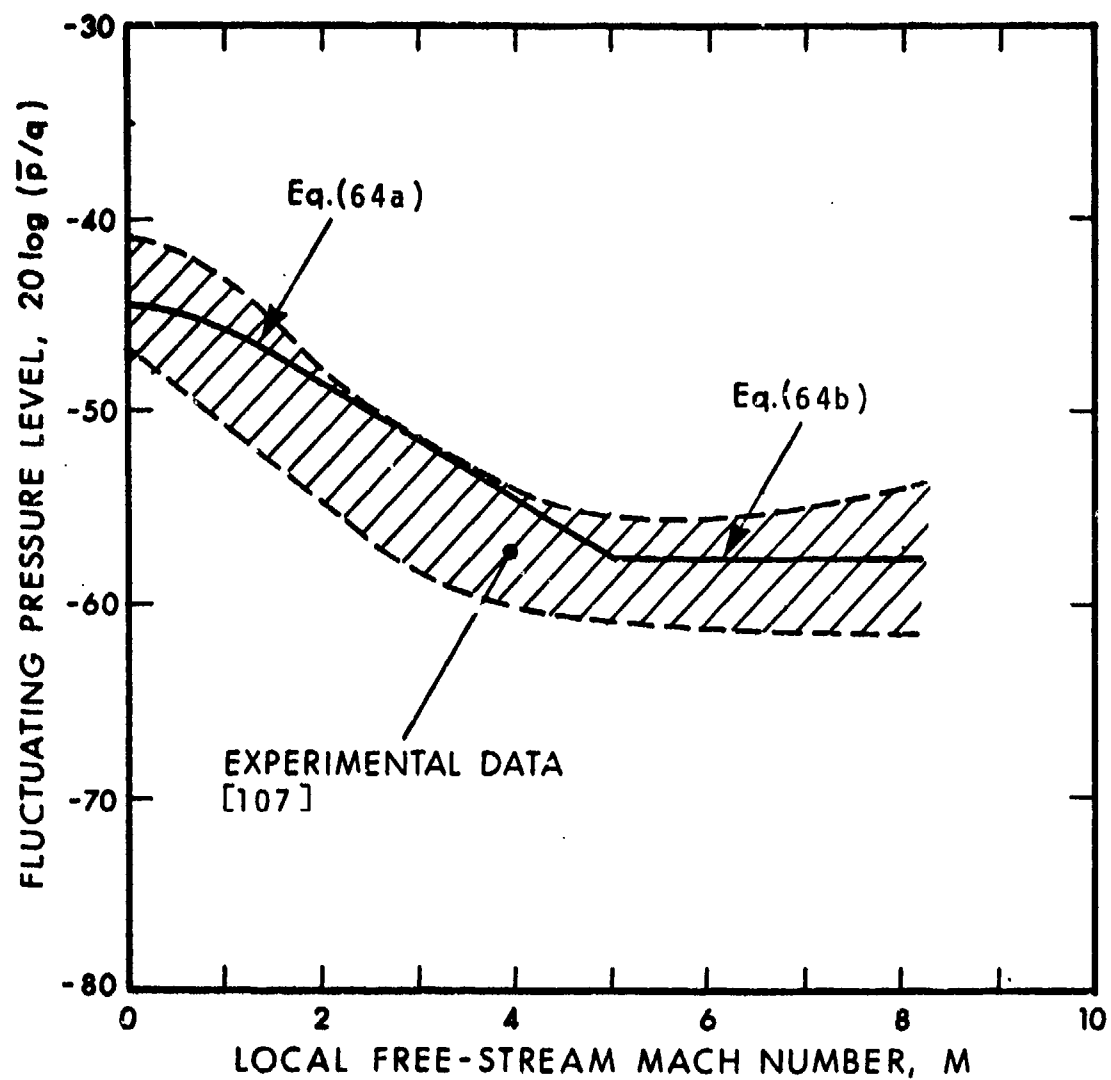
FIG. 84.   RMS PRESSURE FLUCTUATIONS LEVEL FOR ATTACHED
TURBULENT BOUNDARY LAYER FLOWS.

192

have suggested semi-empirical curves or expressions to fit
the data. No single approach appears to have any definite
advantage over the others. The form suggested by Lowson
[107] for M < 5, and a constant for M > 5 is as good as any;
thus, the ratio of the root-mean-square fluctuating pressure
$\bar{p}$ to the dynamic pressure q may be taken to obey

$$\frac{\bar{p}}{q} = \begin{cases} \dfrac{0.006}{1+0.14M^2} & , \quad M < 5 \quad (64a) \\[2em] 0.00133 & , \quad M > 5 \quad (64b) \end{cases}$$

At low subsonic speeds, this expression reduces to $\bar{p}/q = 0.006$,
which falls near the middle of the data band in Figure 4.1.
Recent careful subsonic measurements with very small pressure
transducers have yielded values of $\bar{p}/q$ as high as 0.011,
suggesting that in many earlier measurements the high-frequency
energy has been filtered out, due to the finite transducer size
[108].

5.1.4 Power Spectral Density

Envelopes of normalized experimental data on the power
spectral density of boundary layer surface pressure fluctua-
tions are shown in Figure 85. Separate envelopes are present-
ed for subsonic and supersonic data, based on the summary of
experimental data given by Chaump, *et al* [106]. The subsonic
data corresponds to 0.1<M<0.8 and the envelope includes the ex-
tensive flat-plate data of Blake [109], which was not included
in [106]. The supersonic data corresponds to 1.4<M<3.45; the
slender-cone data for M = 4.0 and 8.0 [106] falls in the
middle of the envelope.
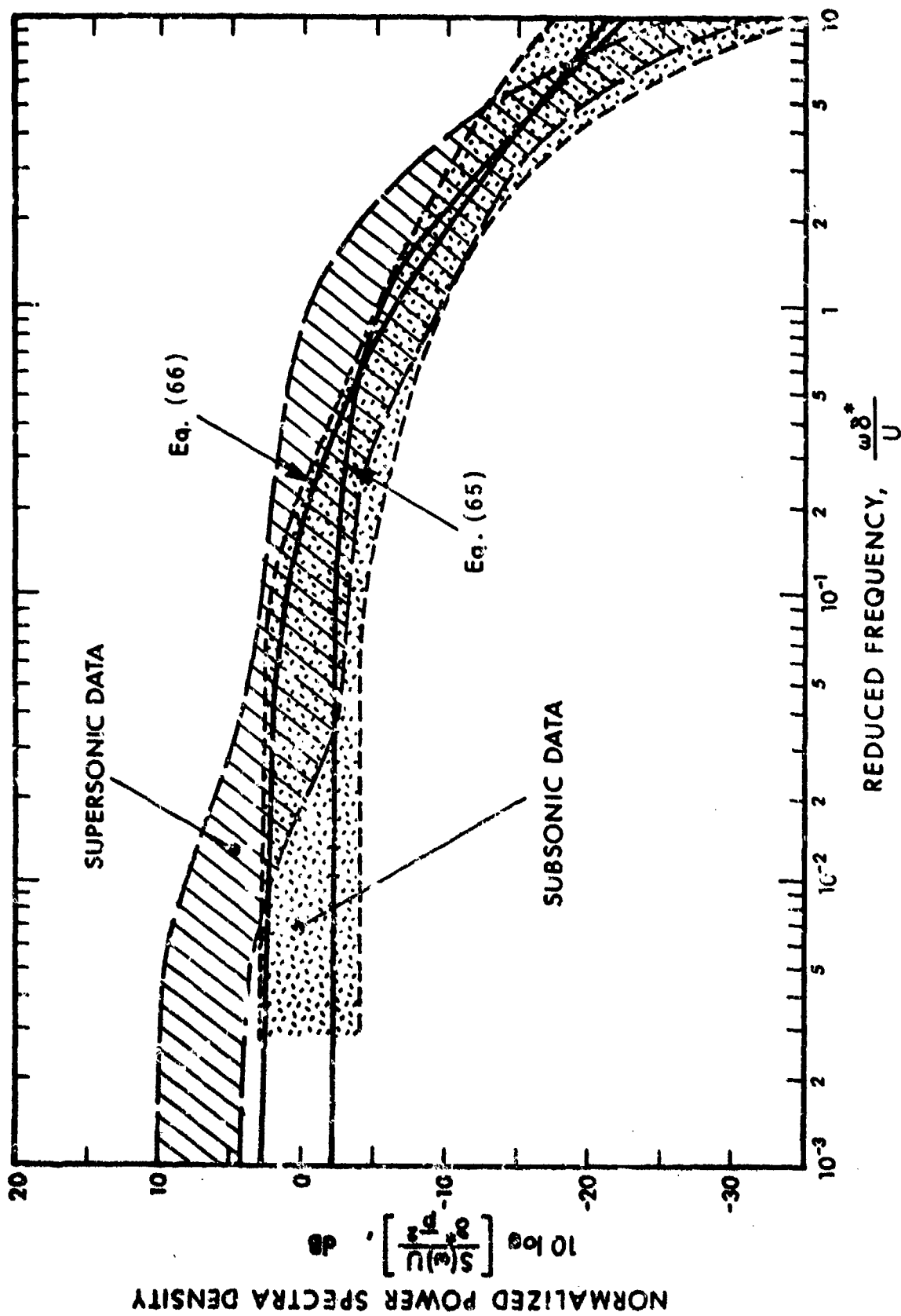
FIG. 85. NORMALIZED ONE-THIRD OCTAVE BAND POWER SPECTRAL DENSITY OF PRESSURE FLUCTUATIONS, ATTACHED TURBULENT BOUNDARY LAYER FLOW.

194

Both the subsonic and the supersonic data are presented here only in envelope form, because no systematic parametric trends are evident. For instance, there is no definite systematic relationship between Mach number and where the data lie within the envelope.

The simple semi-empirical relation of Houbolt [110],

$$\frac{S(\omega)U}{\bar{p}^2 \delta^*} = \frac{2/\pi}{1 + (\omega\delta^*/U)^2} \tag{65}$$

is plotted in Figure 85, as is the relation of Robertson [111],

$$\frac{S(\omega)U}{\bar{p}^2 \delta^*} = \frac{2}{\left[1 + (2\omega\delta^*/U)^{0.9}\right]^2} \tag{66}$$

which is based on supersonic data. The two equations may be seen to yield similar results at high frequencies and to agree reasonably well with the average of the high-frequency data. At very low frequencies, the second equation gives a value that exceeds that of the first equation by a factor of π, at low frequencies, equation (65) represents the average of the subsonic data reasonably well, but equation (66) agrees more closely with the supersonic data.

5.1.5 Convection Velocity

The convection velocity is a measure of the speed at which turbulent pressure disturbances move along with the boundary layer flow. The convection velocity depends on the frequency and spatial scale of the disturbance; low-frequency disturbances generally correspond to large scale, and high-frequency disturbances, to small scale. Large scale disturbances tend to

195

travel at nearly the free-stream speed, whereas small scale
disturbances (which occur primarily very near the wall) travel
more slowly, due to the velocity gradient in the boundary layer.

Convection velocity usually is evaluated from the time
delay indicated by the space-time correlation function ob-
tained from pressure measurements made by sensors located at
known distances apart. Figures 86 shows an envelope of broad-
band convection velocity data, as a function of streamwise
separation distance. The flattening of the curve at large
separation distances is due to smaller, slower eddies decaying
more rapidly and having no effect at sufficiently large separ-
ation distances. Figure 87 shows the variation of narrowband
convection velocity with frequency, for various separation
distances. (These figures are based on data by Chyu and Hanly
[112] and Bull [113], as cited in [106].)

The empirical formula given by Lowson [107], when modi-
fied by taking $\delta = 8\delta^*$, gives the narrow-band convection velo-
city U_c as

$$U_c/U = 0.75 + 0.3 \cdot \exp(-0.88\delta^*\omega/U) - 0.25 \cdot \exp(-0.15\xi/\delta^*) \quad (67)$$

corresponding to which the broadband convection velocity is
given by

$$U_{cb}/U = 0.8 - 0.25 \cdot \exp(-0.15\xi/\delta^*). \quad (68)$$

These formulas are plotted in Figures 86 and 87, together
with corresponding data. The agreements may be seen to be
reasonable in general.
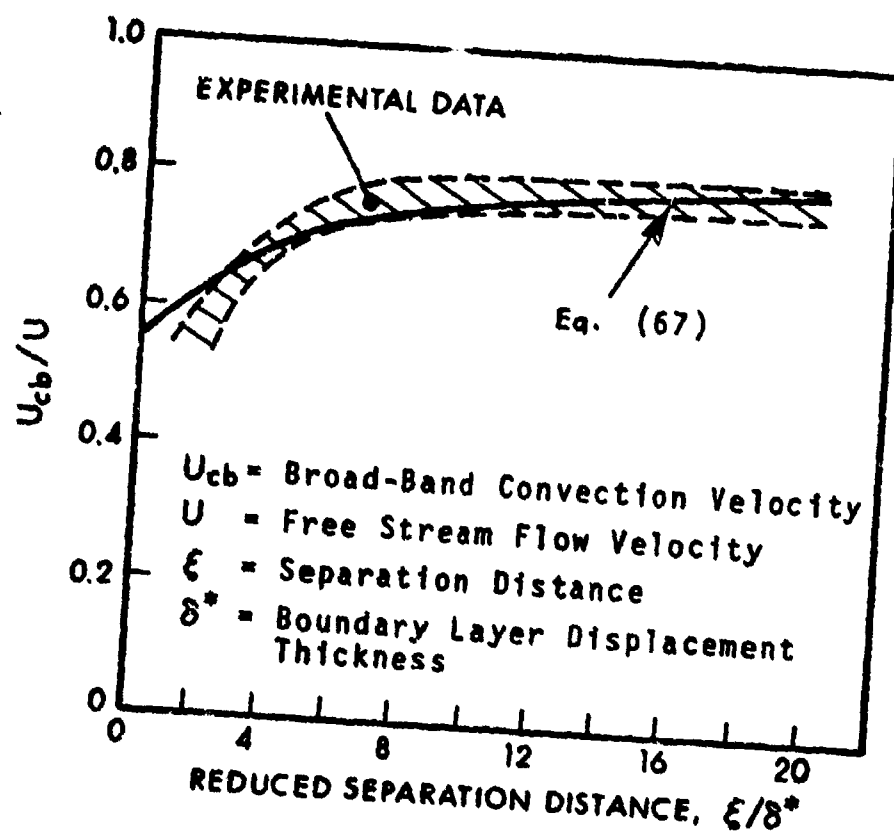
FIG. 86. VARIATION OF BROAD-BAND CONVECTION VELOCITY WITH STREAMWISE SEPARATION DISTANCE.

197
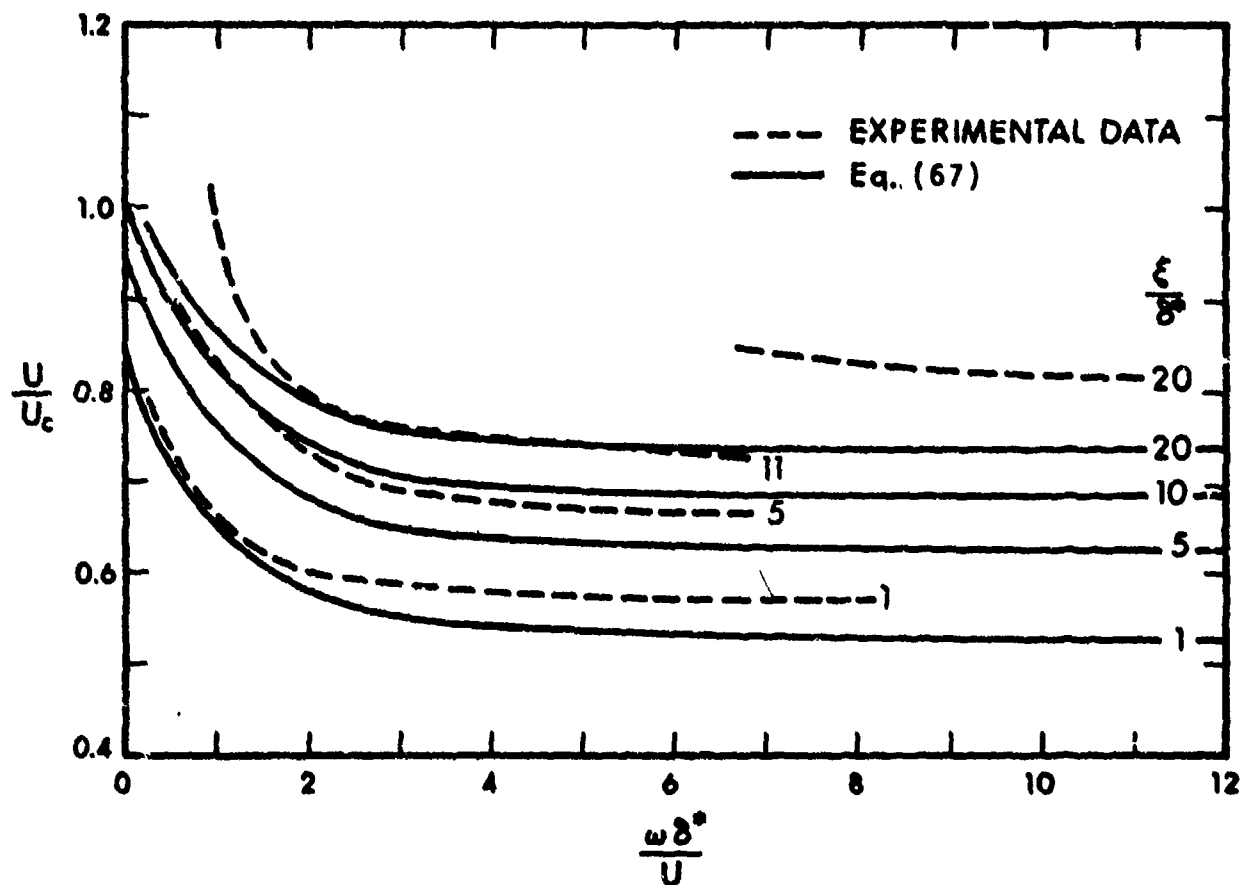
FIG. 87. VARIATION OF NARROWBAND CONVECTION VELOCITY WITH
FREQUENCY, FOR VARIOUS STREAMWISE SEPARATION
DISTANCES.

5.1.6 Broadband Correlations

Normalized broadband space-time correlation functions are shown in Figures 88 and 89 for various streamwise and lateral spatial separations, ξ and η, respectively. The data spans a Mach number range from 0.3 to 3.45. Analytical formulas to fit this data are not available. A time-delayed peak occurs only in the streamwise correlations, since turbulent eddies convect in that direction only.

The contours of broadband spatial correlation at zero time delay ($\tau = 0$) shown in Figure 90 reveal an elongated streamwise structure associated with the greater length scales in that direction. This figure is based on experimental results [114] obtained from subsonic wind-tunnel tests. Data for a wider Mach number range are not available at present; neither are analytical expressions for the contour shapes.

5.1.7 Narrowband Correlations

The principal data on narrowband correlations has been summarized by Chaump, *et al* [106]. A compilation of data on the narrowband streamwise and lateral spatial cross-correlation coefficients for zero time delay appears in Figures 91 and 92, respectively.

Corresponding narrowband space-time correlation data are shown in Figures 93 and 94 respectively. In these two figures, the results presented are for those values of the time delay τ which maximize the correlation for the given value of ξ or η; thus, these figures essentially show the decaying-exponential envelope of oscillatory functions that appear much like those of Figures 91 and 92.
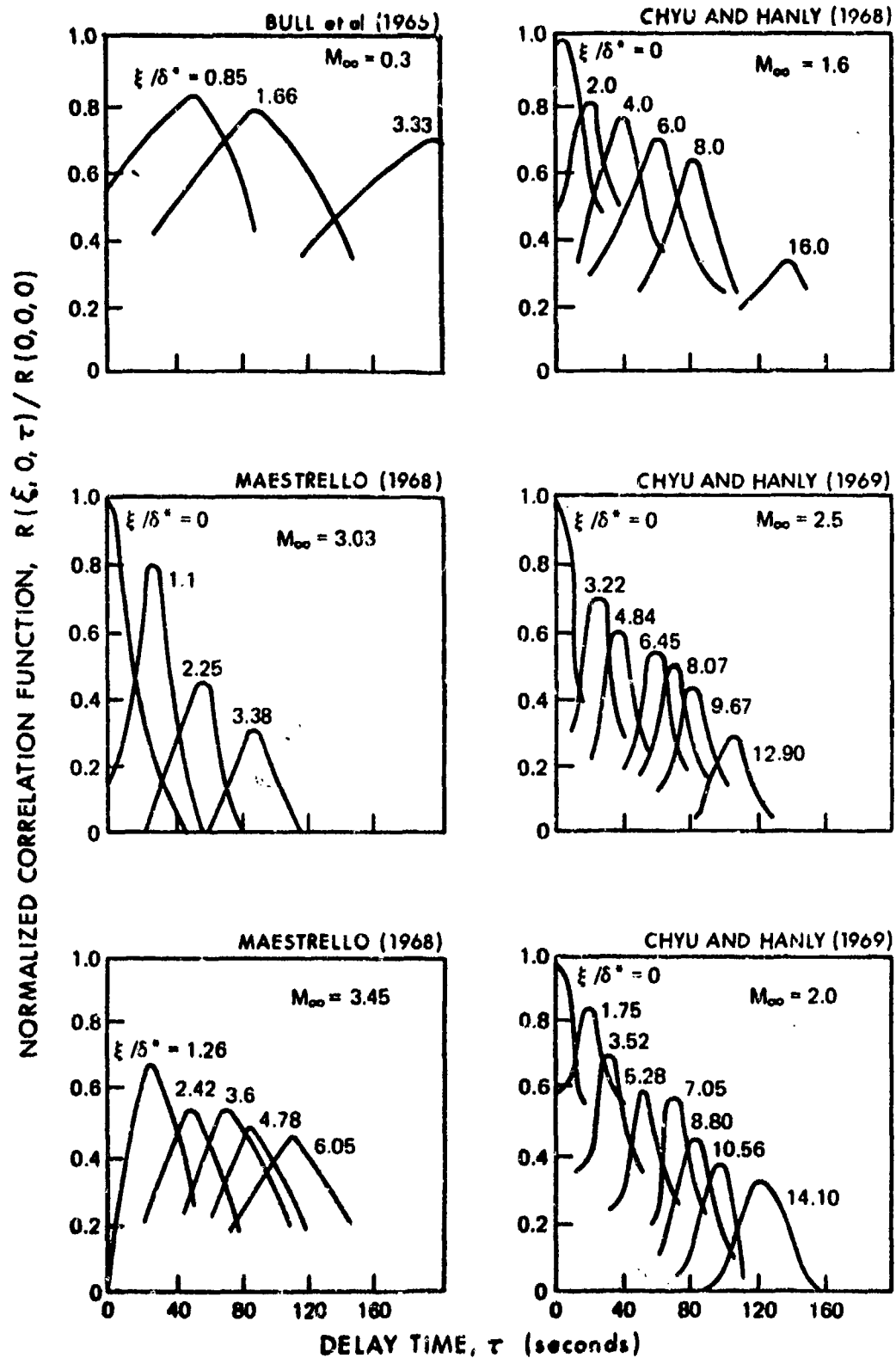
FIG. 88. NORMALIZED BROAD BAND STREAMWISE SPACE TIME
CORRELATION FOR ATTACHED TURBULENT FLOW [106].

200
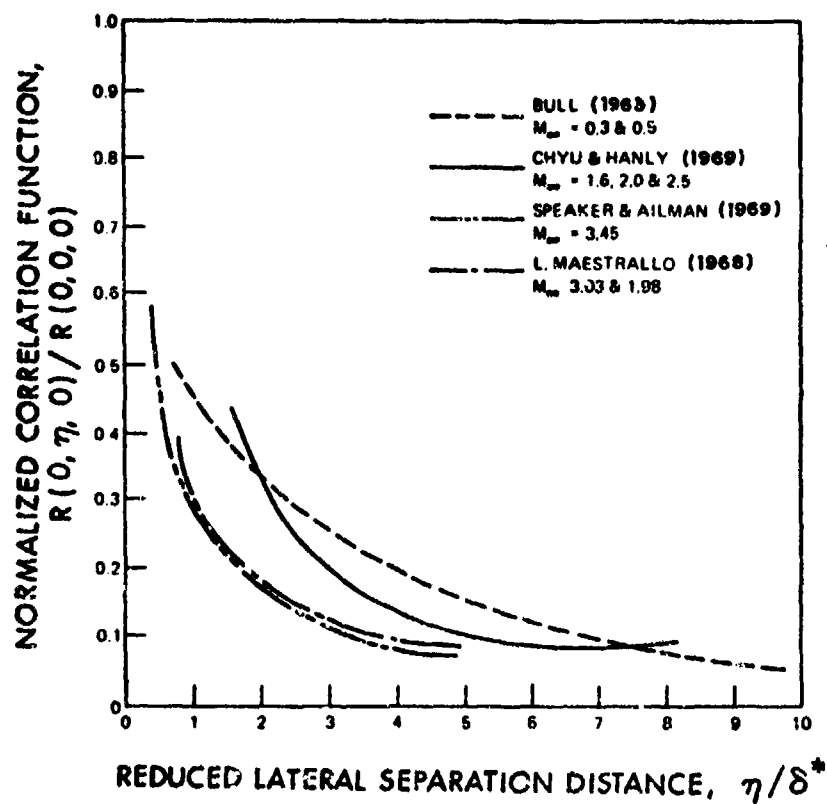
FIG. 89. NORMALIZED LATERAL BROAD BAND SPACE-TIME
          CORRELATION FOR ATTACHED TURBULENT
          FLOW [106].
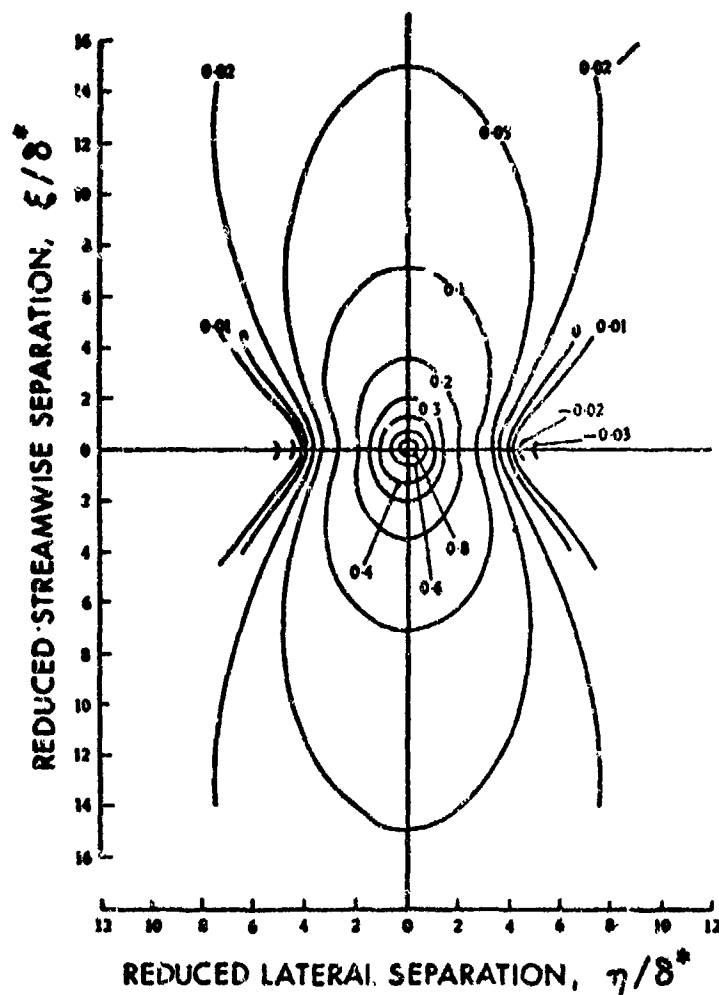
FIG. 90. CONTOURS OF CONSTANT INSTANTANEOUS BROADBAND
SPATIAL CORRELATION $R(\xi,\eta,0)/R(0,0,0)$ OF THE
WALL-PRESSURE FIELD.
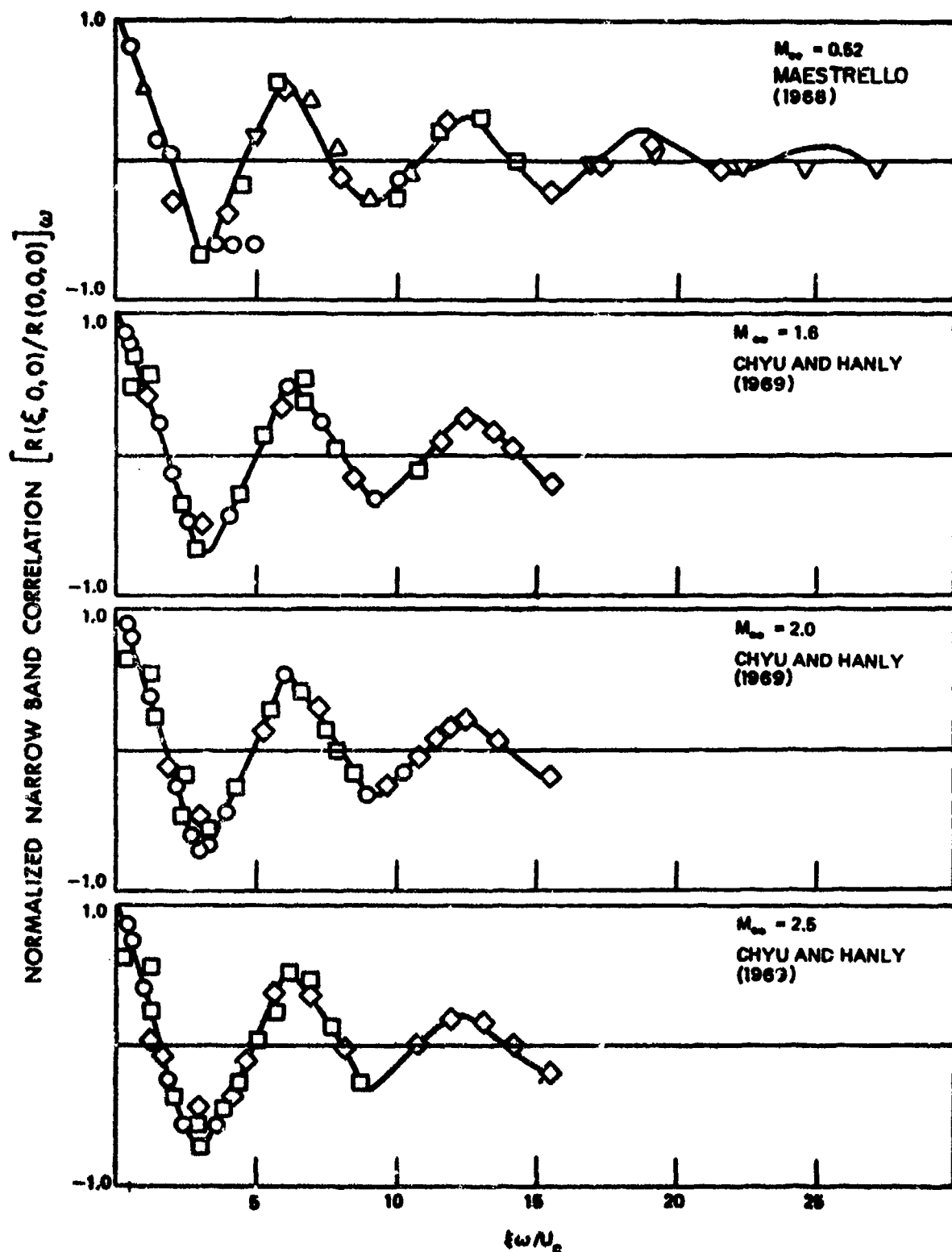
FIG. 91. FREQUENCY-DEPENDENT NARROWBAND STREAMWISE SPATIAL CORRELATION [106].

203
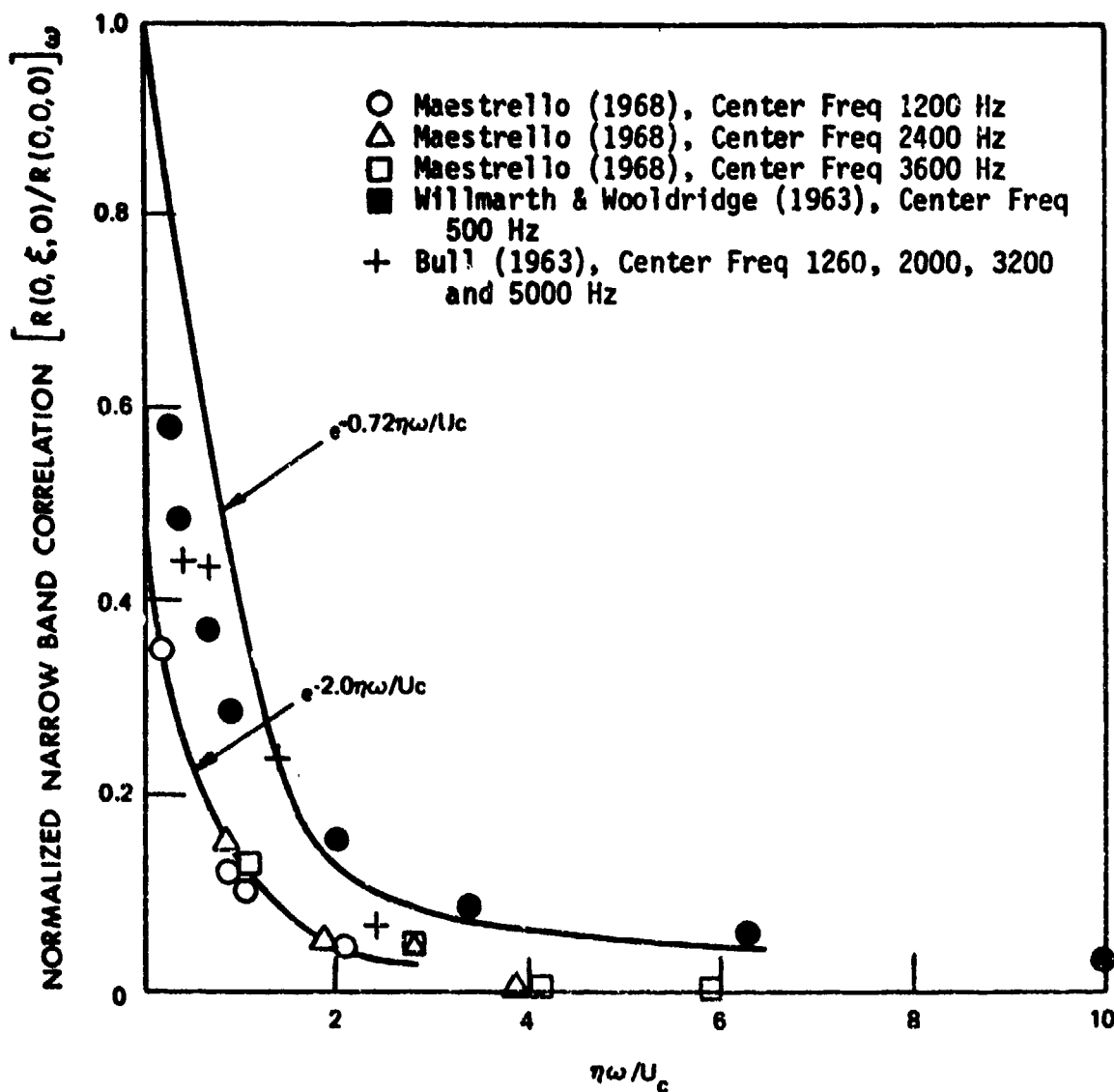
FIG. 92.   FREQUENCY-DEPENDENT NARROWBAND LATERAL SPATIAL
CORRELATION [106].
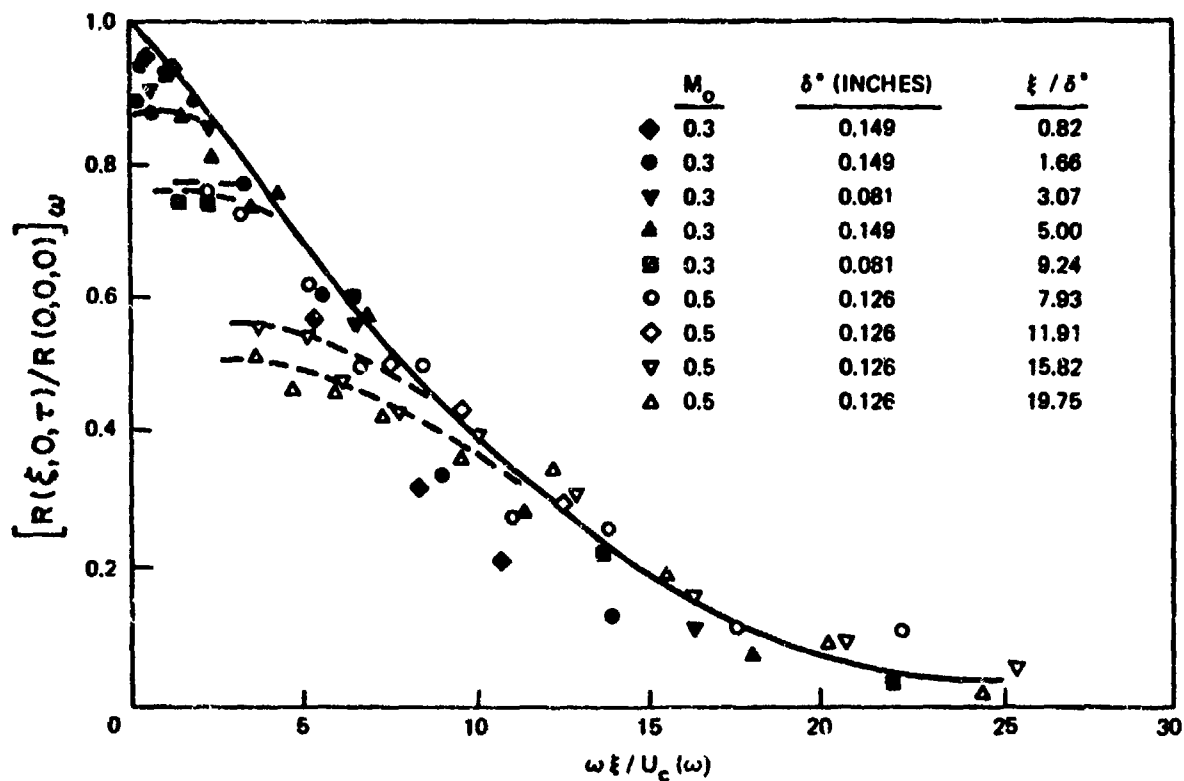
FIG. 93. SPANWISE VARIATION OF NARROWBAND SPACE-TIME
CORRELATION FOR ATTACHED TURBULENT FLOW [106].
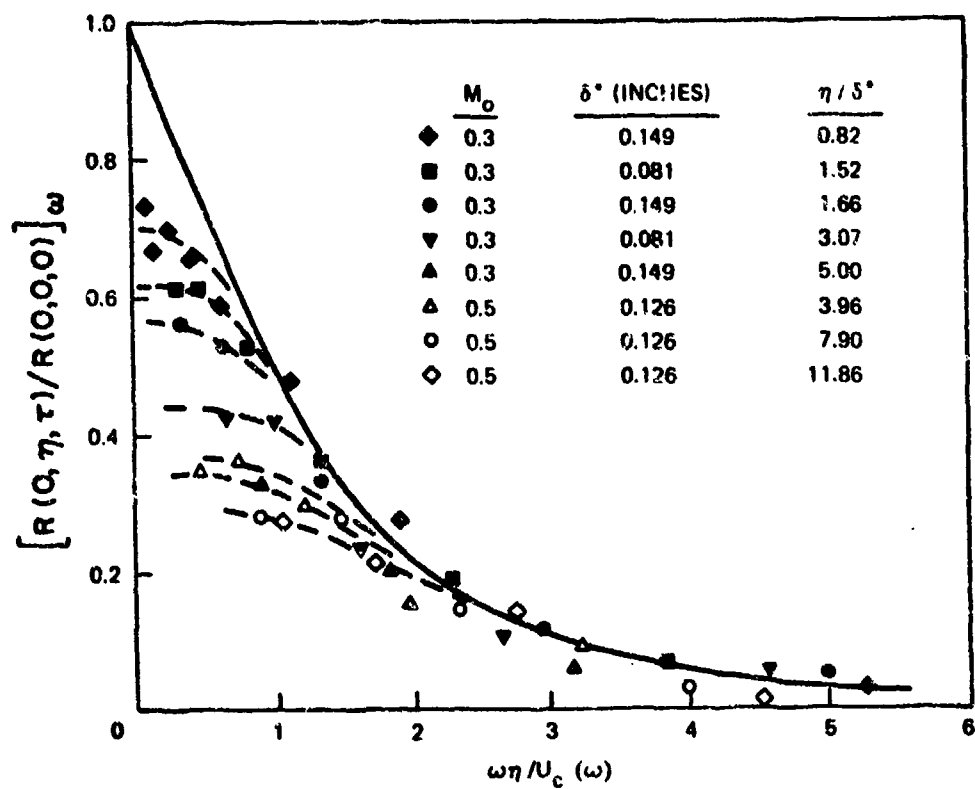
FIG. 94. LATERIAL VARIATION OF NARROWBAND SPACE-TIME
CORRELATIONS FOR ATTACHED TURBULENT FLOW [106].

The data of Figures 93 and 94 may be seen to converge for large values of the Strouhal numbers shown, but to differ considerably for small values of the Strouhal numbers, i.e., for low frequencies. The asymptotic low-frequency values are plotted in Figure 95, as functions of non-dimensionalized separation distance.

The space-time correlation and spectral density functions comprise a Fourier transform pair:

$$S(\xi,\eta,\omega) = \int_{-\infty}^{\infty} R(\xi,\eta,t) \; e^{i\omega t} dt \qquad (69)$$

$$2\pi R(\xi,\eta,\tau) = \int_{-\infty}^{\infty} S(\xi,\eta,\omega) \; e^{-i\omega\tau} d\omega, \qquad (70)$$

and $S(\xi, \eta, \omega)$ is often expressed in terms of the co-spectral density (its real part) and the quad-spectral density, (its imaginary part):

$$S(\xi,\eta,\omega) = \phi_R(\xi,\eta,\omega) - j\phi_1(\xi,\eta,\omega). \qquad (71)$$

The co-spectral density is generally used in defining characteristics of the fluctuating pressure field. Lowson [107] and Robertson [111], using data obtained by Bull [113], described the cross-correlation function for turbulent flow, assuming that the cross-power spectral density is a function of only the separation distances, by

$$\phi_R(\xi,0,\omega) \Big/ \bar{\phi}_R(\xi) = A_\xi(\xi, \omega) \cos(\omega\xi/U_c) \qquad (72)$$

$$\phi_R(0,\eta,\omega) \Big/ \bar{\phi}_R(\eta) = A_\eta(\eta, \omega) \qquad (73)$$
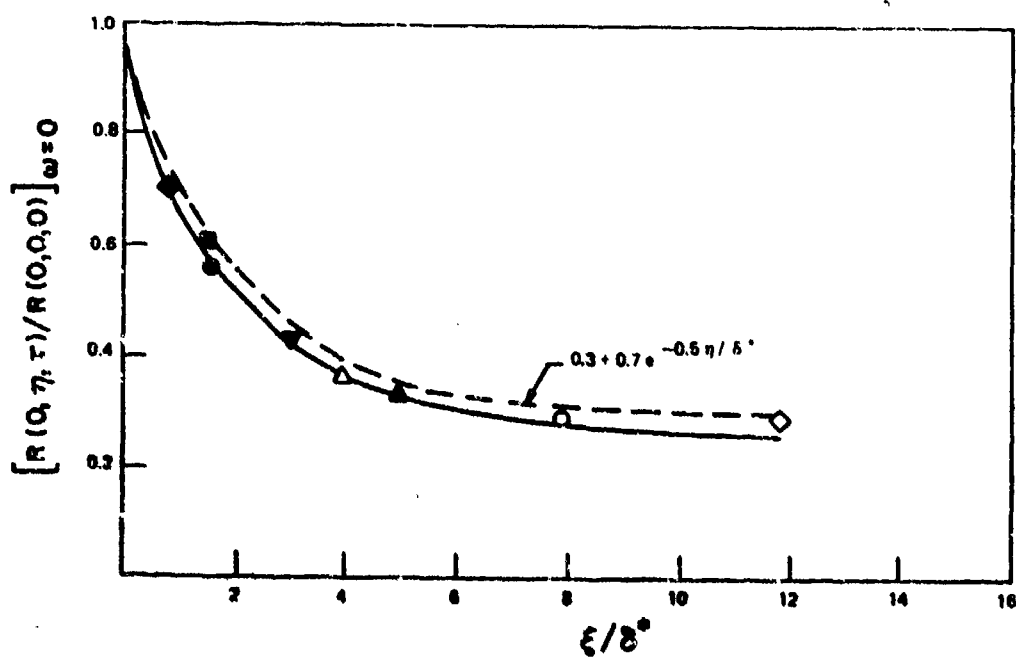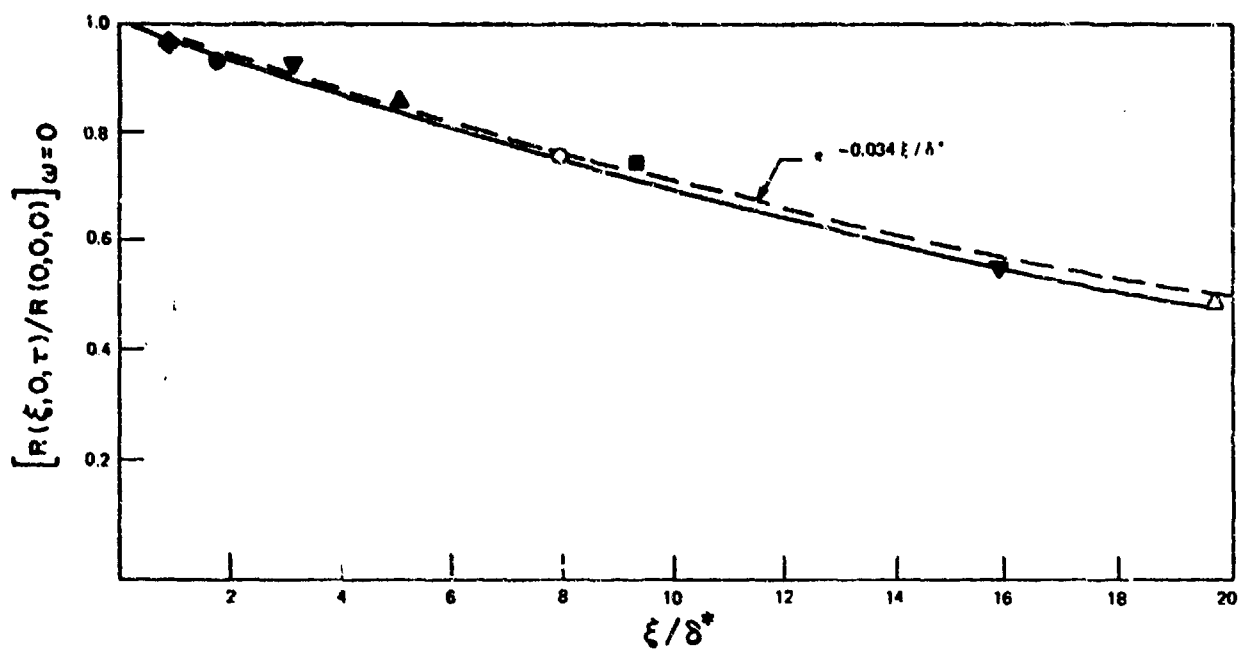
FIG. 95.   LOW-FREQUENCY VALUES OF STREAMWISE AND LATERAL
          CORRELATIONS.

208

where $\overline{\phi}_R (\xi) = [\phi_R (\xi_1) \phi_R (\xi_2)]^{\frac{1}{2}}$, and $\phi_R (\xi_1)$ is evaluated at one measurement location and $\phi_R (\xi_2)$ at another, a distance ξ away. $\overline{\phi}_R (\eta)$ is analogously defined. The correlation coefficients may be expressed as [113]

$$A_\xi(\xi, \omega) = \exp[-0.1\xi\omega/U_c] \ \exp[-0.034\xi/\delta^*] \tag{74}$$

$$A_\eta(\eta, \omega) = \exp[-0.72\eta\omega/U_c]\cdot\{0.3 + 0.7 \exp[-0.5\eta/\delta^*]\} \ , \tag{75}$$

where ξ and η are always taken as positive.

These coefficients are plotted in Figures 91-95, from where one can perceive their relatively good fit to the data.

5.2 Pressure Fluctuations in Transitional Boundary Layers

5.2.1 Introduction

Boundary layer transition is the process by which a laminar boundary layer changes its structure to become a fully turbulent boundary layer. The transition process takes place over a streamwise distance which, for a typical aircraft, represents a small fraction of the total surface area. However, transitional flow may cover much of the surface of a ballistic re-entry vehicle. Boundary layer transition is a sensitive phenomenon which depends strongly on such factors as Reynolds number, surface roughness and discontinuity, and the pressure gradients to which the boundary layer has been subjected.

In a transitional boundary layer, unstable disturbances are amplified and lead to the onset of turbulence. The turbulence occurs first in patches, so that transitional flow becomes a changing mixture of turbulent and disturbed laminar flow regions.

Because of their complexity and sensitivity, transitional flows are particularly difficult to characterize. Furthermore, little reliable data is available and the general validity of particular test results is often difficult to ascertain. Thus, use of any data or prediction scheme may be expected to involve considerable uncertainty for any specific case for which a prediction is desired.

5.2.2 RMS pressure fluctuations

In many cases, particularly those involving supersonic and hypersonic flow, the fluctuating pressure levels in transitional

boundary layers have been observed to exceed, by considerable amounts (as much as 10 to 20 dB), corresponding levels for fully developed turbulent boundary layers. Figure 96 shows an envelope of available data* for the overall rms fluctuating pressure level in transitional boundary layer flows, as a function of Mach number. Comparison of these levels with Fig. 4.1, which pertains to fully developed turbulent flows, shows the levels associated with transitional flows to be substantially higher.

Also shown in Fig. 96 is a plot of the equation

$$\frac{\bar{p}}{q} = \frac{0.006}{1 + 0.013M^2} \tag{76}$$

which represents a modification of an expression given by Chaump et al. [106] to fit data in the Mach number range of 4 to 8. Equation (76), which pertains to transitional flow, gives higher rms pressure values than does Eq. (64a), which pertains to turbulent flow. Equation (76) was constructed so that the values predicted by it for low Mach numbers agree with the corresponding turbulent flow values. However, this range is outside the data base for transitional flows, and use of the equation may lead to considerable error.

5.2.3 Power spectral density

A power spectrum representative of supersonic transitional flow is shown in Fig. 76. This spectrum is described by

---

*The data envelope of Fig. 96 includes the data of [106, 115, 116], all taken on conical models in wind tunnels.
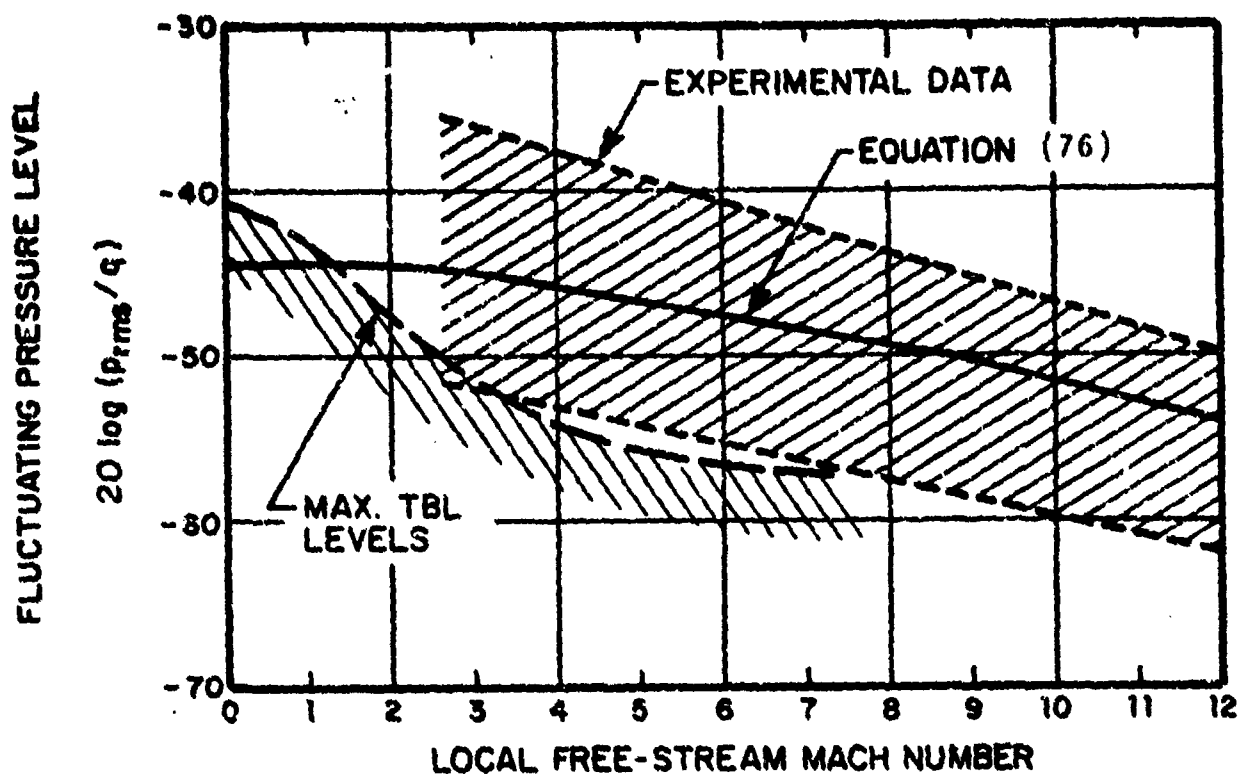
FIG. 96. RMS PRESSURE FLUCTUATION LEVEL OF
TRANSITIONAL BOUNDARY LAYER FLOWS
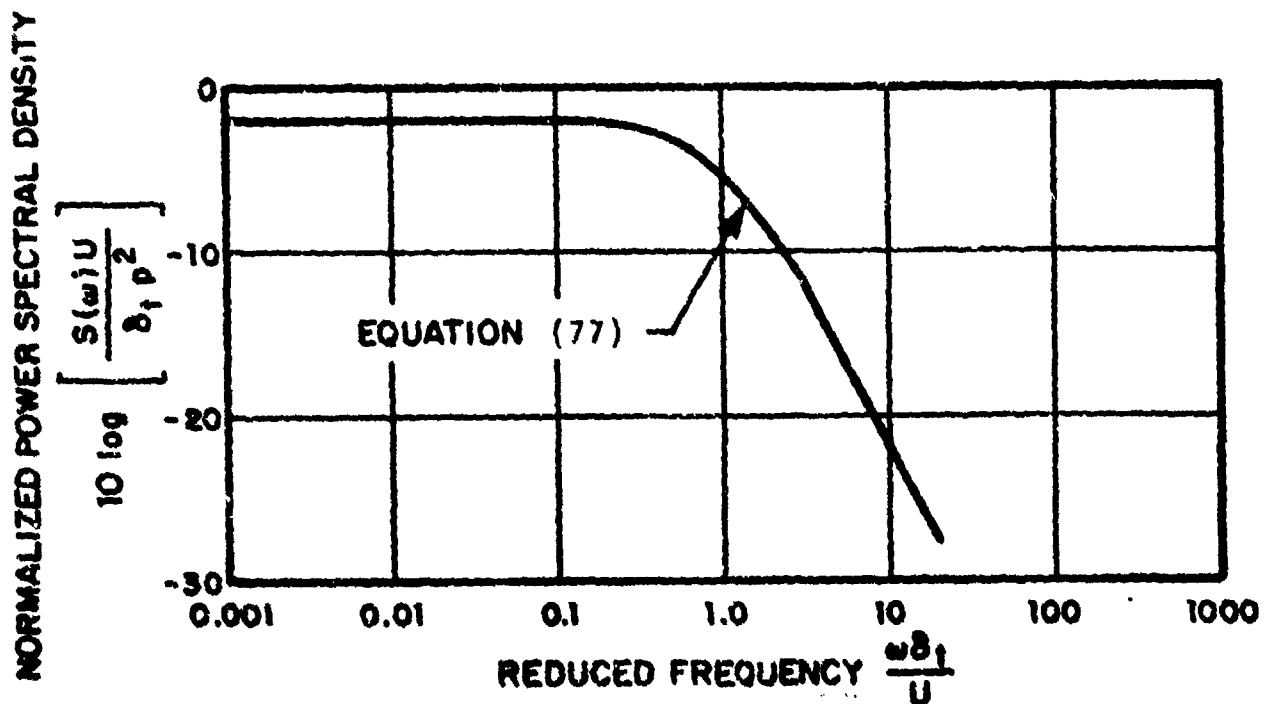
FIG. 97. ONE-THIRD OCTAVE BAND POWER SPECTRAL
DENSITY OF TRANSITIONAL BOUNDARY LAYER
PRESSURE FLUCTUATIONS

$$\frac{S(\omega)U}{\overline{p^2}\,\delta_t} = \frac{2/\pi}{1 + (\omega\delta_t/U)^2}$$

which relation was suggested by Chaump *et al.* [106]. Equation (120) is identical to Eq. (65), except for the transitional flow length parameter δ_t which here replaces the turbulent boundary layer displacement thickness δ^*. Because $\delta_t > \delta^*$ in general, the transitional spectrum in effect is shifted toward lower frequency with respect to the turbulent boundary layer spectrum. For Mach numbers between 3.7 and 8.1, the relation

$$\frac{\delta_t}{\delta^*} = 2.9\ (1 + 0.013M^2)^2 \tag{78}$$

has been suggested.

It should be mentioned that various researchers have measured spectra that differ considerably from that given by Eq. (77); some spectra show a pronounced low-frequency peak. Note also that the data on which Eq. (77) is based lies within an envelope that is up to 6 dB wide, depending on the observation location on the vehicle.

5.2.4 Correlation coefficients and convection velocities

Reliable values for correlation coefficients in transitional flow are not available. The previously discussed formulae for fully turbulent flow may be used, but are likely to be seriously in error in some cases.

Broadband convection velocities have been found to be approximately 0.6 of those in turbulent flow. This trend is physically consistent with the previously indicated fact that $\delta_t > \delta^*$.

5.3 Pressure Fluctuations in Separated Flows

5.3.1 Introduction

The phenomenon of flow separation occurs when a boundary layer detaches from the surface, resulting in a region of flow reversal which is often characterized by unsteadiness and the formation of large turbulent eddies or vortices. Separation often occurs as the result of a loss of energy from the boundary layer, usually due to an adverse pressure gradient, or as the result of a viscous boundary layer's inability to turn a very sharp corner. Separation leads to large energy losses and attendant drag increases; therefore, designers of flight vehicles take care to avoid its occurrence. Nevertheless, in some situations separation is still encountered.

In subsonic flow, separation is associated with either an adverse pressure gradient (due to body shape) or a sharp edge or corner. Common areas of subsonic flow separation are the leading or trailing edges of wings (depending on the airfoil configuration), portions of flaps, and behind bluff bodies, such as protuberances, struts, or landing gear. The separation behind bluff bodies is termed "base flow", and is discussed in Sec. 5.4. In supersonic flow, the occurrence of flow separation and the presence of shock waves are often closely related, because shock waves are associated with body shape changes and

214

also produce very large adverse pressure gradients. Often the region of flow separation and the associated shock wave interact dynamically to produce a shock oscillation phenomenon which produces particularly intense pressure fluctuation levels.

The remainder of this section discusses data and prediction methods for several phenomena associated with flow separation, first for the very important case of supersonic flow, and later for flow over wings. Because flow separation characteristics depend strongly on surface configurations and flow conditions, it must be noted that the suggested prediction methods are limited to cases that correspond to the data on which they are based. In some situations, significant deviations from predictions obtained by these methods may be expected.

5.3.2 RMS pressure levels

The pressure fluctuations in separated flow depend on the condition of flow separation; therefore, several sets of data need to be presented. Figure 98 shows the envelope of data for separated flow induced by an expansion, such as occurs at a slanted rearward step or at the junction between a cone and cylinder. The data on which the envelope is based is taken from the work of several researchers, as summarized by Chaump *et al.* [106], and corresponds to expansion angles between about 15° and 35°. An equation to predict expansion-induced separated flow pressure levels, as proposed by Robertson [111], is

$$\frac{P_{rms}}{q_\infty} = \frac{0.045}{1 + M_e^2} , \tag{79}$$

where M_e denotes the Mach number downstream of the expansion, and q represents the upstream dynamic pressure. As evident from Fig. 98, Eq. (79) agrees well in the available data.

215
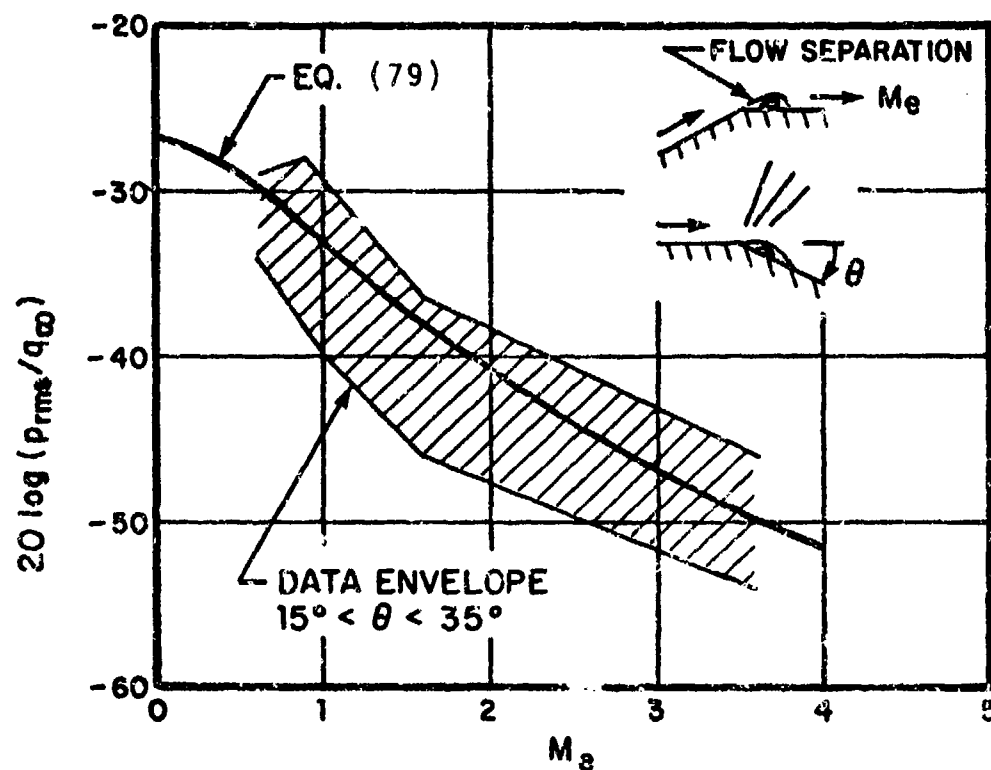
FIG. 98. OVERALL FLUCTUATING PRESSURE LEVEL IN REGIONS OF FLOW SEPARATION CAUSED BY AN EXPANSION CORNER
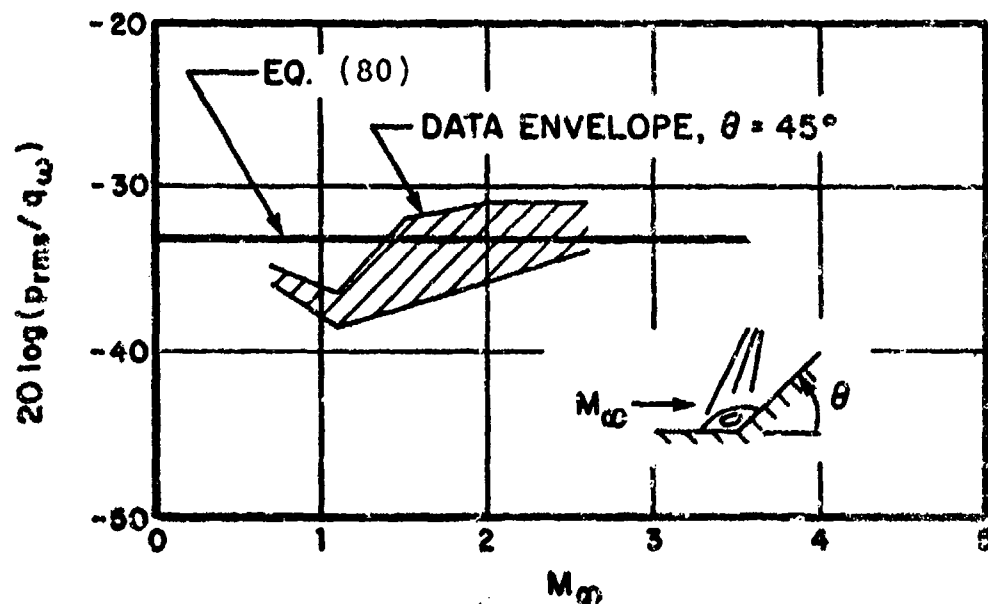
FIG. 99. OVERALL FLUCTUATING PRESSURE LEVEL IN REGIONS OF FLOW SEPARATION PRODUCED BY A COMPRESSION CORNER

Figure 99 shows a data envelope for separated flow upstream of a compression corner or region of rapid area increase of a body. The available data [112, 117] is limited to compression corner angles of 45°. According to [106], an analytical expression has not been developed, because insufficient information is available on local flow conditions. The assumption of a constant level gives acceptable agreement for the presently available data:

$$\frac{p_{rms}}{q_\infty} = 0.022 \quad . \tag{80}$$

At the point on a surface where flow separation begins, the levels tend to be particularly high because the flow alternates between being attached and separated. In the case of supersonic flow, a shock wave oscillation may be associated with the point of initial separation. Chaump et al. [106], on the basis of data from [111, 112], have suggested the following expression for the overall fluctuating rms pressure at a separation point:

$$\frac{p_{rms}}{q_\infty} = \frac{0.14}{1 + 0.5M_\infty^2} \quad . \tag{81}$$

The available data and this expression are indicated in Fig. 100.

Note that the available data are very limited. One may expect, for instance, that the actual levels in the transonic region are higher than those predicted by Eq. (81). High levels may also occur in the region of flow reattachment, particularly if a shock wave is present. Some data points for
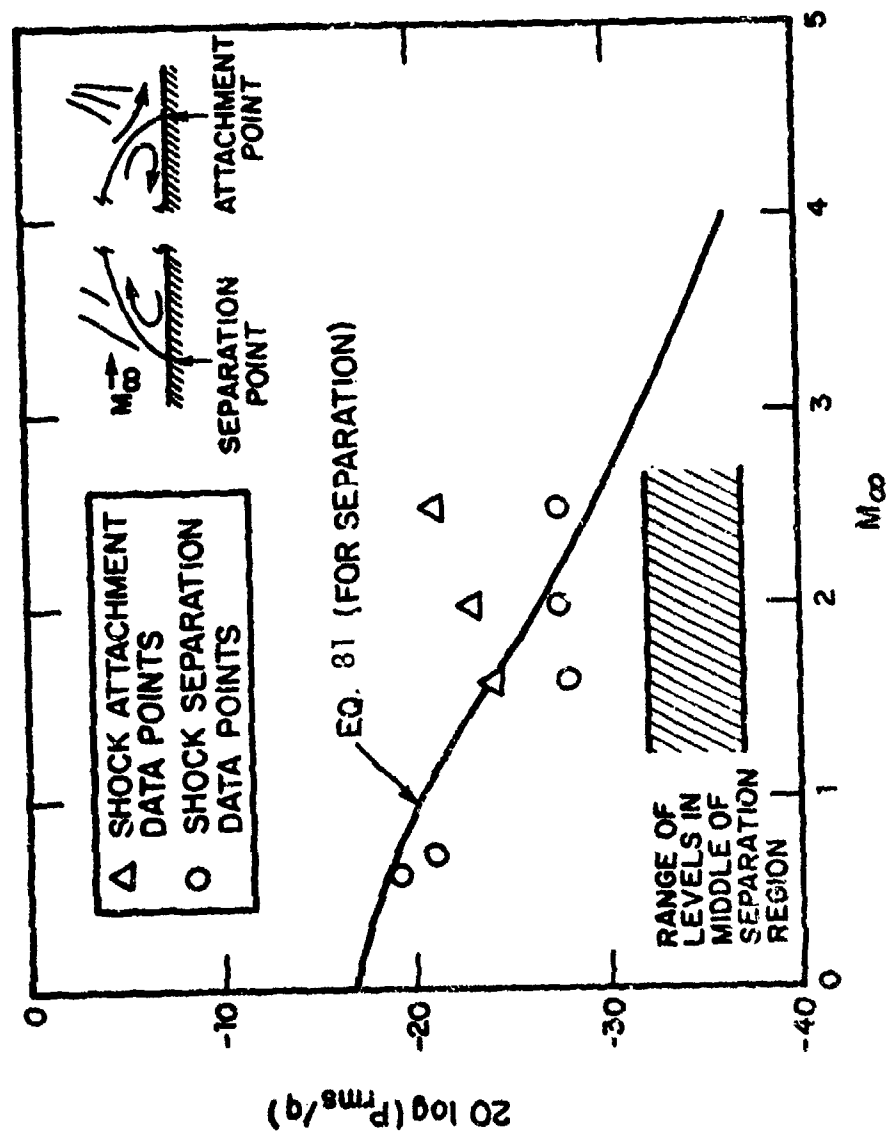
FIG. 100. OVERALL FLUCTUATING PRESSURE LEVELS IN THE REGIONS OF FLOW SEPARATION AND REATTACHMENT

shock reattachment from [112 and 118] are also indicated in Fig. 100. This data is consistent with the levels shown in Figs. 98 and 99 for regions of separated flow in the same

5.3.3 Power spectral density

An expression for the power spectrum, normalized with respect to dynamic pressure, was suggested by Roberton [111]:

$$\frac{S(f)\,U_e}{q_\infty^2 \delta} = 5.9\,\frac{p_{rms}/q_\infty}{\left[1 + \left(0.17\frac{\delta}{fUe}\right)^{0.83}\right]^{2.15}} \quad , \qquad (82)$$

where δ denotes the upstream boundary layer thickness, and U_e is the velocity above the separation region. A comparison of this expression with corresponding data appears in Fig. 101.

The power spectrum normalized to the rms pressure is

$$\frac{S(f)\,U_e}{p_{rms}\,\delta} = \frac{5.9\,q}{\left[1 + \left(0.17\frac{\delta}{fUe}\right)^{0.83}\right]^{2.15}} \quad . \qquad (83)$$

An alternative formula, based on a data curve fit, has been derived by Coe and Chyu [119] and is given by

$$\frac{S(f)\,U_e}{q_\infty^2 \delta} = \exp\,[-8.094-1.239x-0.259x^2-0.090x^3-0.014x^4-0.001x^5] \qquad (84)$$

where

$$x = \ell n\,(f\delta/U_e) \qquad (85)$$
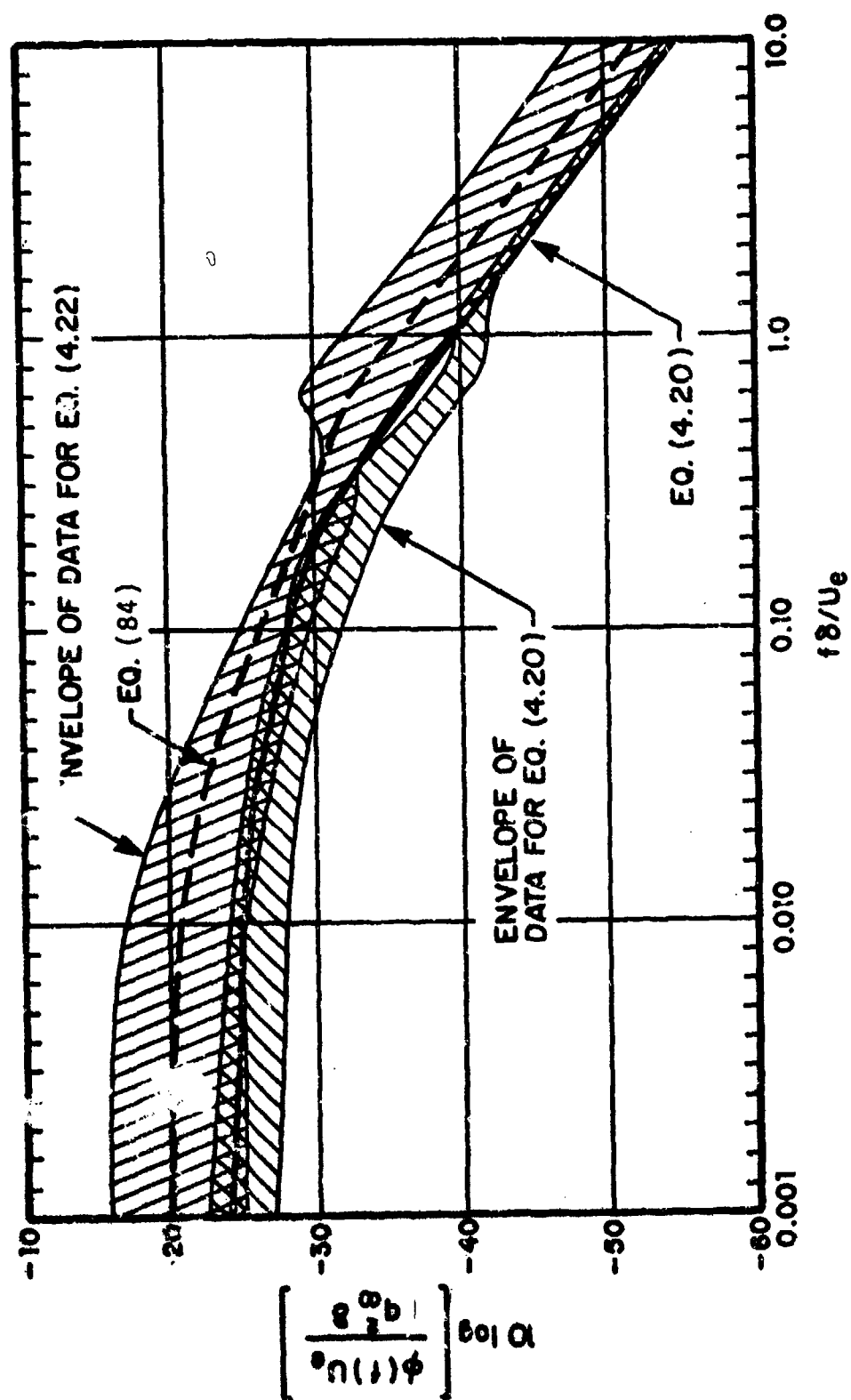
FIG. 101. POWER SPECTRUM FOR SEPARATED FLOWS

220

This formula and the associated data envelope are also shown in Fig. 101 for comparison. It is recommended, however, that Eq. (82) be used for predictions of spectra for all types of separation, with the rms pressure determined from the appropriate case of Sec. .3.2.

An experimental power spectrum [106] for shock wave oscillations with separated flow induced by two and three dimensional protuberances is shown in Fig. 102. The flow disturbances were provided by cylindrical protuberances at approximately M = 1.5 and by a 45° wedge at M = 2.0.

5.3.4 Narrowband convection velocities

Available data show narrowband convection velocities in separated flow to vary from about 0.2 times the freestream velocity at low wavenumbers to nearly 1.0 times at high wavenumbers. Due to this wide variation, broadband convection velocities have considerably less meaning in separated flow than for attached turbulent boundary layer flow.

Some data for M = 2.0 in compression-corner produced separation are shown in Fig. 103. A representative curve for attached flow is also shown in the figure for comparison; the trend is seen to be quite different. A trend similar to that of the data of Fig. 103 also appears in the data of Fig. 104, where frequency is normalized with respect to the distance from the separation point and the flow velocity outside the separation region. The behavior in the low Strouhal number region is dominated by the slow recirculatory flow within the separation region; the behavior at higher Strouhal numbers shows the effect of the outer higher speed separated boundary layer flow.
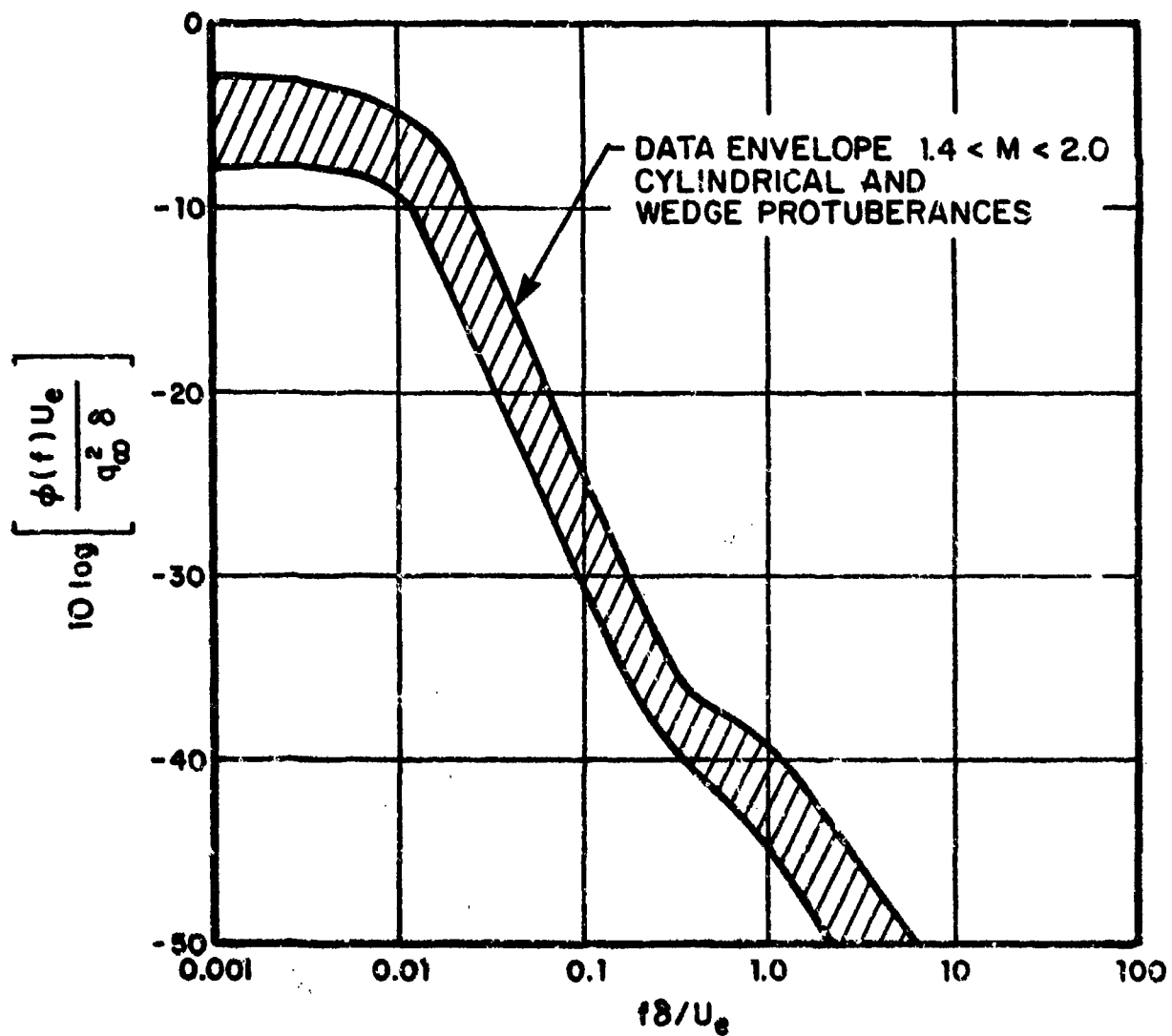
FIG. 102   POWER SPECTRUM FOR SHOCK WAVE OSCILLATIONS
IN SEPARATED FLOW PRODUCED BY PROTUBERANCES.
[106]
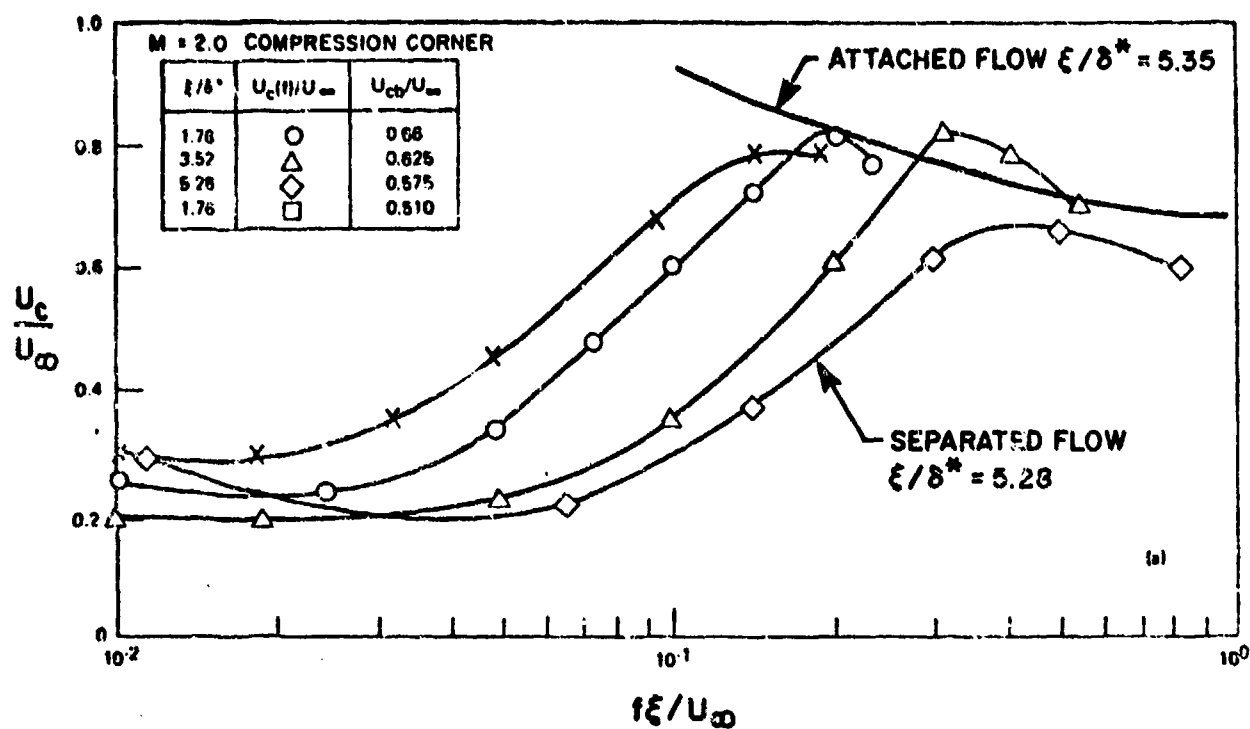
FIG. 103. NARROW BAND CONVECTION VELOCITY VERSUS STROUHAL NUMBER BASED ON STREAMWISE DISTANCE BETWEEN MEASUREMENT POINTS [112]

	M_∞	S	$\underline{U}$	$\underline{x}_S$	ζ
o	1.6	10.7	1323	6.70	1.0
Δ	2.0	9.2	1588	6.70	1.0
+	2.5	8.3	1828	6.95	0.5
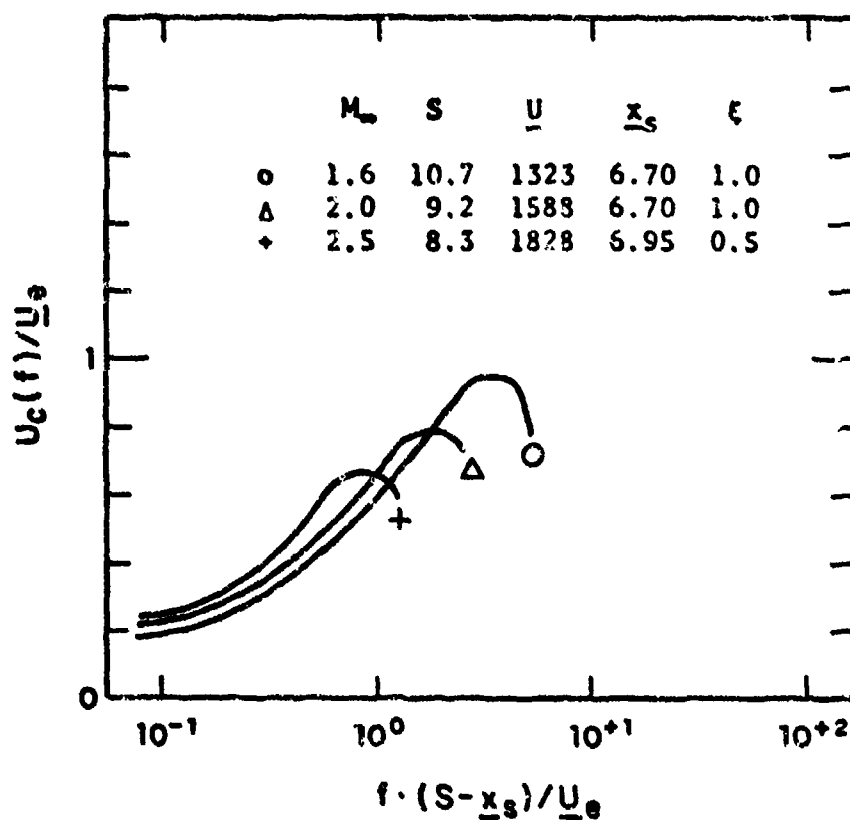
FIG. 104.   NARROW BAND CONVECTION VELOCITY VERSUS
STROUHAL NUMBER BASED ON DISTANCE FROM
SEPARATION POINT [120]

5.3.5 Broadband correlations

Normalized broadband space-time correlation functions for separated flow are shown in Fig. 105 for several streamwide distances. These should be compared with the corresponding functions presented earlier for turbulent boundary layer flow. No data for correlations in the lateral direction are available for separated flow. No expressions have been developed to fit this data.

5.3.6 Narrowband correlations

The principal data on narrowband correlations have been summarized by Chaump et al. [106]. Data for the streamwise spatial cross-correlation coefficients for zero time delay are shown in Fig. 106. Coherence function data are presented in Fig. 107, which compares functions for attached and separated flow. Corresponding analytical expressions for the cross-spectra coefficients, as defined in Sec. 5.1.7, are [112]:

$$A_\eta = \begin{cases} \exp[-0.75\eta] & \text{for } f\delta/U_e < 6\times10^{-3} \\ \exp[-0.75\eta \ (f\delta/6\times10^{-3}U_e)^{0.3}] & \text{for } f\delta U_e > 6\times10^{-3} \end{cases}$$

$$(86)$$

$$A_\xi = \begin{cases} \exp[0.75\xi] & \text{for } f\delta/U_e < 6\times10^{-3} \\ \exp[-0.75\xi \ (f\delta/6\times10^{-3})] & \text{for } 6\times10^{-3} < f\delta/U_e < 6\times10^{-2} \\ \exp[-1.5\xi] & \text{for } f\delta/U_e > 6\times10^{-2} \ . \end{cases}$$

$$(87)$$

Figure 108 shows the degree of correlation that exists under a detached shock wave and the surrounding attached and separated flow region. Weak correlation is observed, except for
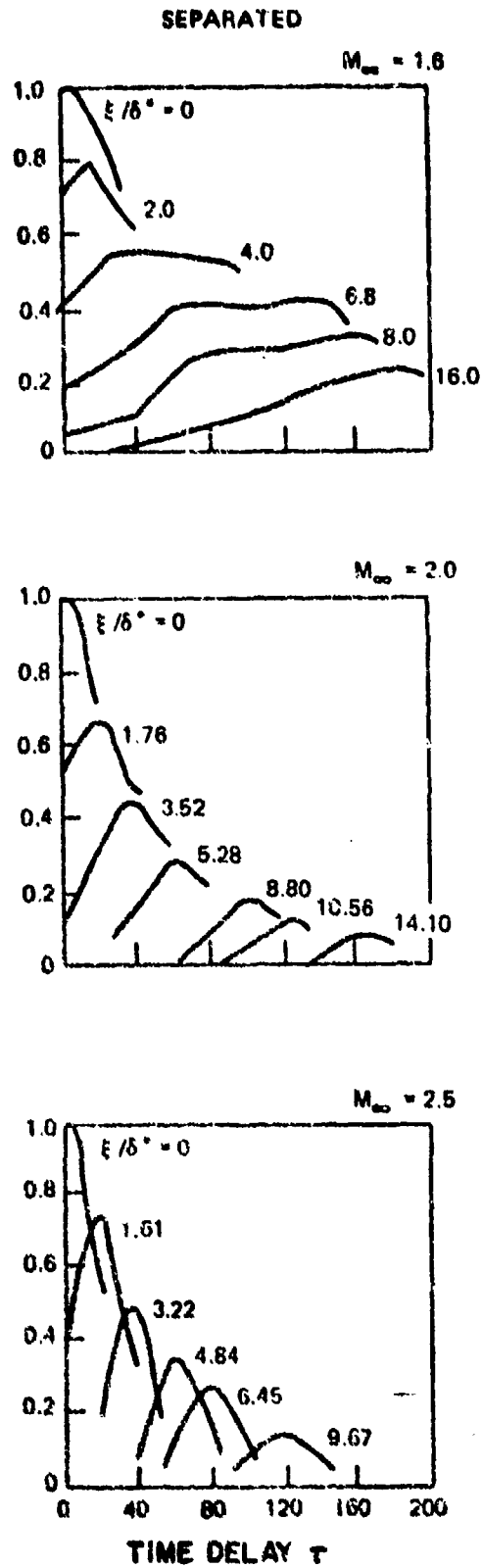
FIG. 105. NORMALIZED BROAD BAND STREAMWISE SPACE TIME
CORRELATION FUNCTIONS FOR SEPARATED FLOW [112]
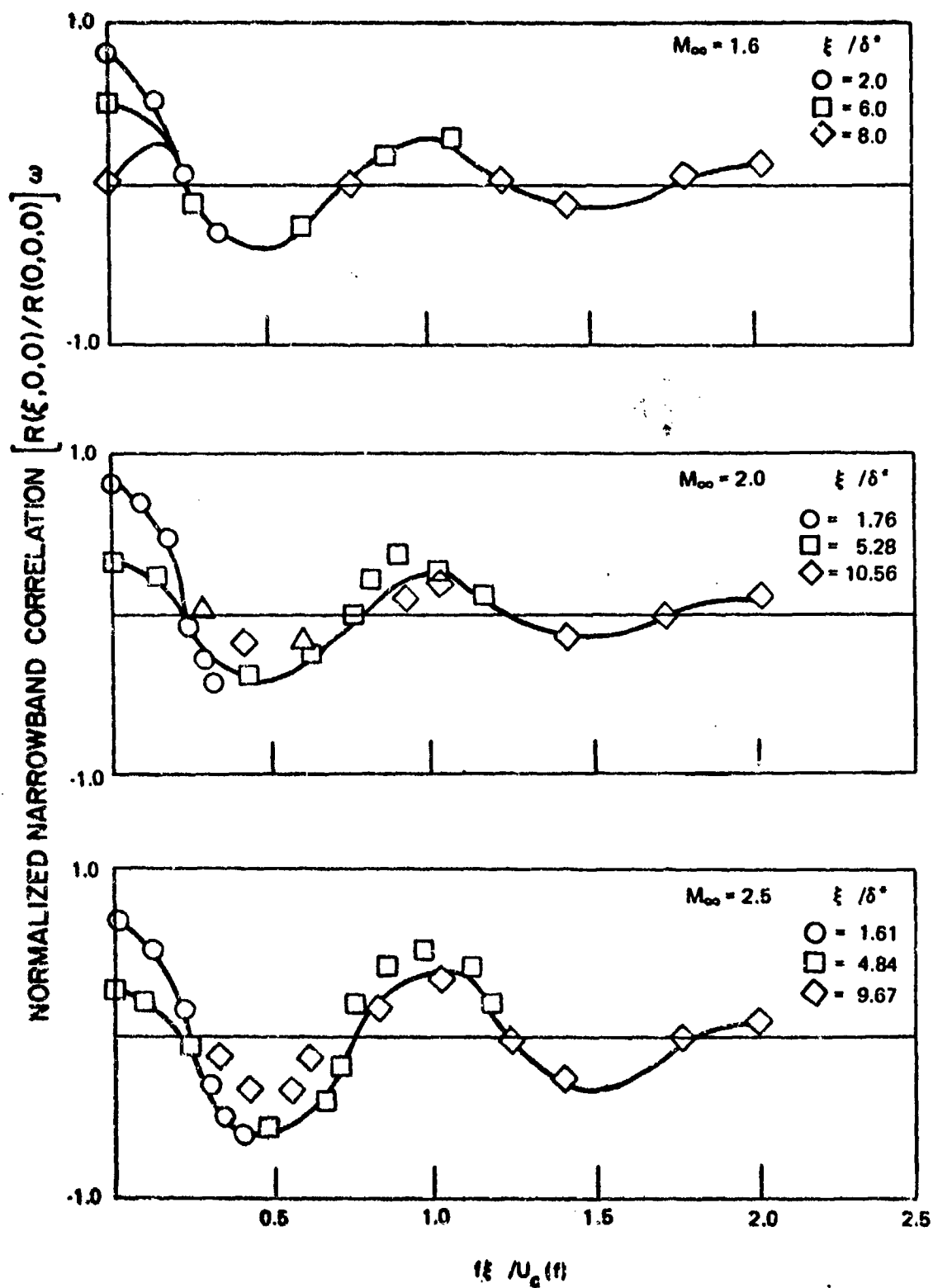
FIG. 106. FREQUENCY DEPENDENT NARROWBAND STREAMWISE
SPATIAL CORRELATION FOR SEPARATED FLOW [112]
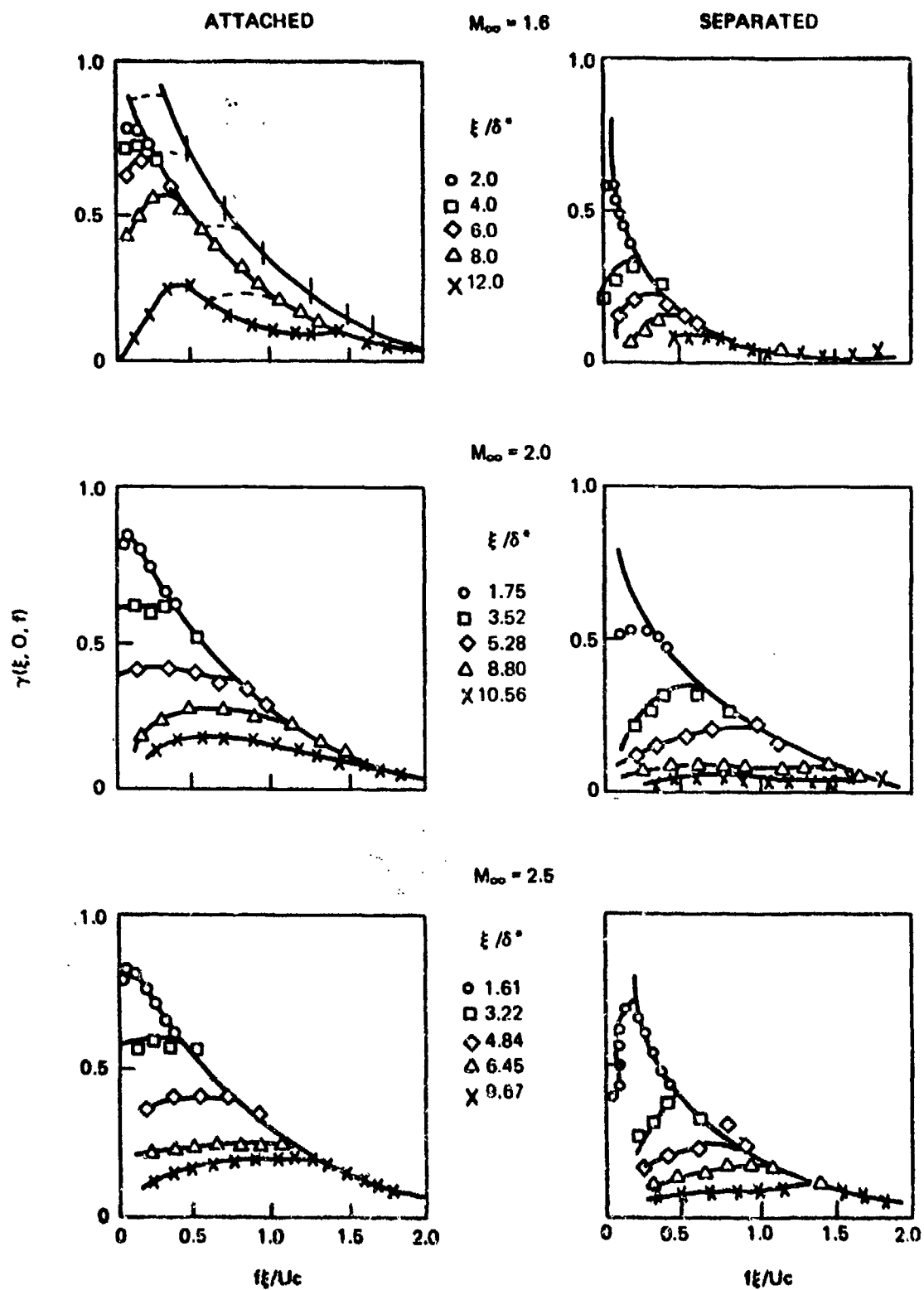
FIG. 107. COMPARISON OF COHERENCE FUNCTIONS FOR ATTACHED AND SEPARATED FLOW [112]

228
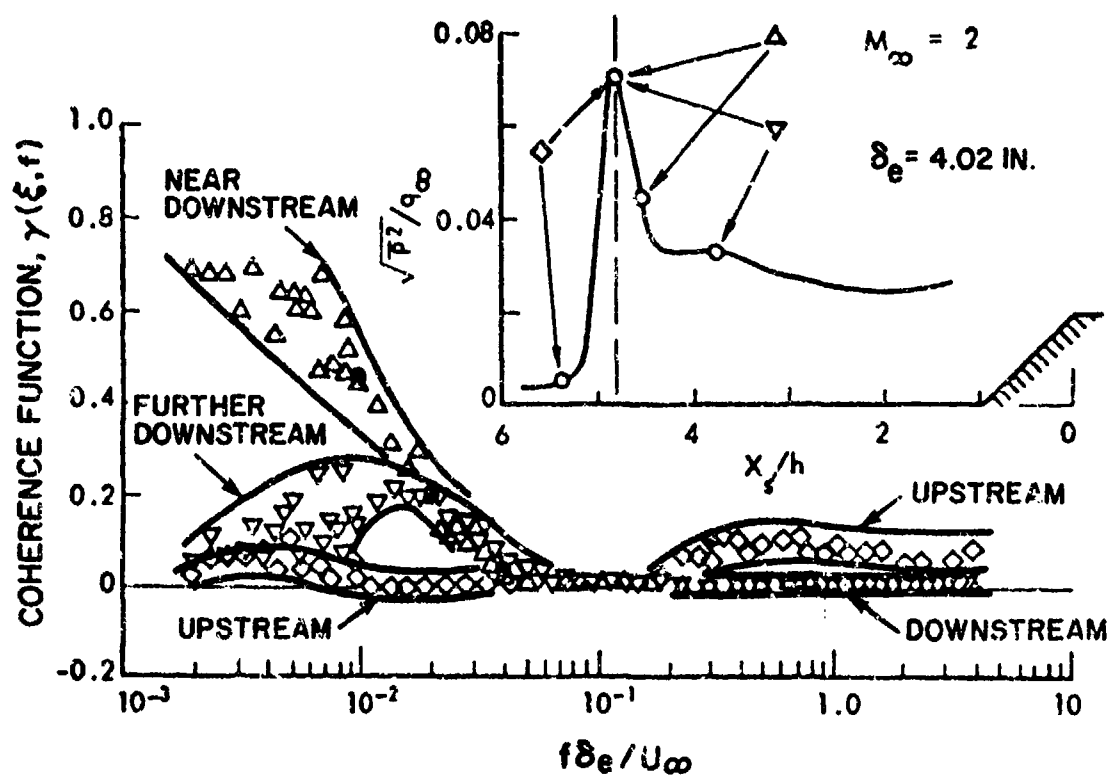
FIG. 108. CORRELATION OF PRESSURE FLUCTUATIONS BETWEEN SHOCK WAVE AND ADJACENT ATTACHED AND SEPARATED FLOW REGIONS [111]

the region in close proximity to the shock. Not surprisingly, the correlation between the shock region and the upstream attached flow region is the weakest.

5.3.7 Pressure spectra for the flow separation on wings in subsonic flow

A wide variety of flow separation phenomena occur on wings in subsonic flow. The presence of flow separation on wings is often associated with the occurrence of flow phenomena which lead to stalling (loss of lift) of the wing if the angle of attack is increased sufficiently. A comprehensive review of information on flow separation and stall on airfoils has been made by Heller *et al.* [121].

On straight wings and airfoils, regions of flow separation can develop in two different ways as the angle of attack is increased. For thicker sections, the flow separation begins near the trailing edge and moves forward as the angle of attack increases. For wings with thinner airfoil sections and sharp leading edges, a region of flow separation occurs at or near the leading edge and reattaches farther back along the wing chord. As the angle of attack increases, the reattachment point moves farther back; stall occurs when the flow fails to reattach. Some sections may also exhibit both leading and trailing edge separation phenomena simultaneously. The highest fluctuating pressure levels occur in the reattachment region of leading edge flow separation. Maximum spectral levels, in this case, tend to be roughly 10 dB higher than the maximum levels associated with trailing edge flow separation.

In an experiment using an airfoil, Heller *et al.* [121] were able to collapse the pressure spectra at the reattachment

point measured under different conditions into a relatively
narrow envelope, as shown in Fig. 109. Peak spectral levels
away from the reattachment point were as much as 20 dB lower.

Separation regions on swept wings can also be characterized
according to whether they occur in the leading or trailing edge
region. Again, leading edge separation phenomena produce the
highest fluctuating pressure levels. On swept wings, the leading
edge separation flow has a very three-dimensional character. An
intense vortex forms in the separation region, becoming larger
near the wing tip. Spanwise flow occurs in the vortex, so that
fluid entering the vortex region spirals outward toward the wing
tip. The presence of the vortex tends to have the effect of
bringing some orderly structure to the flow separation region.
This is most clearly illustrated in the case of highly swept
sharp-edged delta wings. In this case, although the flow separa-
tion region may cover much of the upper surface, the vortex is
so intense and well ordered that the flow in and beneath the
vortex is essentially steady. However, for moderately swept
wings (say a sweep angle of less than 50°), the highest fluctuating
pressure levels occur in the region from directly beneath the
vortex back to the reattachment line. Heller *et al.* [121] were
able to collapse fluctuating pressure data taken in this region
into a reasonably narrow envelope. The results, which are based
on measurements made on a 45° swept-wing model, are shown in
Fig. 110. The fact that spectrum peak occurs at higher frequency
(similarly, nondimensional peak) in Fig. 110 than in Fig. 99
can be attributed to the ordering effect of the vortex which tends
to diminish the quantity of large-scale, low-frequency disturbances.
The spectra of Figs. 109 and 110 can be considered to provide
bounds on the effects of sweep between 0° and 45°.
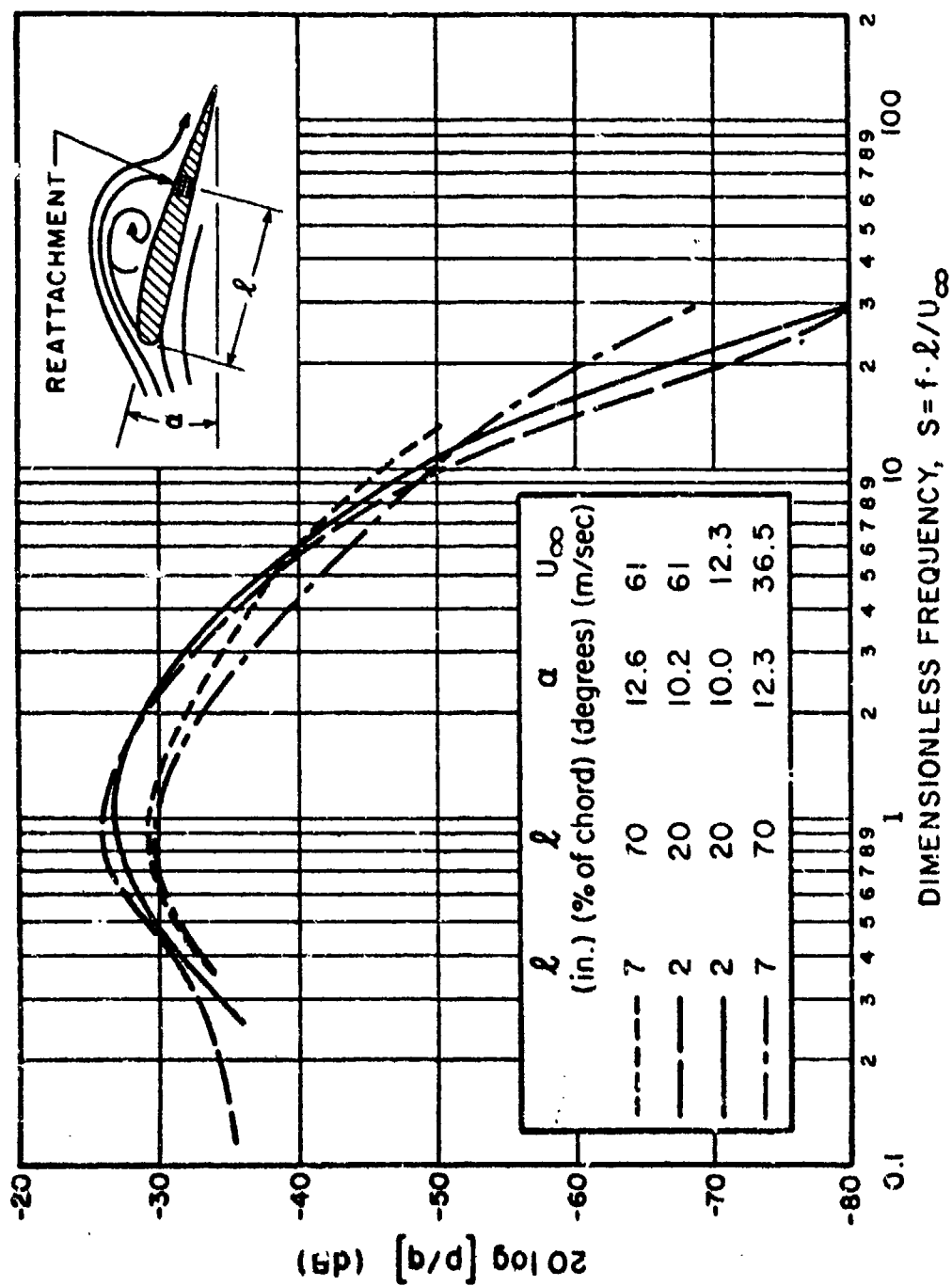
FIG. 109. NORMALIZED FLUCTUATING-PRESSURE SPECTRUM AT REATTACHMENT LOCATION ON NACA 0006 AIRFOIL [121]

p = rms pressure in third-octave band; q = free-stream dynamic pressure; f = frequency; U_∞ = free-stream velocity; ℓ = distance from leading edge to reattachment location in flow direction; α = angle of attack

CROSS-SECTION OF VORTEX
FLOW PATTERN
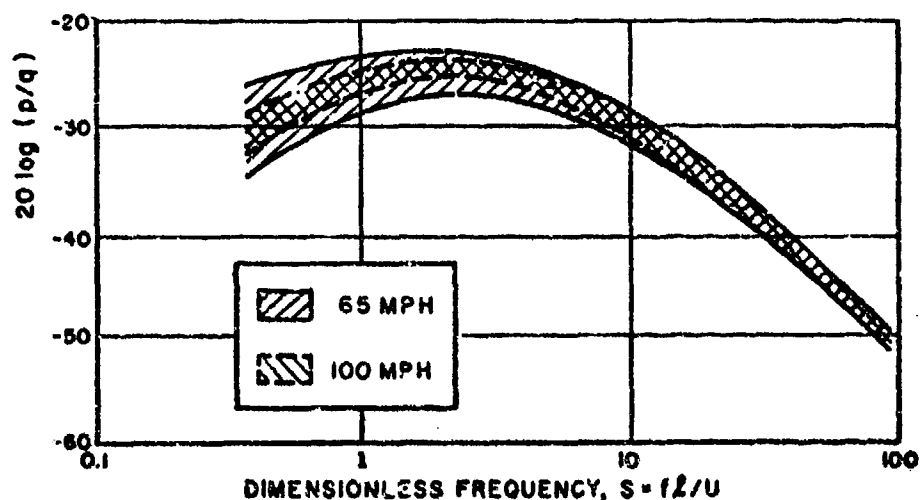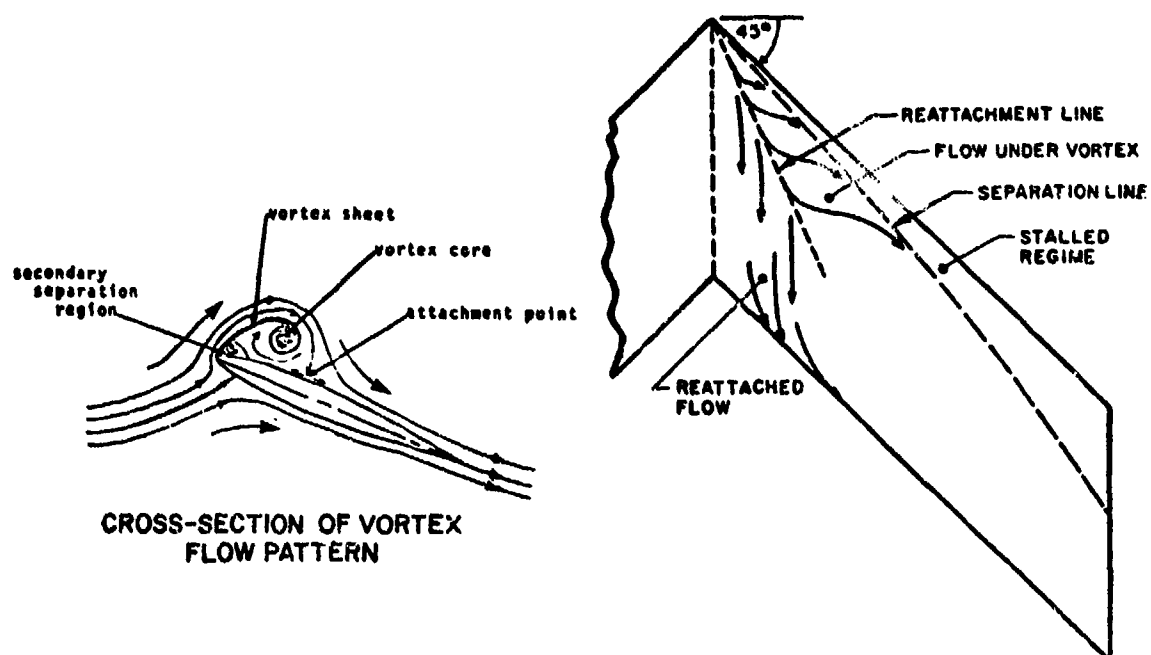
FIG. 110. NORMALIZED FLUCTUATING PRESSURE SPECTRUM IN VORTEX-
FLOW REGIME (on 45° - SWEPT WING) [121]

p = rms pressure in third-octave band; q = free-stream
dynamic pressure; f = frequency; U_∞ = free-strem velocity;
ℓ = distance from leading edge to reattachment location
in flow direction

5.4 Surface Pressure Fluctuations in Base Flow Regions

5.4.1 Introduction

The region of flow separation behind a blunt termination of
a body is referred to as base flow. A typical base flow region
is characterized by flow recirculation and turbulent vortex
shedding. Base flows are found behind blunt bodies, dive brakes,
spoilers, and the blunted rear of conical re-entry vehicles.
The data and prediction formulae reported in these sections are
the result of measurements on circular bases behind otherwise
streamlined shapes.

5.4.2 RMS pressure fluctuations

Subsonic data for base pressure fluctuations were obtained
by Eldred [122] for the blunt base of a cylinder with a stream-
lined nose. High Mach number measurements at the base of a cone
were reported by Chaump et al. [106]. A formula relating the
rms pressure to the base static pressure p_b and to the Mach
number M_b of the adjacent flow just outside the wake was developed
by Houbolt [123] and later modified by Chaump [106].

Figure 111 presents the rms pressure level as a function
of Mach number. Eldred observed that levels were higher away
from the centerline of the cylinder in his experiment; his
results (for $M < 0.4$), which may be summarized by

$$\frac{p_{rms}}{q_\infty} = \begin{cases} 1.5 \times 10^{-2} & \text{at 65\% radius} \\ \\ 7 \times 10^{-4} & \text{at the centerline} \end{cases} \tag{88}$$

are plotted in Fig. 111 on the basis of the assumption that

$$q_\infty \approx q_b = \frac{1}{2} \rho V_b^2 \approx \frac{1}{2} \gamma p_b M_b^2 \quad . \tag{89}$$

The high Mach number data of [106] are also indicated in Fig. 111. It is evident that there is a large Mach number interval for which no data is available; predictions for this interval cannot be made with high confidence.

The prediction formula suggested in [123] and modified in [106] is

$$\frac{p_{rms}}{p_b} = \frac{0.01 M_b^2}{1 + 0.04 M_b^2} \quad , \tag{90}$$

which is also plotted in Fig. 111.

For very low Mach number, Eq. (90) reduces to

$$p_{rms} = 0.14 \; q_b \quad ,$$

which is in general agreement with Eldred's results. At high Mach numbers, Eq. (90) approaches

$$p_{rms} = 0.25 \; p_b \quad ,$$

implying that the rms pressure level here depends only on the base static pressure.

It should be noted that the values of p_b and M_b must generally be determined from a knowledge of the aerodynamics
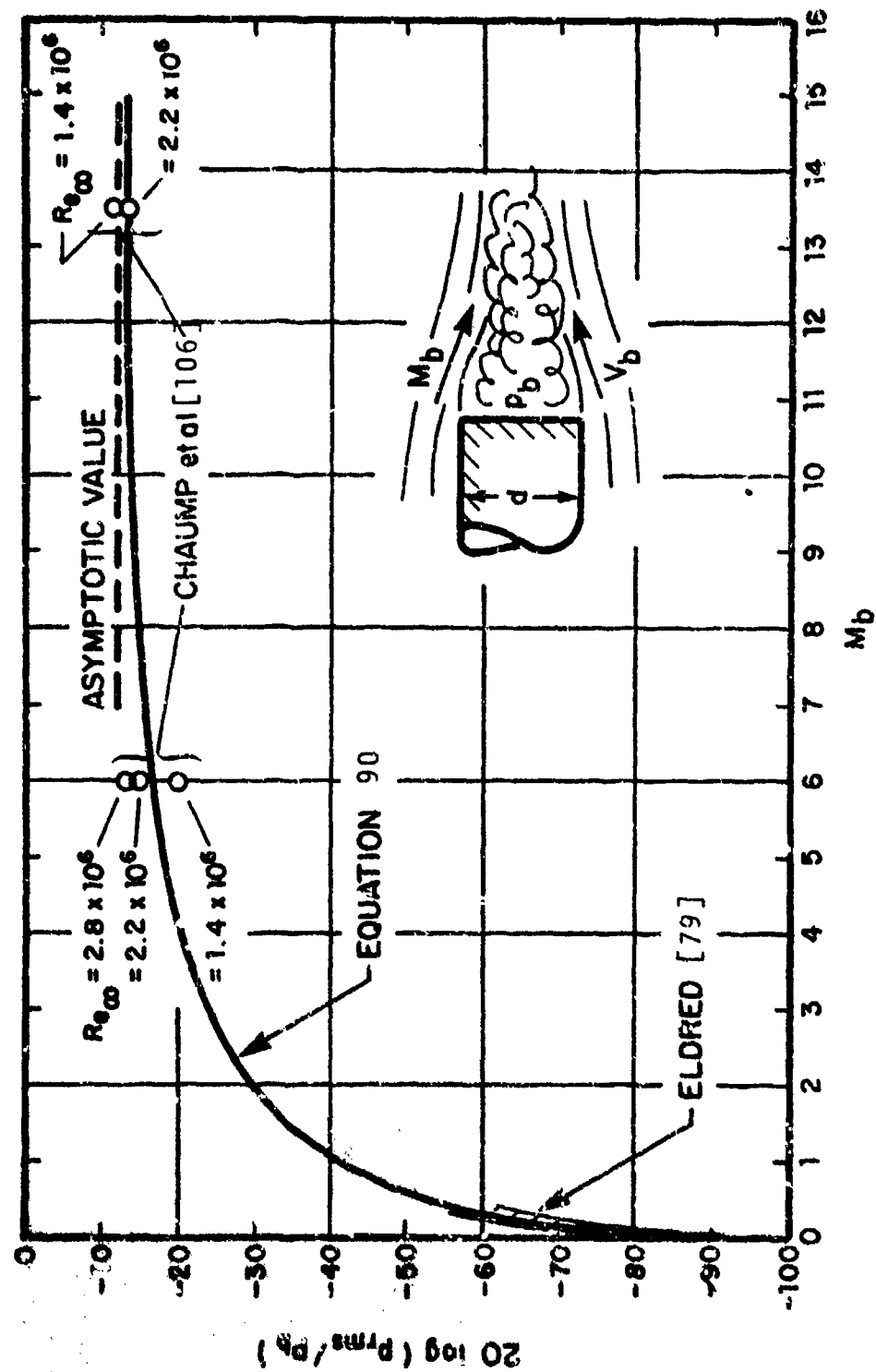
FIG. 111. RNS BASE PRESSURE FLUCTUATION LEVELS

of the particular configuration. The assumption that $q_\infty \approx q_b$ is appropriate for Eldred's experiment, because the flow is subsonic and the base region is at the end of a streamlined body with nearly parallel mean flow upstream of the base. For more blunt bodies in subsonic flow, and all bodies in supersonic and hypersonic flow, this assumption could lead to serious errors.

5.4.3 Power spectral density

A formula for the power spectral density, suggested in [106] on the basis of [123], is

$$\frac{S(f)V_b}{\overline{p}^2 d} = \frac{2}{1 + \left(\pi \, \dfrac{fd}{V_b}\right)^2} \tag{91}$$

This equation is plotted in Fig. 112, together with the low Mach number data envelope of [106], as reported in [123], and the high Mach number data envelopes of [106]. The agreement is seen to be relatively good, considering the large Mach number differences between the data sets.

5.4.4 Correlation functions

No data or validated procedures are available that are sufficiently general to warrant inclusions here. However, a formulation for the cross correlation $R(\tau)$ applicable to the base of a re-entry vehicle was developed by Houbolt [123] and is discussed in [106].
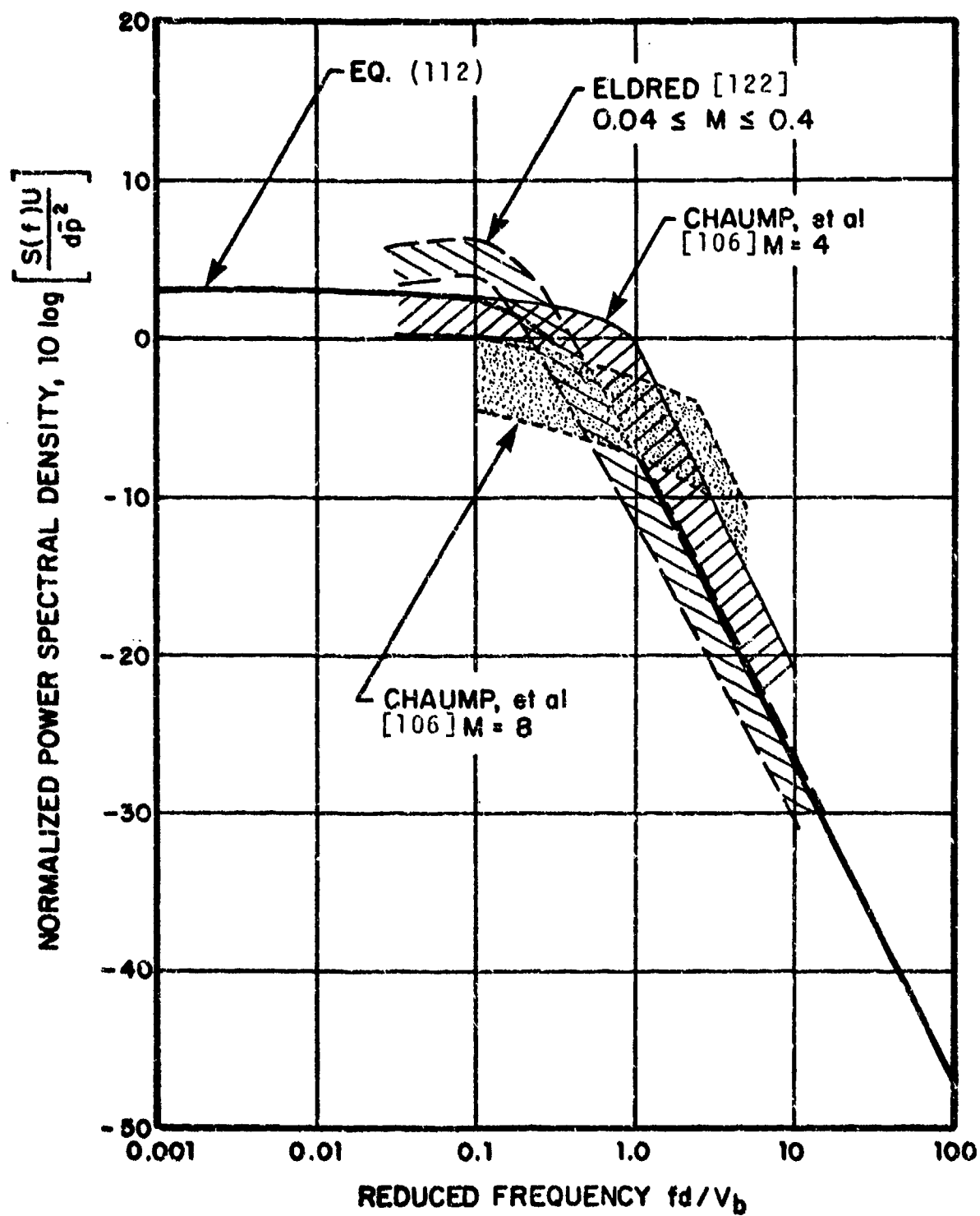
FIG. 112. ONE-THIRD OCTAVE BAND POWER SPECTRAL
DENSITY OF BASE PRESSURE FLUCTUATIONS

238

5.5 List of Symbols for Sec. V*

Symbol	Definition	Units†	
M	Mach number	---	
$R(\xi,\eta,t)$	space-time correlation function	lb^2/ft^4	(N^2/m^4)
$S(\omega);S(f)$	power spectral density	$lb^2 sec/ft^4$	$(N^2 s/m^4)$
U	free-stream velocity	ft/sec	(m/s)
U_c	convection velocity	ft/sec	(m/s)
$\bar{p}$	rms fluctuating pressure	lb/ft^2	(N/m^2)
q	dynamic pressure	lb/ft^2	(N/m^2)
u(y)	local flow speed	ft/sec	(m/s)
y	distance from solid boundary	ft	(m)
	boundary layer thickness	ft	(m)
δ^*	boundary layer displacement thickness	ft	(ns)
δ_t	transitional flow length perometer	ft	(m)
ξ,η	separation distances in axial and lateral directions	ft	(m)
ρ	air density	$slug/ft^3$	(kg/m^3)
τ	delay time	sec	(s)
$\phi(\xi,\eta,\omega)$	spectral density function	$lb^2 sec/ft^4$	$(N^2 s/m^4)$
ω	radian frequency	sec^{-1}	(s^{-1})

---

*Specially defined symbols, such as those for empirically determined constants, which are used only once in the text, are not included here. Such symbols are defined in the text where they occur.

The units given here are typical ones. SI units are given in parentheses where appropriate. Note that some empirical prediction methods require the use of specific units.

SECTION VI

CAVITY NOISE

6.1 Introduction

High-speed flow over cavities or cut-outs in aircraft surfaces frequently produces an intense acoustic field with single-frequency (tonal) pressure fluctuations. The fluctuating pressures can be high enough to jeopardize the integrity of nearby structural components or sensitive instruments, and can subject the areas adjacent to the cavity mouth to intense radiated sound fields.

Flow-induced pressure oscillations in cavities have been studied extensively, particularly for the basic rectangular cavity configuration shown in Figure 113. This configuration is of considerable practical interest itself, but also represents geometries that do not deviate too greatly from the basic rectangular shape. Presently available information permits one to make reasonable estimates of the frequency, levels and modal behavior for shallow rectangular cavities (i.e., for length-to-depth ratios greater than 2) in flows that have boundary layer thicknesses that are much smaller than the cavity depth. The rectangular cavities that have been studied to date tend to respond two-dimensionally; the cavity width seems to be of little importance. Pressure variations do occur in the depth direction, but these variations usually are small.

The oscillation process occurs because of two factors: (1) interaction between the pressure modes within the cavity and the shear layer over the cavity mouth; and (2) interaction of this shear layer with the cavity trailing edge. If the shear layer that impinges on the cavity trailing edge is deflected slightly, then there results a net mass addition or removal at the rear of the cavity; this variable mass
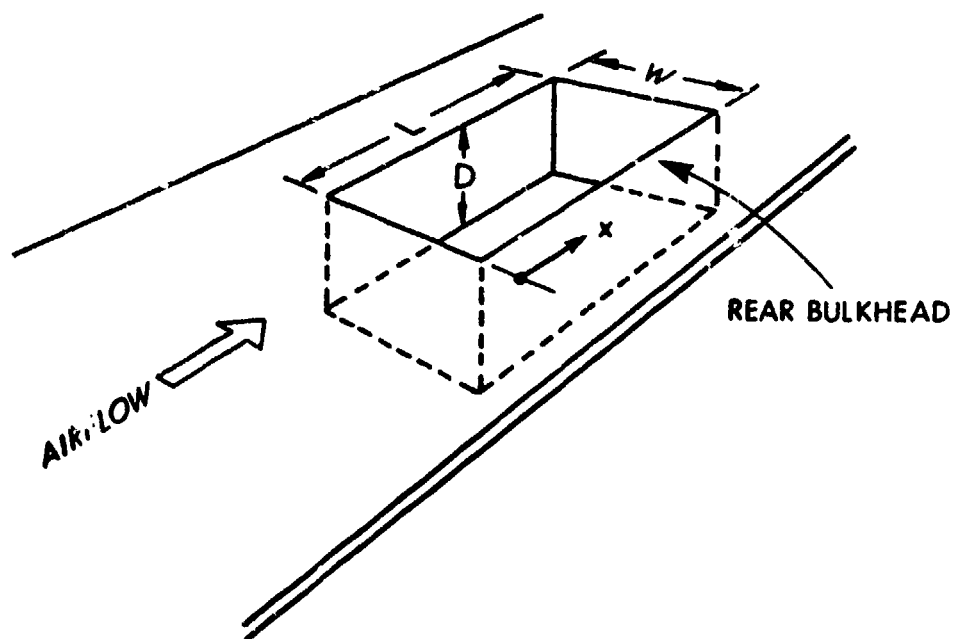
FIG. 113. RECTANGULAR CAVITY.

addition has an effect similar to that of replacing the rear
bulkhead with a moving piston, which excites pressure modes
in the cavity. Under some conditions, the shear layer motion
and the trailing edge mass addition reinforce each other,
setting the system into intense oscillations. The amplitude
is controlled by damping and nonlinearity effects, which often
cause the shear layer to roll up into discrete vortices. Typi-
cally, oscillations begin to appear at low Mach numbers and
become most intense slightly above M = 1.0; at very high Mach
numbers, say M > 3.0, the oscillations are often found to
decrease.

6.2 Prediction of Tonal Frequencies

The oscillation frequencies of shallow cavities (say
$L/D \geq 2.0$) can be predicted with reasonable accuracy by the
modified Rossiter Equation [124],

$$f_n = \frac{U}{L} \frac{(n - 0.25)}{\left[\dfrac{M}{\left(1 + \frac{\gamma-1}{2} M^2\right)^{1/2}} + 1.75 \right]} \quad , \quad n = 1,2,3\ldots \qquad (92)$$

where f_n denotes the frequency of the nth mode, U represents
the free stream speed M the Mach number, L the cavity length,
and $\gamma = 1.4$ is the ratio of specific heats of air. This for-
mula is derived from a semi-empirical form originally suggested
by Rossiter [125], modified to account for the nearly adiabatic
temperature recovery in the cavity.

In Figure 114, results calculated from Equation (92) are
compared to the best available data. One may note that the
predictions best match the data for M > 0.5. For M < 0.5, the
data and Equation (92) agree less well, and there is some
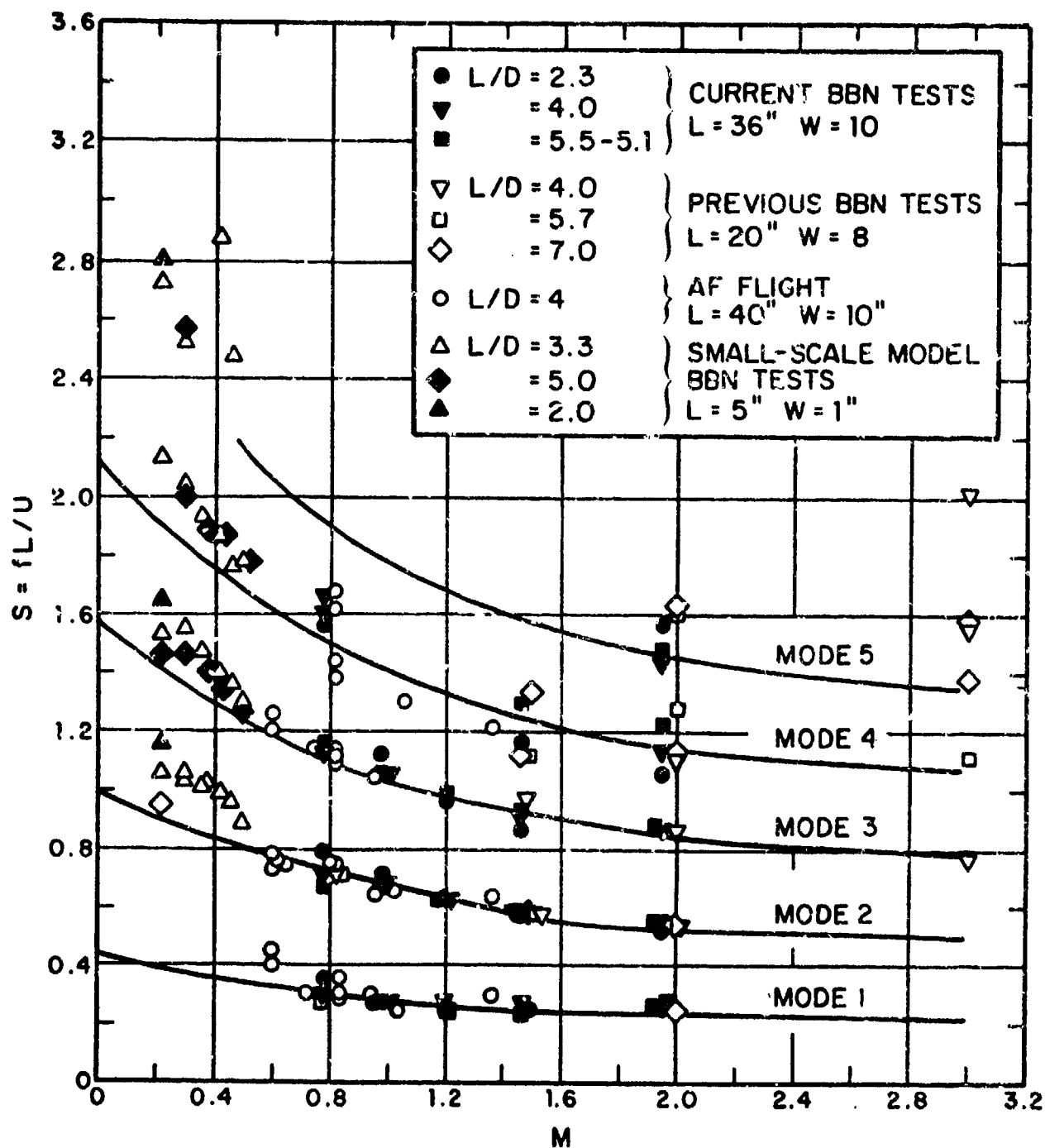
FIG. 114. STROUHAL FREQUENCIES OF CAVITY MODES AS FUNCTION
OF MACH NUMBER [126].

243

evidence of a systematic L/D dependence; however, one should note that the low Mach number data is all based on tests of rather small-scale models.

For deep cavities that respond primarily in depth modes, the oscillation frequencies (at least for low Mach numbers) may be expected to correspond to the resonance frequencies of a pipe that is open on one end and closed on the other, namely

$$f = \frac{2n-1}{4} \frac{c}{D} \qquad n = 1,2,3\ldots \tag{93}$$

where c denotes the speed of sound in air. At higher Mach numbers, the shear layer over the cavity mouth may contribute an effective stiffening effect at the open end, leading to deviations from Equation (93).

Frequency prediction is most uncertain for cavities that are neither clearly shallow nor deep, say for $1.0 < L/D < 2.0$, for which the modal response is difficult to anticipate and for which occurance of "shallow" or "deep" cavity behavior may depend on Mach number (with increasing Mach number tending to make cavities effectively more shallow) [126].

6.3 Prediction of Mode Shapes and Level In Cavities

Two approaches are reviewed here: (1) that of Shaw and Smith [127], whose curve is fitted to Air Force flight test data, and (2) that of Heller and Bliss [126], which is based on wind tunnel tests. Both of these involve the modal frequencies as determined from Equation (92).

6.3.1 The Method of Shaw and Smith

According to this method, the peak sound pressure $\hat{P}_n$ in the one-third octave bands containing the first three cavity oscillation frequencies are obtained from the following relations:

$$20 \log (\hat{P}_2/q) = 9.0 - 3.3 (L/D) + 20 \log (-M^2 + 2M - 0.7)$$

(94a)

$$20 \log (\hat{P}_1/q) = 20 \log (\hat{P}_2/q) - 2(L/D)^2 + 26(L/D) - 86$$

(94b)

$$20 \log (\hat{P}_3/q) = \begin{cases} 20 \log (\hat{P}_2/q) - 11, \text{ for } L/D < 4.5 \\ 20 \log (\hat{P}_2/q), \quad \text{ for } L/D \geq 4.5 \end{cases}$$

(94c)

Here $\hat{P}_n$ represents the maximum value of the fluctuating pressures associated with the nth mode (which maximum pressure occurs near the rear bulkhead) and q denotes the free-stream dynamic pressure.

The variation of the one-third octave band pressure amplitude with distance from the cavity leading edge (i.e., the pressure mode shape) is given by

$$20 \log [\hat{P}_n(x)/q] = 20 \log [\hat{P}_n/q] - 10 \log \left[1.0 + (0.33 L/D - 0.60)(1-x/L) - |\cos(\alpha_n x/L)| \right], \; n = 1,2,3$$

(95)

where $\alpha_1 = 3.5$

$\alpha_2 = 6.3$

$\alpha_3 = 10.0$

6.3.2 The Results of Heller and Bliss

In a series of wind tunnel tests, Heller and Bliss [126] measured pressures at the front and rear of a variable depth cavity and carried out corresponding mode shape surveys. Some of their results are reproduced here, both as the basis for an alternative prediction scheme and to provide an indication of the variation between predictions.

Figures 115 and 116 show one-third octave band pressure levels measured in the cavity front and rear bulkhead regions, for three modes and three length-to-depth ratios, as a function of Mach number. Note that different modes are dominant in different parts of the Mach number range. Also shown in these figures is some of the Air Force flight test data on which the previously discussed method is based, as well as data points from several other tests. The sometimes considerable spread in the data suggests that factors other than those currently taken into account in prediction schemes and scaling methods (e.g., Reynolds number, cavity width, upstream boundary layer thickness) may also be important.

Figures 117 and 118 show measured mode shapes at Mach numbers of 0.8 and 1.0, respectively, for length-to-depth ratios of 2.3, 4.0 and 5.1. In Figure 117, Air Force flight test data points are again shown for comparison. By taking the most rearward value shown to be 3 dB above the trailing-edge levels given in Figure 116, one obtains modal pressure distributions that are within the experimental error. In general, however, it may be more convenient to obtain mode shapes using the method of Shaw and Smith.

FIG. 115. MACH NUMBER DEPENDENCES OF RESONANT MODE LEVELS IN LEADING-EDGE AREAS OF CAVITIES [126].

FIG. 116. MACH NUMBER DEPENDENCES OF RESONANT MODE LEVELS IN
TRAILING-EDGE AREAS OF CAVITIES [126].

248
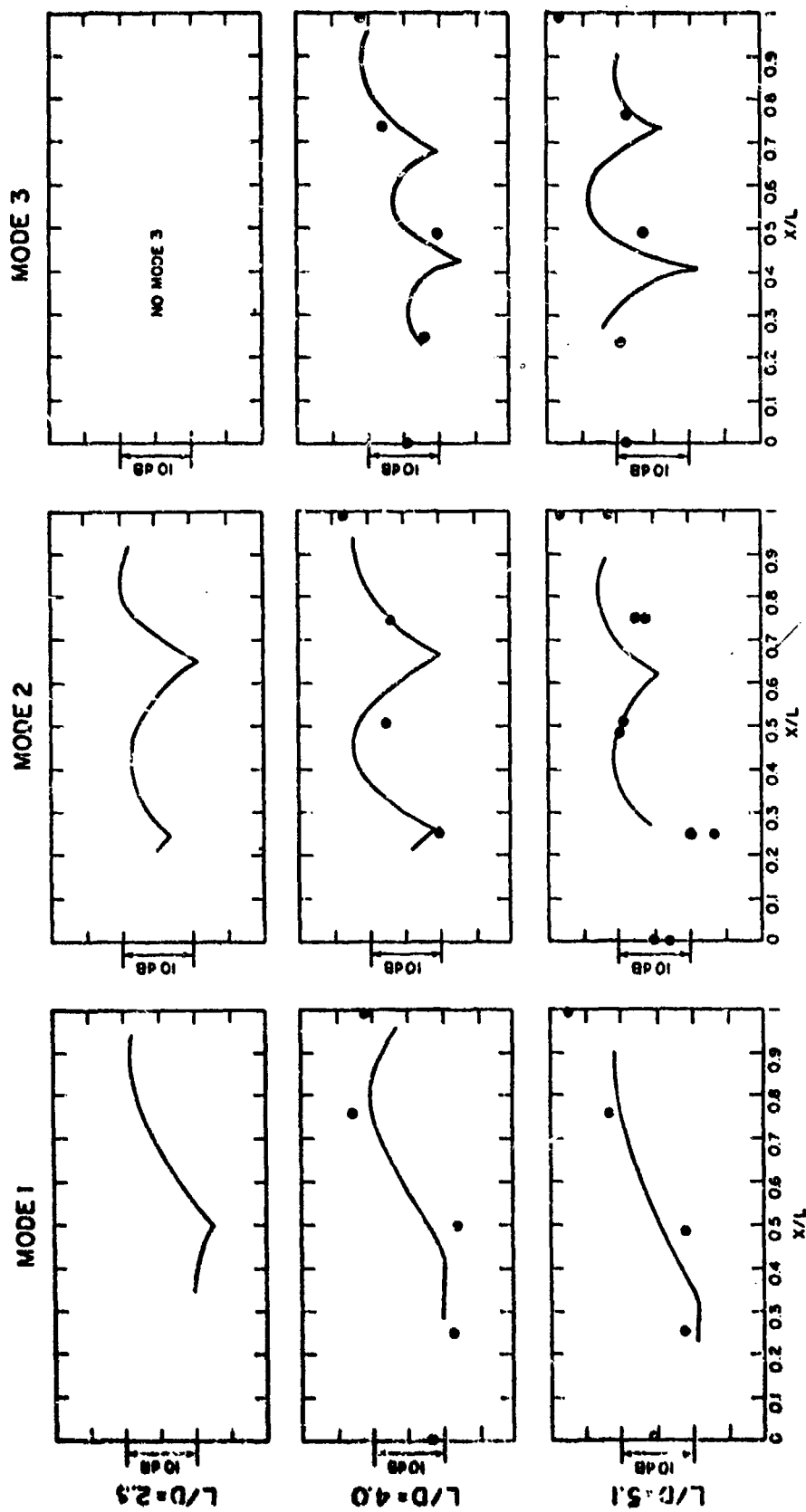
FIG. 117. MODE SHAPES FOR CAVITIES WITH VARIOUS LENGTH-TO-DEPTH RATIOS,
M = 0.8 (continuous lines - Heller and Bliss [126]; data points -
Air Force flight test results).

249

FIG. 118. MODE SHAPES FOR CAVITIES WITH VARIOUS LENGTH-TO-DEPTH RATIOS M = 1.0 (Heller and Bliss [126]).

250

6.4 Prediction of Broadband Spectra In Cavities

According to Shaw and Smith [127], one may determine the one-third octave band spectrum from Figure 119, with the pressure P_b corresponding to the peak of this spectrum given by

$$20 \log [P_b(x/L)/q] = 20 \log (\hat{P}_2/q) + 3.3(L/D) - 28$$
$$+ .3(1-L/D) (1-x/L) \qquad (96)$$

One may note that Equation (96) provides for dependence on length-to-depth ratio and on distance from the cavity leading edge, and that $\hat{P}_2/q$ can be determined from Equation (94a).

The narrow region into which the broadband spectra obtained by Heller and Bliss collapsed for fairly wide ranges of Mach numbers and length-to-depth ratios is illustrated in Figure 120. Also shown in this figure is the result obtained by substituting Equation (94a) into (96), which then becomes independent of L/D for x/L = 1.0 (i.e., for the trailing edge region). The agreement may be seen to be quite reasonable.

6.5 Consecutive Cavities

Closely spaced cavities arranged one behind the other sometimes occur in aircraft designs. In such arrangements, one may expect to be able to treat the upstream cavity as being un-affected by the presence of the downstream cavity, but one may expect the downstream cavity to be affected by the upstream one. The downstream cavity is likely to be subjected to a much thicker incident boundary layer due to the upstream cavity, and this incident flow will contain strong periodic disturbances due to the oscillation of tne upstream cavity. However, since thickening the incident boundary layer tends to reduce pressure os-cillations, while the presence of upstream disturbances at the proper frequencies tend to increase these oscillations, these

251
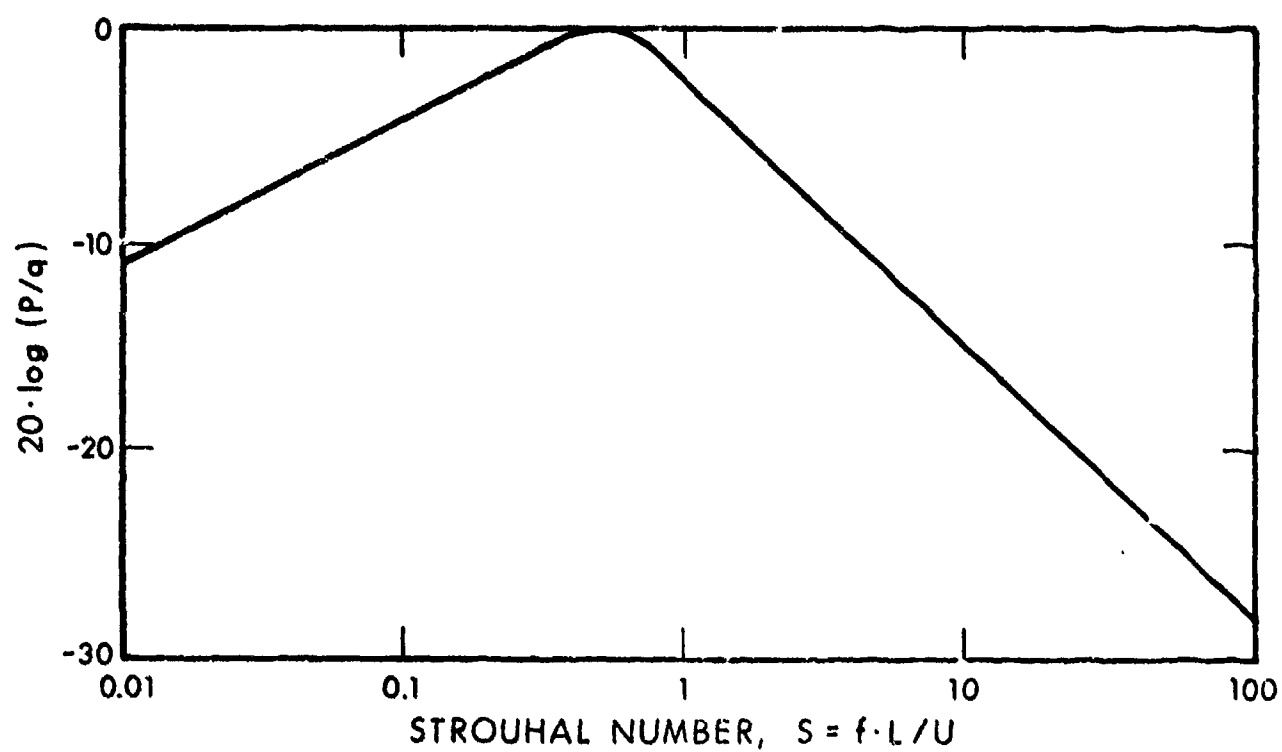
FIG. 119.   BROADBAND CAVITY NOISE SPECTRUM SHAPE, ACCORDiNG
TO SHAW AND SMITH [127].
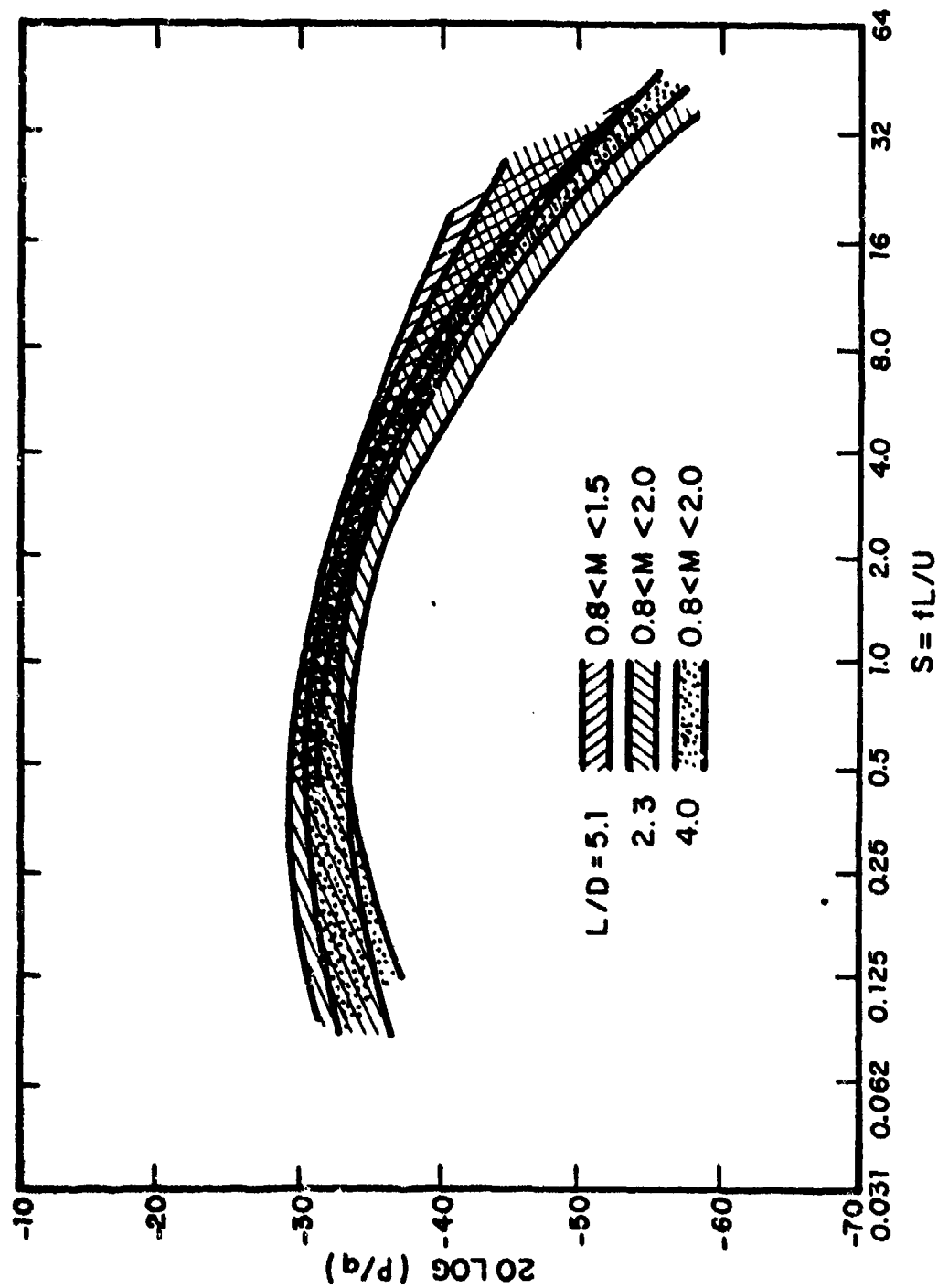
FIG. 120. ENVELOPE OF ALL NONDIMENSIONAL BROADBAND SPECTRA IN 1/3-OCTAVE BANDS AT CAVITY TRAILING EDGE, AS FOUND BY HELLER AND BLISS [126], COMPARED WITH THE RESULTS OF SHAW AND SMITH [127].

two contributions may in effect cancel each other. If the cavities are very closely spaced, the downstream cavity is likely to "lock-in" on the upstream one, so that the two will oscillate almost exactly in phase.

Although consecutive cavities have not been studied extensively, some corresponding leading and trailing edge spectra were measured [126] in consecutive cavities with L/D=3. The corresponding spectra in the front and rear cavities were found to be very nearly identical, particularly as regards the broadband portions. Figure 121 shows the observed differences between the front and rear cavities levels in the transonic and supersonic Mach number range. The data indicates that (1) the differences between the pressures in consecutive cavities may not be great, and (2) there is a general trend towards higher pressure levels in the rear cavity with increasing Mach number.

6.6 Effect of Internal Stores

The presently available information is not sufficient for the systematic prediction of the effect of inserting a given store into a given cavity, particularly since an almost infinite variety of store and cavity configurations is possible. This section therefore only reviews the available results, in order to indicate the nature of the effect and to provide very general guidelines.

The insertion of an internal store into a cavity has often been observed to produce a slight reduction in the oscillatory pressure levels. [124, 128, 129]. The reduction is more dramatic if the store(s) interfere directly with the cavity shear layer over a substantial fraction of the cavity length and span.

254
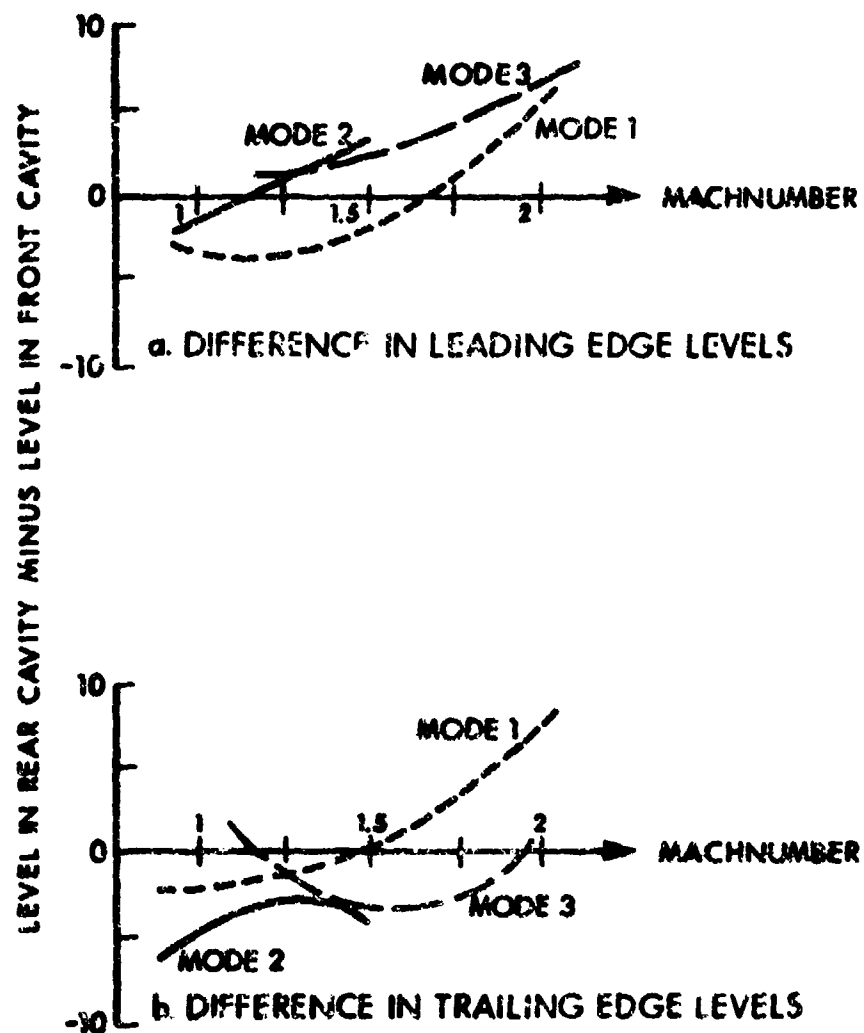
FIG. 121. COMPARISON OF NODAL PRESSURE LEVELS IN CONSECUTIVE CAVITIES OF L/D = 3, AS A FUNCTION OF MACH NUMBER (based on Heller and Bliss [126]).

Apparently, this interference tends to reduce the shear layer motion that is essential to the oscillation process. Figure 122 summarizes the results of Heller, Holmes, and Covert [130] for one and two cylindrical ogive nose-cone stores in a simple rectangular cavity. Tests were performed with the store(s) attached to the movable floor of the model. The distance between the top of a store and the cavity mouth varied as a function of L/D; at L/D=7.0 the outer surface of a store was just in line with the cavity mouth. Notice that in some cases the presence of a store actually caused a slight increase in fluctuating pressure level.

6.7 Noise Radiation To Outside of Cavities

Relatively little quantitative information is available regarding the noise radiation from cavities. Pressure levels on external surfaces immediately upstream and downstream of cavities have been measured by several investigators [124, 126 129, 131]. Their results indicate that the levels measured on adjacent upstream and downstream surfaces, at distances not exceeding the cavity depth dimension, are very nearly equal to those measured in the cavity at the front and rear bulkheads. (Note that disturbances can travel upstream through the subsonic portion of the boundary layer, even in supersonic flow, and intense upstream disturbances were found to persist at supersonic speeds.) Pressure measurements on surfaces to the sides of cavities appear not to have been made, but levels commensurate with adjacent points in the cavity can be expected. Thus, pressures on surfaces around an oscillating cavity may be expected to be dominated by the effects of that cavity, and the pressure levels may be expected to be very nearly equal to those within the cavity, for a distance of at least one cavity depth dimension around the cavity mouth.
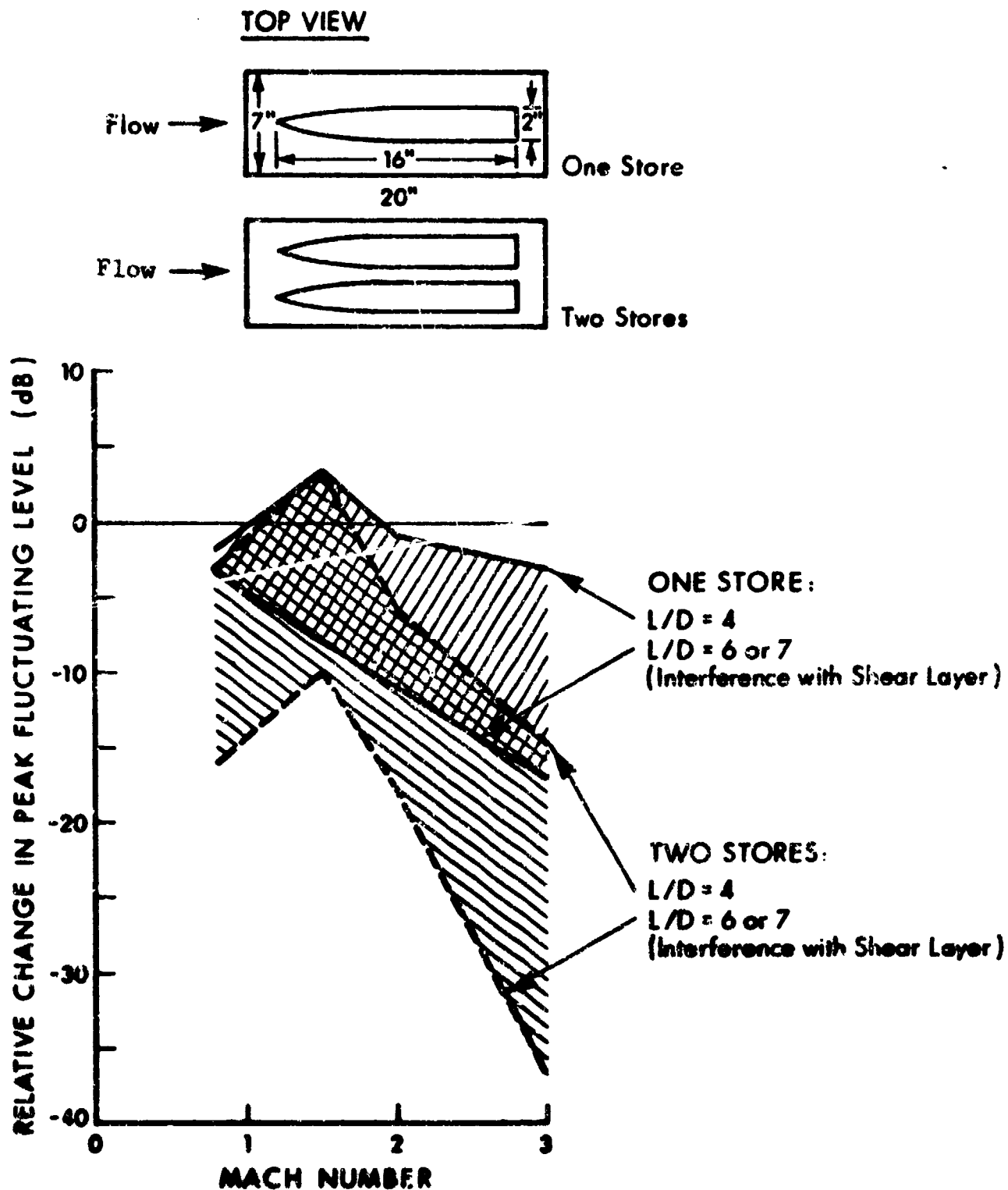
FIG. 122. THE EFFECT OF ONE AND TWO CYLINDRICAL OGIVE NOSE CONE STORES ON THE PEAK PRESSURE FLUCTUATION LEVELS IN OSCILLATING CAVITIES (BASED ON HELLER, HOLMES, AND COVERT) [130].

Schlieren photographs of the external radiation pattern from cavities have been made by several researchers, e.g., [125], [132]. At supersonic speeds, the radiation is extremely directional, with the most intense region falling in a "beam" between the Mach cones at the leading and trailing edges. The most intense portion of the beam is likely to be in the direction normal to the cavity mouth, where it is not likely to affect aircraft surfaces. However, any portions of the aircraft surface which intercept the region between the Mach cones may be expected to be subjected to portions of the intense radiated field, quite possibly for substantial distances away from the cavity. Unfortunately, no quantitative data is presently available to allow estimation of this potentially important nearfield noise source. At high subsonic speeds the radiation still appears directional, but is no longer confined to a narrow beam; the most intense radiation appears to be in the forward arc.

At low subsonic speeds, a cavity radiates sound nearly like a simple monopole [135]. The source of the monopole is presumably the mass addition and removal process at the cavity trailing edge. The mean square pressure $\bar{p}^2$ radiated by this monopole may be estimated from

$$\bar{p}^2 = \left[0.035 \; qS \; \frac{W}{r}\right]^2 \tag{97}$$

where q denotes the dynamic pressure, $S = f_n L/U$ is the Strouhal number given by Figure 114 or Equation (92), W represents the cavity width and r is the distance from the cavity trailing edge to the observation point. Equation (97) generally overestimates the pressure levels; it is not applicable for $M>0.3$ or for modes above the third.

6.8 Suppression Devices

Several devices which can be used to reduce cavity oscillation levels substantially were investigated by Heller and Bliss [126]. As a general rule, all suppression devices are more effective at higher values of L/D, quite possibly because the levels to be suppressed are generally less intense in this case.

Suppression of pressure oscillation in cavities was achieved by placing small spoilers or vortex generators just upstream of the cavity leading edge, which spoilers extend through the upstream boundary layer and are set at high angles of attack so as to disturb the incident flow significantly and to thicken the shear layer over the cavity mouth. In a Mach number range of 0.8 to 1.5 and for length-to-depth ratios between 2.3 and 5.1, the dominant second-mode tone was always reduced by at least 10 dB and was often suppressed entirely. The first mode tone was always suppressed by at least 5 dB and often entirely. The effect of the spoilers on the higher mode tones was less systematic; in some cases they produced substantial reductions, in others, none.

Another effective suppression means consisted of cutting back the upper portion of the cavity trailing edge at a 45 degree slant. This modification has the effect of stabilizing the shear layer impingement process at the cavity trailing edge. In order to achieve this stabilization, the height of the slanted region must exceed the shear layer thickness at the rear of the cavity, so that typically the slant height must exceed 0.2L. When tested in the same Mach number range as the aforementioned spoilers, the slanted trailing edge resulted in reductions of the dominant second mode level by at

259

least 15 dB, and in reductions of 5 to 20 dB in the first mode levels. Some suppression of the third mode levels was usually obtained as well. A reduction of the broadband spectrum level of at least 5 dB was also achieved, except at high frequencies (typically beyond the third mode level).

Leading edge spoilers, in combination with a trailing edge slant, provided more effective suppression than each of the two modifications used separately, but the effects of these two devices are not directly additive; often the first three modes were suppressed entirely. This combination was also found effective in suppressing oscillations in consecutive cavities.

Another suppression device, a slotted trailing edge cowl, was found to be quite effective, but its effectiveness appears to be quite sensitive to its shape and location.

6.9 Illustrative Calculation and Comparison

6.9.1 Problem Statement

Compute the trailing edge spectrum and the shape of the second mode of a cavity 10 ft. long with L/D = 5.0 for M = 1.0 at sea level. Estimate the effect of inserting two cylindrical stores. Estimate the minimum reduction in levels obtained by using simple oscillation suppression devices.

6.9.2 Results

At sea level the density is $\rho = 2.38 \times 10^{-3}$ lb/ft^3 and the sound speed is c = 1120 ft/sec. Thus, at M = 1.0, U = 1120 ft/sec and q = 149 lb/ft^2.

The resonance frequencies found from Equation (92) are:

$$f_1 = 31.5 \text{ Hz} \qquad f_2 - 73.6 \text{ Hz} \qquad f_3 = 115.7 \text{ Hz}$$

The peak third-octave band sound pressure levels, as determined from Equation (94) are:

$$20 \log (\widehat{P_2}/q) = -17.96$$

$$20 \log (\widehat{P_1}/q) = -23.96$$

$$20 \log (\widehat{P_3}/q) = -17.96$$

The leading and trailing edge levels, $20 \log [P_n(x)/q]$, found by use of Equation (95) with x/L = 0 and 1, respectively, are listed below, together with corresponding wind tunnel results from Figures 116 and 117, with the latter shown in parentheses.

n	Leading Edge		Trailing Edge	
1	– 28.5	(–27)	–18.0	(–18)
2	– 34.5	(–33)	–24.6	(–21)
3	– 28.5	(–35)	–20.0	(–23)

Broadband levels predicted from Figure 120 are shown in Figure 123. Agreement between the two methods of prediction is seen to be relatively good.

Figure 124 shows the shape of the second mode computed from Equation (95), together with the corresponding experimental mode shape from Figure 118. (Since Figure 118 does not show absolute levels, its level was determined by extrapolating the shape to the trailing edge point, where the level is known from Figure 117.) It is apparent that the two mode shapes, although qualitatively similar, show appreciable quantitative differences at some locations in the cavity.

The range of effect of inserting two cylindrical stores in the cavity can be estimated from Figure 122. One would be conservative in assuming that there is no effect at this Mach number. However, depending on the configuration, Figures 5.10 suggests that a reduction in peak level of as much as 10 dB might actually occur.

Figure 123 shows that the first three modal peaks extend a little more than 10 dB above the broadband spectrum. The addition of upstream spoilers will reduce these peaks by at least 5 dB, and very likely much more. A trailing edge slant, or a slant and spoiler combination, can be expected to reduce all three peaks to the broadband level.
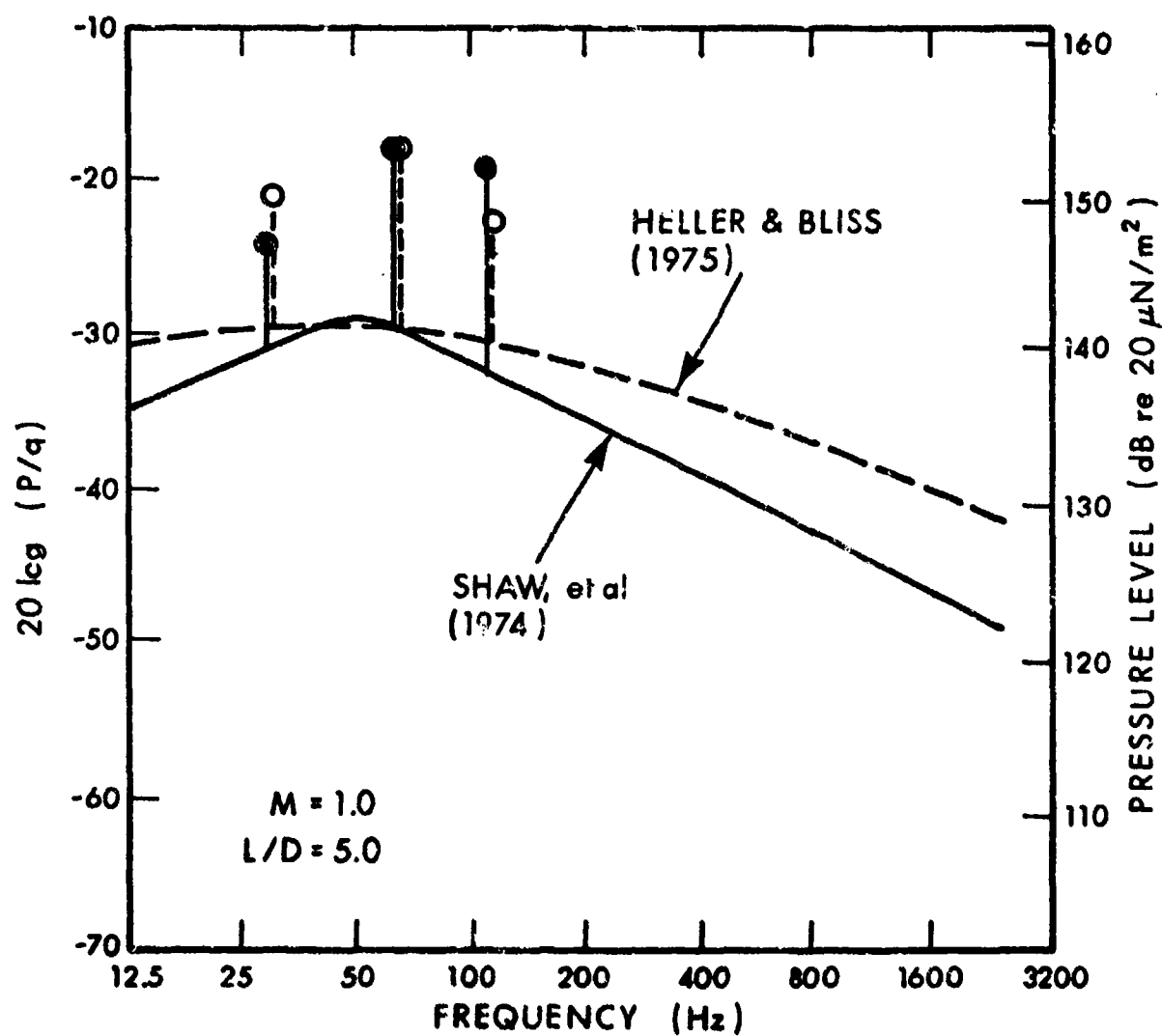
FIG. 123. ILLUSTRATIVE COMPARISON OF ESTIMATED CAVITY TRAILING EDGE FLUCTUATING PRESSURE SPECTRA.
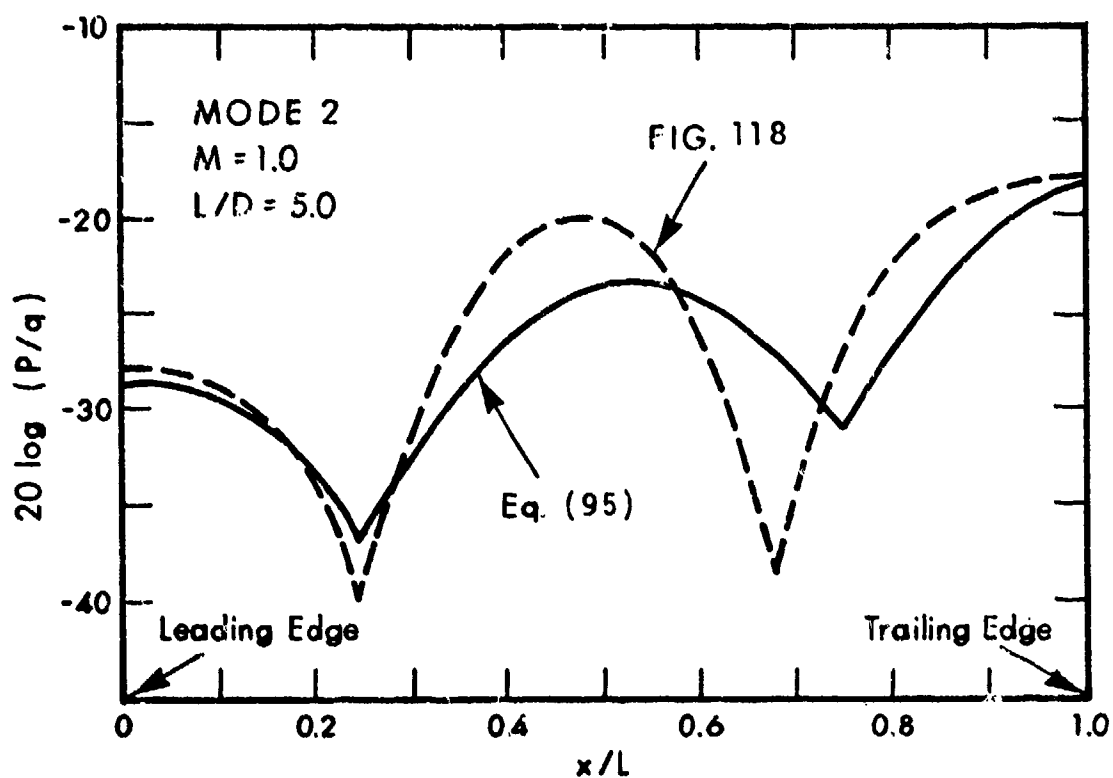
FIG. 124. ILLUSTRATIVE COMPARISON OF CALCULATED AND MEASURED SHAPE OF SECOND MODE OF A CAVITY.

6.10 List of Symbols for Sec. VI*

Symbol	Definition	Units[†]	
D	cavity depth	ft	(m)
L	cavity length	ft	(m)
M	Mach number	---	
$\hat{P}_n$	peak sound pressure in nth mode	lb/ft²	(N/m²)
S	Strouhal number	---	
U	free-stream velocity	ft/sec	(m/s)
W	cavity width	ft	(m)
c	speed of sound in air	ft/sec	(m/s)
f_n	frequency of nth mode	Hz	
n	mode number	---	
$\overline{p^2}$	mean-square pressure	lb/ft²	(N/m²)
q	dynamic pressure	lb/ft²	(N/m²)
γ	ratio of specific heats of air	---	

---

*Specially defined symbols, such as those for empirically determined constants, which are used only once in the text, are not included here. Such symbols are defined in the text where they occur.

†The units given here are typical ones. SI units are given in parentheses where appropriate. Note that some empirical prediction methods require the use of specific units.

SECTION VII

BLAST PRESSURES GENERATED BY ARMAMENT

7.1 Overview of Literature

The key conclusions one may draw from the available literature (Refs. [134] - [144]) are:

(a) In order to account for the different basic blast-generation mechanisms and the correspondingly different blast fields, one may consider weapons in three groups:

Closed-breech weapons
Open-breech weapons
Rockets.

(b) Closed-breech weapons have been studied widely; corresponding scaling laws and blast-field prediction techniques are well developed.

(c) Open-breech weapons also have been investigated to a considerable extent, and much data is available.● The back-blast through the nozzle at the breech tends to be more severe than the muzzle blast.

(d) Although steady-state noise fields from rockets exhausts can be predicted reliably, attempts to scale and predict blast fields from rockets generally have been unsuccessful.

(e) For weapons fired from high-speed aircraft, the forward motion of the aircraft results in increasing the effective blast energy forward of the blast source and in decreasing that aft of the source.

7.2 Scaling of Blast Fields From Stationary Explosives

Scaling laws for blast fields about weapons have their origin in the scaling laws used for explosives. Therefore it is helpful to review the scaling laws for explosives that are stationary; the theory must be modified considerably to account for motion of the explosive. (However, moving explosions best describe the blast fields generated by weapons.) In 1915, Hopkinson established a pair of scaling laws relating peak overpressure and positive impulse to charge weight (or charge energy) and standoff distance. These laws may be expressed in the following forms:

$$\Delta P = \Pi_1 \; (L/W^{1/3})$$
$$I/W^{1/3} = \Pi_2 \; (L/W^{1/3}) \tag{98}$$

or

$$\Delta P = \Pi_1 \; (L/E^{1/3})$$
$$I/E^{1/3} = \Pi_2 \; (L/E^{1/3}) \tag{99}$$

or

$$\Delta P = \Pi_1 \; (L/d)$$
$$I/d = \Pi_2 \; (L/d) \tag{100}$$

where Π_1 and Π_2 represent functions and

ΔP = free-field peak overpressure (psi)
I = positive impulse (area under positive overpressure time history) (psi-msec)
L = standoff distance (distance from explosion center to observer) (ft)
W = charge weight (proportional to E and to d^3) (lb)
E = energy release of explosion = $(1.55 \cdot 10^6 \; \text{ft} \cdot \text{lb/lb}) \cdot W$ for TNT (ft-lb)
d = equivalent spherical diameter of charge (ft)

TNT is generally taken as the standard against which the "yield" of other explosive materials is evaluated. Figure 125 shows curves of ΔP and $I/W^{1/3}$ as functions of $L/W^{1/3}$ for TNT explosions
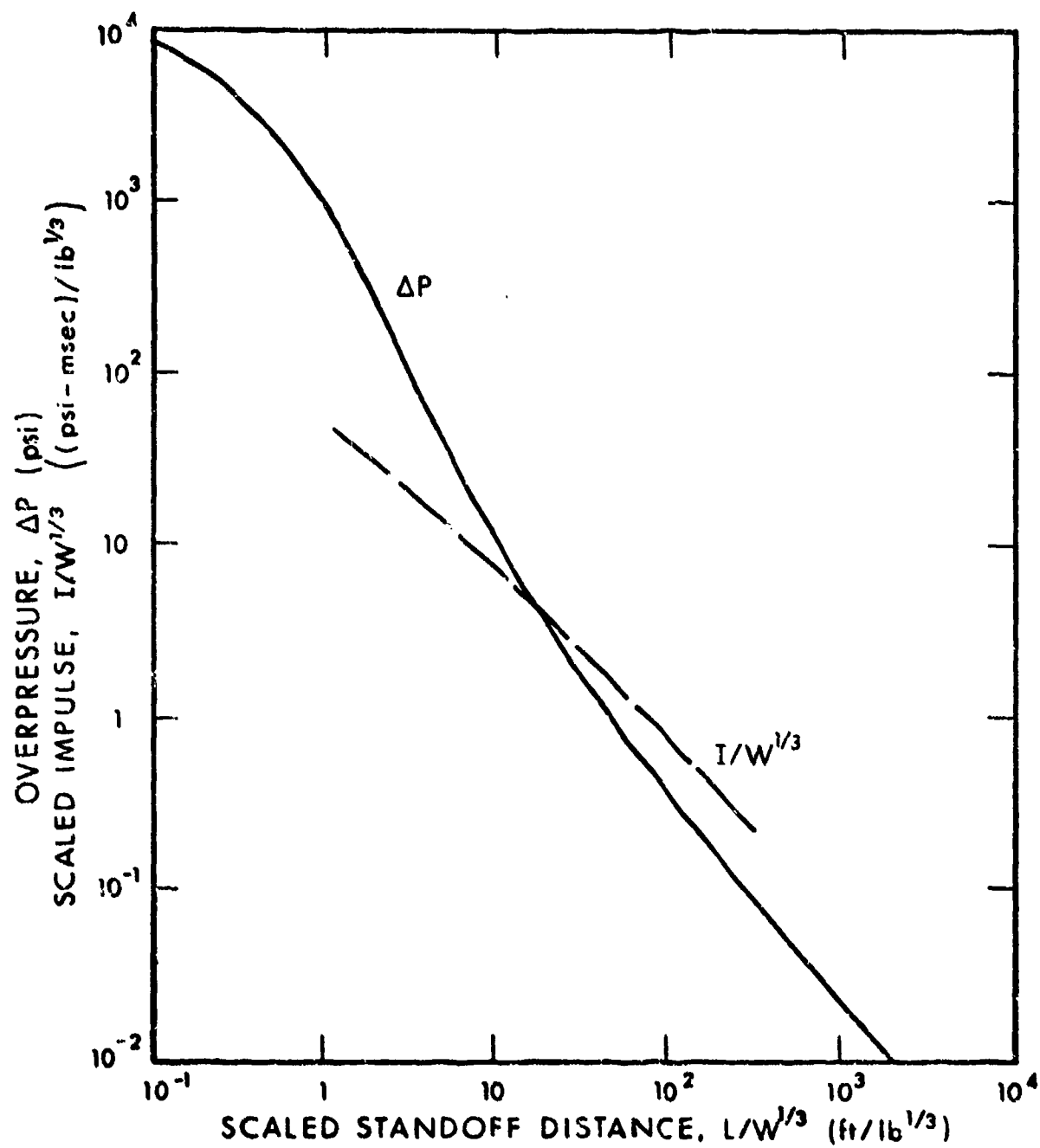
FIG. 125. EMPIRICAL RELATIONSHIPS BETWEEN OVERPRESSURE, IMPULSE,
CHARGE WEIGHT AND STANDOFF DISTANCE FOR GROUND SURFACE
FIRING OF TNT [134].

occurring at the surface of the ground. These curves were developed as the result of statistically averaging a large quantity of blast measurements.

The above scaling laws, when generalized to stationary explosions occurring at any altitude above the ground, where reduced ambient air pressure effects must be included, may be written as

$$\Delta P/Po = \Pi_1 [L/(E/P_O)^{1/3}]$$

$$I/(E/Po)^{1/3} = \Pi_2 [L/(E/P_O)^{1/3}] \tag{101}$$

where P_O is the ambient atmospheric pressure (psi). All of the above scaling laws correspond to free-field blasts, for which the direct blast wave dominates and there are no reflections from ground or other surfaces.

7.3 Scaling of Free-Field Blasts From Stationary Weapons

Scaling laws for free blast fields around stationary weapons are developed in a manner similar to those of Section 6.2 above, except that the parameters are modified to account for the more complicated blast fields generated by weapons. The scaling laws for weapons may be expressed in the form [135]

$$\Delta P \cdot C^2 \cdot b/E = \Pi_1 [X/C, R/C]$$

$$IC^2 a_O/E = \Pi_2 [X/C, R/C] \tag{102}$$

where Π_1 and Π_2 again represent functions and

C = caliber = inside diameter of barrel
b = barrel length
a_O = speed of sound in air
E = energy release from gun blast
x = axial distance from muzzle to observer = L cos θ
R = lateral distance from muzzle to observer = L sin θ
L = standoff distance from muzzle to observer
θ = angle between barrel axis and muzzle-observer line

269

7.4 Free-Field Blasts From Stationary Closed-Breech Weapons

Figure 126 shows a summary of side-on overpressure data points measured in the muzzle plane (x=0) at various lateral distances for fourteen different Army weapons. All data pertain to ground level, and thus do not contain the effects of altitude, and all pertain to short standoff distances of less than 400 calibers. Scatter about the regression line is seen to be relatively small, considering the wide range of caliber sizes, energy levels, barrel lengths, and standoff distances included. Thus, the regression equation given in this figure provides a fairly accurate method for predicting side-on overpressure levels for a wide range of closed-breech weapons.

Figures 127 summarizes impulse data in the same manner that Figure 126 summarizes overpressure data, again showing tight clustering about the regression line. Although both of those figures only indicate variations in the muzzle plane, similar scaling appears to hold also for variations in the direction of the barrel axis, so that one can develop curves of constant reduced (scaled) overpressure and of constant reduced impulse, as indicated in Figures 128 and 129.

7.5 Scaling Laws for Blast Fields From Moving Explosions

Thornhill's theoretical solution [136] for the blast field generated by a moving explosion may be expressed [137] as

$$\frac{V}{a_o} = \frac{K \cdot \eta}{a_o^2} \cdot \left[1 + \frac{v^2}{2\eta} \right] \cdot f(1-0.20f^2) \tag{103}$$

$$\frac{E}{E_o} = \left[1 + \frac{v^2}{2\eta} \right] \cdot \left[f \cdot \cos\theta + (1-f^2\sin^2\theta)^{1/2} \right]^3 \tag{104}$$
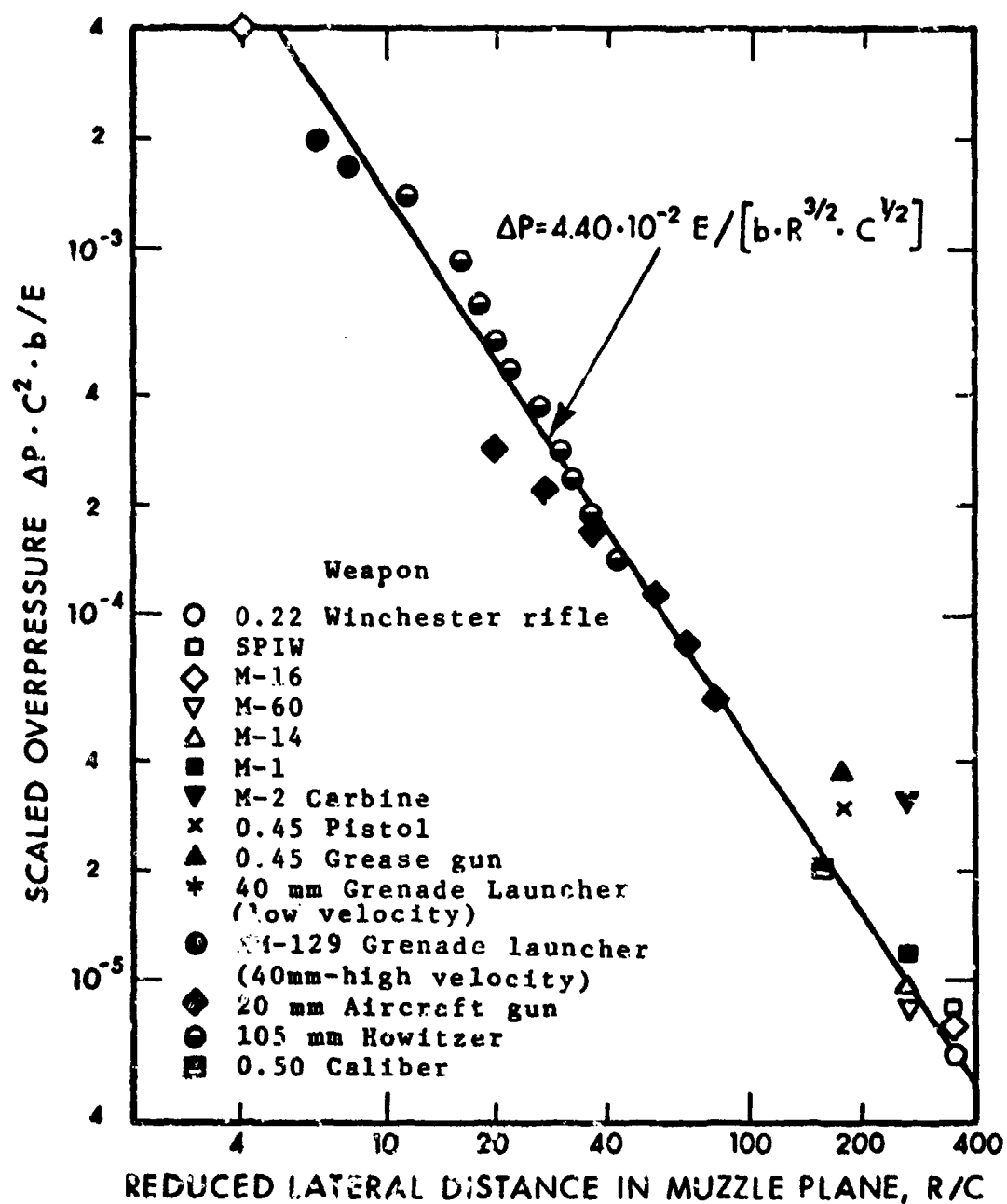
FIG. 126. SCALED SIDE-ON OVERPRESSURE FOR CLOSED-BREECH WEAPONS [135].
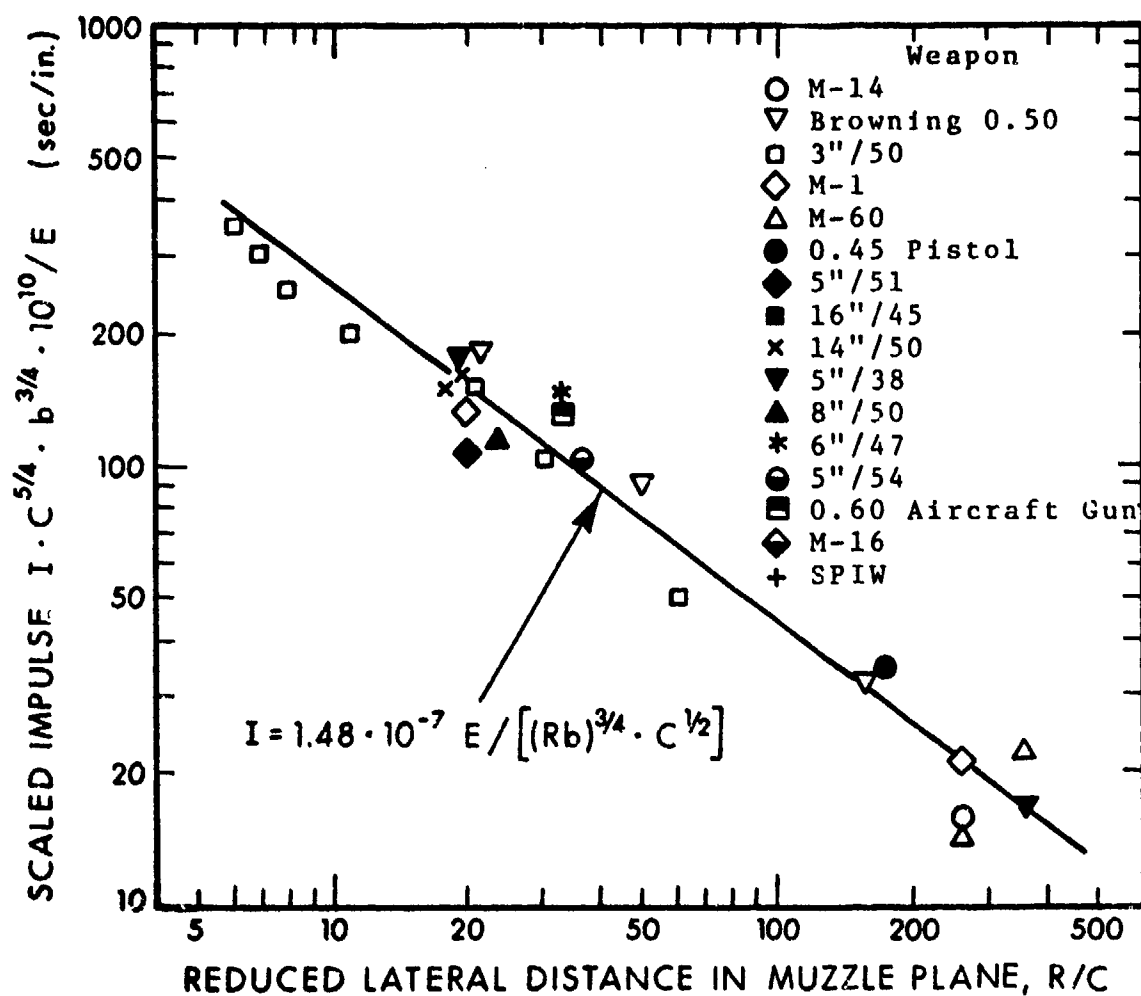
FIG. 127. SCALED SIDE-ON IMPULSE FOR CLOSED-BREECH WEAPONS [135].

$$I = 1.48 \cdot 10^{-7} \, E / \left[(Rb)^{3/4} \cdot C^{1/2} \right]$$
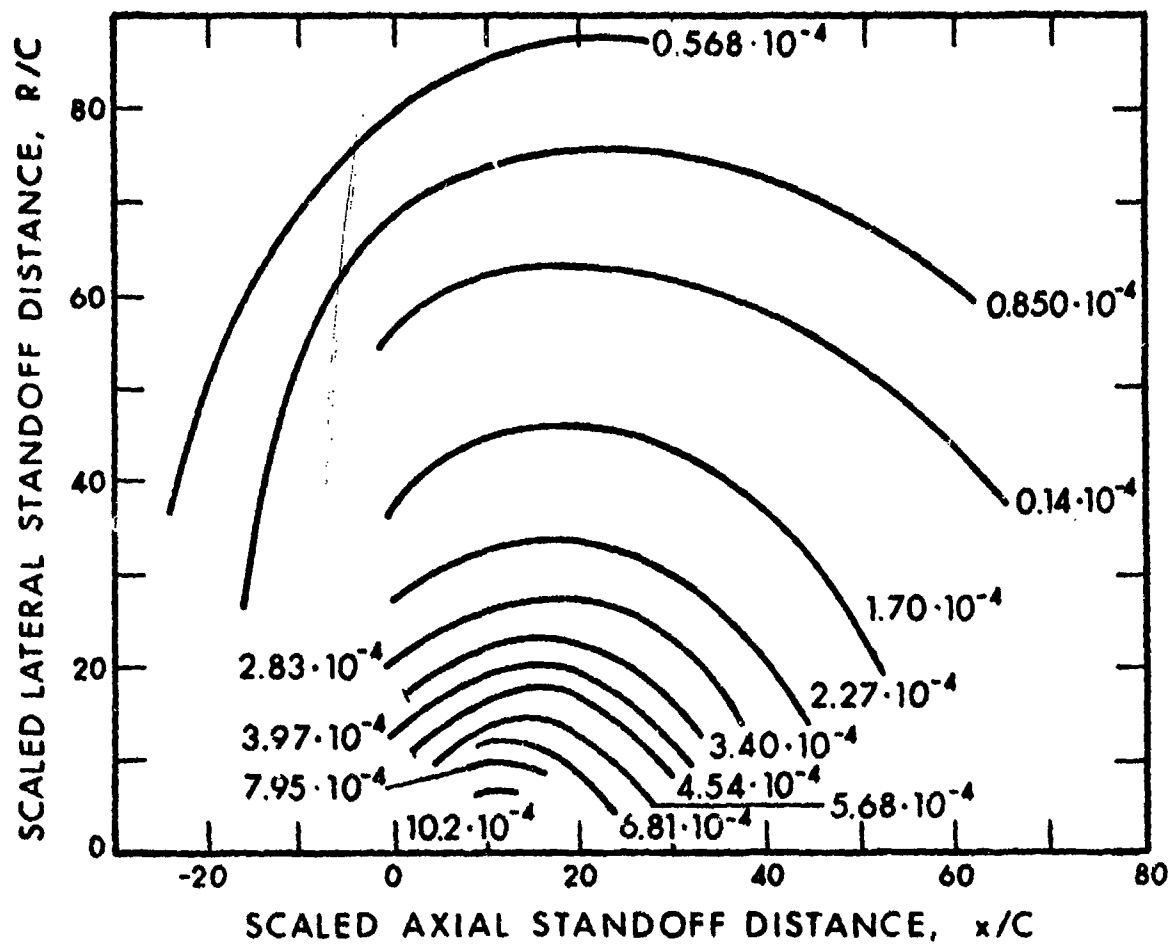
FIG. 128. CURVES OF CONSTANT SCALED OVERPRESSURE $\Delta P \cdot C^2$ b/E
FOR CLOSED-BREECH WEAPONS [135].

273
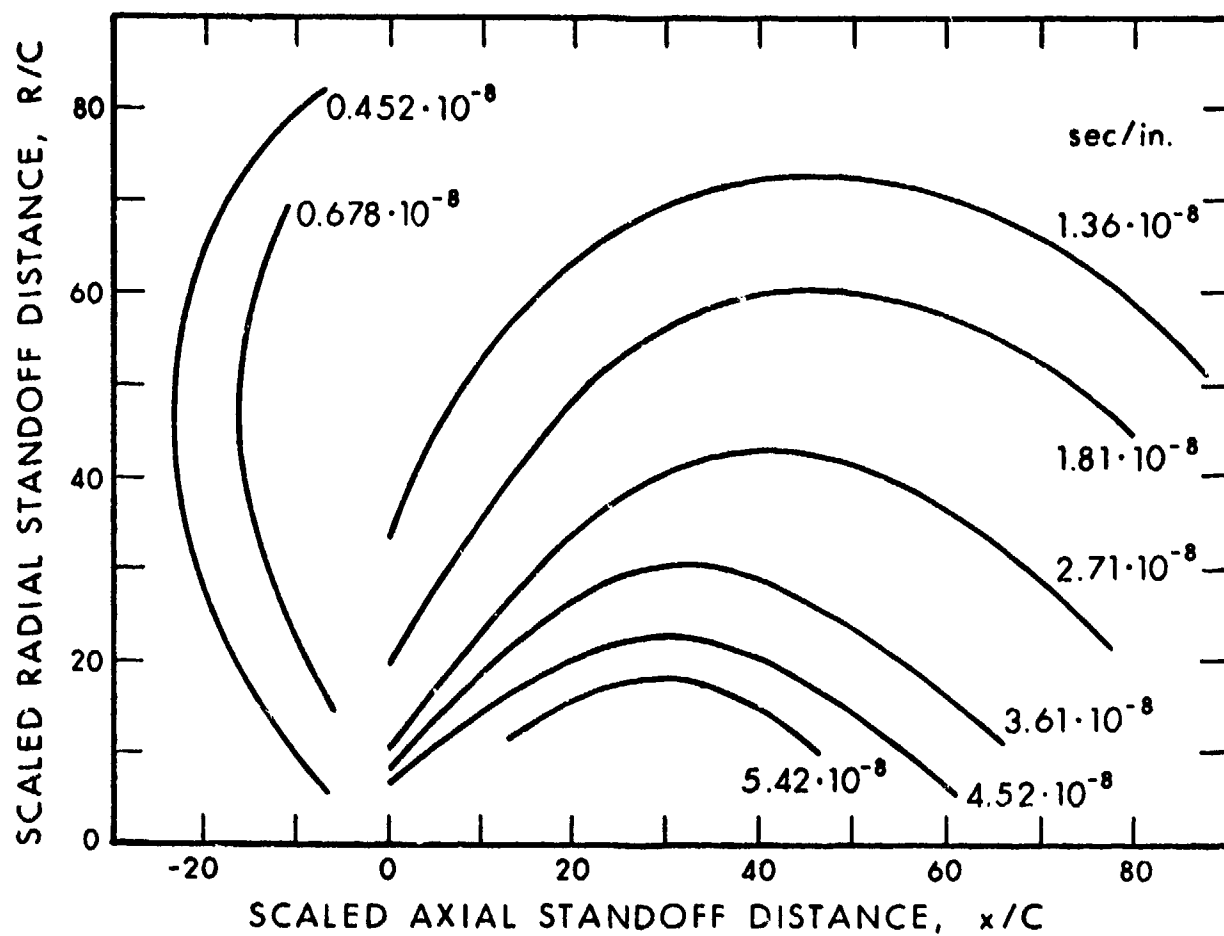
FIG. 129. CURVES OF CONSTANT SCALED IMPULSE $IC^{5/4} b^{3/4}/E$ FOR CLOSED-BREECH WEAPONS [135].

where

> V = velocity of moving charge
> a_o = speed of sound in the ambient atmosphere
> K = constant associated with explosive material
> = 0.157 for TNT
> n = explosive energy per unit mass of explosive material
> E = effective stationary energy of moving explosive
> E_o = energy of explosive
> θ = azimuth angle measured from the direction of motion
> f = parameter evaluated from Equation (103)

If, as usually is the case, the quantities V, a_o, K,n are known, one may use Equation (103) to solve for the parameter f. Then one can determine the effective stationary energy E corresponding to the moving charge from Equation (104).

The effect of the velocity V is to alter the directivity pattern of the blast pressure (increasing the pressure forward of the moving explosive and decreasing it aft of the explosive) and to increase the net energy release from the explosive.

7.6 Theoretical Prediction of Blast Field From Closed-Breech Weapon

Smith [137] ascribes the blast field about a stationary closed-breech weapon to the gas efflux from the barrel subsequent to emergence of the projectile. The gas efflux velocity V_e is given by

$$V_e = \frac{2}{\gamma+1} a_s + \frac{\gamma-1}{\gamma+1} U_s \tag{105}$$

where

> γ = ratio of specific heats for the propellant gas
> a_s = speed of sound in the compressed propellant gas
> U_s = speed of projectile as it emerges from the barrel

The flow energy density η is given by

$$\eta = \frac{V_e^2}{2} + \frac{V_e^2 - a_r^2}{\gamma(\gamma-1)} \qquad (106)$$

where a_r is the speed of sound in the propellant gas at ambient conditions. According to Smith, the extra energy term V^2/η in Equation (103) and (104) is not needed, because the gas efflux velocity is obtained at the expense of the internal energy of the propellant gas. Thus, the momentum equation, Equation (103), for gas efflux reduces to

$$f(1-0.20f^2) = V_e\, a_0/K\eta \qquad (107)$$

and the energy equation, Equation (104), reduces to

$$\frac{E}{E_0} = f \cdot \cos\theta + (1-f^2 \cdot \sin^2\theta)^{1/2} = [F(f,\theta)]^3 \qquad (108)$$

The results of applying these equations to a 7.62 mm closed-breech rifle [137] are shown in Figure 130, together with corresponding experimental data. From these results, the values of f and K for an equivalent stationary explosion were found to be $f = 0.70$ and $K = 0.185$.

Smith's gas efflux theory appears to provide a good method for theoretically predicting the distribution of the blast field about a closed-breech weapon. For this purpose, the above value of K might be reasonable for different weapons. Interestingly, this value of K is within 20% of the value for a TNT explosion. Smith also uses the above equations, along with experimental data, to show that the nearfield blast of a weapon depends on gas efflux, whereas the farfield blast is determined only by the total energy release.

276
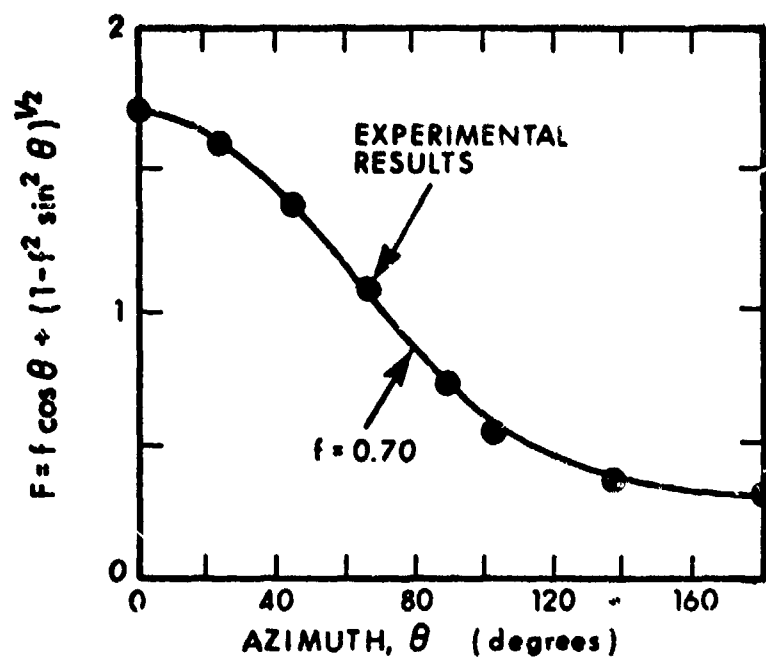
FIG. 130.   COMPARISON BETWEEN THEORY AND EXPERIMENT
FOR 7.62 mm RIFLE [137].
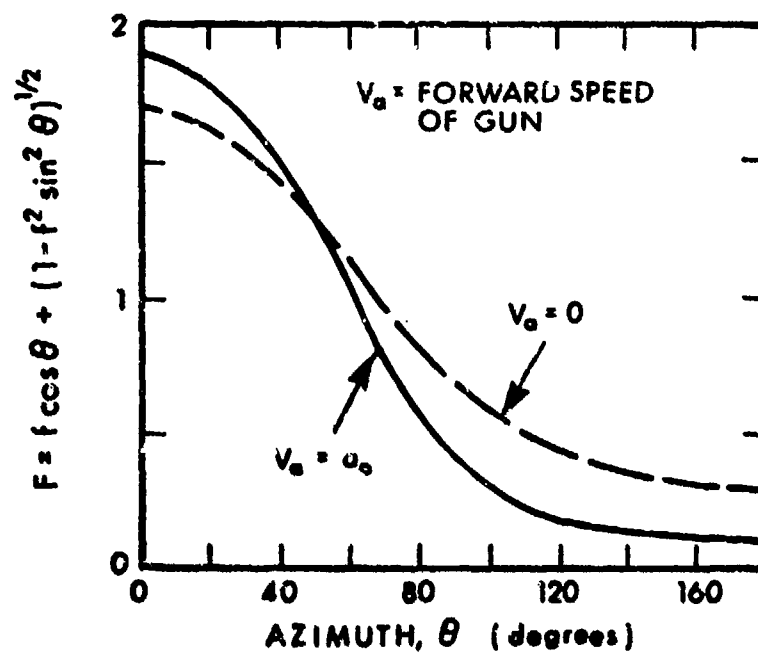
FIG. 131.   EFFECT OF FORWARD SPEED ON THEORETICAL
GUN BLAST PRESSURE DISTRIBUTION [137].

Smith [137] also extends the above theory to the prediction of the modified blast field about a weapon having a forward velocity. The general effect of the forward velocity can be seen in Figure 131, which shows the increased blast energy forward of the gun and the reduced blast energy aft of the gun.

7.7 Prediction of Free-Field Blasts From Recoilless Rifles

A recoilless rifle has a nozzle at the breech, so as to allow a fraction of the propellant gas to excape rearward, in order to reduce the transient shock load on the rifle support. Thus, a recoilless rifle may be designated as an open-breech weapon.

In a recoilless rifle, a blast field is generated rearward of the breech, as well as forward of the muzzle. Because of the highly directional nature of the sound waves emanating from these two blast fields, overpressure and impulse values forward of the muzzle are dominated by the blast field generated at the muzzle, whereas the blast field aft of the breech is dominated by that associated with the breech [138]. Thus, for purposes of evaluating measured data, scaling of the bast fields, and blast field predictions, these two blast fields can be treated independently.

7.7.1 Scaling Laws

For closed-breech weapons, the scaling law for overpressure [Equation (102)] employs the ratio $\Delta P/(E/C^2 b)$. The quantity $(E/C^2 b)$ has the units of pressure; as described in Reference [138], for recoilless weapons this quantity should be replaced by the chamber pressure P_c for best scaling results, because a given recoilless rifle can be operated with different nozzles that result in different chamber pressures and differe... blast

field characteristics. The scaling laws that yield the best results [138] are of the form

$$\Delta P / P_c = \Pi_1 [x/C, R/C]$$

$$IC / [P_c E^2]^{1/3} = \Pi_2 [x/C, R/C] \tag{109}$$

7.7.2 Blast Field Data

Reference [138] contains an extensive summary of data, collected from eight different sources, for thirteen different rifle models.

Figures 132 and 133 summarize blast overpressure data aft of the breech, for observation positions along lines at two angles from the weapon axis; Reference [138] also contains similar data for other angles. Figure 134 shows all of the mean lines of these data plots and indicates how overpressure decreases with increasing angle from the axis.

Figures 135 and 136 summarize blast overpressure data at three angles ahead of the muzzle. The mean lines of these figures and of other similar ones of Reference [138] essentially overlap, indicating absence of a directivity effect (as for a spherical shock) ahead of the muzzle.

In addition to the overpressure data discussed above, Reference [138] also presents similar data on the impulse; the scatter here is somewhat greater, but the general conclusions are the same.

Analysis [138] of these data correlations leads to the empirical prediction equations given below.

Forward of Muzzle:

$$\frac{10^3 P}{P_c} = 11.8 \left(\frac{C}{L}\right)^{1.10}$$

$$\frac{10\, I_c}{P_c^{1/3}\, E^{2/3}} = 3.35 \left(\frac{C}{L}\right)^{0.208} \tag{110}$$

Aft of Breech:

$$\frac{10^5 P}{P_c} = \exp\,(5.82 - 0.0428\theta) \cdot \left(\frac{L}{C}\right)^{(0.00663\theta - 1.48)}$$

$$\frac{10\, I_c}{P_c^{1/3}\, E^{2/3}} = \exp\,(6.30 - 0.0362\theta) \cdot \left(\frac{L}{C}\right)^{(0.00379\theta - 0.904)} \tag{111}$$

Note that the pressure field forward of the nozzle is independent of the angle θ, whereas the field aft of the breech exhibits an angle-dependence.

No data is available on the effect of forward motion on the blast field.

Sym.	Weapon	Sym.	Weapon
✕	57 mm M18A1	○	106 mm T170E1
⬭	90 mm T219 (PAT)	□	106 mm M40A1
◇	75 mm T21	△	105 mm M27
△	105 mm T19	○	57 mm M18
◊	75 mm T21	◇	105 mm M27
⬠	57 mm T66E6		(modified)

R = 0

SCALED OVERPRESSURE, $\Delta P \cdot 10^3 / P_c$

SCALED AXIAL DISTANCE AFT OF BREECH
X/C
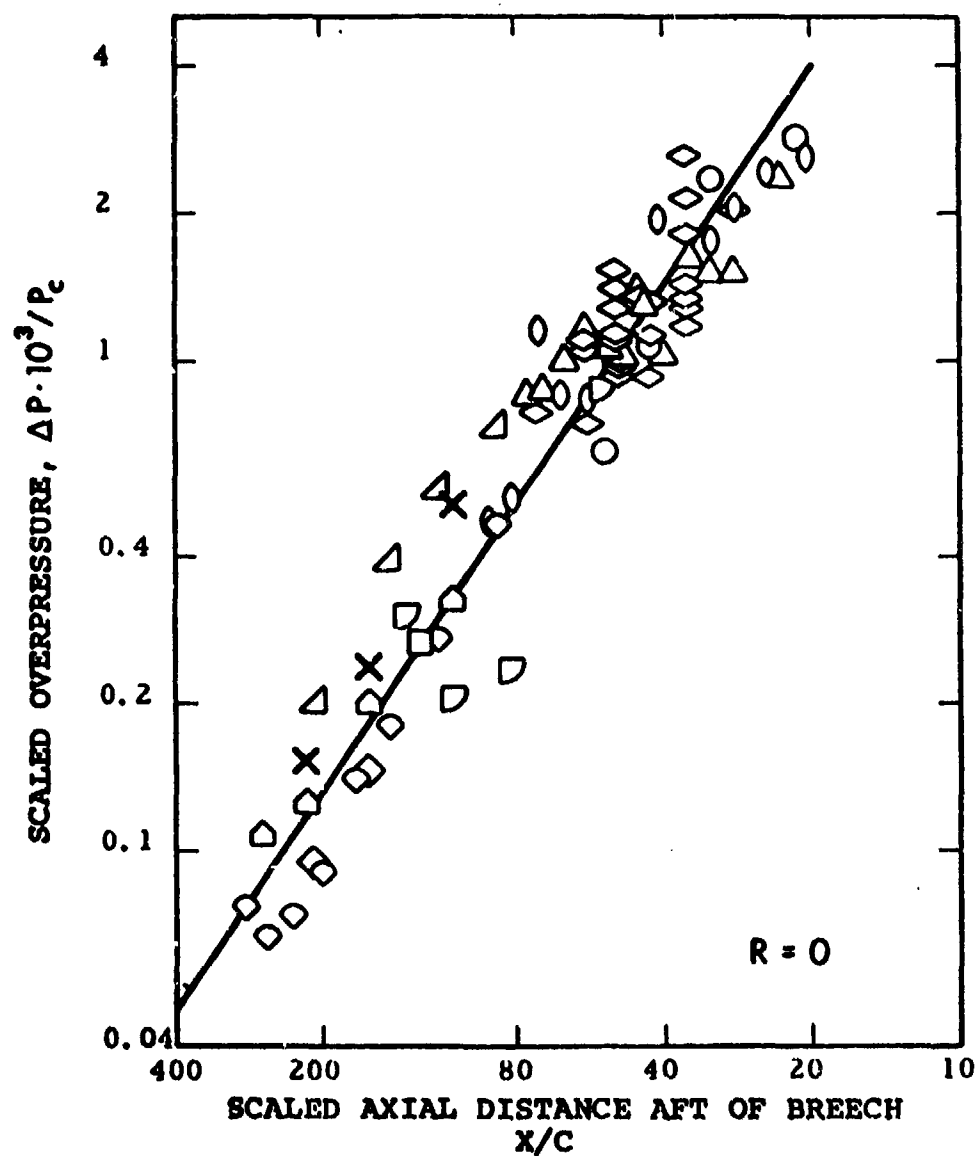
FIG. 132. BLAST OVERPRESSURES OF RECOILLESS RIFLES, ALONG THE AXIS, AFT OF THE BREECH [138].

281

Sym.	Weapon	Sym.	Weapon
▱	90 mm T219 (PAT)	◇	106 mm T170E1
◇	75 mm T21	△	105 mm M27
◁	105 mm T19	○	57 mm M18
0	75 mm T21	◇	105 mm M27
△	57 mm T66E6		(modified)

SCALED OVERPRESSURE, $\Delta P \cdot 10^3 / P_c$

SCALED STANDOFF DISTANCE AFT OF BREECH
L/C
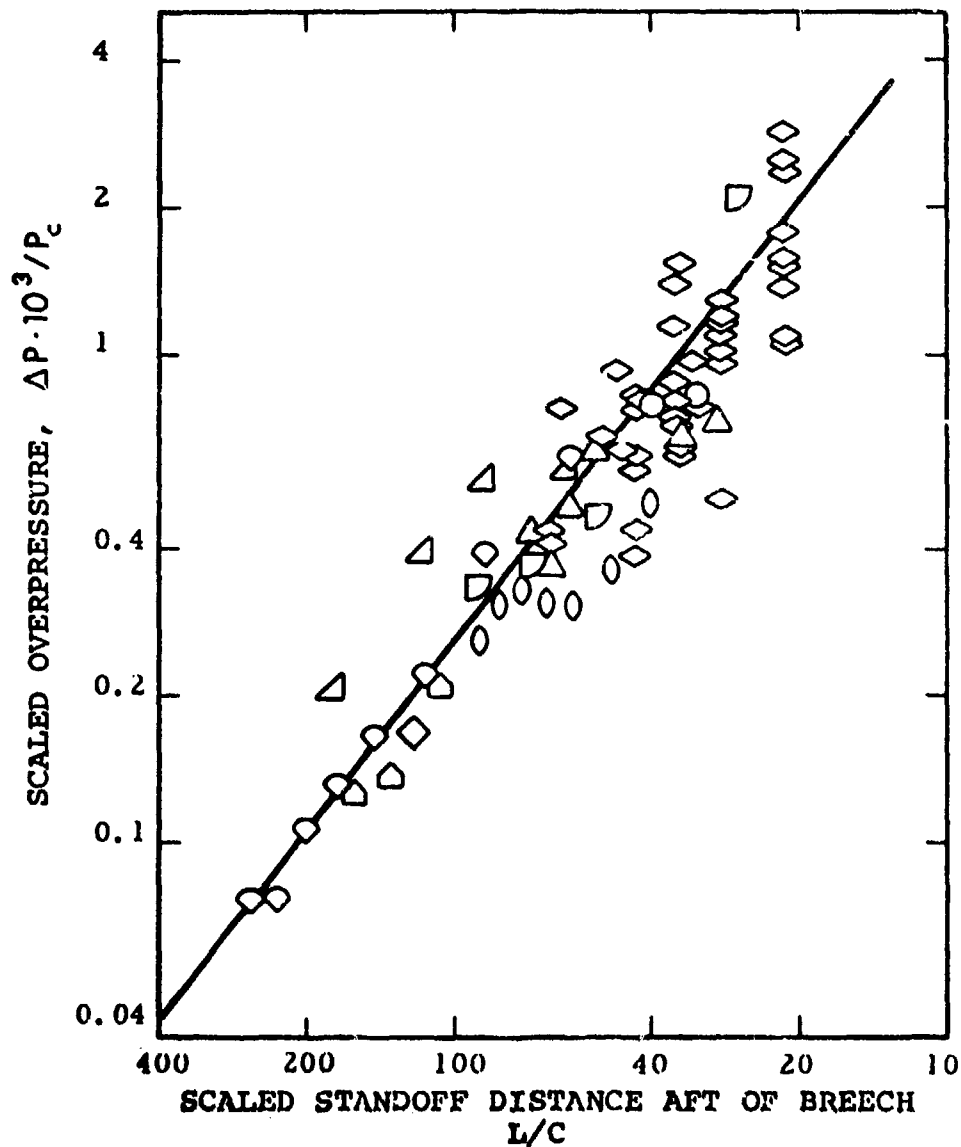
FIG. 133. BLAST OVERPRESSURES OF RECOILLESS RIFLES, AFT OF BREECH, AT 30° FROM AXIS [138].
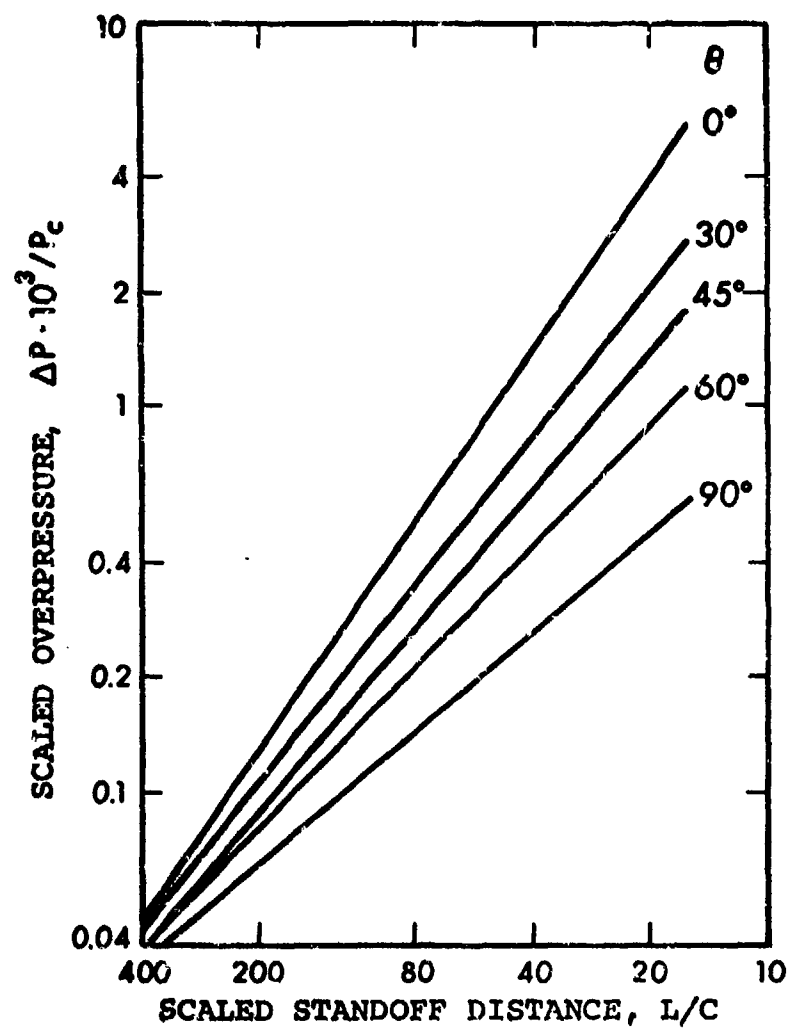
FIG. 134. OVERPRESSURES OF RECOILLESS RIFLES AT VARIOUS ANGLES Θ FROM AXIS, AFT ᴼF BREECH.
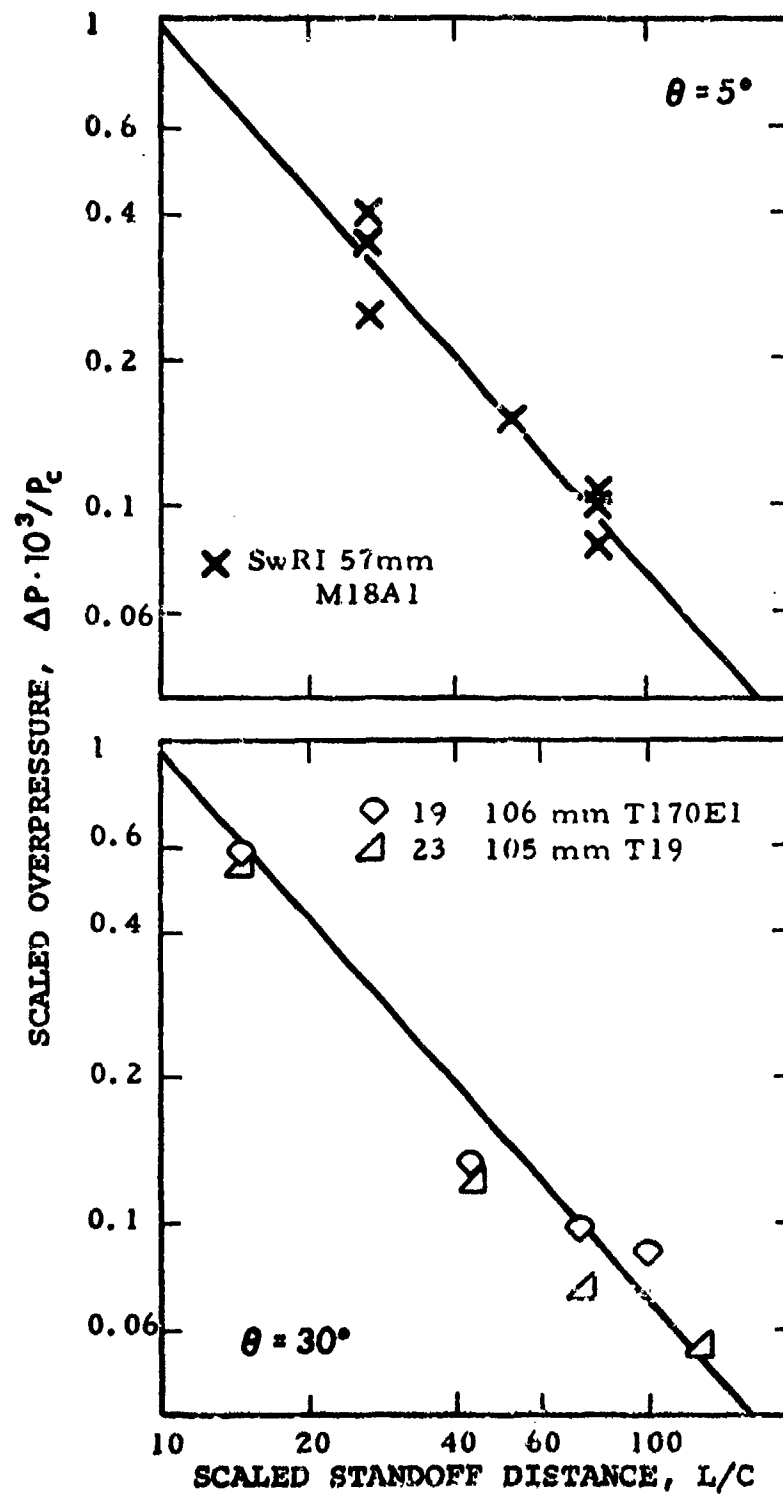
FIG. 135. OVERPRESSURES OF RECOILLESS RIFLE AHEAD OF MUZZLE AT 5° AND 30° FROM AXIS [138].
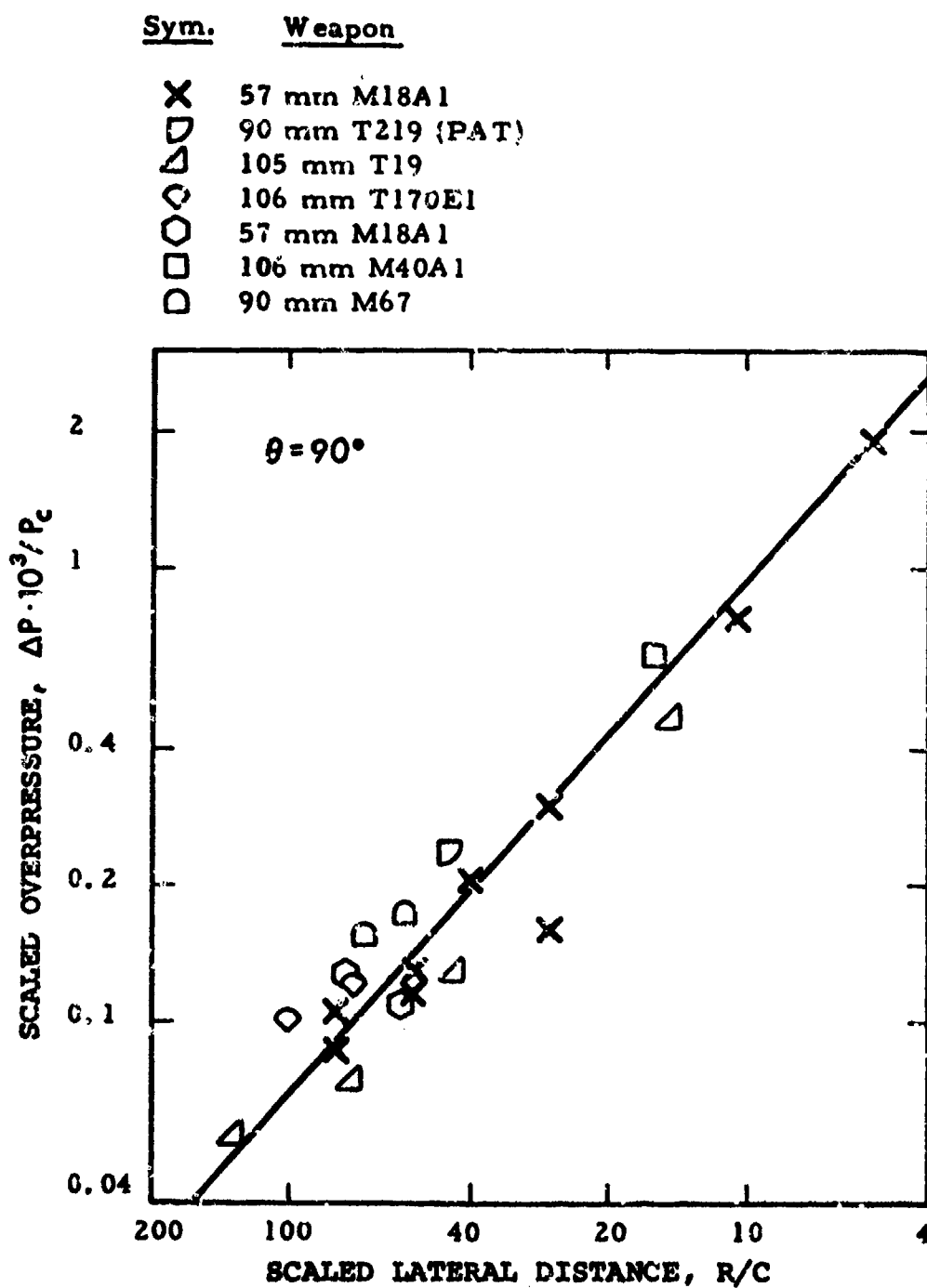
FIG. 136. OVERPRESSURES OF RECOILLESS RIFLE, TO SIDE OF MUZZLE [138].

7.8 List of Symbols for Sec. VII

Symbol	Definition	Units[†]	
C	caliber	ft	(m)
E	energy release	ft lb	(Nm)
I	impulse	lb sec/ft^2	(Ns/m^2)
L	standoff distance	ft	(m)
P_0	ambient atmospheric pressure	lb/ft^2	(N/m^2)
R	lateral distance from muzzle to observer	ft	(m)
U_s	muzzle velocity of projectile	ft/sec	(m/s)
V	velocity of moving charge	ft/sec	(m/s)
V_e	gas efflux velocity	ft/sec	(m/s)
W	charge weight	lb	(N)
a_0	speed of sound in air	ft/sec	(m/s)
a_s	speed of sound in propellant gas	ft/sec ___	(m/s)
b	barrel length	ft	(m)
d	equivalent charge diameter	ft	(m)
x	axial distance from muzzle to observer	ft	(m)
γ	ratio of specific heats of propellant gas	---	
η	explosive energy per unit mass	ft lb/slug	(Nm/kg)
θ	angle between barrel axis and source-to-observer line	deg	
ΔP	peak overpressure	lb/ft^2	(N/m^2)

---

*Specially defined symbols, such as those for empirically determined constants, which are used only once in the text, are not included here. Such symbols are defined in the text wh re they occur.

†The units given here are typical ones. SI units are given in parentheses where appropriate. Note that some empirical prediction methods require the use of specific units.

REFERENCES

1. Chen, C.Y., "Calculations of Far-Field and Near-Field Jet Noise," AIAA Paper 75-93 (January 1975).

2. Chen. C.Y., Knott, P.R., Benazkein, M.J., "Analytical Near Field Acoustic Model Formulations," Chap. III "Supersonic Jet Noise," AFAPL-TR-72-52 (August 1972).

3. Benzakein, M.J., Chen, C.Y., Knott, P.R., "A Computational Technique for Jet Aerodynamic Noise," AIAA Paper No. 71-583 (June 1971).

4. Franz, G.J., "The Near-Sound Field of Turbulence," David Taylor Model Basin, Rept. 986, AD 630684 (October 1959).

5. Maestrello, L., McDaid, E., "Near-Field Characteristics of a High Subsonic Jet," AIAA Paper No. 71-155 (January 1971).

6. Plumblee, H.E., Ballentine, J.R., Passinos, B., "Near Field Noise Analysis of Aircraft Propulsion System with Emphasis on Prediction Techniques for Jets," AFFDL-TR-67-43 (August 1967).

7. Ffowcs Williams, J.E., "Some Thoughts on the Effects of Aircraft Motion and Eddy Convection on the Noise from Air Jets," University of Southampton, Dept. of Aero/Astro, USAA Rept. 155 (1960).

8. Ribner, H.S., "The Generation of Sound by Turbulent Jets," *Advances in Solid Mechanics* 8, 104-178, Academic Press, New York and London (1964).

9. Lilley, G.M., "On the Noise from Air Jets," ARC (U.K.) 20,376 (1958).

10. Thomson, A.G.R., "Acoustic Fatigue Design Data Part I, NATO AGARD-AG-162-Part I (May 1972).

11. Cockburn, J.A., Jolly, A.C., "Structural-Acoustic Response, Noise Transmission Losses and Interior Noise Levels of an Aircraft Fuselage Excited by Random Pressure Fields," AFFDL-TR-68-2 (August 1968).

12. Hermes, P.H., Smith, D.L., "Measurement and Analysis of J57-P21 Noise Field," AFFDL-TR-66-147 (November 1966).

REFERENCES *(Cont.)*

13. Sutherland, L.C., Brown, D., "Prediction Methods for Near Field Noise Environments of VTOL Aircraft," AFFDL-TR-71-180 (1972).

14. Rudder, F.F., Plumblee, H.E., "Sonic Fatigue Design Guide for Military Aircraft," AFFDL-TR-74-112 (May 1975).

15. Smith, D.L., Paxson, R.P., Talmadge, R.D., Plazak, G.A., "Near Field Noise Prediction for Linear Array of Turbojet Engines," Rept. AFFDL-TM-74-139-FY? (July 1974).

16. Cox, R.J., Parry, H.J., Clough, J., "A Study of the Characteristics of Modern Engine Noise and the Response Characteristics of Structures," WADD-TR-60-220 (December 1961).

17. Howes, W.L., Mull, H.R., "Near Noise Field of a Jet-Engine Exhaust," NACA-TN-3763 (October 1956).

18. Tanna, H.K., Fisher, M.J., Dean, P.D., "Effect of Temperature on Supersonic Jet Noise," AIAA Paper No. 73-991.

19. Powell, A., "On the Mechanism of Choked Jet Noise," *Proc. Phys. Soc.* 66B, 1039-1056 (1953).

20. Stone, J.R., "Interim Prediction Method for Jet Noise," NASA TM X-71618 (1974).

21. Olsen, W.A., Gutierrez, O.A., Dorsch, R.G., "The Effect of Nozzle Inlet Shape, Lip Thickness, and Exit Shape and Size on Subsonic Jet Noise," NASA TM X-68182 (January 1973).

22. Grande, E., Large, J.B., "Possibilities and Devices for the Suppression of Jet Noise," Boeing Document D6-20609 (February 1968).

23. MacGregor, G.R., Simcox, C.D., "The Location of Acoustic Sources in Jet Flows by Means of the 'Wall Isolation' Technique," AIAA Paper No. 73-1041 (October 1973).

24. Potter, R.C., Crocker, M.J., "Acoustic Prediction Methods for Rocket Engines, including the Effects of Clustered Engines and Deflected Flow," NASA CR-566 (October 1966).

25. Eldred, K.M., White, R.W., Mann, M.A., Cottis, M.G., "Suppression of Jet Noise with Emphasis on the Near Field," ASD-TDR-62-578 (February 1963).

REFERENCES *(Cont.)*

26. Abramovich, G.N., *The Theory of Turbulent Jets*, M.I.T. Press (1963).

27. Seiner, J.M., Reethof, G., "On the Distribution of Souice Coherency in Subsonic Jets," AIAA Paper No. 74-4 (January 1974).

28. Chu, W.T., Kaplan, R.E., "Jet Noise Measurements by Means of a Directional Microphone," Paper H5, *86th* Meeting, Acoustical Society of America, Los Angeles, California (November 1963).

29. Grosche, F.R., Jones, J.H., Wilhold, G.A., "Measurement of the Distribution of Sound Source Intensities in Turbulent Jets," AIAA Paper No. 73-989 (October 1973).

30. Howes, W.L., Callaghan, E.E., Coles, W.D., Mull, H.R., "Near Noise Field of a Jet-Engine Exhaust," NACA Rept. 1338 (June 1957).

31. Bhat, W.V., "Exterior Pressure Fluctuations due to Turbulent Boundary Layer and Jet Engine Noise on Boeing Model 737 Airplane. Vol. II Jet Engine Noise," Boeing Document D6-24497-II (September 1970).

32. Darchuk, G.V., Balombin, J.R., "Noise Evaluation of Four Exhaust Nozzles for Afterburning Turbojet Engine," NASA TM X-2014 (May 1970).

33. Putnam, T.W., "Investigation of Coaxial Noise and Inlet Choking Using an F-111A Airplane," NASA TN D-7376 (August 1973).

34. Franken, P.A., Kerwin, E.M., *et al.*, "Methods of Flight Vehicle Noise Prediction," WADC-TR-58-343 (October 1958).

35. Dunn, D.G., Peart, N.A., "Aircraft Noise Source and Contour Estimation," NASA CR-114649 (July 1973).

36. Bielak, G.W., "Coaxial Flow Jet Noise," Boeing/Aeritalia Document D6E-10041-1 (April 1972).

REFERENCES (Cont.)

37. Simcox, C.D., "Effect of Temperature and Shock Structure on Choked Jet Noise Characteristics," AIAA Paper 71-582 (June 1971).

38. Knott, P.R., Brausch, J.F., Nagamatsu, H.T., "Shock Noise Experiments for Hot Model Scale Supersonic Jets," Chap. TV, Supersonic Jet Exhaust-Noise AFAPL-TR-72-52 (August 1972).

39. Davies, M.G., Oldfield, D.E.S., "Tones from a Choked Axisymmetric Jet," *Acoustica* 12, 4, 257-277 (1962).

40. Westley, R., Woolley, J.H., "An Investigation of the Near Noise Fields of a Choked Axi-symmetric Air Jet," pp. 147-167, *Aerodynamic Noise* (Ed. H.S. Ribner), University of Toronto Press (1969).

41. Westley, R., Woolley, J.H., "The Near Field Sound Pressures of a Choked Jet During a Screech Cycle," Chap. 23, *Aircraft Engine Noise and Sonic Boom*, AGARD CP 42 (May 1969).

42. Howlett, D.P., "Model and Full Scale Investigations of Shock-Cell Noise," *ARC (U.K.)* 28, 563 (December 1966).

43. Hay, J.A., "Shock-Cell Noise — Aircraft Measurements," *J. Sound Vib.* 17, 4, 509-516 (August 1971).

44. Powell, A., "The Reduction of Choked Jet Noise," *Proc. Phys. Soc. London* 67B, 313-327 (1954).

45. Ffowcs Williams, J.E., "The Noise from Turbulence Convected at High Speed," *Phil. Trans. Roy. Soc. London* Series A, 255, 1061, 469-503 (April 1963).

46. Kobrynski, M., "On the Calculation of the Maximum Sound Pressure Spectrum from Stationary and Mobile Jets," *J. Sound Vib.* 7, 2, 263-286 (March 1968).

47. Pinkel, B., "Jet Noise Analysis Utilizing the Rate of Decay of Kinetic Power," AIAA Paper 75-94 (January 1975).

48. Cocking, B.J., Bryce, W.D., "Subsonic Jet Noise in Flight Based on Some Recent Wind-Tunnel Tests," AIAA Paper 75-462 (March 1975).

49. Franken, P.A., *et al.*, "Methods of Space Vehicle Noise Prediction," WADC TR 58-343, Vol. II (September 1960).

50. Powell, A., "On the Effect of Missile Motion on Rocket Noise," *J. Acous. Soc. Amer.* 30, 11, 1048 (November 1958).

51. Rudder, F.F., Plumblee, H.E., "Sonic Fatigue Design Guide for Military Aircraft," AFFDL-TR-74-112 (May 1975).

52. Reed, D.H., "Effect of Forward Velocity on the Noise Characteristics of Dual-Flow Jet Nozzles," ASME Paper 74-WA/ Aero-4 (November 1974).

53. Von Glahn, U., Groesbeck, D., Goodykoontz, J., "Velocity Decay and Acoustic Characteristics of Various Nozzle Geometries with Forward Velocity," AIAA Paper 73-629 (July 1973).

54. Kay, J.A., Rose, E.G., "In-Flight Shock Cell Noise," *J. Sound Vib.* 11, 4, 411-420 (April 1970).

55. Stone, J.R., Gutierrez, O.A., "Target-Type Thrust Reverser Noise," *J. Aircraft* 10, 5, 283-288 (May 1973).

56. Stone, J.R., Gutierrez, O.A., "Noise Tests of a High-Aspect-Ratio Slot Nozzle with Various V-Gutter Target Thrust Reversers," NASA TMX-71470 (October 1973).

57. Fink, M.R., "Thrust Reverser Noise Estimation," *J. Aircraft* 10, 8, 507-508 (August 1973).

58. Gutierrez, O.A., Stone, J.R., Freidman, R., "Results from Cascade Thrust Reverser Noise and Suppression Experiments," AIAA Paper 74-76 (January 1974).

59. Potter, R.C., "Correlation Patterns of the Acoustic Pressure Fluctuations on the S-1C Vehicle Due to the Exhaust Noise at the Test and Launch Stand," Wyle Rept. WR66-19 (1966).

60. Franklin, R.E., "Space-Correlations in the Fluctuating Pressure Field Near to a Jet Engine," *J. Royal Aero. Soc.* 65, 670-676 (October 1961).

61. Mollo-Christensen, E., "Measurements of Near Field Pressure of Subsonic Jets," AGARD Rept. 449 (April 1963).

REFERENCES (Cont.)

62. Clarkson, B.L., "The Design of Structures to Resist Jet Noise Fatigue," *J. Royal Aero. Soc.* 66, 603 (October 1962).

63. Olson, M.D., Lindberg, G.M., "Jet Noise Excitation of an Integrally Stiffened Panel," *J. Aircraft* 8, 11, 847-855 (November 1971).

64. Maestrello, L., Gedge, M.R., Reddaway, A.R.F., "The Response of a Simple Panel to the Pseudo-Sound Field of a Jet," pp. 189-203, *Aerodynamic Noise* (Ed. H.S. Ribner) University of Toronto Press, 1969.

65. Clarkson, B.L., "Scaling of the Near Field Pressure Correlation Patterns Around a Jet Exhaust," pp. 19-38, *Acoustic Fatigue in Aerospace Structures*, (Ed. W.J. Trapp and D.M. Forney, Jr.), Syracuse Press, 1965.

66. Clarkson, B.L., "Structural Vibrations Caused by Pressure Fluctuations in the Audio Frequency Range," Symposium on Aeronautical Acoustics, Toulouse, France (March 1968).

67. Hayden, R.E., "Fundamental Aspects of Noise Reduction from Powered-Lift Devices," SAE Paper 730376 (1973).

68. Samanich, N.E., Heidelberg, L.J., "Effect of Exhaust Nozzle Configuration on Aerodynamic and Acoustic Performance of an Externally Blown Flap System with a Quiet 6:1 Bypass Ratio Engine," AIAA/SAE 9th Propulsion Conference (November 1973) AIAA Paper No. 73-1217.

69. Hayden, R.E., Kadman, Y., Chanaud, R.C., "A Study of the Variable Impedance Surface Concept as a Means for Reducing Noise from Jet Interaction with Deployed Lift-Augmenting Flaps," NASA CR-112166.

70. Hayden, R.E., "Fundamental Aspects of Noise Reduction from Powered-Lift Devices," SAE Paper 730376 (1973).

71. Clark, B.J., Dorsch, R.G., "Flap Noise Prediction Method for a Powered Lift System," AIAA Aero-Acoustics Conference, October 1973. AIAA Paper No. 73-1028.

72. Goodykoontz, J., von Glahn, U., Dorsch, R., "Forward Velocity Effects on Under-the-Wind Externally Blown Flap Noise," Technical Paper presented to Second Aero-Acoustics Specialists Conference sponsored by AIAA (March 1975). NASA TM X-71656.

REFERENCES *(Cont.)*

73. Lansing, D.L., Mixson, J.S., Brown, T.J., Drischler, J.A., "Externally Blown Flap Dynamic Loads," NASA SP-320 (1973).

74. Mixson, J.S., Schoenster, J.A., Willis, C.M., "Fluctuating Pressures on Aircraft Wing and Flap Surfaces Associated with Powered-Lift Systems," presented at AIAA Second Aeroacoustics Specialists Conference (March 1975).

75. Schoenster, J.A., Willis, C.M., Schroeder, J.C., Mixson, J.S., "Acoustic Loads Research for Powered-Lift Configurations," Paper No. 27, Conference on Powered-Lift Aerodynamics and Acoustics (May 1976).

76. Scharton, T.D., Pinkel, B., Wilby, J.F., Hansen, G.L., "A Study of Trailing Edge Blowing as a Means of Reducing Noise Generated by the Interaction of Flow with a Surface," NASA CR-132270 (September 1973).

77. Hayden, R.E., Kadman, Y., Chanaud, R.C., "A Study of the Variable Impedance Surface Concept as a Means for Reducing Noise from Jet Interaction with Deployed Lift-Augmenting Flaps," NASA CR-112166.

78. Gibson, J.S., Searle, N., "Characteristics of USB Noise," Paper No. 15, Conference on Powered-Lift Aerodynamics and Acoustics (May 1976).

79. Reed, J.B., Sussman, M.B., Harkonen, D.L., "USB Environment Measurements Based on Full Scale Engine Ground Tests," Paper No. 30, Conference on Powered-Lift Aerodynamics and Acoustics (May 1976).

80. Hayden, R.E., "Exploratory Investigation of Aero-Acoustic Optimization of the Variable Edge Concept Applied to Upper Surface Blown Configuration", NASA CR-145072, Feb 76.

81. Sussman, M.B., Reed, J.B., Harkonen, D.L., "USB Environment Measurements Based on Full Scale Engine Ground Tests," Paper No. 30, Conference on Powered-Lift Aerodynamics and Acoustics (May 1976).

82. Wilby, J.F., Scharton, T.D., "A Study of Noise Source Location on a Model Scale Augmentor Wing Using Correlation Techniques," BBN Rept. No. 2955 (November 1975).

REFERENCES *(Cont.)*

83. Campbell, J.M., Lawrence, R.L., O'Keefe, J.V., "Design Integration and Noise Studies for Jet STOL Aircraft Final Report, Vol. IV, Static Test Program," NASA CR 114285 (May 1972).

84. Hayden, R.E., Chandiramani, K.L., Scharton, R.D., "Considerations in the Design of Quiet Lift Augmentation System for STOL Transport Aircraft," BBN Rept. No. 2261 (January 1972).

85. Wilby, J.F., Scharton, T.D., "A Study of Noise Source Location on a Model Scale Augmentor Wing Using Correlation Techniques," BBN Rept. No. 2955 (November 1975).

86. Reddy, N.N., Blakney, D.F., Tibbets, J.G., Gibson, J.S., "V/STOL Aircraft Noise Prediction (Jet Propulsors)," U.S. Dept. of Transportation Rept. No. FAA-RD-75-125 (June 1975).

87. Maglieri, D.J., Hubbard, H.H., "Preliminary Measurements of the Noise Characteristics of Some Jet-Augmented-Flap Configurations," NASA Memo 12-4-58L (January 1959).

88. Hayden, R.E., "Noise from Interaction of Flow with Rigid Surfaces: A Review of Current Status of Prediction Techniques," NASA CR-2126.

89. Hayden, R.E., Fox, H.L., Chanaud, R.C., "Some Factors Influencing Radiation of Sound from Flow Interaction with Edges of Finite Surfaces," BBN Rept. No. 2797 (1976).

90. Reddy, N.N., Blakney, D.F., Tibbets, J.G., Gibson, J.S., "V/STOL Aircraft Noise Prediction (Jet Propulsors)," U.S. Dept. of Transportation Rept. No. FAA-RD-75-125 (June 1975).

91. Hayden, R.E., Murray, B.S., Galaitsis, A.G., "Preliminary Investigation of Acoustic Requirements for NLR 8x6 m Low Speed Wind Tunnel," BBN Rept. No. 3087 (June 1975).

92. Campbell, J.P., "Overview of Powered-Lift Technology," Paper No. 1, Conference on Powered-Lift Aerodynamics and Acoustics (May 1976).

REFERENCES *(Cont.)*

93. Hayden, R.E., Galaitsis, A.G., Alakel, M.N., "Diagnosis of Flap Noise Sources on a Full Scale Upper Surface Blown Flap System," BBN Rept. No. 2998 (March 1975).

94. Jones, W.L., Heidelberg, L.J., "Investigation of Noise From Full-Scale High Bypass Engine and Blown Flap System," Air Transportation Meeting, Dallas, Texas (April 30-May 2, 1974).

95. Fink, M.R., "Scrubbing Noise of Externally Blown Flaps," AIAA *2nd* Aero-Acoustics Conference (March 1975).

96. Heidelberg, L.J., Homyak, L., Jones, W.L., "Full-Scale Upper-Surface-Blown Flap Noise," Technical Paper presented to National Air Transportation Meeting sponsored by SAE (May 1975). NASA TM X-71708.

97. Coles, W.D., "Jet-Engine Exhaust Noise from Slot Nozzles," NASA TN D-60 (September 1959).

98. Hayden, R.E., Scharton, T.D., Kadman, Y., Wilby, J., Rudd, M.J., "A Preliminary Evaluation of Noise Reduction Potential for the Upper Surface Blown Flap," BBN Rept. No. 2478 (November 1972).

99. Ollerhead, J.B., Lowson, M.V., "Problems of Helicopter Noise Estimation and Reduction," AIAA Paper 69-195 (February 1969).

100. Gutin, Y., "On the Sound Field of a Rotating Propeller," NACA TM 1195 (October 1948).

101. Garrick, I.E., Watkins, C.E., "A Theoretical Study of the Effect of Forward Speed on the Free-Space Sound-Pressure Field Around Propellers," NACA TR 1198 (1954).

102. Hubbard, H.H., Regier, A.A., "Free-Space Oscillating Pressures Near the Tips of Rotating Propellers," NACA TR 996 (1950).

103. Metzger, Magliozzi, Towk, and Gray, "A Study of Propeller Noise Research," United Aircraft (1961).

104. Ungar, E.E., *et al.*, "A Guide for Predicting the Aural Detectability of Aircraft," AFFDL TR-71-22 (March 1972).

REFERENCES *(Cont.)*

105. Sutherland, L.C., Brown, D., "Prediction Methods for Near-field Noise Environment of VTOL Aircraft," AFFDL TR-71-180 (May 1972).

106. Chaump, L.E., **Martellucci**, A., Montfort, A., "Aeroacoustic Loads Associated with High Beta Re-Entry Vehicles," AFFDL-TR-72-138, Vol. I (1973).

107. Lowson, M.V., "Prediction of Boundary Layer Pressure Fluctuations," AFFDL-TR-67-167 (1968).

108. Willmarth, W.W., "Pressure Fluctuations Beneath Turbulent Boundary Layers," *Ann. Rev. Fluid Mech.* 7:13 (1975).

109. Blake, W.K., "Turbulent Boundary Layer Wall Pressure Fluctuations on Smooth and Rough Walls," *J. Fluid Mech.* 44:637 (1970).

110. Houbolt, J.C., "On the Estiamation of Pressure Fluctuations in Boundary Layers and Wakes," GE-TIS 66SD296 (1966).

111. Robertson, J.E., "Prediction of In-Flight Fluctuating Pressure Environments Including Proturberance Induced Flow," Wyle Laboratories Research Rept. WR 71-110 (1971).

112. Chyu, W.J., Hanly, R.D., "Power-and-Cross-Spectra and Space-Time Correlations of Surface Fluctuating Pressures at Mach Numbers between 1.6 and 2.5," NASA TN D-5440 (1969).

113. Bull, M.K., Wilby, J.F., Blackman, D.R., "Wall Pressure Fluctuations in Boundary Layer Flow and Response of Simple Structures to Random Pressure Fields," University of Southampton AASU Rept. 243 (1963).

114. Bull, M.K., "Wall Pressure Fluctuations Associated with Subsonic Turbulent Boundary Layer Flow," *J. Fluid Mech.* 28:719 (1967).

115. Saunders, H., Jonnson, R.J., Macourek, M.N., "Boundary Layer Acoustic Measurements in Transitional and Turbulent Flow at M-4.0," AIAA Fourth Aerodynamic Testing Conference (April 1969).

REFERENCES *(Cont.)*

116. Brown, M.D., Pate, S.R., "Acoustic Measurements in Supersonic Transitional Boundary Layers," AEDC-TR-69-182 (1969).

117. Coe, C.F., "Surface Pressure Fluctuations Associated with Aerodynamic Noise," NASA SP-207 (July 1969).

118. Speaker, W.V., Ailman, C.M., "Spectral and Space-Time Correlations of the Fluctuating Pressures at a Wall Beneath a Supersonic Turbulent Boundary Layer Perturbed by Steps and Shock Waves," NASA CR-486 (1969).

119. Coe, C.F., Chyu, W.J., "Pressure Fluctuation Inputs and Response of Panels Underlying Attached and Separated Supersonic Turbulent Boundary Layers," Paper No. 5 AGARD-CP-113 (1972).

120. Rechtien, R.D., "A Study of the Fluctuating Pressure Field in Regions of Induced Flow Separation at Supersonic Speeds," University of Missouri, Rolla, UMR Research Report (May 1970).

121. Heller, H.H., Bliss, D.B., Ungar, E.E., Widnall, S.E., "Feasibility of Aircraft Stall Detection by Means of Pressure-Fluctuation Measurements," AFFDL-TR-70-147 (November 1970).

122. Eldred, K. Mck., "Base Pressure Fluctuations," *J. Acoust. Soc. Am.* 33 (1), 59 (January 1961).

123. Houbolt, J.C., "On the Estimation of Pressure Fluctuations in Boundary Layers and Wakes," GE-TIS 66SD296 (April 1966).

124. Heller, H., Holmes, G., and Covert, E., "Flow Induced Pressure Oscillations in Shallow Cavities," AFFDL-TR-70-104 (1970).

125. Rossiter, J.E., "Wind Tunnel Experiments on the Flow over Rectangular Cavities at Subsonic and Transonic Speeds," Royal Aircraft Establishment ARC R&M 3438 (1966).

126. Heller, H.H., and Bliss, D.B., "Aerodynamically Induced Pressure Oscillations in Cavities – Physical Mechanisms and Suppression Concepts," AFFDL-TR-74-133 (1974).

REFERENCES *(Cont.)*

127. Shaw, L.L., Smith, D.L., "Aero-Acoustic Environment of Rectangular Cavities with Length to Depth Ratios in the Range of Four to Seven," Paper presented at the *45th* Shock and Vibration Symposium, Dayton, Ohio (1974).

128. Leupold, M.J., Baker, R.W., "A Report on Research Directed Toward the Design, Development, Construction, and Testing of 'Aerodynamic Cavities'," MIT Aero-Physics Lab. Tech Rept. 417 (November 1959).

129. Smith, D.L., Shaw, L.L., Talmadge, R.D., Seely, D.C., "Aero-Acoustic Environment of Rectangular Cavities with Length-to-Depth Ratios of Five and Seven," AFFDL-TM-74-79-FYA (1974).

130. Heller, H., Holmes, G., and Covert, E., "Flow Induced Pressure Oscillations in Shallow Cavities," AFFDL-TR-70-104 (1970).

131. Shaw, L.L., Smith, D.L., Talmadge, R.D., Seely, D.E., "Aero-Acoustic Environment of Rectangular Cavities with Length-to-Depth Ratios of Four," AFFDL-TM-74-19-FYA (1974).

132. Karamacheti, K., "Acoustic Radiation from Two Dimensional Rectangular Cutouts in Aerodynamic Surfaces," NACA TM 3478 (1955).

133. Bliss, D.B., Hayden, R.E., "Landing Gear and Cavity Noise Prediction," NASA CR-2714 (1976).

134. Sutherland, L.C., "Sonic and Vibration Environments for Ground Facilities," Wyle Laboratories Research Staff Rept. No. 68 — 2 (March 1968).

135. Westline, P.S., "The Blast Field About the Muzzle of Guns," *Shock and Vib. Bull.* 39, Part 6, pp 139-149 (March 1969).

136. Thornhill, C.K., "A Stationary Model of the Explosion From a Moving Spherical Charge," ARDE Rept. (B) (November 1957).

137. Smith, F., "A Study of Gun Blast in Relation to That From a Moving Explosion," RARDE Memorandum 28 (1970).

REFERENCES *(Cont.)*

138. Baker, W.E., Westine, P.S., Bessey, R.L., "Blast Fields About Rockets and Recoilless Rifles," Final Technical Report SwRI Project 02-27-67 (May 1971).

139. Armour Research Foundation, "Investigation of the Effect of Blast from Recoilless Rifles," prepared for Frankford Arsenal (June 30, 1954).

140. Zimmerman, J.R., Vechio, R.A., "Back Blast Determination of a 105 mm Recoilless Rifle for an Aerial Artiller Weapons System," Ammunition Engineering Directorate, Picat ny Arsenal, Tech Rept. 3420 (August 1966).

141. Baker, W.E., Silverman, S., Cox, P.A., Young, D., "Structural Response of Helicopter to Muzzle and Breech Blast," Ballistics Research Laboratories (Aberdeen) Report March 1969. Also *Shock and Vib. Bull.* 40, Part 2, pp 227-241, (December 1969).

142. Smith, F., "Loads on Surfaces Due to Gun Blasts," Royal Armament Research and Development Establishment, RARDE Memorandum 29/70 (1970).

143. Sevy, R.W., Ruddell, E.E., "Low and High Frequency Aircraft Gunfire Vibration; Predictions and Laboratory Simulation," AFFDL-TR-74-123 (August 1974).

144. McIntosh, V.C., Bolds, P.G., "Vibration and Acoustic Environment of UH-IC Helicopter Configured With and Using M-5 and XM-21 Armament," AFFDL-TR-73-160 (February 1974).